

A LAB-ON-A-CHIP SYSTEM INTEGRATING DIELECTROPHORETIC
DETECTION AND IMPEDANCE COUNTING UNITS FOR CHEMOTHERAPY
GUIDANCE IN LEUKEMIA

A THESIS SUBMITTED TO
THE GRADUATE SCHOOL OF NATURAL AND APPLIED SCIENCES
OF
MIDDLE EAST TECHNICAL UNIVERSITY

BY

YAĞMUR DEMİRCAN YALÇIN

IN PARTIAL FULFILLMENT OF THE REQUIREMENTS
FOR
THE DEGREE OF DOCTOR OF PHILOSOPHY
IN
ELECTRICAL AND ELECTRONICS ENGINEERING

MAY 2018

Approval of the thesis:

**A LAB-ON-A-CHIP SYSTEM INTEGRATING DIELECTROPHORETIC
DETECTION AND IMPEDANCE COUNTING UNITS FOR
CHEMOTHERAPY GUIDANCE IN LEUKEMIA**

submitted by **YAĞMUR DEMİRCAN YALÇIN** in partial fulfillment of the requirements for the degree of **Doctor of Philosophy in Electrical and Electronics Engineering Department, Middle East Technical University** by,

Prof. Dr. Halil Kalıpçılar
Dean, Graduate School of **Natural and Applied Sciences**

Prof. Dr. Tolga Çiloğlu
Head of Department, **Electrical and Electronics Engineering**

Prof. Dr. Haluk Külâh
Supervisor, **Electrical and Electronics Engineering Dept., METU**

Examining Committee Members:

Prof. Dr. Tayfun Akın
Electrical and Electronics Engineering Dept., METU

Prof. Dr. Haluk Külâh
Electrical and Electronics Engineering Dept., METU

Assoc. Prof. Dr. A. Elif Erson Bensen
Biological Sciences Dept., METU

Assoc. Prof. Dr. Barbaros Çetin
Mechanical Engineering Dept., Bilkent University

Assist. Prof. Dr. Ender Yıldırım
Mechanical Engineering Dept., Çankaya University

Date: 31.05.2018

I hereby declare that all information in this document has been obtained and presented in accordance with academic rules and ethical conduct. I also declare that, as required by these rules and conduct, I have fully cited and referenced all material and results that are not original to this work.

Name, Last name: Yağmur Demircan Yalçın

Signature:

ABSTRACT

A LAB-ON-A-CHIP SYSTEM INTEGRATING DIELECTROPHORETIC DETECTION AND IMPEDANCE COUNTING UNITS FOR CHEMOTHERAPY GUIDANCE IN LEUKEMIA

Demircan Yalçın, Yağmur
PhD., Department of Electrical and Electronics Engineering
Supervisor: Prof. Dr. Haluk Külâh

May 2018, 209 pages

Precision medicine is defined as therapies, directed to the requirements of individual patients on the basis of genetic, biomarker, phenotypic, or psychosocial characteristics, discriminating a given patient from others with similar clinical states. Oncology is the foremost application area of precision medicine. Although the aim of precision medicine is very clear and simple, the clinical practice of it in cancer patients has some challenges, such as tumor heterogeneity.

Tumor heterogeneity can be the most challenging part, causing that the targeting a single genetic abnormality cannot be optimum way of controlling the cancer. Multidrug resistant sub-clone formation is one of the heterogeneity concepts.

The detection of multidrug resistance in leukemia cancer cells is the main aim of this thesis. Biological and electrical characterization, Annexin V/PI apoptosis assay and ion release-based impedance spectroscopy, respectively, have been carried out to determine the parameters of drug resistance detection, based on dielectrophoresis. The cell lines in our laboratory were classified as high-level laboratory and clinically relevant model of resistance. Next, the aim in the apoptosis assays was to determine correct time and doses for the screening of *imatinib* and *doxorubicin* effects on K562 and CCRF-CEM cells by electrical analysis. For CCRF-CEM/wt cells, time and dose were determined as 18h and 250 nM doxorubicin while the major death mode in K562/wt cells was not observed as apoptosis. Therefore, 24h and 300 nM imatinib

were chosen for K562/wt cells' electrical examinations. Cell cytoplasmic conductivity is one of the key parameters, changing according to physiological properties of cells. Ion release-based impedance spectroscopy was utilized for the first time in the literature to determine average total ion concentration of a cell. Results show that the total ion concentration of K562/imaR cells was 1.78 times higher than that of K562/wt ones while CCRF-CEM/doxR cells have 1.2 times higher ion concentration than wild type ones. Using the ratio between K562 cells, DEP medium conductivity and operation frequency were determined as 200 mS/m and 8.59 MHz. Values were identified as 160 mS/m and 6.15 MHz for CCRF-CEM cells.

3D and planar electrodes were implemented in LOC system integrated with the IS counting units for quantification of trapped cells by DEP. Although higher DEP force is necessary in high conductivity buffer-based DEP, 3D-obstacle electrodes acted like hydrodynamic traps due to the elasticity of leukemia cells and misinterpretation in trapping analysis occurred. Therefore, analyses were continued with planar electrode devices.

Under normal growth conditions, 3 biological replicates of K562/wt and K562/imaR cells were analyzed with this LOC system at 8.59 MHz and 20 V_{pp} voltage immersing them into a DEP solution, having 200 mS/m conductivity. 57.6% ($\pm 6.7\%$) of resistant cells were trapped on electrodes while wild type ones were trapped with a ratio of 20.3% ($\pm 4.2\%$). This can be interpreted as the tumor heterogeneity can be determined in terms of MDR level. Drug exposed K562 cells during 24h were analyzed by the LOC system. Results show that the trapping ratio of wild type cells exposed to drug was decreased to half of control group, endorsing that DEP can achieve drug screening.

In conclusion, DEP can achieve both the quantification of tumor heterogeneity in terms of drug resistance and drug screening. As a future work, cell adhesion to parylene, cell precipitation in inlet reservoir, and channel cleaning problems should be solved by optimizing channel coating procedure, using zero-dead-volume interfaces, and constructing a valve-tubing system at the inlet of LOC system, respectively.

ÖZ

KEMOTERAPİNİN YÖNLENDİRİLMESİNİ SAĞLAYACAK DİELEKTROFORETİK TEŞHİS VE EMPEDANS SAYMA BİRİMLERİNİN ENTEĞRE EDİLDİĞİ ÇİP-ÜSTÜ-LABORATUVAR SİSTEMİ

Demircan Yalçın, Yağmur
Doktora, Elektrik ve Elektronik Mühendisliği Bölümü
Tez Yöneticisi: Prof. Dr. Haluk Külâh

Mayıs 2018, 209 sayfa

Hassas tıp, hasta diğer hastalarla benzer klinik özelliklere sahip olsa dahi, hastanın genetik, biyo-işaretçi, fenotipik ya da fiziko-sosyal karakteristikleri dikkate alınarak; kişiye özel geliştirilecek şekilde tasarlanan tedavilerin genel adıdır. Onkoloji, hassas tıbbın önde gelen uygulama alanlarından biridir. Fakat, amacı oldukça açık ve basit olmasına rağmen, hassas tıbbın klinikte kanser hastalarına uygulanmasının bazı zorlukları bulunmaktadır.

Tümör heterojenliği bu zorlukların en önemlilerinden bir tanesidir. Bu durum tek bir genetik anormalliği hedef alarak optimum tedaviye ulaşmayı imkânsız kılmaktadır. Tümör içerisinde, çoklu ilaç dirençliliğine sahip alt popülasyonların oluşması bir tümör heterojenliği konseptidir.

Bu tezin ana amacı, lösemi hücrelerinde çoklu ilaç dirençliliğinin tespitidir. Dielektroforez yöntemi ile çoklu ilaç dirençliliğinin tespitini sağlayacak sistemin, analiz parametrelerinin belirlenmesi adına; Annexin V/PI şeklinde adlandırılan biyolojik analizler ve iyon salınımını ölçme temelli empedans spektrum analizi (elektriksel) tamamlanmıştır. Tez sürecinde kullanılan hücre hatları yüksek-seviye laboratuvar ve klinik ile alakalı rezistans modeli olarak sınıflandırılmıştır. Ardından, apoptozis analizleri sayesinde, elektriksel analizlerde K562 hücrelerine imatinib CCRF-CEM hücrelerine doxorubicin uygulanması gereken doz ve saatler belirlenmiştir. Bu saat ve doz doxorubicin ve CCRF-CEM hücreleri için 18s ve 250

nM iken, K562 hücreleri ve imatinib uygulaması için 24s ve 300 nM oluştur. Hücrenin sitoplazmik iletkenliği fizyolojik özelliklerine bağlı olarak değişen anahtar parametrelerden birisidir. Bu değere ulaşılabilmesi adına, iyon salınımını ölçme tabanlı empedans spektroskopisi metodu literatürde ilk defa bir hücrenin ortalama toplam iyon konsantrasyonunu belirlemek için bu çalışmada kullanılmıştır. Sonuç olarak, imatinib dirençli K562 hücrelerinin toplam iyon konsantrasyonu “wild type” olanlardan 1.78 kat fazla çıkarken, CCRF-CEM hücrelerinde bu oran 1.2 olarak tespit edilmiştir. Bu oranlar kullanılarak, K562 hücreleri için DEP solüsyonu iletkenliği 200 mS/m ve çalışma frekansı 8.59 MHz olarak belirlenmiştir. Bu parametreler CCRF-CEM hücreleri için 160 mS/m ve 6.15 MHz'dir.

Tasarlanan çip-üstü-laboratuvar sistemi DEP alanı için hem 3 boyutlu hem de planar elektrot tipleri seçilmiş ve hücre sayma birimleri ile entegre edilmesi sağlanmıştır. Yüksek iletkenlikli DEP solüsyonları ile çalışırken yüksek DEP kuvvetine ihtiyaç olmasına rağmen, 3 boyutlu elektrotlar, lösemi hücrelerinin elastikliği sebebi ile kanal içinde hidrodinamik hücre yakalama alanları yarattıkları için DEP kuvveti ile yakalanan hücrelerin yorumlanmasında yanlış yorumlama yarattığından analizlere planar elektrotlar ile devam edilmiştir.

Normal büyüme şartlarında 3 biyolojik örnekle tekrar edilen K562 hücreleri deneylerinde, DEP etkisi altında imatinib dirençli K562 hücreleri %57.6 ($\pm 6.7\%$) tutunma gösterirken, “wild type” K562 hücreleri %20.3 ($\pm 4.2\%$) yakalanabilmiştir. Bu durum, tümör heterojenliğinin ÇİD seviyesi açısından DEP ile belirlenebildiğini göstermektedir. Ayrıca, 24s ilaç etkisi altında büyütülmüş K562 hücreleri aynı sistem ile analiz edildiğinde, tutunmanın yarıya düştüğü ilaç etkisi analizlerinin de bu sistemle yapılabileceğine örnek oluşturarak gösterilmiştir.

Sonuç olarak, tasarlanan çip-üstü-laboratuvar sisteminin hem tümör heterojenliğinin hem de ilaç dirençliliğinin nicel olarak değerlendirilmesinde kullanılabileceği gösterilmiştir. Ayrıca, parilen kanala hücre yapışması, inlet rezervuarında hücre çökmesi ve kanalın her hücre analizi arasında temizlenmesi sorunları; kanal kaplama prosedürlerinin optimize edilmesi, ölü hacim oranını azaltan ara parçaların

kullanılması ve kanal girişinden önce vana ve mikro tüplerden oluşan bir kanal temizleme sisteminin entegre edilmesi ile çözülebilir.

To my mother, father, grandmother and “zuzum”

ACKNOWLEDGEMENT

After lots of academic writing and reading, I could not find the correct and emotional words to start. However, I should write my thankfulness and explain my feelings at the end of all these 5 years since all these successes were not achieved alone. Firstly, I would like to express my deep thanks to my thesis advisor, *Prof. Dr. Haluk Klah* for believing and supporting me during my undergraduate and graduate studies. I would like to thank to my jury members, *Prof. Dr. Tayfun Akın*, *Assoc. Prof. Dr. Barbaros etin*, *Assoc. Prof. Dr. A. Elif Erson Bensan*, and *Assist. Prof. Ender Yldırım*. Moreover, I would like to thank to *Prof. Dr. Rengl etin Atalay* and her PostDoc *Deniz Cansen Kahraman* for sharing me their laboratory and helping me to make some of my biological analyses. I would like to thank to members of METU Central Laboratory, *Assoc. Prof. Dr. ağdam Devrim Son*, *Dr. Nalan Kamalı Babacan*, and *Harun Gndz*. I am also thankful to *Prof. Dr. Ufuk Gndz* and *Dr. Gneş Esendağlı* and his student *Utku Horzum* to collaborate us with providing cancer cell lines.

I would like to thank to The Scientific and Technological Research Council of Turkey (TUBITAK) for the scholarship support for me.

I am particularly thankful to my colleague *Taylan Tral* for making all my long and challenging fabrications. Also, many thanks to *zge Zorlu* and *Ender Yldırım* to help me for making clear of all my puzzles about lots of results and tests. Moreover, many thanks to my friend *Tuğe Temir* to make reviews of my thesis and her friendship.

I would also thank to Sukas family members, *zlem*, *Gke*, and *Kemal* for their love. I am very happy to meet them. And *Sertan*, he changed my scientific point of view and taught lots of things that I cannot count all of them here. Thank you for all your support.

Many thanks to all BioMEMS Research Group and Mikro Biyosistemler Elektronik members to create a very enjoyable work environment for me. Above all, I am very thankful to them for being good friends. I would also like to thank all METU-MEMS Center staff for their kind helps in cleanroom. Many thanks particularly to *Orhan Akar* for sharing his deep knowledge on microfabrication and for his helps in the cleanroom and *Murat Yağcı* for the wire-bonding step of my LOC systems.

Seçil...I am very sorry to lose you; but, I am very lucky to share some time and feelings with you. I could not say anything in your funeral but now, it is the time. Thank you for all your support and sincerity. You taught me the pure humanity. Again, I am dedicating this study to you and all cancer patients. I hope that a day, all their indescribable pain will end.

I would like to thank to Tufan family: *Mehtap* and *Gökhan*. I love you guys. Many thanks for your support and listening all my complaints about everything.

Coming towards to end, I would like to express my deepest thankfulness to my mother, *Günay Kahraman*, my father, *Rahmi Demircan*, and my grandmother, *Kübra Kahraman*, for their endless, priceless and ineffable patience and support. Moreover, I am thankful to them to give me the freedom for achieving all my dreams.

In this journey, I had another family. I would thank to all of them, my mother *Gülşüm Yalçın*, my father *Ali Yalçın*, and my brother *Onur Yalçın* for their support, patience, and love.

Finally, I would like to thank to my love of life, my spouse, my “*zuzu*”, actually my everything, *Hüseyin Yalçın*, for his patience, support, love, and never leave me alone all my life and the long testing nights in laboratory. Thanks to him, all question marks are deleted from my life.

Finally, I would like to thank to my soul to stand up and continue to try after all my failures. Lots of tears and energy were spent through this journey. On the other hand, lots of valuable things were earned so never stop and please live all the moments in your lives.

TABLE OF CONTENTS

ABSTRACT	v
ÖZ.....	vii
ACKNOWLEDGEMENT.....	xiii
TABLE OF CONTENTS	xv
LIST OF TABLES	xix
LIST OF FIGURES	xxi
CHAPTERS.....	1
1 INTRODUCTION.....	1
1.1 Precision medicine: Customization of healthcare.....	2
1.1.1 Evolution of precision medicine	2
1.1.2 Precision medicine in oncology	4
1.1.3 Challenges of precision medicine in oncology	6
1.2 Multi-drug resistance (MDR)	9
1.2.1 Potential mechanisms of MDR in cancer chemotherapy	9
1.2.2 Overcoming MDR.....	14
1.2.3 MDR detection approaches	15
1.3 Dielectrophoresis (DEP): As a potential tool for the detection of MDR.....	17
1.3.1 DEP theory	17
1.3.2 Challenges in DEP	19
1.3.3 MDR detection through DEP	22
1.4 Research objectives and thesis organization.....	24
2 CYTOTOXICITY, APOPTOSIS, AND CELL CYCLE ANALYSIS IN CHRONIC MYELOGENOUS, ACUTE LYMPHOID, AND ACUTE PROMYELOCYTIC LEUKEMIA CELLS	27
2.1 Cell cycle, cell death, and cancer.....	28
2.1.1 Cell cycle.....	28

2.1.2 Cell death	31
2.1.3 Cancer	36
2.2 Leukemia	37
2.2.1 Information about CML, ALL, and APL.....	37
2.2.2 Treatment of leukemia	39
2.2.3 Precision medicine in leukemia	41
2.3 Drug pharmacodynamics	43
2.3.1 Imatinib, doxorubicin, and ATRA (Tretinoin).....	43
2.3.2 <i>In vitro</i> models for drug pharmacodynamics: <i>Cell lines</i>	46
2.3.3 Drug effect on cell proliferation through XTT assays	48
2.3.4 Drug effects on apoptotic cell death: Time and dose dependency.....	62
2.3.5 Cell cycle effects of drugs.....	69
2.4 Conclusion	70
3 ELECTRICAL CHARACTERIZATION OF WILD TYPE AND DRUG RESISTANT LEUKEMIA CELLS USING IMPEDANCE SPECTROSCOPY ...	71
3.1 Overview of membrane transport proteins	71
3.1.1 Ion channels	72
3.1.2 ATP-powered Pumps	73
3.1.3 Transporters: Symporters and Antiporters.....	74
3.2 Ions, apoptosis, and multidrug resistance	75
3.3 Cell ion release-based impedance spectroscopy (IRbIS) using microfluidic systems.....	79
3.3.1 Interdigitated electrode (IDE) design.....	82
3.3.2 Fabrication	85
3.3.3 Method of operation.....	87
3.3.4 Results: Total ion concentration of leukemia cells under typical growth conditions	97
3.3.5 Estimation of DEP operation conditions.....	108
3.4 Conclusion	110
4 DIELECTROPHORETIC DETECTION AND IMPEDOMETRIC QUANTIFICATION OF LEUKEMIA CELL HETEROGENEITY IN TERMS OF DRUG RESPONSE.....	111

4.1 Examination of P-gp, MRP1, and BCRP in K562 and CCRF-CEM cell lines by flow cytometry	114
4.1.1 Materials and methods	115
4.1.2 Results	116
4.1.3 Discussion	118
4.2 LOC system based on a microfilter integrated DEP system for MDR cell separation from RBCs.....	118
4.2.1 The effect of drug resistance level on DEP response of cancer cells....	118
4.2.2 The separation of MDR and wild type cells.....	119
4.2.3 System design.....	121
4.2.4 Fabrication.....	123
4.2.5 Materials and methods	125
4.2.6 Results	126
4.2.7 Discussion	127
4.3 LOC system integrating DEP detection and IS counting units for chemosensitivity analyses.....	128
4.3.1 System design.....	128
4.3.2 Fabrication.....	134
4.3.3 Materials and methods	137
4.3.4 Theory of operation.....	139
4.3.5 Results	141
4.4 Conclusion	144
5 CONCLUSION AND OUTLOOK	147
REFERENCES	151
Appendix A: MATLAB code for $Re(f_{CM})$ vs frequency simulations	167
Appendix B: MATLAB code for the analysis of LOC system	169
CURRICULUM VITAE	181

LIST OF TABLES

Table 2.1: IC ₅₀ and EC ₅₀ values of K562 cells under the exposure of imatinib for 48h. Data is presented as mean±stdev. BR: Biological replicate.	57
Table 2.2: IC ₅₀ and EC ₅₀ values of CCRF-CEM cells under the exposure of <i>doxorubicin</i> for 24h. Triplicate measurements at each drug level were carried out in the analysis of each biological replicate (BR).	59
Table 2.3: K562/wt cell viability under the effect of <i>imatinib</i> during 24 and 48h..	66
Table 2.4: CCRF-CEM/wt cell viability under the effect of <i>doxorubicin</i> during 18 and 24h. One measurement was taken.....	67
Table 3.1: Typical ion concentrations inside a mammalian cell and blood [98].....	72
Table 3.2: Geometrical properties of IDEs.....	85
Table 3.3: Calculated cell constants for 3 different IDE devices.	91
Table 3.4: Minimum and maximum cell numbers were used in the analyses of total ion concentration inside cytoplasm.	94
Table 3.5: Cell radius (r). Measurements are presented as mean±stdev (n=3). AVG: average and pl: picolitre.	100
Table 3.6: Total ion concentrations [I] of K562/wt and K562/imaR cells. Calculations are presented as mean±stdev (n=3). AVG: average and mM: millimolar.....	100
Table 3.7: Cell radius (r). Measurements are presented as mean±stdev (n=3). AVG: average, pl: picolitre, and BR: biological replicate.	104
Table 3.8: Total ion concentrations [I] of CCRF-CEM/wt and CCRF-CEM/doxR cells. Calculations are presented as mean±stdev for 3 different measurements (n=3). AVG: average, mM: millimolar, and BR: biological replicate.	104
Table 3.9: Estimated cytoplasmic conductivity (mS/m) of K562 and CCRF-CEM cells.....	108
Table 4.1: P-gp expression in K562 and CCRF-CEM cell lines.....	118
Table 4.2: The ratio of trapped MDR K562 cells to trapped RBCs for 4 cell mixtures, injected into channel with different ratios of MDR K562 cells to RBCs.....	127

Table 4.3: Adhesion and trapping ratio of K562/imaR and K562/wt cells when DEP voltage is OFF and ON..... 143

LIST OF FIGURES

Figure 1.1: Evolution of the term precision medicine [7].	4
Figure 1.2: Functional schematic of ABC transporters (TMD: Transmembrane domain, NBD: Nucleotide-binding domain) [25].....	10
Figure 1.3: $Re(f_{CM})$ vs. frequency graph of three particles with different conductivities ($\sigma_{p1} > \sigma_{p3} > \sigma_{p2}$).	19
Figure 1.4: Effective membrane conductance (G_{eff}) (top) and cytoplasmic conductivity (σ_{cyt}) (bottom) variation of RBCs according to circadian rhythm [39].	20
Figure 1.5: The images of inlet (a) and outlet (b) of separation channel, and efficiency (c) [43].	21
Figure 1.6: Trapping of imatinib resistant (a) and path of sensitive K562 cells (b) at a flow rate of 10 μ l/min under 9 V_{pp} voltage at 48.64 MHz.	23
Figure 2.1: Cell cycle in eukaryotic cells [54].....	29
Figure 2.2: The stages of mitosis [55].	29
Figure 2.3: Annihilation of tail through apoptosis while a tadpole is metamorphosed into a frog [59].	32
Figure 2.4: Stages of apoptosis [63].	33
Figure 2.5: A healthy white blood cell (a) and a late apoptotic one (b) [64].	34
Figure 2.6: SEM images of an apoptotic cells stage by stage. (a) Cell shrinkage, (b) Nuclear condensation, (c) Cell shrinkage, (d) Blebbing [65].	35
Figure 2.7: Invasion of normal tissue by a growing tumor [66].	37
Figure 2.8: Blood cells in chronic (a) and blast (b) phase of a CML patient.	38
Figure 2.9: Image of leukemia cells of an APL patient.	38
Figure 2.10: Translocation, t[9, 22], in Philadelphia chromosome.	42
Figure 2.11: <i>Imatinib</i> action mode [79].	44
Figure 2.12: Differentiated cancer cells of a patient into matured cells under the effect of <i>ATRA</i> [84].	45

Figure 2.13: Cell morphologies: (a) K562, (b) CCRF-CEM, and (c) HL60. 63X was utilized in the microscope Leica LED 2000 with bright field.	48
Figure 2.14: Induction of XTT to its colorful product formazan.	50
Figure 2.15: XTT assay procedure.	51
Figure 2.16: Dose response nonlinear curve fitting in <i>OriginPro 2017</i>	53
Figure 2.17: <i>Imatinib</i> response of K562/wt cells for 8h (a) and 18h (b). Data is presented as mean±stdev for duplicate measurement at each drug level (n=1).	54
Figure 2.18: <i>Imatinib</i> response of K562/wt cells for 24h (a) and 48h (b). Data is presented as mean±stdev for duplicate measurement at each drug level (n=1).	55
Figure 2.19: IC ₅₀ values of K562/wt (a) (n=3) and K562/imaR cells (n=2) (b) obtained at the end of 48h. (c) Comparison of IC ₅₀ values of K562/wt and K562/imaR cells. Data is presented as mean±stdev. * p<0.05 significantly different calculations. BR: Biological replicate.	56
Figure 2.20: <i>Doxorubicin</i> response of CCRF-CEM cells for 8, 18, and 24h.	57
Figure 2.21: Dose response curve of CCRF-CEM/wt cells under <i>doxorubicin</i> exposure for 8h (a), 18h (b), and 24h (c) (n=1). Measurements were taken from 2 different well for each drug dose.	58
Figure 2.22: IC ₅₀ values of CCRF-CEM/wt (n=3) (a) and CCRF-CEM/doxR cells (n=2) (b). (c) Comparison of IC ₅₀ values of CCRF-CEM/wt and CCRF-CEM/doxR cells. Data is presented as mean±stdev. * p<0.05 significantly different results. BR: Biological replicate.	60
Figure 2.23: 48h <i>ATRA</i> response of HL60 cells. Measurements were taken from 3 different wells (n=1). Data presented as mean±stdev.	61
Figure 2.24: As an early sign of apoptosis, PSs translocate into outer leaflet. Fluorescently tagged Annexin-V can bind to PSs. Utilizing flow cytometry PSs can be detected.	64
Figure 2.25: Time dependent effect of 0.5 μM staurosporine on Jurkat cells, examined with Annexin-V/PI assay by using flow cytometry [93].	64
Figure 2.26: MUSE cell analyzer.	65
Figure 2.27: Apoptosis profile of K562/wt cells under the effect of <i>imatinib</i> for 24h.	66

Figure 2.28: Apoptosis profile of K562/wt cells under the effect of <i>imatinib</i> for 48h.	67
Figure 2.29: Apoptosis profile of CCRF-CEM/wt cells under the effect of 250 nM <i>doxorubicin</i> during 18h (a) and 24h (b).	68
Figure 2.30: <i>Imatinib</i> response of K562 cell with cell cycle assay.	70
Figure 3.1: Membrane transport proteins: Ion channels, ATP-powered pumps, and transporters [98].....	72
Figure 3.2: Four main sub-classes of ATP-powered pumps.	73
Figure 3.3: Transportation of glucose by the aid of sodium symporter [100].....	74
Figure 3.4: Ions and ion channels, having role in apoptosis [104].....	76
Figure 3.5: Anti- and pro-apoptotic ion channels in cell membrane, involved in MDR (Adapted from [109]).....	77
Figure 3.6: Water (a) and ion content (Cl^- (b), K^+ (c), and Na^+ (d)) of wild type EATC cells under the effect of 5 μM <i>cisplatin</i> during apoptosis.	78
Figure 3.7: Cell volume change (a) and caspase 3 activity (b) in MDR and wild type (Wt) EATC cells under the effect of 5 μM <i>cisplatin</i> according to time.....	79
Figure 3.8: Cl^- (a), K^+ (b), and Na^+ (c) content during apoptosis in wild type and MDR EATC cells under the exposure of <i>cisplatin</i> (5 μM) [110].....	79
Figure 3.9: (a) A constricted cell and (b) Schematic view of geometrical model of its.	82
Figure 3.10: Structure (a), electrical equivalent circuit (b), magnitude (c) and phase (d) characteristics of an IDE.....	84
Figure 3.11: Si-glass fabrication flow of IDE devices.	86
Figure 3.12: Fabricated devices and IDE structure.	86
Figure 3.13: Chip holder designed by Dr. Sertan Sukas.	87
Figure 3.14: Representative fitting curves and experimental data.	88
Figure 3.15: Linear fitting curves of IDE cell ₁ (a), cell ₂ (b), and cell ₃ (c) for cell constant calculation.	90
Figure 3.16: Calibration curves of IDE devices.	92
Figure 3.17: Cell lysis procedure.....	94
Figure 3.18: Experimental setup.....	97

Figure 3.19: Comparison of (a) K562/wt cells' radius and (b) K562/imaR cells' radius for 3 biological replicates (BR) (n=3) with duplicate measurements for each replicate. (c) The radius comparison between K562/wt and K562/imaR cells (n=3). Data is presented as mean±stdev. * p<0.05 significantly different measurements. # shows that means are not significantly different at 0.05 level. 99

Figure 3.20: Conductivity vs total cell number plots of the of K562/wt (a) and K562/imaR (b) cells. 2 measurements were taken for each cell number. Linear fitting was applied and $R^2>0.99$ criteria were taken into account..... 100

Figure 3.21: Total ion concentrations (mM) of a single cell inside 3 biological replicates of K562/wt (a) and K562/imaR (b) cells. (c) The comparison of total ion concentration inside cytoplasm of a single cell of wt and imaR. Data is presented as mean±stdev. * p>0.05 not significantly different measurements. # shows that means are significantly different at 0.05 level (n=3)..... 101

Figure 3.22: Comparison of (a) CCRF-CEM/wt cells' radius (n=3) and (b) CCRF-CEM/doxR cells' radius (n=3). (c) The radius comparison between CCRF-CEM/wt and CCRF-CEM/doxR cells (n=3). Data is presented as mean±stdev. * shows that means are significantly different at 0.05 level. 103

Figure 3.23: Total ion concentrations (mM) of a single cell for 3 biological replicates of CCRF-CEM/wt (a) and CCRF-CEM/doxR (b) cells (n=3). (c) The comparison of total ion concentration inside cytoplasm of a single cell of wt and doxR (n=3). Data is presented as mean±stdev for triplicate measurements for each replicate. * p>0.05 not significantly different measurements. 105

Figure 3.24: Total ion concentrations (mM) of a single cell for 2 biological replicates of HL60/wt (a) and HL60/ATRAR (b) cells (n=2). (c) The comparison of total ion concentration inside cytoplasm of a single cell of wt and ATRAR (n=6). Data is presented as mean±stdev for triplicate measurements. * p>0.05 not significantly different measurements. 107

Figure 3.25: Simulations of $Re(f_{CM})$ to determine frequencies at which the maximum $Re(f_{CM})$ value obtained for K562/imaR cells in DEP medium, having conductivity of (a) 221, (b) 265, and (c) 331 mS/m. 109

Figure 4.1: P-gp expression in the cancer cells of patients. Although the overexpression of P-gp was observed, patients may not be resistant or vice versa.	113
Figure 4.2: P-gp (a, d), BCRP (b, e), and MRP1 (c, f) expressions in K562 (left column) and CCRF-CEM (right column) cells.	117
Figure 4.3: The relationship between the drug resistance level and DEP responses of K562 MDR cells.	119
Figure 4.4: Pseudo-colored images taken during the detection of imatinib (A) and doxorubicin (B) resistance in K562 cells at a flow rate of 6.67 $\mu\text{l}/\text{min}$, utilizing the MDR and drug sensitive cell mixtures. Flow rate performance analysis of DEP devices through the separation of K562/imaR cells and sensitive K562 cells at a flow rate of 10 $\mu\text{l}/\text{min}$ (C). Working solution was the mixture of K562/imaR and sensitive K562 cells with 2.5×10^3 cells/ml and 2.5×10^5 cells/ml, respectively ($f = 48.64$ MHz, $V = 9 V_{pp}$). Pseudo-colored images taken during tests with only sensitive K562 cells (D). No trapping occurs until $t=12$ s. A few cells, trapped during the flow, were carried away at the end of 45 s, necessary duration to reach steady state conditions. Through all tests, only one side-wall electrode array was energized to provide better visualization [22].	121
Figure 4.5: Device schematic. The system consists of 2 consecutive DEP units for the depletion of RBCs and capturing of MDR K562 cells [49].	122
Figure 4.6: $Re(f_{CM})$ vs. frequency graphs of RBCs, drug sensitive and MDR K562 cells in a medium with 2.5 mS/m conductivity and 78 permittivity coefficient. ..	123
Figure 4.7: Fabrication flow.	124
Figure 4.8: Fabricated device [49].	124
Figure 4.9: Pseudo-colored images taken during detection of MDR-K562 cells, green screens. Red screens show RBCs. Working solution was the mixture of MDR-K562 cells and RBCs with different concentrations ($f=1$ MHz and $f=48.64$ MHz for depletion and detection units, respectively. $Flow\ rate = 10 \mu\text{l}/\text{min}$, $voltage = 20 V_{pp}$) [49].	126
Figure 4.10: Conical filters placed on the side-walls of microchannel.	127
Figure 4.11: Cell escape (a) and clogging (b) in the conical filters.	128
Figure 4.12: Schematic of the LOC system.	129

Figure 4.13: Schematic and electric field gradient simulations of castellated (a, b) and diamond (c, d) electrodes.....	130
Figure 4.14: Comparison of cell trapping efficiency of circular electrodes (a) and circularly placed circular electrodes.....	132
Figure 4.15: Particle tracing results of distribution unit for planar (a) and 3D-electrodes (b).	133
Figure 4.16: Fabrication flow of LOC-1.	134
Figure 4.17: Fabricated LOC-1 focusing on the planar electrodes, IS unit, and microfluidic connection between units.....	135
Figure 4.18: Fabrication flow of LOC-2.	136
Figure 4.19: Fabricated device with 3D-electrodes.....	137
Figure 4.20: Rigid PCB connecting LOC system to signal generator and impedance spectrometer (left) and flexible PCB carrying LOC system (right).	138
Figure 4.21: Re(fCM) vs frequency simulation of cells with cytoplasmic conductivity changing between 180-400 mS/m in a DEP solution at a conductivity of 200 mS/m.	140
Figure 4.22: Impedance vs time data taken by both IS units (E_1 : at the inlet and E_2 : at the outlet). Cross-correlation was carried out in MATLAB to eliminate delay between data.	141
Figure 4.23: Trapped cells inside 3D-electrode cages due to cell elasticity.	141
Figure 4.24: Trapped cell ratio of K562/imaR (left column) and K562/wt (right column) cells under the same experimental conditions (frequency=8.59 MHz, voltage=20 V_{pp} , solution conductivity=200 mS/m, cell concentration= 5×10^5 cells/ml). Results are presented as mean \pm stdev. * $p < 0.05$ significantly different trapping trends (n=3).	143
Figure 4.25: Flexible Hydraulic Reservoir (FHR) proposed by [133] as zero-dead volume sample loading interface.....	145

CHAPTER 1

INTRODUCTION

Cancer is a common term for a large group of diseases, affecting any part of the body. Malignant tumors and neoplasms can be used instead of it. One hallmark of cancer is the rapid creation and growth of abnormal cells, invading parts of the body. The crucial part of the adequate and effective cancer treatment is the accurate diagnosis since every cancer type requires a specific treatment regimen. Cancer has been identified based on organ-based classification, such as lung, liver, and breast cancer, for centuries. On the other hand, due to patient to patient differences, this classification was not enough to provide complete recovery with common therapies [1]. This requires a way to customize healthcare. Precision medicine became the term which is given to this approach. However, this method has some challenges in the application of oncology area. The major one of them is the tumor heterogeneity. Multidrug resistance (MDR) is one of the tumor heterogeneity concepts and almost half of cancer patients suffer from MDR [2]. It can be defined as a condition enabling a cancer cell to resist distinct drugs or chemicals targeted at eradicating the cell [3].

My MSc thesis have been inspired a study in which differences in dielectrical properties of multidrug resistant and drug sensitive cells were reported [4]. At the end, I claimed and proved that MDR detection can be achieved by utilizing dielectrophoresis (DEP), a cell manipulation technique based on dielectrical properties. However, results were not repeatable for all conditions. I could not determine the specific conditions at which MDR detection by DEP is possible. Therefore, I have started to my PhD thesis to identify these conditions. Moreover, there is not either an electrical or a biological threshold value to categorize a cell as drug resistant. Therefore, biological and electrical characterizations have been included into my PhD thesis scope. XTT, apoptosis, and cell cycle assays have been used for biological characterization. By means of ion release-based impedance

spectroscopy, electrical characterization has been achieved. As a result, “chemotherapy guidance” has become the term chosen for the aim of this thesis. This chemotherapy guidance system has two impedance-based counting units for quantification and a DEP unit for detection. Details about this system will be explained in Chapter 4.

In this chapter, firstly, evolution and challenges of precision medicine in oncology are explained. Next, mechanisms, detection, and overcoming approaches of MDR are presented. Finally, theory, challenges, and MDR detection studies of DEP are reviewed.

1.1 Precision medicine: Customization of healthcare

Precision medicine is defined as therapies, directed to the requirements of individual patients on the basis of genetic, biomarker, phenotypic, or psychosocial characteristics, discriminating a given patient from others with similar clinical states [5]. It is a relatively new term. On the other hand, concept has been exploited in healthcare for many years. For example, the blood type of donor should match the blood type of recipient in blood transfusion to reduce the risk of complications [6].

1.1.1 Evolution of precision medicine

In 1871, by the identification of nuclein, known as DNA today, the basis of genomics was established. In 1953, Watson and Crick determined the double-helix structure of DNA as a pivotal step to human genome project, started in 1990 and completed in 2003. With the experiences of human genome project and by utilizing technological advances, data recording and interpretation have been accelerated, providing comparative and rapid study on the patient situations. All these improvements led to the evolution of a term, precision medicine, defined as customization of healthcare (Fig. 1.1) [7].

In 2011, a committee hold a meeting to develop a new taxonomy of human diseases based on molecular biology. A report was presented as “Towards Precision Medicine” at the end of the meeting [8]. Conclusions of this meeting are as follows:

- A new taxonomy will lead to better healthcare since the disease taxonomy of today classifies the subtypes of many disease as one disease even they have distinct molecular evidences. Conversely, multiple different diseases can share a common molecular evidence. This misinterpretation prevents the evaluation of patients in subgroups for the determination of efficient therapies.
- The time is right to update disease taxonomy because molecular biology showed dramatically rapid development in the fast, comprehensive, and cost-effective analysis of clinical samples. In addition, information technologies developed in parallel with these advances, enabling the storage and sharing of clinical data.
- A new taxonomy will bring the biomedical-research, public health, and healthcare-delivery communities together around the purposes of evolving the figuring out the disease pathogenesis, improving health, and describing the diseases, based on their intrinsic biology in addition to the traditional physical signs and symptoms.
- A knowledge network of disease will be constructed.
- New models for population-based research will enable development of the knowledge network and new taxonomy.
- The initiative to develop a new taxonomy is required to modernize the current approaches, integrating molecular, environmental, and phenotypic data.

A major outcome of the proposed knowledge network of disease and new taxonomy is termed as precision medicine. The committee comprehended that in order to provide the best available care for each individual, researchers and healthcare providers should access to vary large sets of health and disease-related data linked to individual patients.

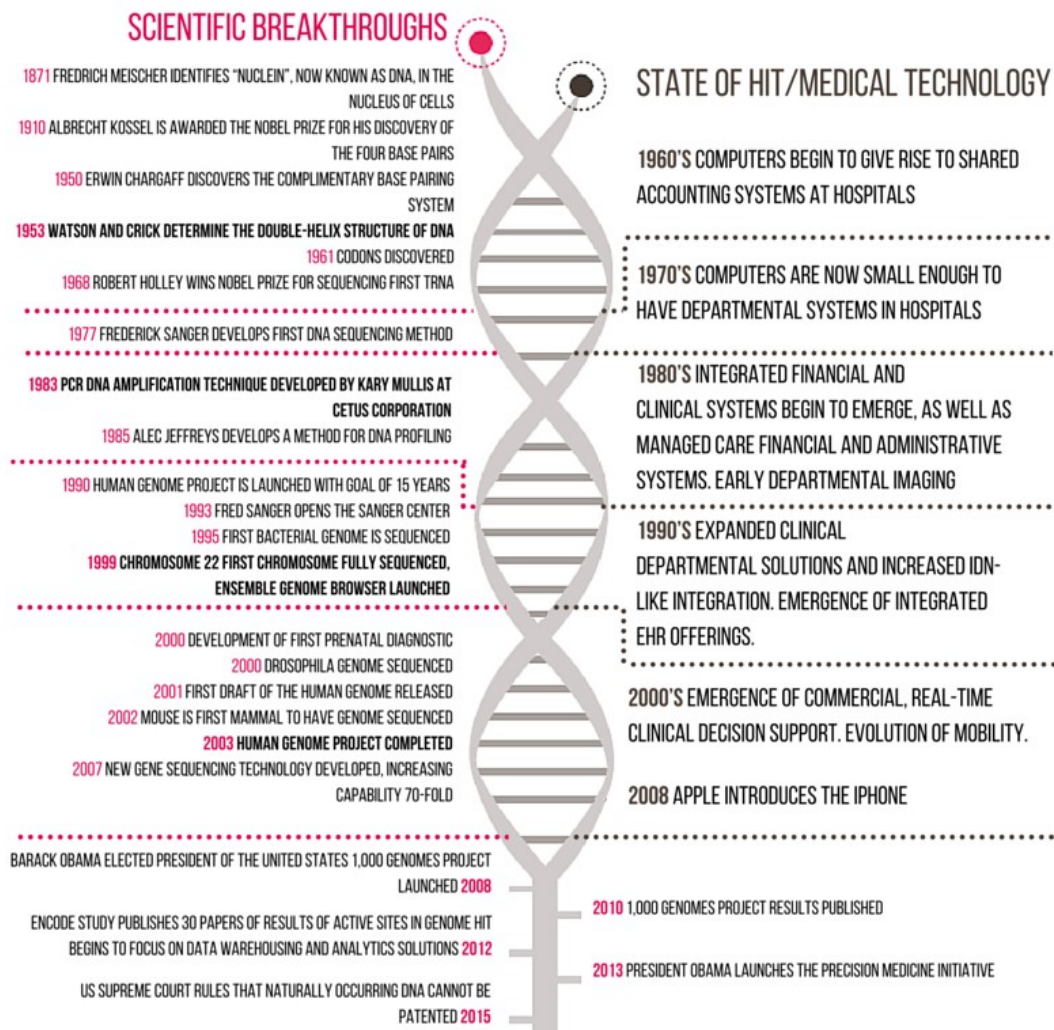


Figure 1.1: Evolution of the term precision medicine [7].

1.1.2 Precision medicine in oncology

Chemotherapy, developed in the 1950s, is the usage of drugs to treat cancer [9]. The main aim of the chemotherapy is to cease or slow down cancer. Conventional chemotherapy is defined as the application of one or few drugs at a time or merged with other treatments, such as radiation therapy and surgery, pursued by numerous cycles of chemotherapy [10]. Generally, chemotherapeutic drugs target the fast proliferating cells, blocking mitosis by inhibiting DNA synthesis and cellular machinery, having role in cell cycle process. All of these aim the induction of apoptosis which is programmed cell death (Explained detailed in Chapter 2).

Chemotherapy drugs attack rapidly growing cancer cells as affecting healthy body cells. They cannot categorize healthy and cancerous cells. This creates various side effects, including neutropenia, infection, anemia, thrombocytopenia, vomiting, and diarrhea, etc. [11]. According to the news in *The Telegraph* (August, 2016), S. Knapton claims that chemotherapy drugs cause the death of up to 50% of patients in some hospitals [12]. Besides adverse effects, chemotherapy resistance is a significant problem and can cause failure in more than 90% of patients with metastatic disease [13]. Therefore, the selection of drug(s) and the determination of dosages are the key parameters for the treatment efficiency. On the other hand, each tumor is unique. Tumor cells interact with the extracellular matrix and host non-neoplastic cells in the tumor milieu, influenced by genomic discrepancies, hormones, dietary, lifestyle, and environmental exposures [14]. All of these make cancer as a complex multifactorial disease. This intrinsic complexity nominates it as a primary target of precision medicine [15].

By high throughput genomic techniques, the molecular profiling of each tumor is achievable. This can make tumor classification go beyond the organ-based type, providing new insights to predict the disease progression and treatment response for each individual. Identifications of genomic alterations with the development of molecularly targeted agents (MTAs) have endorsed the utilization of precision medicine in oncology.

In 1978, the epidermal growth factor (EGF, HER1) protein and receptor were discovered [16]. The dysregulation of EGF gene causes the development of some cancers, such as breast cancer [17]. A few years later, EGFR reactive antibodies were described. Finally, *trastuzumab* (1st MTA), monoclonal antibody that inhibits the EGFR, was released to the market. This makes breast cancer as the first cancer, successfully treated with molecularly targeted therapy [16]. Likewise, *imatinib*, another MTA, has dramatically improved the outcome of chronic myelogenous leukemia (CML) patients, targeting BCR-ABL1 fusion gene [15]. BRAF mutation is commonly related with melanoma. It can be treated with *vemurafenib*, another example of MTAs. Up to 2014, around 40 MTAs had been identified and approved for the treatment of cancer. The opportunity to search “actionable/druggable”

alterations by high-throughput techniques within each tumor enables the usage of precision medicine in oncology [15].

1.1.3 Challenges of precision medicine in oncology

Oncology is the foremost application area of precision medicine, going out of the conventional chemotherapy utilizing molecular profile of each tumor to enhance the management of cancer. Patient is the center of therapy in precision medicine, promising to decrease the harmful effect of therapy and increase its efficacy, avoiding over- and under-treatment [18]. Although the aim of precision medicine is very clear and simple, the clinical practice of precision medicine in cancer patients has some challenges as in the followings:

i. Tumor heterogeneity, molecular evolution, and drug resistance:

Under the effect of selectivity agents, different clones can be observed in the cancer of individual patient. This is caused by significant genetic heterogeneity. This situation can be the most challenging part of precision medicine, causing that the targeting a single genetic abnormality cannot be optimum way of controlling the cancer [19]. By the development of next-generation sequencing like technologies, genomic map of the cancer of each individual patient can be defined. This can provide the measurement of heterogeneity.

A cell transforms into a cancer cell due to mutations in some genes, such as BCR-ABL or BRAF. To develop sub-clones, other mutations are added to them. Drug resistant sub-clone formation is one of the heterogeneity concepts, such as T315I mutations in BCR-ABL positive acute myeloid leukemia sub-clones, or BRAF-mutant melanoma with a sub-population of cells with NRAS mutations. In these subpopulations, while ABL or BRAF inhibition provides to kill some of the cancer cells, cells having resistance due to T315I or NRAS mutations continue to proliferate. Therefore, the usage of another inhibitor can be the solution. On the other hand, these examples are the straightforward cases. Generally, much more complex mechanisms exist under the drug resistance development [19].

The answer of question, “*Can this heterogeneity be overcome?*”, can be derived from obtaining a road map of the cancers of individual patients with advanced genomic and epigenetic examination of their cancers in terms of their heterogeneity [19]. For example, Zhao *et al.* reported the effect of tumor heterogeneity on treatment response utilizing computational modeling and functional validation in *Eμ-Myc; p19^{Arf} -/-* mouse lymphoma cells. They claimed that drug combinations can be developed that minimizes the derivation of specific subpopulations in a heterogeneous tumor. This increased the tumor-free survival rate of mice according to their studies [20]. Such studies show the importance of computational approaches in the modeling of biological behaviors. Moreover, during the past decade, developments in systems biology have improved the knowledge about complexity of biologic systems, including cancer. Drug screening and/or large scale molecular analyses were carried out with human cancer cell lines and reported as the studies of Cancer Cell Line Encyclopedia and Genomics of Drug Sensitivity [19, 20]. In addition, although the understanding of solid tumors with a single biopsy is significantly difficult, monitoring of solid tumor progression by circulating tumor cells (CTCs) and cell-free DNA (cfDNA) can be possible without further invasive biopsy.

Presently, by means of next-generation sequencing, detailed map of genetic composition of a cancer patient can be obtained. Although the dynamic nature of cancer (genomic instability) makes the systematic modeling unclear, precision medicine can be applied in most of the cancers when these kinds of information are combined with the knowledge about drug abilities. Information about the composition of patient’s cancer may provide the prediction of therapy response, allowing clinicians to make rational decisions on treatment strategies [19].

ii. Precise diagnosis and predictive biomarker definition of therapeutic response:

Mutations in the tumor and germline may affect the response to therapy. These mutations are named as predictive/prognostic markers, defining the subpopulations of patients. Lately, pharmacodynamics biomarkers have been used to endorse decisions about the validation of drug target and dose. They are very promising markers in cancer medicine. In fact, there exist more than 500 clinical biomarkers in drug labels.

Lots of drugs in clinical development consist of a biomarker. This causes some regulatory issues to be reevaluated and resolved, including some advantages and disadvantages. The selection of validation method is crucial since it should prove the effectiveness and safety of drug. The guideline of European Medicines Agency on anticancer drug evaluation regulates the biomarker development, specifying assay methods [18].

In order to make effective biomarker analysis, firstly, the biomaterial should have suitable quality. If biomaterial does not work properly, assay results are not reliable. Also, procedures of trials may dictate the analysis of samples in both pre- and post-treatment and during the treatment. This requires the informed consent of patients. For the collection and storage of biomaterials, clinical research organizations and biobanks provide standards in commercial clinical trials. Although single-diagnostic/single-drug is an efficient method, with the invention of more clinically actionable biomarkers, multiple single tests lose their feasibility. As an alternative, full molecular characterization has been offered, such as next generation sequencing. On the other hand, all of these platforms should be evolved, providing more potent tools.

The examination of relation between obtained data from lots of patients is one of the most challenging parts. On the other hand, associated improvements in computational area make possible the automation of these analytical and interpretative procedures. Moreover, there are some collaborative international programs, including AURORA, Lungscape, and SPECTAcOLOR, to make connection between each tumor and specific biomarkers and prescribe accordingly with exact validation.

Data obtained from these analyses should be open-source. However, this may bring some undesirable consequences besides scientific benefits. Therefore, all data should be tracked with caution, providing the elimination of potential risks for both patients and trial sponsors [18].

iii. Integration of genomic data with clinical data:

Massive amount of genetic information should be integrated with clinical data to provide customization of cancer medicine. After integration, they should be analyzed and translated into material, guiding the clinical decisions. Furthermore, efficient information flow between laboratory and clinical scientists is crucial. Although there are some automation studies in computational area, healthcare knowledge engineering is a requirement to overcome this transmission barrier [18].

iv. Communication with patients:

Whole genome sequencing can detect the people, having cancer risk. For example, prophylactic surgery can be applied individuals with BRCA1/2 mutations, preventing cancer. Moreover, feedbacks about the therapies may contribute to treatment of others. Nevertheless, studies related to the preferences and expectations of cancer patients are not enough. Much more genetic analyses should be carried out and all of them should be open-source. In addition, the involvement of the patient and their relatives into these procedures is crucial [18].

1.2 Multi-drug resistance (MDR)

Chemotherapy guidance by examining the drug response of cells to overcome tumor heterogeneity problem in precision medicine is the focus of this thesis. Therefore, multidrug resistance (MDR) is examined in detail.

Chemotherapy resistance is observed approximately 50% of all cancers and the major challenge to treating resistant cancer cells is the development of MDR, a condition enabling a cancer cell to resist distinct drugs or chemicals targeted at eradicating the cell [2, 21]. This resistance can be acquired during the treatment or it exists inherently in the cancer cells, named as primary resistance.

1.2.1 Potential mechanisms of MDR in cancer chemotherapy

There are some potential mechanisms which are causes of MDR although all mechanisms behind MDR have not been fully explained, yet. These are explained as follows [23]:

i. *Increased drug efflux and decreased drug uptake:*

ATP binding cassette (ABC) transporter proteins are the major family in the ATP-powered pumps. They enable the transportation of ions and numerous small molecules against their concentration gradients by ATP-driven energy (Explained in Chapter 3 in detail). On the other hand, the drug efflux is increased by the overexpression of these proteins in the drug resistant cells. Although MDR can develop against drugs, not the substrates of ABC transporters, this overexpression is accepted as one of the most important mechanisms [24]. Figure 1.2 presents the functional schematic of them.

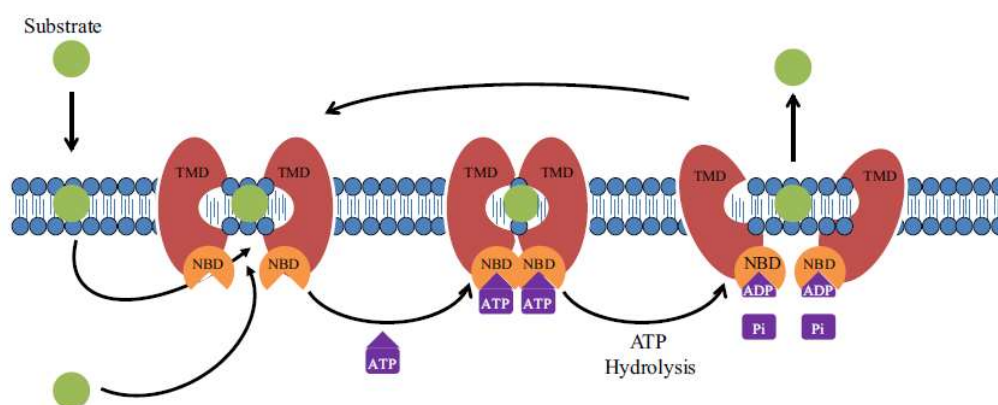


Figure 1.2: Functional schematic of ABC transporters (TMD: Transmembrane domain, NBD: Nucleotide-binding domain) [25].

The most common ABC transporters in MDR cells are P-glycoprotein (P-gp/MDR1, encoded by ABCB1), multidrug resistance associated protein (MRP1, encoded by ABCC1), and breast cancer resistance protein (BCRP, encoded by ABCG2) according to. Overexpression of P-gp, the first member of ABC transporters, was discovered in 1976 in colchicine resistant cell lines [26]. It is normally expressed on the intestine mucosal membrane, liver, and blood brain barrier, having role in the protection of cells against xenobiotics and cellular toxicants, and the substrate spectrum of P-gp is significantly wide, including analgesics, chemotherapy drugs, and immunosuppressive agents. Therefore, P-gp appears to be an important element of pharmacokinetics and an important mediator of transporter-mediated drug–drug

interactions [25]. On the other hand, there are some evidences supporting the development of MDR in the absence of P-gp. In some of them, MRP1 was found to be overexpressed. In contrast to P-gp, MRP1 can efflux drugs, changed by glycosylation, sulfation, and glutathione.

BCRP is frequently expressed in malignant hematopoietic and lymphoid cells. Therefore, it has a potential influence in the development of MDR in hematologic malignancies, including chronic and acute myeloid leukemia [23].

Lung resistance protein (LRP) is not a cell membrane protein. On the other hand, it is located on the cytoplasm, providing vesicular trafficking. According to literature, there is a relation between MDR development and LRP expression in acute myeloid leukemia and ovarian cancer patients. In addition, its overexpression was discovered in MDR colon carcinoma cells [23].

Drug uptake is decreased as another mechanism in MDR development. Drug transportation is provided into cells through variable routes, such as receptor-mediated and non-specific endocytosis. In receptor mediated type, drugs are loaded into some receptors that can easily pass through membrane. On the other hand, drug resistant cells can change the structure of these receptors or block them, preventing drug uptake. As an example, it was presented that CCRF-CEM leukemia cells substituted an amino acid, decreasing the uptake of methotrexate [27].

ii. Alterations in drug targets:

Targeted therapies are specific to some molecules inside a cell. These can be varied in drug resistant cells. For example, their levels can be increased or decreased, losing their therapeutic potential. During *tamoxifen* application, chemotherapeutic applied in breast cancer therapy, patient can lose estrogen receptors in the tumor cells, becoming resistant to endocrine therapy. Moreover, cells can mutate the target of drug, protecting its cancerous activity without being the target of the drug [23]. For example, to provide treatment in chronic myeloid leukemia (CML), *imatinib*, *nilotinib* and *dasatinib*, tyrosine kinase inhibitors, are frequently applied for the treatment of CML. They target the ATP binding site of BCR-ABL oncoprotein, leading cancer

cells to apoptosis. On the other hand, some point mutations can occur in this site of BCR-ABL proteins and imatinib resistance can develop. Other examples can be examined in the supplementary documents of review [23].

iii. Enzyme mediated drug resistance:

In cells, glutathione (GSH) is an essential antioxidant, preventing oxidative stress and providing redox homeostasis. However, in cancer cells, resistant to alkylating agents, including doxorubicin, GSH levels were determined as higher than that of their sensitive progenies, causing drug resistance, since drugs can be detoxified by glutathione S-transferase (GST), providing the conjugation of GSH and drugs [23]. For example, in brain tumors, it was reported that GST system is responsible for the drug resistance through the increasing level of GSH levels. Moreover, a direct relation was detected between enhanced GSH levels and cyclophosphamide and 4-hydroperoxy-cyclophosphamide resistance in medulloblastoma cell lines [28].

iv. Altered cell cycle events:

Under normal conditions, cell cycle checkpoints prevent the proliferation of cells with damaged DNA, providing a repair time to cells (explained in detail in Chapter 2). If some defects occur in the checkpoint mechanisms, the development of cancer and MDR progression in these cells can ensue. Especially, cell cycle arrest in G₂ phase activates Chk1, a DNA damage checkpoint component. This can give an opportunity to cells for protection of viability even drug treatment. For example, human lung cancer cells can accumulate at G₂/M phase and return into G₁ phase via doxorubicin treatment if they develop MDR through defective G₂/M checkpoint [29]. This type of MDR is mostly observed in combination therapies. For example, in the combination therapy of flavopiridol with paclitaxel, the application of flavopiridol as the first agent causes the decrease in paclitaxel sensitivity of cells, inhibiting Cdk2, Cdk4, and Cdk6 at G₁ and cyclin B1-Cdk2 kinase at G₂. It was shown that this resistance can be overcome by changing the order of agents [30].

v. *Defective apoptotic machinery:*

Apoptosis is defined as the programmed cell death. This mechanism is inhibited in cancer cells, proliferating in uncontrollable manner. Chemotherapeutic agents aim the apoptosis in cancer cells. On the other hand, due to some defects in apoptosis machinery, cells can develop MDR, including p53 inhibition, uncontrolled expression of Bcl-2, and mutations in PTEN [23]. MDR development sourced by the defective apoptotic machinery is one of the subjects of this thesis. Therefore, detailed explanations are presented in Chapter 2.

vi. *Compartmentalization:*

Drug sequestration is another important mechanism in MDR development. Cellular compartments have different properties, including having different pH, composition of lipids, and proteins. These factors affect the location of drugs inside a cell.

pH partition can be defined as the vulnerability of a weak acid to a basic environment, or of a weak base to an acidic environment, providing an electrical charge generation. This decreases cell membrane permeability, resulting in the drug accumulation in cell. Especially in targeted therapy, the localization of drugs is important. For example, if the target is topoisomerase, drug should be localized in nucleus. It was determined that in different types of MDR cells, *doxorubicin* and *daunorubicin*, whose target is DNA, are compartmentalized in different cellular parts instead of nucleus [23].

vii. *Alterations in membrane lipids:*

Cancer cells can have different lipid content when compared with healthy cells. Merchant *et al.* showed that breast cancer cells and healthy ones have different phosphatidylserine, sphingomyelin, phosphatidylcholine, phosphatidylethanolamine and phosphatidylinositol levels [31]. Likewise, it was reported that these phospholipids are in distinct levels in healthy and cancerous esophagus cells [32]. These variations in membrane lipids can be the factor in development of MDR [23]. For example, phosphatidylcholine is decreased while sphingomyelin is increased in *doxorubicin* resistant P388 murine leukemia cells. Moreover, phospholipid and

cholesterol levels of resistant T-lymphoblast cells are significantly higher than that of sensitive ones.

1.2.2 Overcoming MDR

In order to overcome MDR, the most preferred way is the application of combination therapy, which can be described as the combination of two or more drugs not only in an additive but also in a complementary/synergistic manner [32, 33] since cancer cells can induce alternative salvage pathways to escape from a single drug.

The expose of high dose drugs can prevent the construction of resistant colonies. On the other hand, the cost of this therapy to a patient is significantly high. Therefore, less destructive strategies should be defined. First of all, the inhibition of ABC transporters, which is thought that the most prevalent and important reason behind MDR, takes more attention. There exist lots of agents, also the substrates of ABC transporters, to modulate these proteins, providing longer times to drug in cell without being effluxed [33]. The excessive consumption of modulators has some undesirable effects. For example, it was shown that in mice with knockout gene MDR1, significantly high-level drug accumulation is observed in the brain, causing the toxicity in normal tissue. Moreover, polyspecific antibodies can also be used to inhibit P-gp [33].

As another way, the transcriptional and translational inhibition of MDR proteins can be applied through the introduction of antisense oligonucleotides or ribozymes. In addition, by means of interference, knocking out of specific mRNAs can be achievable [33].

In recent years, by the development of nanotechnology, other formulations have been developed to target more than one MDR mechanisms. Nano-particle based drug delivery becomes hot topic in this area. For example, *doxorubicin* loaded lipid-modified dextran nanoparticles provided the treatment in osteosarcoma cell lines, enhancing the drug accumulation in cells through P-gp independent path [35]. Likewise, the drug encapsulation in liposomes suppressed both drug efflux pump and

non-pump MDR both in vitro and in vivo, dramatically enhancing drug induced apoptosis [35].

1.2.3 MDR detection approaches

Both clinical and laboratory approaches exist to detect MDR, including gene/biomarker detection, drug sensitivity tests, drug efflux assays, and in vivo imaging.

Polymerase chain reaction (PCR) is a technique which aims the examination of target genes, providing the amplification of specific segments of DNA/RNA. This technique can be utilized in the analysis of MDR genes, especially the genes of drug efflux pumps. PCR technology has been automated and operated in basic molecular biology and clinical applications although this technique is affected by contamination significantly [36]. Fluorescence in situ hybridization (FISH) is another gene detection method which can also be used in the detection of MDR related genes [36]. This method works in fixed or intact cells and requires fluorescent antibodies. Although it has some shortcoming, such as expensiveness and labor-intensiveness, some technologies have been trying to overcome these challenges [36]. Gene detection does not directly mean that the protein will be overexpressed. Therefore, protein analyses are also suggested to detect MDR, including Western blotting and protein microassays. Western blotting is a method, invented by Towbin and Staehelin (1977-1979), providing immunologic detection and quantification of particular proteins [36]. Although the technique is simple, some problems can occur, reviewed in [37]. On the other hand, troubleshooting procedures have been developed [37]. Protein assays diagnose MDR by detecting the existence of drug efflux pumps. In flow cytometry, isolated cancer cells are tagged with fluorescently labeled antibodies raised against membrane proteins to detect MDR. DNA/RNA and protein extraction are crucial for all of these techniques. This makes all procedures complex, time-consuming, and dependent to trained personal [22].

In order to provide detection of MDR utilizing the information about dynamic functions of P-gp and MRPs, *in vivo* imaging techniques are employed, including single-photon emission tomography and positron emission tomography. Substrates of

P-gp and MRPs, labeled with particular isotopes, are injected to patient's body in these techniques. Tagging is accomplished with undamaging dosages, but frequent administration of such isotopes is not allowed due to the adverse effects [2].

Research-use-only drug efflux tests are commercially available, including Vybrant™ Multidrug Resistance Assay Kit (*ThermoFisher Scientific*) and EFLUXX-ID® Green multidrug resistance assay kit (*Enzo Life Sciences Inc.*). Their mechanisms depend on the detection of functional activity of membrane transporters, including P-gp, MRP1, BCRP, and MRP2, in living cells through fluorescence microscopy. DiOC2, digoxin, and rhodamine 123 are mostly used for P-gp while tariquidar can detect both P-gp and BCRP [36]. For example, EFLUXX-ID® Green multidrug resistance assay kit measures the MDR related activities of all 3 major ABC transporters, P-gp, MRP1, and BCRP. These kits make labeling with fluorescent agents and monitoring can be achieved through flow cytometry and fluorescence microscopy. These kits can only detect these three proteins, but there exists other mechanism behind MDR. In addition, studies showed that although these proteins were overexpressed, MDR development did not occur [38].

In order to understand the drug susceptibility of cells, their proliferation is measured under the exposure of drugs. As a result of these experiments, growth curve of cells is obtained and comparative data can be presented. MTT, XTT or WST-8 assays can be chosen in these analyses at cellular level. On the other hand, histo-culture drug response assay (HDRA) technology provides organizational level drug sensitivity tests, measuring the susceptibility of individually removed tissues or cell groups, continuing to live outside their organisms [36]. This provides information about the tumor microenvironment effects of the development of MDR.

High content screening and analysis systems have been utilized without any harmful effect on cells and offering multiple target fluorescence screening to provide information about intra and intercellular conditions under drug expose. By means of these systems, information about cell morphology, differentiation/growth, and apoptosis can be obtained.

These conventional techniques necessitate expensive laboratory equipments and trained personnel; although, they are sensitive for the detection of MDR. Moreover, they are time consuming due to the labeling procedures, and they cannot be exploited frequently during prognosis due to the adverse effects. Hence, a cost effective, label-free, and user-friendly method is desired to provide effective diagnosis of MDR in cancer cells without compromising the sensitivity and specificity [22].

1.3 Dielectrophoresis (DEP): As a potential tool for the detection of MDR

Dielectrophoresis (DEP) is the manipulation of particles under nonuniform electric field. This technique was enabled by means of MEMS technology and applied in lots of areas, including environmental research, defense, food industry, and biomedical, etc. [3]. In recent years, there is a great interest in the usage of DEP in biomedical area. Lots of studies showed that DEP is an effective tool to make biological analyses in a totally label-free manner, having significantly lower complexity and cost, although it has some challenges. In this part, firstly the theoretical fundamentals of DEP are presented. Next, challenges are explained and it is completed with an application of DEP: MDR detection.

1.3.1 DEP theory

DEP is an electrical particle manipulation technique defined as the relative motion of particles and medium under non-uniform electric field. The movement of particles is a result of the time-averaged DEP force, which is defined for a homogenous spherical particle as [1]:

$$\langle F_{DEP} \rangle = 2\pi\epsilon_m r^3 Re(f_{CM}) \nabla E_{rms}^2 \quad (1.1)$$

where ϵ_m is the medium permittivity, r is the particle radius, $Re(f_{CM})$ is the real part of Clausius-Mossotti factor of the particle, and ∇E_{rms}^2 is the gradient of external electric field.

f_{CM} carries information about the particle and the medium dielectric properties, and the frequency dependence of DEP force. For spherical particles, f_{CM} is formulized as [1]:

$$f_{CM} = \frac{\varepsilon_p^* - \varepsilon_m^*}{\varepsilon_p^* + 2\varepsilon_m^*} \quad (1.2)$$

where ε_p^* and ε_m^* are the complex permittivities of the particle and the suspending medium, respectively. Complex permittivities of particle and medium are frequency dependent variables.

$$\varepsilon^* = \varepsilon - j \frac{\sigma}{\omega} \quad (1.3)$$

where ε is permittivity, σ is conductivity, and ω is the angular frequency.

Based on applied frequency, the relation between ε_p^* and ε_m^* changes. If $\varepsilon_p^* > \varepsilon_m^*$, particle is pulled towards stronger electric field region, observing positive DEP (pDEP) force. If $\varepsilon_p^* < \varepsilon_m^*$, particle is pushed towards weaker electric field region, observing negative DEP (nDEP) force. Utilizing Eq. 2, the frequency at which the particle observes no net DEP force (i.e., $Re(f_{CM})=0$) can be calculated. This frequency is named as crossover frequency (f_{cross}). Figure 1.3 is an illustration of the separation of three particles depending on their f_{cross} values. It shows that at the f_{cross} of particle 3, particle 1 ($f_{cross1} > f_{cross3}$) is pulled by pDEP and particle 2 ($f_{cross2} < f_{cross3}$) is pushed by nDEP. Particles with similar sizes but different f_{cross} values can be separated by pDEP or nDEP approach, at a certain signal frequency. If f_{cross} values of particles are not different enough for separation, size-based separation of particles can be achieved through DEP, due to the dependence of DEP force to particle radius (Eq. 1).

$Re(f_{CM})$ depends on particle and medium dielectric properties. Medium properties can be attuned, but particle dielectric properties are out of control and should be measured. After the measurement of dielectric properties of particles, they should be modeled to choose the proper structures for DEP operation. Biological cell membrane and cytoplasm have different dielectric properties. These properties provide cell-specific characteristics as cells vary in their molecular content. This can be exploited as a discriminatory feature in DEP cell identification, manipulation or separation [1]. Cancer cells are modeled with single shell cell modeling technique. Effective complex

permittivity (Eq. 4) is obtained with this technique and it is used instead of particle complex permittivity ε_p^* in the expression of f_{CM} (Eq. 2) [1].

$$\varepsilon_{eff,p}^* = \varepsilon_s^* \left\{ \frac{[(r+d)/r]^3 + 2[(\varepsilon_i^* - \varepsilon_s^*)/\varepsilon_i^* + 2\varepsilon_s^*]}{[(r+d)/r]^3 - [(\varepsilon_i^* - \varepsilon_s^*)/\varepsilon_i^* + 2\varepsilon_s^*]} \right\} \quad (1.4)$$

where d is the thickness of the cell membrane, ε_i^* and ε_s^* are the cell interior and shell complex permittivities, respectively.

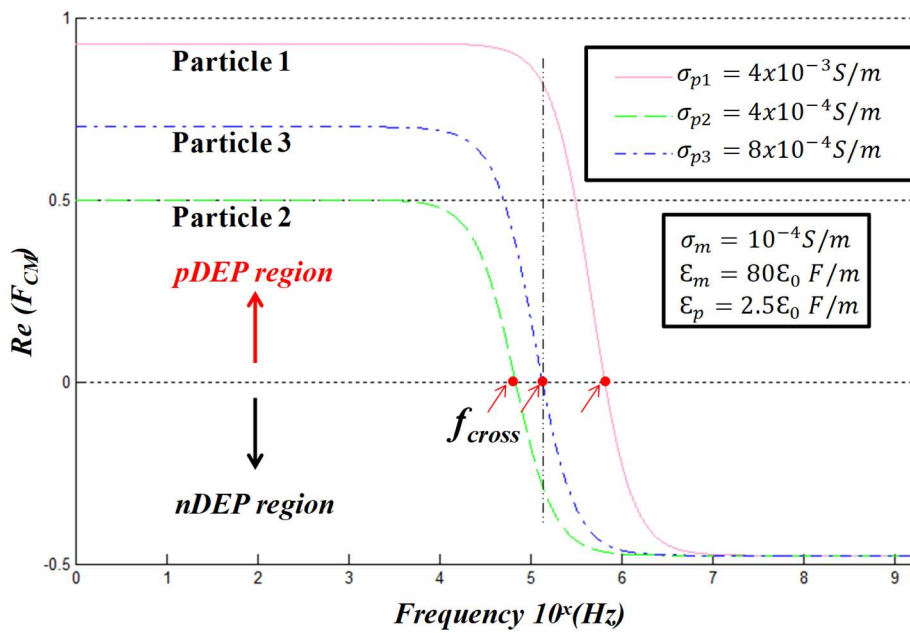


Figure 1.3: $Re(f_{CM})$ vs. frequency graph of three particles with different conductivities ($\sigma_{p1} > \sigma_{p3} > \sigma_{p2}$).

1.3.2 Challenges in DEP

DEP is a powerful tool for the biomedical analyses. Demircan *et al.* reviewed that it can be used in a wide range of point-of-care (POC) devices [3]. Although DEP has lots of application areas and provide enhanced sensitivity and reduced analysis time/cost, it has some challenges. One of the major issues is the accurate determination of cell's dielectric properties in designing a DEP-based device. Crossover frequency determination, impedance measurement, and electrorotation are utilized to determine dielectric characteristics of cells. On the other hand, dielectric

properties of the same cell line can vary from study to study due to the dynamic nature of cells. For example, Henslee *et al.* reported that the cytoplasmic conductivity and membrane conductance of RBCs change during the day according to the circadian rhythm, biological clock (Fig. 1.4) [39]. This is an inevitable situation since DEP has considerably high resolution and dielectric properties of cells are affected by size, developmental stage, and the physiological state of the cells, and their milieu. Therefore, experimental conditions and cell's physiological state should be examined conscientiously. If possible, the variation pattern of dielectric properties should be determined before the manipulation of cell by DEP.

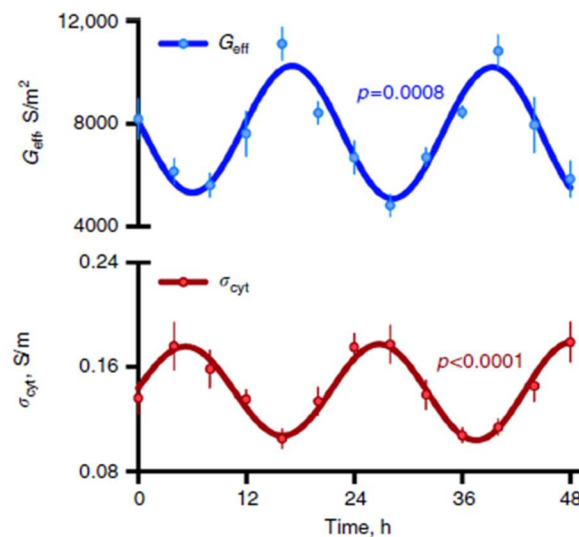


Figure 1.4: Effective membrane conductance (G_{eff}) (top) and cytoplasmic conductivity (σ_{cyt}) (bottom) variation of RBCs according to circadian rhythm [39].

DEP devices operate in low flow rates since drag force dominates the DEP force at high flow rates. Therefore, high volume sample analyses take extremely long time, i.e. throughput is low. Device parallelization can be the possible solution of this situation [40].

In order to produce enough polarization to manipulate cells with DEP, suspending solution conductivity should be significantly low. In fact, DEP solution, having 8.5% (w/v) sucrose and 0.3% (w/v) dextrose, presented by Gascoyne *et al.*, is generally

preferred in DEP studies, adjusting its conductivity to the desired values in the range of 1-50 mS/m [41]. On the other hand, when living cells are suspended into low conductivity medium, they start to make ion exchange and cell volume regulations to stay alive, changing the DEP response of cells. Sabuncu *et al.* made some analyses to observe the variations in DEP response of Jurkat and chondrocyte cells in low ionic content buffer. They showed that chondrocytes had stable crossover frequencies when they were compared with Jurkat cells. These results are reasonable since chondrocytes live in unstable environmental conditions, being more tolerant to alterations in extracellular ionic content [42]. Moreover, if cells stay in these buffers for long-term, their viability can be lost [42]. This situation is not proper for the downstream analysis after DEP manipulation. To prevent these drawbacks, DEP experiments are tried to be carried out in short durations (~10 min) [42]. As another solution, cross-link in cell membrane by some chemicals, such as glutaraldehyde, can be applied [42]. Furthermore, the physiological medium of cells has high conductivities (1.2-1.5 S/m). Therefore, cells should be resuspended in a low conductivity DEP manipulation buffer before analyses. This makes direct analysis of blood or other physiological fluids challenging; although, there are lots of blood studies with DEP. Studies with high conductivity (HC) DEP buffers also exist, depending on the manipulation of cells with nDEP force. Park *et al.* indicated that *E. coli*, spiked in cerebrospinal fluid (CSF, $\sigma=1.8$ S/m), can be directed to desired outlet by nDEP (Fig. 1.5), providing concentration of desired cell in physiological sample [43].

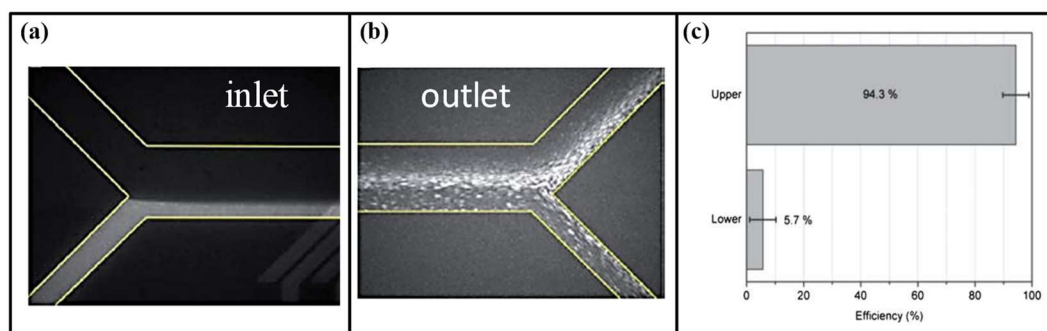


Figure 1.5: The images of inlet (a) and outlet (b) of separation channel, and efficiency (c) [43].

Although there are still some challenges to be resolved, DEP has an important potential to be a part of future applications. With the elimination of these challenges in the near future, DEP will result in accurate, rapid, stand-alone, noninvasive, and low-cost test systems for early diagnosis and prognosis of some diseases.

1.3.3 MDR detection through DEP

In 2003, Labeed *et al.* proposed that DEP can reveal the dielectrical differences between MDR and sensitive cancer cells. They examined the DEP spectrum of sensitive and doxorubicin resistant K562 cells. Utilizing single shell cell modeling, they claimed that drug sensitive K562 cells have lower cytoplasmic conductivity (0.23 S/m) than that of *doxorubicin* resistant ones (0.5 S/m). Moreover, they indicated no significant difference between membrane properties of two cell types [4]. In 2007, Duncan *et al.* reported that while K^+ and Ca^{2+} values are similar in parental, showing cytoplasmic conductivity as 0.28 S/m, and doxorubicin resistant K562 cells, showing cytoplasmic conductivity as 0.50 S/m, resistant ones have three folds higher Cl^- than that of parental ones. They correlated this difference with the claim of which P-gp is a chloride channel [44]. In the same year, Coley *et al.* published a study about the dielectrical differences between drug sensitive and MDR MCF7 cell lines. They showed that while *doxorubicin* resistant progeny of MCF7 cell line have higher cytoplasmic conductivity (0.4 S/m) than that of parental cells (0.23 S/m), *taxol* resistant ones have lower cytoplasmic conductivity (0.14 S/m) than that of parental cells [45]. These discrepancies prevent to claim that MDR cancer cells have higher cytoplasmic conductivity than that of sensitive ones.

In 2013, Demircan *et al.* reported that *imatinib* resistant K562 (K562/ima) cells could be trapped by DEP force, while the sensitive ones were not affected under the same experimental conditions at crossover frequency of sensitive K562 cells, obtained through single shell cell modeling (Fig. 1.6) [46]. In 2014, the same group also showed that DEP can be effective to detect drug resistance level in K562 cell without requiring the examination of P-gp dynamic functions [47]. In the same year, they presented that *doxorubicin* resistant MCF7 cells can be detected in a mixture, composed of parental and doxorubicin resistant cell lines [48].

Demircan *et al.* presented a novel approach in which the 3D-electrodes are placed in the microchannel but they are isolated from the medium with a thin insulating parylene layer ($\sim 0.5 \mu\text{m}$), eliminating the electrode delamination, and reduces the Joule heating and cell damaging, without increasing the applied voltages. A label-free detection of MDR in K562 leukemia cells under continuous flow through this approach has been achieved at considerably low voltages ($< 9 V_{pp}$) by means of very thin ($0.5 \mu\text{m}$) parylene coating on electrodes [22]. Finally, they achieved that label-free detection of MDR K562 leukemia cells in a cell mixture, consisting of RBCs and MDR K562 cells through a DEP-based lab-on-a-chip (LOC) system, for the first time in the literature. The system consists of 2 consecutive DEP units, one for the depletion of RBCs and the other for capturing of MDR K562 cells. RBCs are depleted by 60% in the first unit. In the second unit, MDR K562 cell detection is performed with 100% selectivity at a flow rate of $10 \mu\text{l}/\text{min}$ and at $20 V_{pp}$ in a cell mixture, containing less than 25% MDR K562 cells [49].

All these studies indicate that although DEP has not been standardized yet, it is a potential tool to detect MDR in cancer cells.

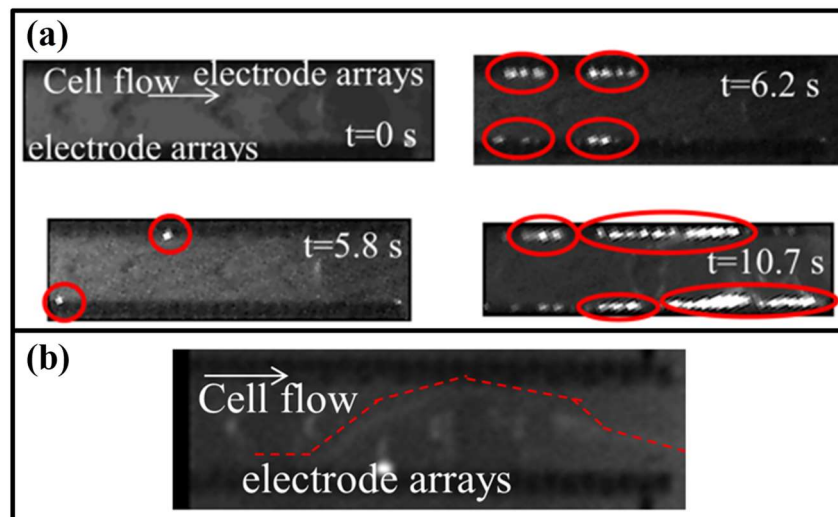


Figure 1.6: Trapping of imatinib resistant (a) and path of sensitive K562 cells (b) at a flow rate of $10 \mu\text{l}/\text{min}$ under $9 V_{pp}$ voltage at 48.64 MHz .

1.4 Research objectives and thesis organization

This thesis presents a lab-on-a-chip (LOC) system integrating a DEP detection unit and two impedance based counting units. This LOC system was designed to cope with tumor heterogeneity challenge in cancer application of precision medicine. Leukemia was chosen as main cancer type and 3 of its sub-types were examined with their drug resistant progenies: K562, CCRF-CEM, and HL60.

2 main purposes were determined. The first aim is the quantification of heterogeneity inside a cancer cell population by examining the cells in terms of drug resistance, electrically. The second one is to provide drug screening by electrical methods. To achieve these 2 main objectives, following studies need to be carried out in a systematical manner.

- i. Differences in drug response alter electrical properties of cells. Drug responses changes according to exposure time and dose. To find accurate time and doses,
 - Cytotoxicity analysis through XTT assay,
 - Apoptosis analysis through Annexin-V/PI assay in flow cytometry,
 - Cell cycle assay by flow cytometry will be carried out.

- ii. Cell cytoplasmic conductivity is one of the key parameters, changing according to physiological properties of cells. To find an average value for this parameter, providing the differentiation of cells by DEP, ion release-based impedance spectroscopy will be utilized for the first time in the literature. For this purpose,
 - Design and fabrication of a Si-glass microchannel with interdigitated electrodes (IDEs), made of Pt,
 - Design and fabrication of a chip holder to provide electrical and microfluidic connections,
 - Method development of characterization and calibration of this IDE based microchannel, and cell lysis,
 - Determination of total ion concentration of a cell as average under normal growth condition,

- Utilizing total ion concentration and single shell cell modeling in MATLAB, estimation of DEP unit's experimental parameters will be achieved.
- iii. Cell discrimination will be achieved by a LOC system, having one DEP unit and two impedimetric counting units. To acquire this system,
- Device design and fabrication,
 - Development of a method, providing both DEP and IS units work at the same time accurately, will be accomplished.
- iv. In order to provide accurate analysis of cells,
- The method of cell preparation and testing,
 - The procedure of channel preparation and cleaning,
 - A result analysis method will be formed.
- v. Utilizing the methods introduced above, results will be obtained and analyzed. Discussions and conclusions with outlook will be presented.

Thesis organization is as follows:

Chapter 2 presents biological characterization of leukemia cells and their drug resistant progenies. XTT, apoptosis, and cell cycle assays were exploited for these characterizations.

Chapter 3 first describes the ion content and transporters in the mammalian cells. Next, ion release-based impedance spectroscopy, utilized for the electrical characterization of cells, is explained with the details of device design and results.

In chapter 4, LOC system integrating DEP and counting units is explained in detail about its design and fabrication. Moreover, chemotherapy guidance in leukemia as application of this system is presented.

Chapter 5 concluded this thesis with a brief summary and possible future studies.

CHAPTER 2

CYTOTOXICITY, APOPTOSIS, AND CELL CYCLE ANALYSIS IN CHRONIC MYELOGENOUS, ACUTE LYMPHOID, AND ACUTE PROMYELOCYTIC LEUKEMIA CELLS

The accuracy of the treatment method in cancer is the key to increase the disease-free survival of patients. As explained in Chapter 1, tumor heterogeneity is the biggest challenge in determination of the right treatment method since it is caused by the presence of genetically, epigenetically, and phenotypically different sub-clones inside cancer cell population of an individual patient, preventing to target a single genetic abnormality to control the cancer optimally [50]. The chemotherapy response of these sub-clones can differentiate. Some of them can develop resistance against chemotherapeutics. If a cancer cell resists distinct drugs or chemicals, this condition is named as multidrug resistance (MDR). According to [2], 50% of cancer patients suffer from it. Therefore, its rapid diagnosis is of the utmost importance. Cell lines, as models, have been utilized to study the drug pharmacodynamics and pharmacokinetics for diagnosis of MDR and drug screening. In this chapter, chemotherapy drugs were examined in terms of their effects, dependent on the exposure time and dose on the wild types of 3 different leukemia cell lines and their drug resistant progenies, namely:

- i. Chronic myelogenous leukemia: K562/wt,
- ii. Acute lymphocytic leukemia: CCRF-CEM/wt,
- iii. Acute promyelocytic leukemia: HL60/wt,
- iv. *Imatinib* resistant K562 (K562/imaR),
- v. *Doxorubicin* resistant CCRF-CEM (CCRF-CEM/doxR),
- vi. *ATRA* resistant HL60 (HL60/ATRAR).

2.1 Cell cycle, cell death, and cancer

Cell cycle is a well-controlled mechanism, where each of its steps has checkpoints. This feature allows cells arrest from proliferation if a problem occurs. In case the problem is not solved, cell dies. Therefore, cell death mechanisms are essential to protect the integrity of multicellular organisms and prevent the proliferation of damaged cells. The pathways of cell cycle and cell death have been investigated since problems in regulation of those mechanisms cause growth of cancer cells. The development of some insight about these dysregulations can provide to produce novel cancer therapies [51].

2.1.1 Cell cycle

Cell cycle is the way of transferring genetic heritage to the next generation. The key parameters of cell cycle are accurate duplication and equal partition of all genome to daughter nuclei [52]. Mitotic cell cycle has 2 steps in eukaryotic cells: (1) Interphase (I) and (2) Mitosis (M) (Fig. 2.1). In mammalian cells, while mitosis takes almost one hour, interphase period may continue for days or weeks [53].

Interphase is divided into 3 phases: G_1 , S, and G_2 . In phase G_1 , cell grows in size and RNAs and proteins are synthesized to produce DNA replicate. During S phase, DNA replication and chromosome duplication occur. In G_2 , cell decides to proceed with M phase or not. If replicated DNA has damage, cell does not continue to divide and stay in phase G_0 until the damage in DNA is repaired [53]. This process is called as “cell cycle arrest”.

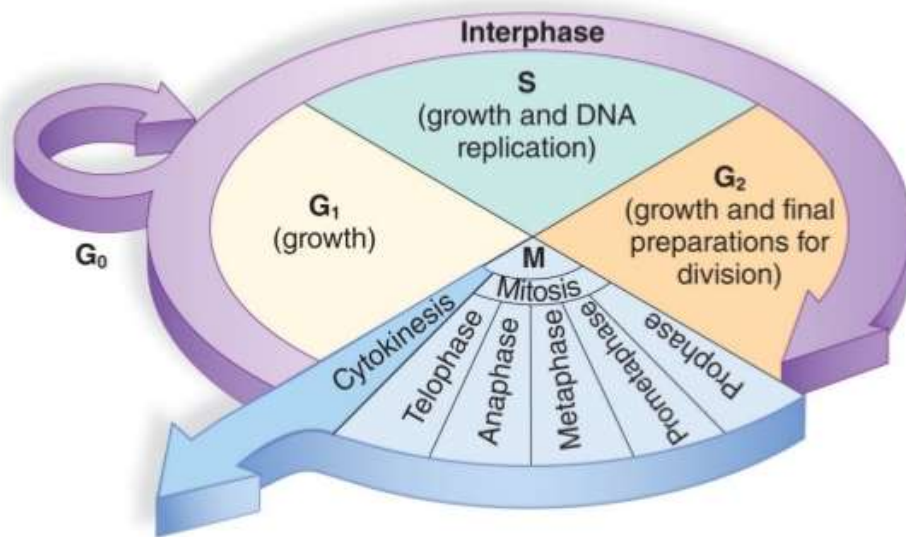


Figure 2.1: Cell cycle in eukaryotic cells [54].

M phase is composed of two main stages: (1) Karyokinesis, the nuclear division, and (2) Cytokinesis, the cytoplasmic division. Karyokinesis consists of four sub-phases [52]:

- i. Prophase: chromosome condensation
- ii. Metaphase: alignment of chromosomes on the cell mid-plane
- iii. Anaphase: separation of sister chromatids
- iv. Telophase: daughter nuclei formation and the beginning of cytoplasmic separation (Fig. 2.2).

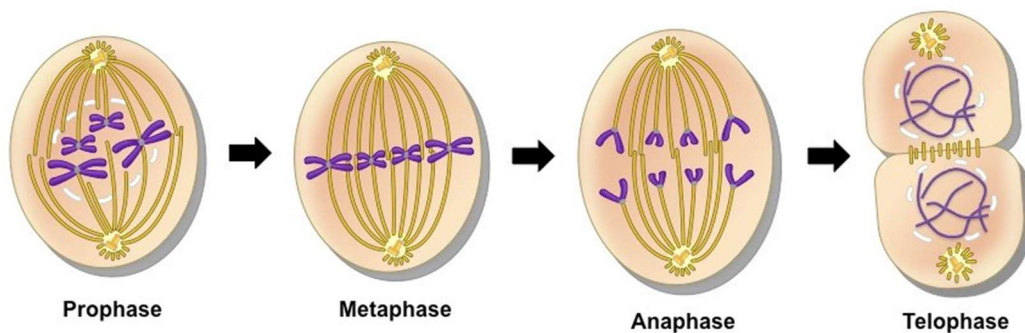


Figure 2.2: The stages of mitosis [55].

2.1.1.1 Cell cycle checkpoints

It is crucial that the correct number of chromosomes is accurately replicated and equally divided into daughter cells at the end of cell cycle. However, a number of DNA-damaging agents exist on earth. To cope with this threat, live organisms utilize highly conserved DNA-repair and cell cycle checkpoint pathways [56]. These checkpoints can be sorted as follows [57]:

i. G₁ and G₂ checkpoints:

When cell DNA is damaged because of irradiation or chemical exposure, it becomes arrested in G₁ and G₂ until this damage is fixed. Replication of impaired bases is prevented in G₁ arrest, where DNA double-stranded breaks are repaired before mitosis in G₂.

ii. S checkpoint:

All chromosomes of replicating cells must be duplicated before entering mitosis. If DNA replication fails, then the cell cannot pass the S checkpoint and cannot enter to mitosis.

iii. M checkpoint:

In this checkpoint, the formation of mitotic spindle is controlled. If it is not properly assembled, cell arrests in mitosis. Chromosomes remain condensed and reformation of nuclear envelope does not occur.

2.1.1.2 Cell cycle analysis

Studies on proliferation of mammalian cells are beneficial for explaining the molecular mechanisms of cell cycle control. This information is valuable for understanding the effects of perturbing agents, such as chemotherapeutic drugs. Moreover, they are crucial for understanding the loss/inhibition of cell cycle controls in cancer [58].

Light microscopy is the most convenient way for detecting a mammalian cell at any phase of the karyokinesis (e.g. round cells in mitosis), as well as observation of cytokinesis since cells can be examined without labeling or pre-treatment. However, this technique is not proper for the classification of interphase phases since morphological changes does not exist for them. To make decision about the state of a cell for G₁, S, and G₂ phases, DNA content is monitored. This is achieved by means of flow cytometry and fluorescent DNA-binding dyes as one of the most direct ways [58]. Propidium iodide (PI) and DAPI are frequently used dyes for this purpose as cells are fixed. Hoechst 33242 is permeable DNA stain for living cells. Therefore, if the viability of cells is crucial, it can be exploited. Flow cytometry identifies the distribution of cells inside a population based on the phase of interphase. This information enables the examination of cell cycle arrest, providing the accurate analysis of drugs. The relation between cell cycle arrest and chemotherapy drugs will be explained in “*Cancer*” subsection in detail.

2.1.2 Cell death

Cell death is a strongly regulated mechanism like cell proliferation since cells inside a multicellular organism are highly organized population. Cells commit suicide by controlled cell death progress if they are not needed anymore [59].

The classification of cell death can be achieved according to morphological criteria, without an obvious reference to exact biochemical mechanisms. The Nomenclature Committee on Cell Death (NCCD) suggests unified criteria to define the type of cell death and differences between morphologies to prevent misusages and to speed up the cell death research [60]. NCCD recommends that to decide whether a cell is death, any one of the following molecular or morphological criteria is encountered: (1) The loss of plasma membrane integrity, (2) The formation of complete fragmentation into discrete bodies, (3) Engulfment of discrete bodies by an adjacent cell *in vivo*. By this frame, they separated cell death into 5 different groups: (1) Apoptosis, (2) Autophagy, (3) Necrosis, (4) Cornification, and (5) Atypical cell deaths. Exclusively, cells should be evaluated as alive in cell cycle arrest [60]. Chemotherapy drugs aims to induce

apoptosis in cancer cells. Therefore, apoptotic cell death will be explained in detail below:

2.1.2.1 Apoptosis

The name, apoptosis, has been given to a specific cell death type by Kerr *et al.* in 1972 [61]. In this type of cell death, rounding-up of cell, condensation of chromatin, decrease in cell volume, nuclear disintegration, blebbing in plasma membrane, and engulfment by phagocytes (*in vivo*) are occurred [60].

In developing and adult animal tissues, apoptosis rate can be surprising. For example, billions of cells die in the bone marrow and intestine of a healthy adult human every hour. In some cases, cells die when the structure, formed by them, is not needed. For example, while a tadpole metamorphoses into a frog, the cells in the tail die since frog does not need that tail (Fig. 2.3). In many other cases, the regulation of cell proliferation is aided by cell death. For example, nervous system should have a specific number of cells to provide innervation. Cell death adjusts this exact number through apoptosis [59].

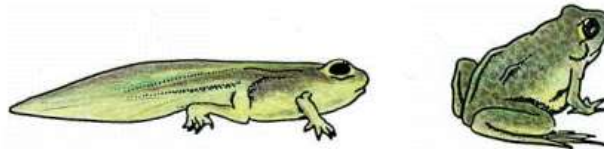


Figure 2.3: Annihilation of tail through apoptosis while a tadpole is metamorphosed into a frog [59].

Cell proliferation is balanced by cell death in adult tissues. For example, if part of the liver is taken, cell proliferation increases. Contrariwise, if liver tissue grows under the effect of a chemical and then chemical is ceased, apoptosis rate increases and liver turns to original size. As a result, tissue remains at a constant size [59]. Apoptosis substantiates in 4 stages as follows [62]:

- i. Triggering by a death signal,
- ii. Killing by activation of intracellular enzymes,

- iii. Engulfment of cell fragments by other cells,
- iv. Degradation of cell parts in another cell.

Cells are classified as early apoptotic, late apoptotic or death while they follow these stages (Fig. 2.4). As an example, a white blood cell is seen in the late apoptosis stage in Figure 2.5.

i. Early apoptosis:

The most deterministic property of early apoptosis is the variation in mitochondrial membrane potential. These variations can be measured by tagging with some fluorescence stains and examination in flow cytometry. Another key indicator is the translocation of phosphatidylserine (PS) into outer membrane from inner membrane. Annexin V can be utilized to label PS in outer membrane. In addition, chromosome condensation and cell shrinkage occur during early apoptosis.

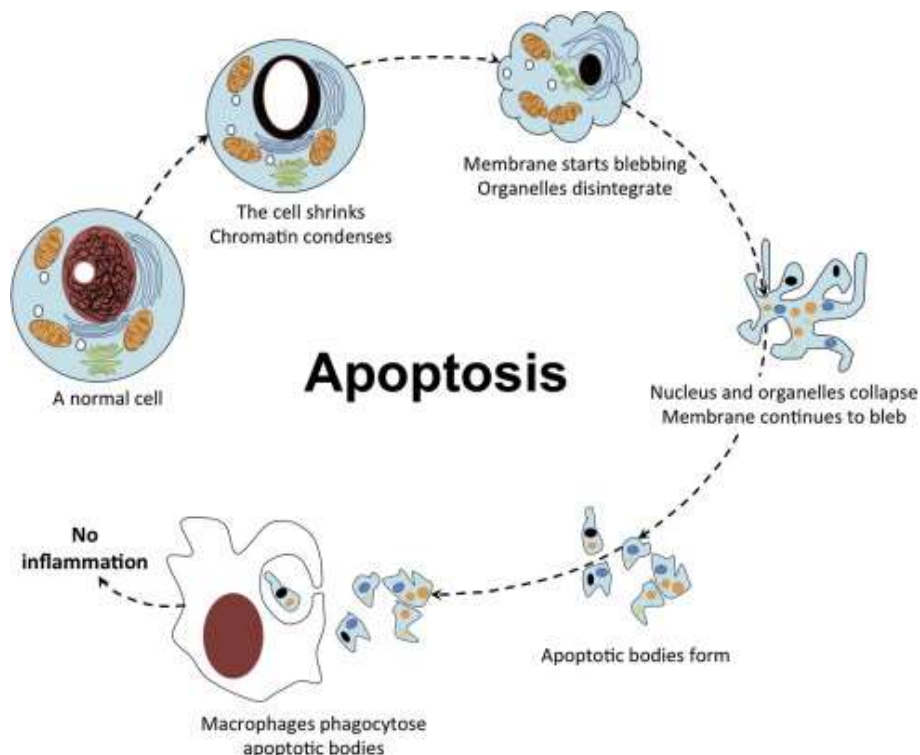


Figure 2.4: Stages of apoptosis [63].

ii. Late apoptosis:

The defragmentation of DNA occurs in late stage of apoptosis. Moreover, cell blebbing and apoptotic body formation arise in this phase.

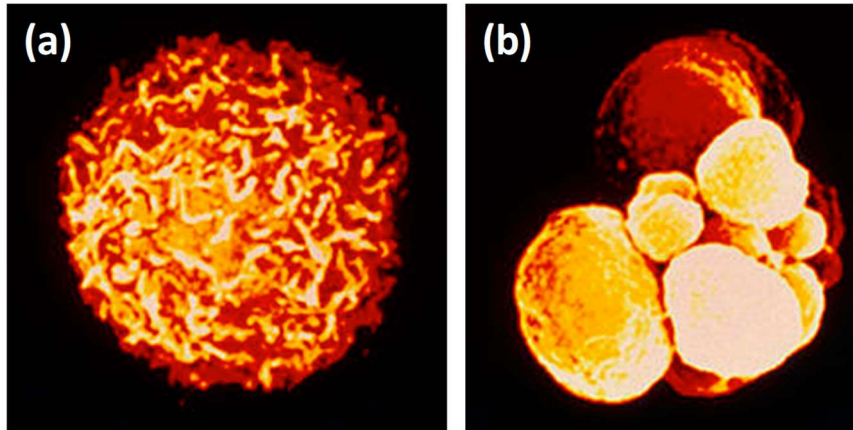


Figure 2.5: A healthy white blood cell (a) and a late apoptotic one (b) [64].

2.1.2.2 Analyses for the detection of apoptosis

Apoptosis detection can be achieved through several methods, such as light and electron microscopy, gel electrophoresis, and flow cytometry [65]. All of these methods have advantages and disadvantages. Therefore, correct technique can be determined according to the aim of study.

i. Light microscopy:

Morphological changes, including cell shrinkage and pyknosis, can be observed by light microscopy. Although it is a cost-effective method, quantification is not reliable in this method.

ii. Electron microscopy:

The resolution of this technique is better. The chromatin condensation and changes in nuclear membrane can be detected by electron microscopy. On the other hand, this is

an expensive and time-consuming technique. Moreover, due to region of interest, it makes quantification difficult.

As an example, Figure 2.6 shows the apoptotic body formation through scanning electron microscopy (SEM).

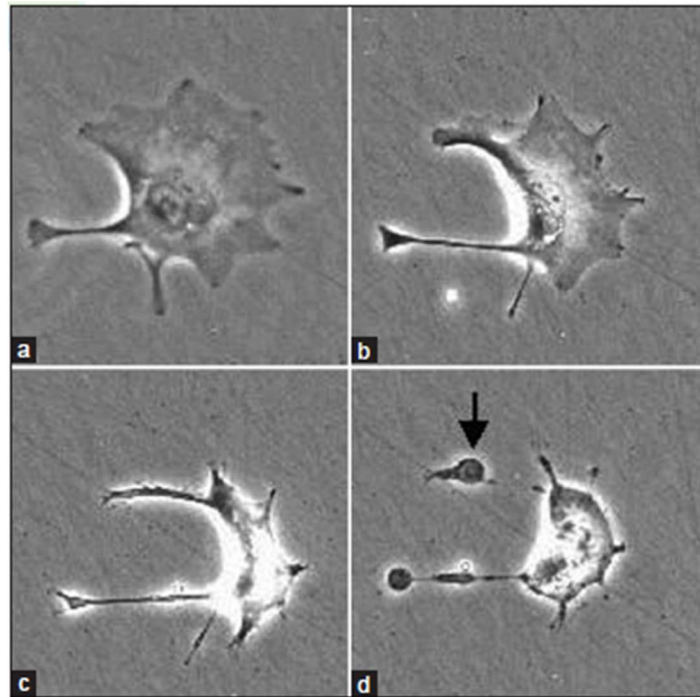


Figure 2.6: SEM images of an apoptotic cells stage by stage. (a) Cell shrinkage, (b) Nuclear condensation, (c) Cell shrinkage, (d) Blebbing [65].

iii. Gel electrophoresis:

Through apoptosis, DNA fragmentation occurs. Single and double stranded breaks can be detected by gel electrophoresis. Although it has high sensitivity, this technique is time-consuming and gives qualitative results.

iv. Flow cytometry:

Flow cytometry is the most accurate quantification method of apoptosis. This technique can provide examination, quantification, and sorting of apoptotic cells according to their apoptosis stage. Cells are stained with fluorescent dyes and flow

from cytometry device as a single cell. Next, scatter graphs are obtained and interpreted based on immunophenotypic properties. However, cell preparation steps for flow cytometry analysis are time-consuming and expensive. Moreover, cells should be as single cell; hence, intact tissue analysis can be challenging.

2.1.3 Cancer

Cancer is the uncontrolled cell division and growth, caused by the genetic changes. Eventually, these cells invade surrounding tissue by forming malignant tumors (Fig. 2.7). Actually, while being older, tumor formation frequency increases in humans or animals. On the other hand, most of them remain localized. They do not invade into healthy tissue. These are named as benign tumors [66]. In contrast, malignant tumor cells divide more rapidly and they are invasive. When a malignant tumor cell passes into the circulatory system, goes to another side of the body and continues to uncontrollable growth in there, this is called metastasis. Malignant tumors are separated into two groups: (1) Carcinoma, derived from endoderm and ectoderm, (2) Sarcoma, derived from mesoderm. Leukemia cells are actually a type of sarcoma but they do not form solid tumors. They grow as individual cells in blood [66].

Exposure of carcinogenic chemicals, radiation, viruses, etc. can damage some signaling pathways, responsible for cell cycle control. Therefore, cells can lose the control of cell cycle. For example, there exist some tumor suppressor genes. Their inactivation causes the formation of tumor cells. The most frequently mutated tumor-suppressor gene related with human cancers is p53. This gene encodes p53 protein and it has roles in checkpoints of cell cycle, providing G₁ and G₂ arrest in cells with damaged DNA. If a cell does not have functional p53, it cannot arrest and cell cycle continues with damaged DNA [57].

Chemotherapy drugs are designed to induce apoptotic cell death in cancer cells. However, some of them can cause cell cycle arrest and senescence-like phenotype, providing that cancer cells are still alive. Lüpertz *et al.* presented that *doxorubicin* mediated DNA damage in Hct-116 colon carcinoma cell lines can lead to cell cycle arrest dose- and time-dependently. They concluded that at a particular dose and treatment conditions, *doxorubicin* can induce apoptosis while under a threshold with

continuous exposure, cells can show senescence-like phenotype. Therefore, in order to make exact cytotoxicity analysis for a drug, cell cycle and apoptosis assays should be carried out besides XTT [67].

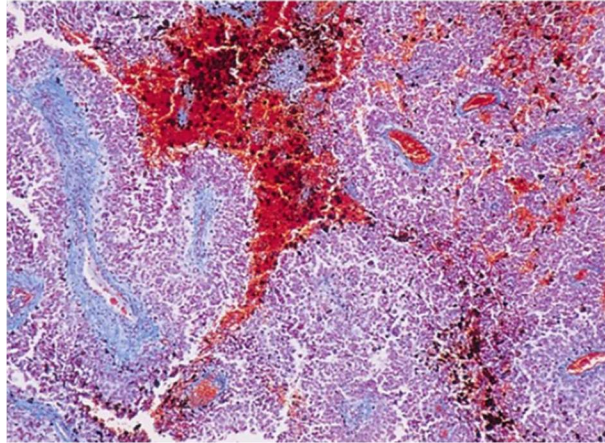


Figure 2.7: Invasion of normal tissue by a growing tumor [66].

2.2 Leukemia

Blood has 3 types of cells: Erythrocytes (RBCs: Red blood cells), leukocytes (WBCs: White blood cells), and platelets. Leukemia is the cancer of blood cells, commonly WBCs. Mainly, it is divided into 2 groups: Acute and chronic. As a rare type, hairy cell leukemia is also observed in leukemia patients. Moreover, there are different sub-groups, including acute myeloid, acute lymphocytic, chronic myeloid, and chronic lymphocytic. In the scope of this thesis, chronic myelogenous leukemia (CML), acute lymphocytic leukemia (ALL), and a sub-type of acute myeloid leukemia, acute promyelocytic leukemia (APL), were studied. The general information about these types and their treatments are presented below [68].

2.2.1 Information about CML, ALL, and APL

CML takes origin from the myeloid blood stem cells in bone marrow and mostly seen in older people (>50 years old). After abnormal growth, they spread out to the blood. To diagnose, full blood count and biopsy of bone marrow are utilized. This disease has 3 stages: Chronic, accelerated, and blast. Passing to the fatal blast stage from

benign chronic stage can take 3 to 5 years [69]. To decide the stage of patient, number of immature WBCs is determined. Figure 2.8 presents a pathologic view of the blood cell of a patient in chronic and blast phase of CML. The increase in WBCs can be observed in these images.

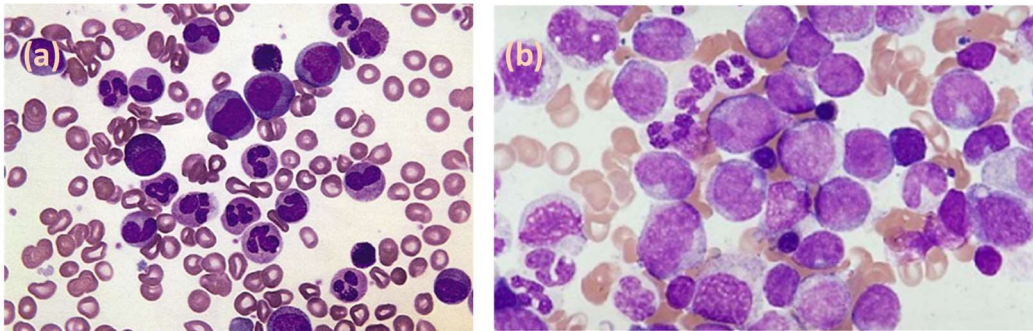


Figure 2.8: Blood cells in chronic (a) and blast (b) phase of a CML patient.

In **ALL**, lymphoid progenitor cells have malignant disorder. This type of leukemia is mostly seen in children and diagnosed by flow cytometry according to immunophenotype of them [70]. Moreover, full blood counting and bone marrow biopsy are used to make diagnosis.

APL is a sub-type of acute myeloid leukemia, caused by the abnormal growth of immature granulocytes, named as promyelocytes. In Figure 2.9, pathological image of cells, having APL, is presented.

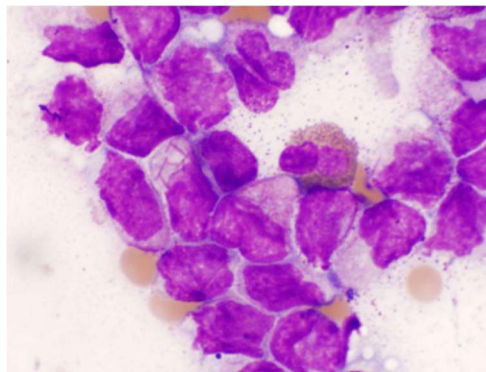


Figure 2.9: Image of leukemia cells of an APL patient.

2.2.2 Treatment of leukemia

In the treatment of acute leukemia, 3 stages are followed. Induction is the 1st phase, aiming complete remission. Consolidation stage is applied to get rid of any cancer cell remained in the body. It can be named post-remission therapy as well. Finally, maintenance step is the prevention of relapse. For chronic type, according to the diagnosis stage, treatment changes as explained in the following section.

2.2.2.1 Treatment strategies of CML

Chronic leukemia has 3 phases: Chronic, accelerated, and blast. Their treatment is carried out according to the phase of disease. Targeted therapy is commonly utilized method in this type. On the other hand, some patients can be treated with interferon, radiation, and stem cell transplantation.

Tyrosine kinase inhibitors (TKIs), including *imatinib* or *nilotinib*, are the drugs utilized for the treatment in chronic phase. For example, for *imatinib*, starting dose is 400 mg per day. If this dose does not work or stop working after a while, dose or drug can be changed.

In accelerated phase, the division of leukemia cells gains speed and causes strong symptoms, acquiring new mutations since treatments become less effective. Up to accelerated phase, if patient has not had any treatment yet, *imatinib* can be utilized for this phase, also. *Dasatinib* and *nilotinib* are newer drugs, mostly used in this phase. While taking *imatinib*, if patient passes to the accelerated phase, dose of the drug can be increased or another TKI can be applied. Some mutation analyses can be carried out to find which TKI is effective for the patient [68].

Leukemia cells become irregular in the blast stage. If any treatment is not applied up to this point, high-dose *imatinib* may be applied. On the other hand, *dasatinib* and *nilotinib* can be more effective. If all other TKIs are tried, *ponatinib* can be utilized. Although leukemia cells in blast phase behave like the cells of acute myeloid leukemia (AML), they are generally resistant to standard chemotherapy drugs, utilized in AML. The cells of small portion of patient at blast phase can act like acute lymphoblastic

leukemia. They are more sensitive to standard chemotherapy drugs, such as *vincristine*, *prednisone*, and *doxorubicin* [68].

Some of the drugs approved for CML: Bosutinib, busulfan, clafen, cytarabine, dasatinib, imatinib, nilotinib, etc. [71].

2.2.2.2 Treatment strategies of ALL

Mainly, chemotherapy, targeted therapy, and stem cell transplant are used for the treatment of ALL. As induction chemotherapy, an intensive treatment is applied and the combinations of some drugs are utilized, including *vincristine*, *prednisone*, and *doxorubicin* (*anthracyclines*). According to prognostic results of patients, *cyclophosphamide* (*Cytoxan*), *L-asparaginase*, *etoposide* (*VP-16*), *methotrexate*, and *cytarabine* (*ara-C*) can also be used in induction step. Moreover, if Philadelphia chromosome exists, *imatinib* is often applied to ALL patients [68].

Applying short course of drugs, used in induction therapy, is the way of consolidation stage. Generally, high drug dosages are preferred. If there is a risk for relapse, stem cell transplant can be chosen. *Methotrexate* and *6-mercaptopurine* (*6-MP*) are used in the maintenance part of treatment. *Vincristine* and *prednisone* can be combined with them [68].

Some of the drugs and combinations approved for ALL: Methotrexate, nelarabine, inotuzumab ozogamicin, blinatumomab, daunorubicin hydrochloride, clafen, dasatinib, doxorubicin, imatinib, mercaptopurine, oncaspar, etc. [71].

2.2.2.3 Treatment strategies of APL

APL should be diagnosed as early as possible and treated very rapidly since it can cause serious bleeding and blood-clotting problems. Differentiating drugs like *all-trans-retinoic acid* (*ATRA*) are mostly used ones for the treatment. Other treatment options also exist, including chemotherapy and transfusions of platelets or other blood products. For induction step, *ATRA* is applied by combining with anthracycline chemotherapy drugs, such as *doxorubicin*. As another option, *ATRA* can be combined with *arsenic trioxide* in the patients, who cannot tolerate *anthracyclines*. *ATRA* and

anthracyclines are utilized as cycles in consolidation stage. After consolidation, a maintenance step can be applied in some patients with *ATRA* for at least a year [68].

Some of the drugs approved for APL: Mercaptopurine, methotrexate sodium, daunorubicin, trisenox, purixan, etc. [72].

2.2.3 Precision medicine in leukemia

Cancer cells must be demolished as soon as possible and this related with both early diagnosis and accurate therapy method. Although there exist lots of methods, including chemotherapy, radiotherapy, and stem cell transplantation, accurate way varies patient to patient.

As explained in detail in Chapter 1, precision medicine is the individualization of therapy. For overcoming leukemia, precision medicine techniques have been utilized like in other cancer types.

In 95% of all diagnosed ***CML*** cases, the fusion of BCR gene to ABL1 proto-oncogene is the main reason. Translocation, t[9, 22], in human Philadelphia chromosome (Ph), is responsible for this fusion (Fig. 2.10). BCR-ABL1 oncogene activates non-receptor tyrosine kinases (TKs), developing leukemia cells [73]. Therefore, this oncogene is the target of chemotherapy for CML. Some inhibitors have been developed to obstruct the TK activity, including *imatinib*. On the other hand, mutations can occur in BCR-ABL1. As a result, cells can gain resistance to *imatinib*. For example, it was reported that 20% of all cases of *imatinib* resistance is caused by the T315I mutation. These indicators have revealed the necessity of alternative therapeutic approaches. *Dasatinib* is produced as second-generation drug, having broader capability than *imatinib*. It can be utilized in the *imatinib* resistant patients [73]. *Nilotinib*, another improved version of *imatinib*, is the recently approved drug can be utilized in *imatinib* resistant patients. Moreover, other agents, including *bosutinib* and *INNO-406*, are in clinical development. As a result, CML patients have multiple drug options. Therefore, the resistance (or mutation) detection makes possible the individualization of therapy. In the future, CML treatment may be composed of some drug combination strategies [74].

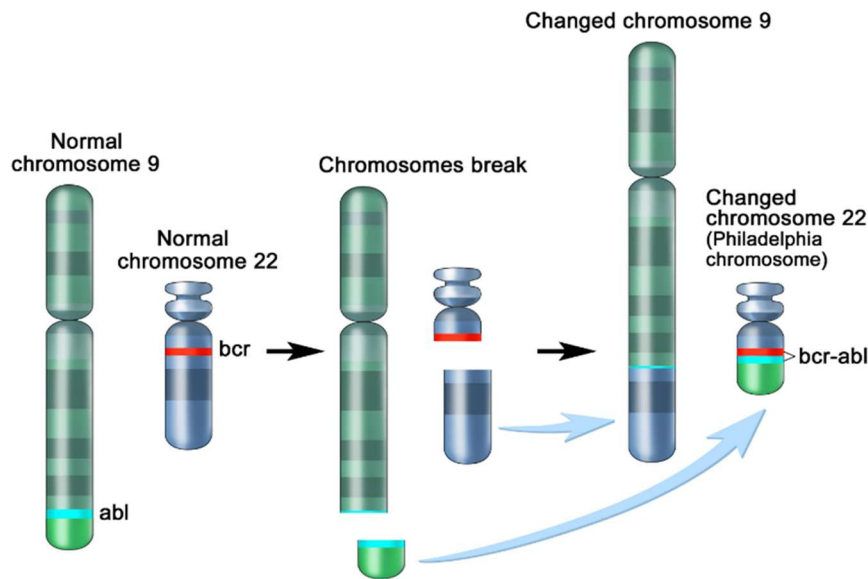


Figure 2.10: Translocation, t[9, 22], in Philadelphia chromosome.

Surface antigens can be target for the treatment of ALL. For example, *rituximab*, an anti-CD20 monoclonal antibody, usage improved 3-year overall survival rates in <60 years old patients. There exist some other types of monoclonal antibodies, including anti-CD19, anti-CD22, and anti-CD52. Moreover, *imatinib* and *dasatinib* are also used in ALL patients, having Ph chromosome. According to Hunger *et al.*, the genome related with ALL has still been under process. Especially, for older patients, amount of sequenced ALL genomes is not enough. Moreover, information about the frequently mutated genes of ALL is insufficient. It is crucial to make systematic and comprehensive sequencing of coding and noncoding alterations. This makes complete understanding of key pathways behind leukemia possible to construct the right models of it. These models are utilized to design new therapies, improving patient outcome [75].

According to the criterion of 5-year disease free survival, merely 35% to 45% of the patients were evaluated as cured by complete remission although it was reported that APL cells had been sensitive to chemotherapy with 55% complete remission rate in 1973. On the other hand, in most of APL patient, translocation, t(15;17)(q22;q21) is characterized, causing the fusion of promyelocytic leukemia and retinoic acid receptor

proteins (PML-RARA). This protein is crucial to detect the phenotype of APL. Therefore, by the discovery of *ATRA* in 1985, a new page was opened in the history of APL treatment. By optimizing the *ATRA*-based therapies, complete remission rates increased up to 90% and 6-year disease free survival up to 86% [76].

2.3 Drug pharmacodynamics

Pharmacodynamics is a branch of pharmacology, defined as the study of relationship between drug concentration at the site of action and the resulting effect time-dependently [77].

3 different drugs have been examined in this thesis according to the leukemia types: (1) *Imatinib* for CML, (2) *Doxorubicin* for ALL, and (3) *All-trans retinoic acid (ATRA or tretinoin)* for APL. This chapter presents their pharmacodynamics, both overviewing information in the literature and analyzing their effects on K562 (CML), CCRF-CEM (ALL), HL60 (APL) cell lines, and their drug resistant progenies.

2.3.1 Imatinib, doxorubicin, and ATRA (Tretinoin)

Imatinib is a potent inhibitor of all ABL tyrosine kinases, including cellular, viral ABL, and BCR-ABL, utilized in the targeted therapy of CML [78]. Figure 2.11 shows its mode of action [79].

Studies with the cell lines, having Ph chromosome, indicates that 50% inhibitory concentration (IC₅₀) values of *imatinib* were in the range of 100-500 nM. This shows efficient penetration from cell membrane. Phase 1 studies of *imatinib* started in 1998. The aim of these studies was to determine the maximally tolerated dose. As a result, hematologic responses were observed at dosages of >140 mg. Noteworthy, 53 of 54 patients had complete hematologic responses with >300 mg. In 1999, Phase 2 studies began with applying at all phases of CML. Including Ph chromosome positive ALL patients, phase 2 studies endorsed the phase 1 trial results [78].

Commonly, nausea, vomiting, diarrhea, headache, muscle pain and cramps, feeling tired, dizziness, blurred vision, stuffy nose, and sinus pain can be seen as adverse

effects of *imatinib*. More seriously, gastrointestinal bleeding, easy bruising or bleeding, black or bloody stools, and dark urine can be observed [80].

Although *imatinib* increases the complete remission rate in CML patients, cancer cells can develop resistance against it. As it is seen in Figure 2.11, *imatinib* binds to BCR-ABL from its ATP binding site. On the other hand, BCR-ABL can mutate and change this site. For example, according to Shah *et al.*, mutations of 17 different amino acids within the BCR-ABL kinase domain have been detected up to 2004, accompanying with clinical resistance to *imatinib* in CML patients. Therefore, novel kinase inhibitors have been developed to overcome *imatinib* resistant CML cells, including *nilotinib* and *ponatinib* [81].

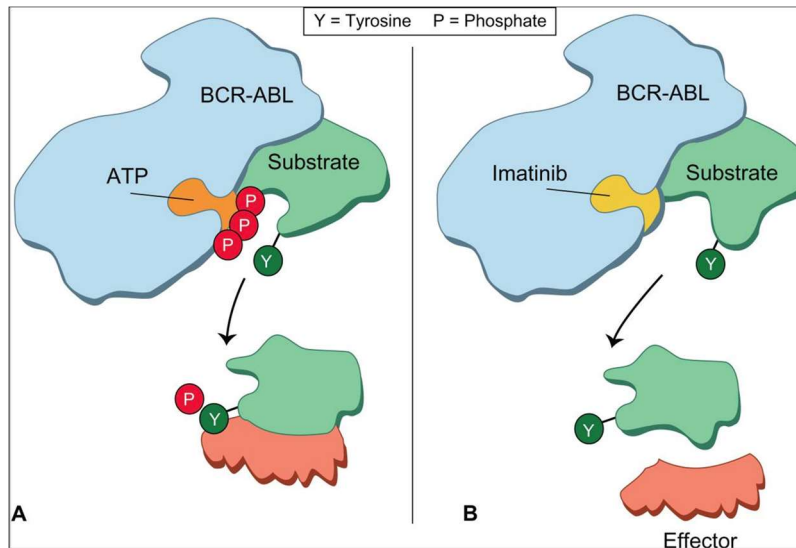


Figure 2.11: *Imatinib* action mode [79].

Doxorubicin is an inhibitor of topo isomerase 2, which has been utilized for almost 40 years in most of the cancer therapies, including drug combinations. On the contrary, its mechanisms of action have not been explained clearly. There are some possible mechanisms: (1) Intercalation into DNA, (2) producing free radicals, (3) alkylation of DNA, (4) DNA crosslinking, (5) DNA damage by inhibiting topo isomerase 2, (6) inducing apoptosis [82]. In addition, *doxorubicin*-mediated DNA damages can cause cell cycle arrest in cancer cells. This prevents the death of cancer

cells since some of them can escape from cell cycle arrest and return to cell cycle. On the other hand, some DNA damages can develop permanent cell cycle arrest. *Doxorubicin*-mediated cell cycle arrest can form at G_0/G_1 or G_2 checkpoints [67]. Lüpertz *et al.* studied *in vitro* effects of *doxorubicin* on Hct-116 colon cancer cells. They reported that at a particular dose and treatment conditions, *doxorubicin* can induce apoptosis while under a threshold with continuous exposure, cells can show senescence-like phenotype [67].

All-trans-retinoic-acid (ATRA or Tretinoin) has been proposed to the treatment of APL in 1988, increasing the rate of complete remission [83]. Retinoic acid is an analogue of vitamin A, utilized to induce differentiation to mature cells and cease cell cycle in APL cells. As a case study with 24 patients, Meng-er *et al.* reported that all patients had complete remission. When 15 of 24 patients' bone marrow was examined, 14 of them had maturation in their cells as response to *ATRA* [84]. For example, Figure 2.12 shows the maturation of cell (Patient 10) both *in vivo* and *in vitro*.

According to phase 2 studies, most patients with APL have treated with complete remission utilizing *ATRA*. However, the duration of it was considerably short. Therefore, post remission therapy is crucial to prevent relapse [85].

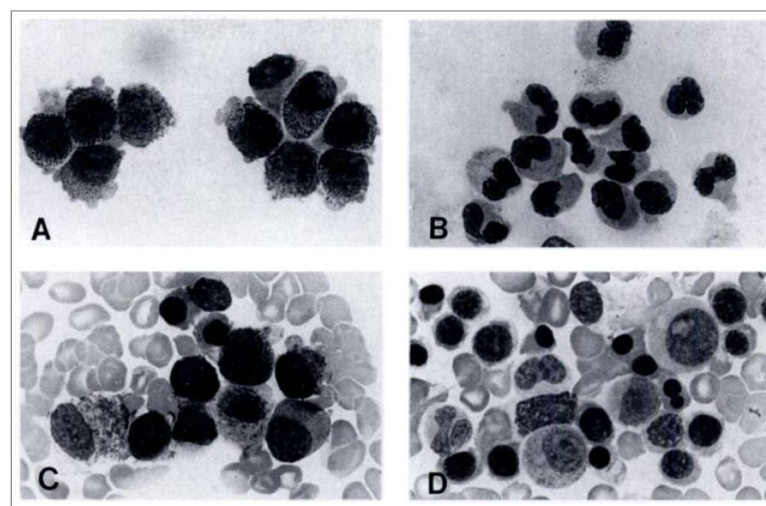


Figure 2.12: Differentiated cancer cells of a patient into matured cells under the effect of *ATRA* [84].

ATRA resistance in APL can be observed. Proposed mechanisms behind that is the mutations causing amino acid substitution, amplified catabolism of *ATRA*, and existence of cytoplasmic *ATRA* binding protein [86]. To overcome this resistance, some therapeutics has been discovered. For example, *As₂O₃* became effective in *ATRA* treated patients having relapse. Moreover, *Am80*, a kind of synthetic retinoid is 10 times stronger than *ATRA* according to *in vitro* studies, carried out with HL60 and NB-4 cells [86].

During treatment, *ATRA* syndrome can be observed with fever, problems in respiratory system, and pericardial effusions. To manage this syndrome, some changes in the therapy regime can be followed. Firstly, *dexamethasone* is applied for at least 3 days. Next, *ATRA* is re-applied at 75% of initial dose. If all symptoms are vanished, dose is increased to 100% after 3 or 5 days [85].

2.3.2 *In vitro* models for drug pharmacodynamics: Cell lines

Cell line is an established cell culture from a single cell, having the same genetic structure. National Cancer Institute (NCI; Bethesda, MD) described a new approach for drug screening, named as "disease-oriented" drug screening, utilizing 60 human cancer cell lines in 1990s. The aims of this approach are to speed-up the screening of large number of drugs and determine the most auspicious drug candidates before more time-consuming, expensive, and labor-intensive xenograft studies. On the other hand, due to the following reasons, patient-derived xenograft concept was defined to determine drug response profiling [87].

- Cell line can change in culture.
- Tumor heterogeneity cannot be preserved in culture.
- Tumor microenvironment properties cannot be reflected in cell lines.

With developing technology, the number of examined cell lines has been dramatically increased. Therefore, it can be possible to compare gene mutations, structure and copy number changes, and mRNA expression profiles between cell lines and primary cancers for the same tissue type. Studies report that cell lines may ensure demonstrative genetic substitutions for primary tumors in many cancer types [87].

As a limitless supply, cell lines are extensively obtainable and easy to proliferate; therefore, they are the source for lots of the assays. It is absolutely practicable to make large number of drug combination analyses by means of utilization of cell lines.

By following the same approach, chemotherapy resistance in cancer cells can also be modeled by exploiting cell lines. Developed resistance in cell lines is divided into 2 groups: Clinically-relevant drug resistance and high-level laboratory models. Drug dosages are low and pulsed treatment strategy is applied in the former one to mimic the chemotherapy conditions of patient. Generally, 2- to 8-fold resistance compared to parental cells is acceptable for clinically-relevant type. High-level laboratory models are manipulated to understand MDR mechanisms. Drug dosages are high and increased over time [88].

In this thesis, K562/wt and K562/imaR cells were used as high-level laboratory models (Fig. 2.13 (a)). CCRF-CEM/wt and CCRF-CEM/doxR cells were clinically-relevant ones (Fig. 2.13 (b)). HL60 cells were aimed to be clinically relevant ones under the effect of ATRA (Fig. 2.13 (c)).

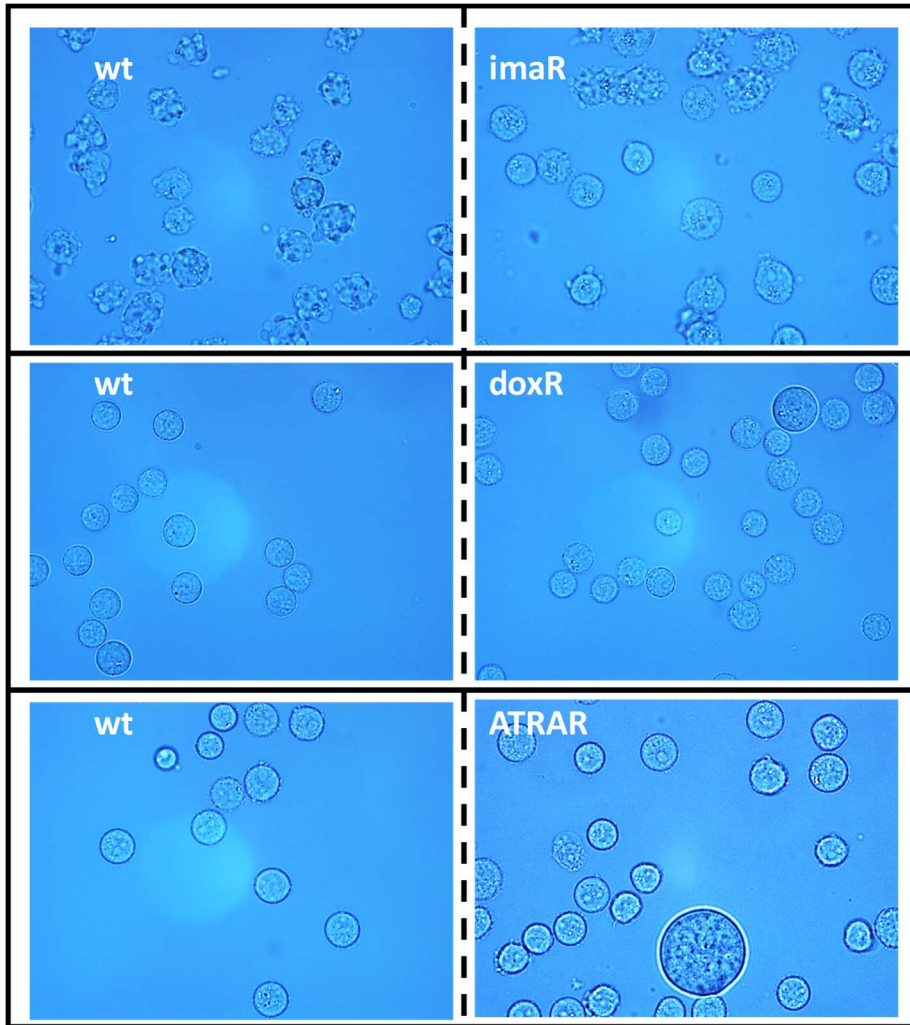


Figure 2.13: Cell morphologies: (a) K562, (b) CCRF-CEM, and (c) HL60. 63X was utilized in the microscope Leica LED 2000 with bright field.

Resistance is developed on wild type cell line. To develop resistance, selection by drugs has been applied starting from very low doses. However, the definition of very low doses is highly dependent on the type of cancer cell. Therefore, before resistance development cytotoxicity of drug on wild type cell line should be determined as explained in the following section.

2.3.3 Drug effect on cell proliferation through XTT assays

Dose and time effect of drugs on cancer cells should be analyzed to understand drug response of the cells. IC_{50} determination is one of the hallmarks of these analyses. IC_{50} is named as the half maximal inhibitory concentration at which the biological process

in half of the cells of population is inhibited. EC_{50} can also be used as another parameter to identify this inhibition. EC_{50} can be defined as the molar concentration of a drug that produces 50% of the maximal possible effect of it. For chemotherapy drugs, this biological process is cell growth [89]. Henslee *et al.* reported IC_{50} values of Jurkat cells under the exposure of *doxorubicin* for 8, 16, and 32h by using MTT assays. Results showed that after 8h, IC_{50} value is 370 nM while it was 1210 nM under 16h drug exposures. Remarkably, IC_{50} (330 nM) is at the lowest value for 32h. In conclusion, MTT (or XTT) assays can over/underestimate the cytotoxicity of cells if accurate time is not determined.

In the scope of this thesis, cytotoxicity analyses were carried out through XTT assays for different exposure times and dosages according to cell type.

2.3.3.1 Materials and methods

Cell culture: All cells were cultivated into RPMI1640 medium (1X, Gibco) enriched with 10% fetal bovine serum (Gibco), 1% nonessential aminoacids (Gibco), and 1% penicillin/streptomycin (Sigma Aldrich) in T25 flasks. K562 and HL60 cells were subcultured every 48h. Medium change was made for CCRF-CEM cells every 48h. They were subcultured by Trypsin-EDTA solution (0.2%, Sigma Aldrich) treatment (1 ml, 3 min for T25 flask) when 100% confluency were reached. At each subculture, 7×10^5 cells were seeded into T25 flask for all cell types.

K562/wt and K562/imaR cells were taken from the research laboratory of Prof. Dr. Ufuk Gündüz. K562/imaR cells were cultivated under the 500 nM *imatinib* (Selleckchem) exposure. CCRF-CEM cell line was bought from DSMZ. To develop resistance, *doxorubicin* (*Adrimisin*, *Saba*) was added to different culture medium with gradual increment in the concentration until 100 nM. HL60 cells were kindly gifted by Dr. Güneş Esendağlı from Hacettepe University. To develop resistance, *ATRA* (*Selleckchem*) were added to different culture medium with gradual increment in their concentration up to 5 μ M.

Drug preparations: *Imatinib* and *ATRA* were bought from Selleckchem as powder, 100 mg and 50 mg, respectively. 20 mM stock solution with DMSO (Sigma Aldrich)

was prepared and stored at -80°C as suggested in their datasheets. 1 mM stock was prepared, stored at $+4^{\circ}\text{C}$, and utilized in cell culture for 2 weeks. DMSO greater than 0.2% is toxic to cells. Therefore, while adding drugs to cells, this ratio was protected.

Commercial form of *doxorubicin* (*Adrimicin*, Saba, 10 mg as powder) was utilized in this study. It was dissolved in its 5 ml injection water, having 3.4 mM concentration, and stored at -20°C for one month. While utilizing it in cell culture, dilution was carried out with PBS (1X, Sigma Aldrich).

Cell proliferation: XTT assay (BI) was utilized to detect cell viability and measure proliferation by determining IC_{50} and EC_{50} values. In cell biology assays, tetrazolium salts have been utilized for many years. XTT, a second-generation tetrazolium dye, is efficiently used in cytotoxicity assays. XTT is reduced its fluorescent and colored orange derivative under the effect of some cellular mechanisms. XTT sensitivity is increased by the utilization of intermediate electron carrier [90]. Evidences report that reduction of XTT dye is achieved at the cell surface by means of transplasma membrane electron transport (Fig. 2.14). Studies suggest that the pyridine nucleotide redox status of cells is determined through XTT assays [90].

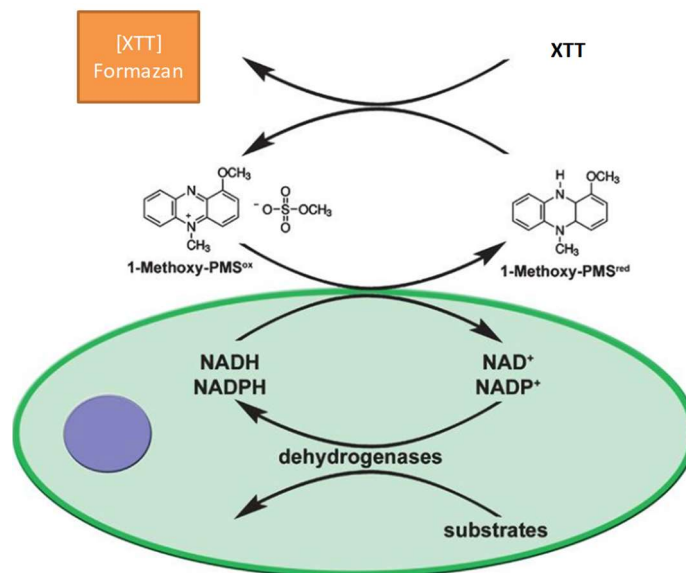


Figure 2.14: Induction of XTT to its colorful product formazan.

Procedure is well-defined in [91] (Fig. 2.15). Firstly, optimum cell number should be determined since it varies from cell line to cell line. Optimized cell number should be chosen from the linear portion of cell growth curve. K562 cells can grow more rapidly than CCRF-CEM and HL60 cells. According to growth curves, cell amount was determined as 9×10^3 cells/well for K562 cells while for CCRF-CEM and HL60 cells, it was 1.2×10^4 cells/well. After seeding, cells were incubated in humidified incubator (5% CO₂ and 95% humidity at 37.5°C) for 24 hours. Next, drug was exposed according to plate-dose plan. After that, they were incubated for pre-defined analysis durations. XTT reagent and activation reagent were mixed and added into cells 4-5 hours before ELISA reading. Incubation was also made in incubator for this step. Finally, absorbance was measured at 475 nm and 660 nm in ELISA reader (SpectraMax 340PC384, Molecular Devices Co, USA).

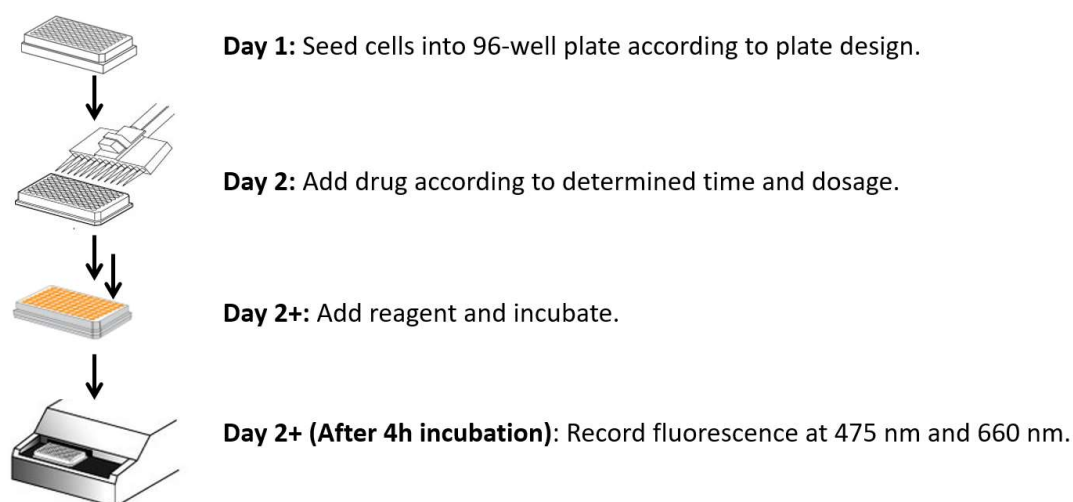


Figure 2.15: XTT assay procedure.

Statistical analysis: 2 or 3 measurements were taken for each drug level and analyses were repeated with 3 biological replicates. In order to determine correlation between repeated measurements, one-way ANOVA test with Fisher LSD for means comparison and Levene test for equal variance were utilized in all XTT tests. $p < 0.05$ were evaluated as statistically different.

2.3.3.2 Results

Control groups were the cell line examined without drug and experimental groups were grown under drug exposures at different concentrations/durations. While calculating light intensity, Equation 2.1 was utilized according to XTT assay manual. In this calculation, non-specific absorbance and auto-fluorescence of drugs were taken into account. Standard deviation and mean determination of measurements were carried out through “*Descriptive Statistics*” tool of *OriginPro 2017*.

$$A = A_{exp} (475 \text{ nm}) - A_{exp} (660 \text{ nm}) - A_{bg} (475 \text{ nm}) \quad (2.1)$$

A, exp, and bg stand for absorbance, experimental group, and background, respectively.

Cell proliferation was defined as:

$$CP(\%) = \frac{\text{absorbance of experimental group}}{\text{absorbance of control group}} \times 100 \quad (2.2)$$

Standard deviation in cell proliferation was derived from the standard deviation in the absorbance of experimental and control group by following the Equation 2.3.

$$err_i = \frac{\partial y}{\partial x_i} \text{ at } x = x_{avg} \quad (2.3a)$$

$$err = \sqrt{\sum_{i=1}^{i=n} (err_i \times \overline{u_{x_i}})^2} \times 100 \quad (2.3b)$$

err is the standard deviation, err_i is the error parameter caused by variable x_i . x_{avg} average value of the related variable. $\overline{u_{x_i}}$ stands for the standard deviation of variable x_i due to measurement. n is the number of variable.

Dose response should fit to a sigmoidal curve equation (Eq. 2.4). This equation is defined in *Pharmacodynamics (or Growth/Sigmoidal)* module under the *Nonlinear Curve Fitter* of *OriginPro 2017* (Fig. 2.16). X-axis represents dose in log range while Y-axis stands for cell proliferation in percentage. After determination of the relation

between X and Y axes, IC₅₀ value can be calculated by assigning “50” as “y” value in Equation 2.4. Additionally, this software can automatically calculate EC₅₀ value. If curve does not fit to sigmoidal equation but it covers 50% cell proliferation having at least 2 values under and above it, linear regression can be utilized.

$$y = A_1 + \frac{A_2 - A_1}{1 + 10^{(logx_0 - x)p}} \quad (2.4)$$

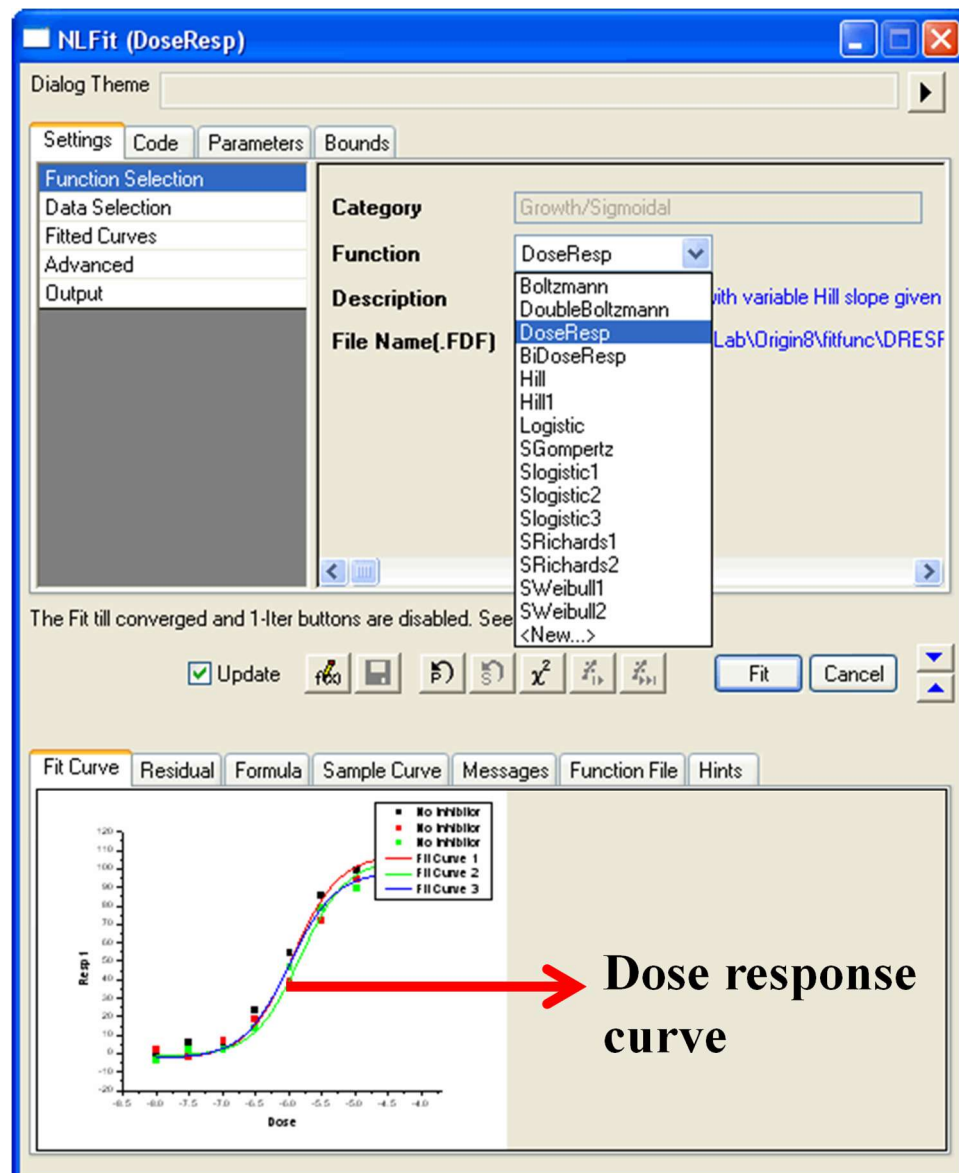


Figure 2.16: Dose response nonlinear curve fitting in *OriginPro 2017*.

After obtaining IC_{50} values, Equation 2.5 is used to reach resistance level of cells.

$$R = \frac{IC_{50} \text{ of resistant cells}}{IC_{50} \text{ of wild type cells}} \quad (2.5)$$

Assay time and drug concentrations change from cell line to cell line. Therefore, for each cell line, these two parameters were determined and presented as follows:

K562/wt and K562/imaR cells under imatinib exposure: In order to determine assay time, XTT assay of K562/wt cells with one biological replicate by seeding them into duplicate wells for each drug concentrations were carried out for 8, 18, and 24h (n=1). Results show that data did not fit to sigmoidal growth equation for 8h and 18h (Fig. 2.17 (a) and (b)). Data of 24h fitted to sigmoidal growth while it did not cover 50% cell proliferation (Fig. 2.18 (a)). This means that extrapolation should be made for IC_{50} calculation. This method can decrease the accuracy of IC_{50} calculation by overestimating the results. Therefore, 48h was chosen to determine IC_{50} and EC_{50} values. These analyses were carried out with 3 biological replicates of both K562/wt and 2 biological replicates of K562/imaR cells. Figure 2.18 (b) shows the results of first K562/wt cells as an example.

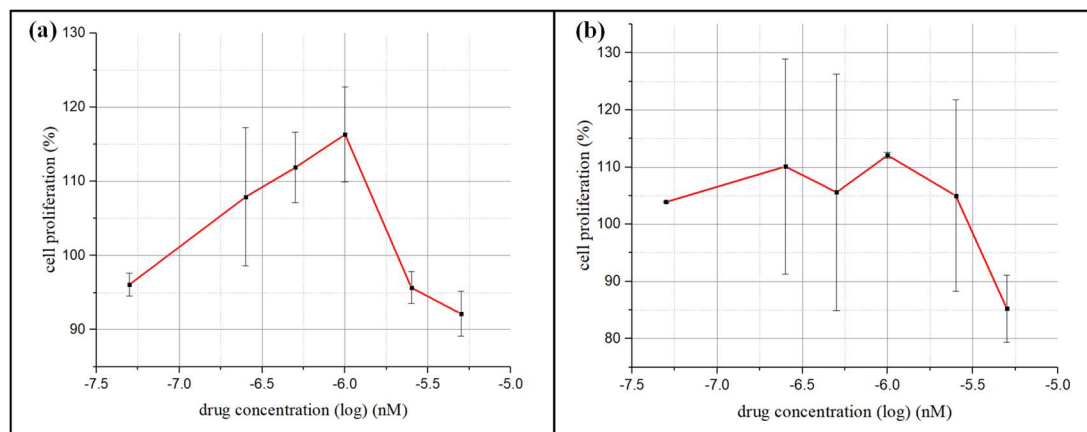


Figure 2.17: *Imatinib* response of K562/wt cells for 8h (a) and 18h (b). Data is presented as mean±stdev for duplicate measurement at each drug level (n=1).

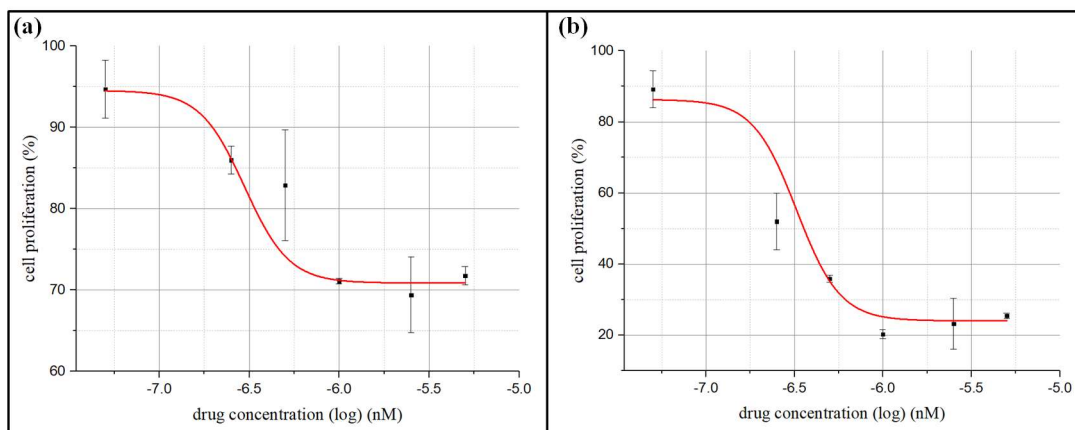


Figure 2.18: *Imatinib* response of K562/wt cells for 24h (a) and 48h (b). Data is presented as mean \pm stdev for duplicate measurement at each drug level (n=1).

Figure 2.19 (a) presents the correlation between IC_{50} values of 3 biological replicates of K562/wt cells. At $p < 0.05$ level, there were no significant difference between them (n=3). *Imatinib* resistant cells' dose response curves did not fit to sigmoidal equation. Therefore, linear regression was utilized. The results were the same for the 2 biological replicates of K562/imaR cells (n=2) (Fig. 2.19 (b)). When the IC_{50} of these cells were compared (Eq. 2.5), it was obtained that K562/imaR cells were almost 60-fold resistant to *imatinib* than K562/wt ones (Fig. 2.19 (c)). This can be interpreted that these cells can be used as high-level laboratory models as intended. Table 2.1 reports the IC_{50} and EC_{50} values of K562 cells, obtained in these analyses.

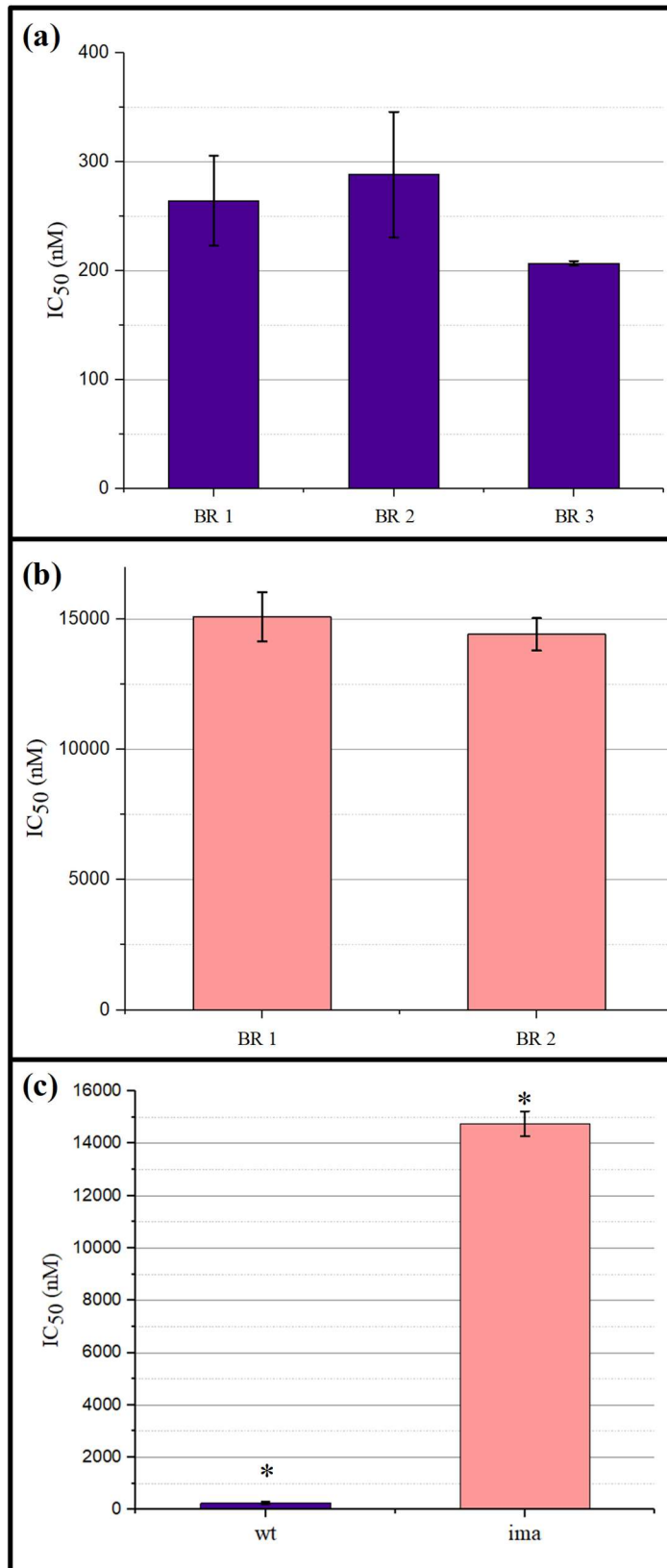


Figure 2.19: IC₅₀ values of K562/wt (a) (n=3) and K562/imaR cells (n=2) (b) obtained at the end of 48h. (c) Comparison of IC₅₀ values of K562/wt and K562/imaR cells. Data is presented as mean±stdev. * p<0.05 significantly different calculations. BR: Biological replicate.

Table 2.1: IC₅₀ and EC₅₀ values of K562 cells under the exposure of imatinib for 48h. Data is presented as mean±stdev. BR: Biological replicate.

Drug (nM)	BR 1		BR 2		BR 3		Average	
	IC ₅₀	EC ₅₀	IC ₅₀	EC ₅₀	IC ₅₀	EC ₅₀	IC ₅₀	EC ₅₀
K562/wt	264±41	212±37	288±57	245±44	206±2	191±13	253±42	220±40
K562/imaR	15092±944	-	14416±623	-	-	-	14754±478	-

CCRF-CEM/wt and CCRF-CEM/doxR cells under doxorubicin exposure: In order to determine assay time, one set XTT assay of CCRF-CEM/wt cells by seeding them into duplicate wells for each drug concentrations were carried out for 8, 18, and 24h (n=1). Figure 2.20 presents proliferation responses of cells for 4 dosages at 3 different durations as examples of this assay, indicating that 8h and 18h were not enough for correct analysis. For the same dosages, cells were death at 24h while they were alive at 8h. By supporting these results, dose response curves of 8h exposure did not fit to sigmoidal growth equation (Fig. 2.21).

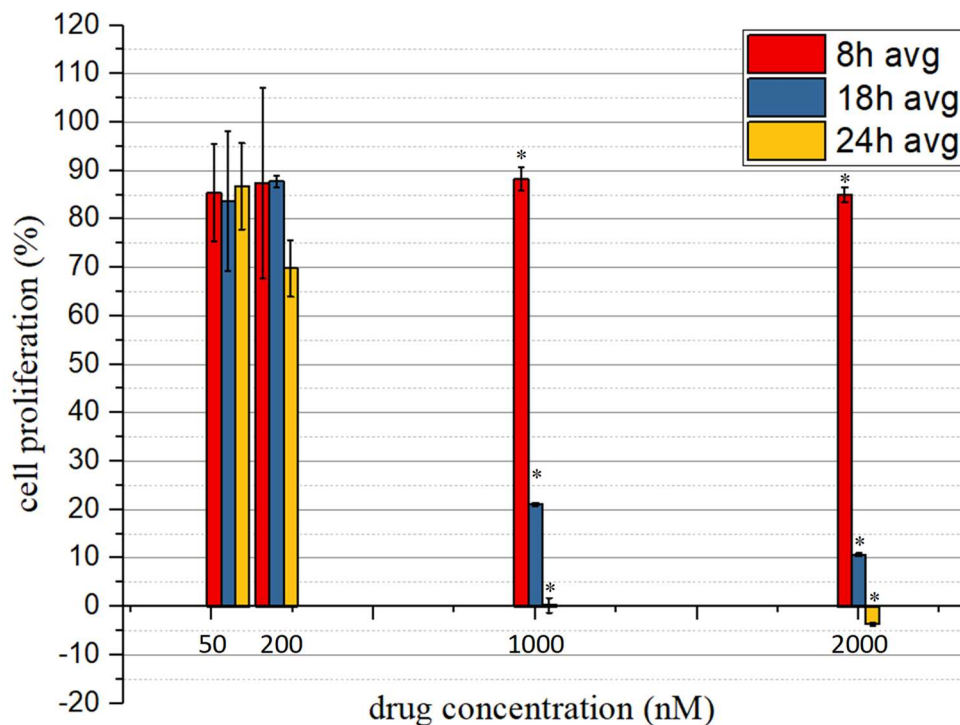


Figure 2.20: Doxorubicin response of CCRF-CEM cells for 8, 18, and 24h.

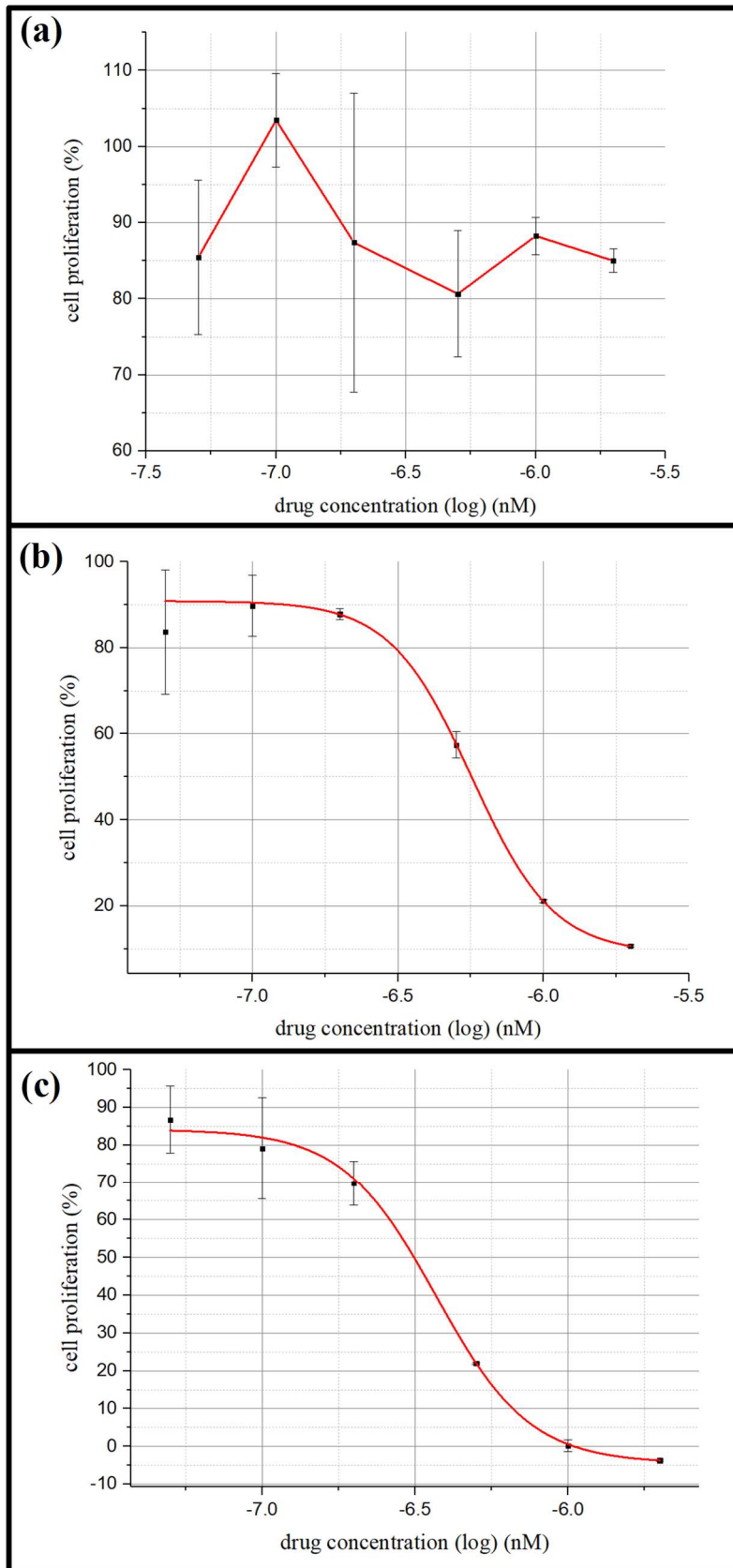


Figure 2.21: Dose response curve of CCRF-CEM/wt cells under *doxorubicin* exposure for 8h (a), 18h (b), and 24h (c) (n=1). Measurements were taken from 2 different well for each drug dose.

Results show that 24h is the most appropriate duration for IC₅₀ analysis (Fig. 2.21). Table 2.2 reports the IC₅₀ and EC₅₀ values of CCRF-CEM cells, obtained in these analyses. Figure 2.22 (a) and (b) present the correlation between IC₅₀ values of 3 biological replicates of CCRF-CEM/wt and 2 biological replicates of CCRF-CEM/doxR cells, respectively. When they are compared, IC₅₀ of wt and doxR cells are significantly different at 0.05 level (Fig. 2.22 (c)). According to these results, CCRF-CEM/doxR cells are almost 4-fold resistant to *doxorubicin* than CCRF-CEM/wt ones. This can be interpreted that these cells can be used as clinically-relevant models as intended.

Table 2.2: IC₅₀ and EC₅₀ values of CCRF-CEM cells under the exposure of *doxorubicin* for 24h. Triplicate measurements at each drug level were carried out in the analysis of each biological replicate (BR).

Drug (nM)	BR 1		BR 2		BR 3		Average	
	IC ₅₀	EC ₅₀	IC ₅₀	EC ₅₀	IC ₅₀	EC ₅₀	IC ₅₀	EC ₅₀
CCRF-CEM/wt	147±25	155±24	224±45	194±21	184±8	177±10	179±42	172±24
CCRF-CEM/doxR	665±25	616±23	812±51	737±85	-	-	738±104	676±86

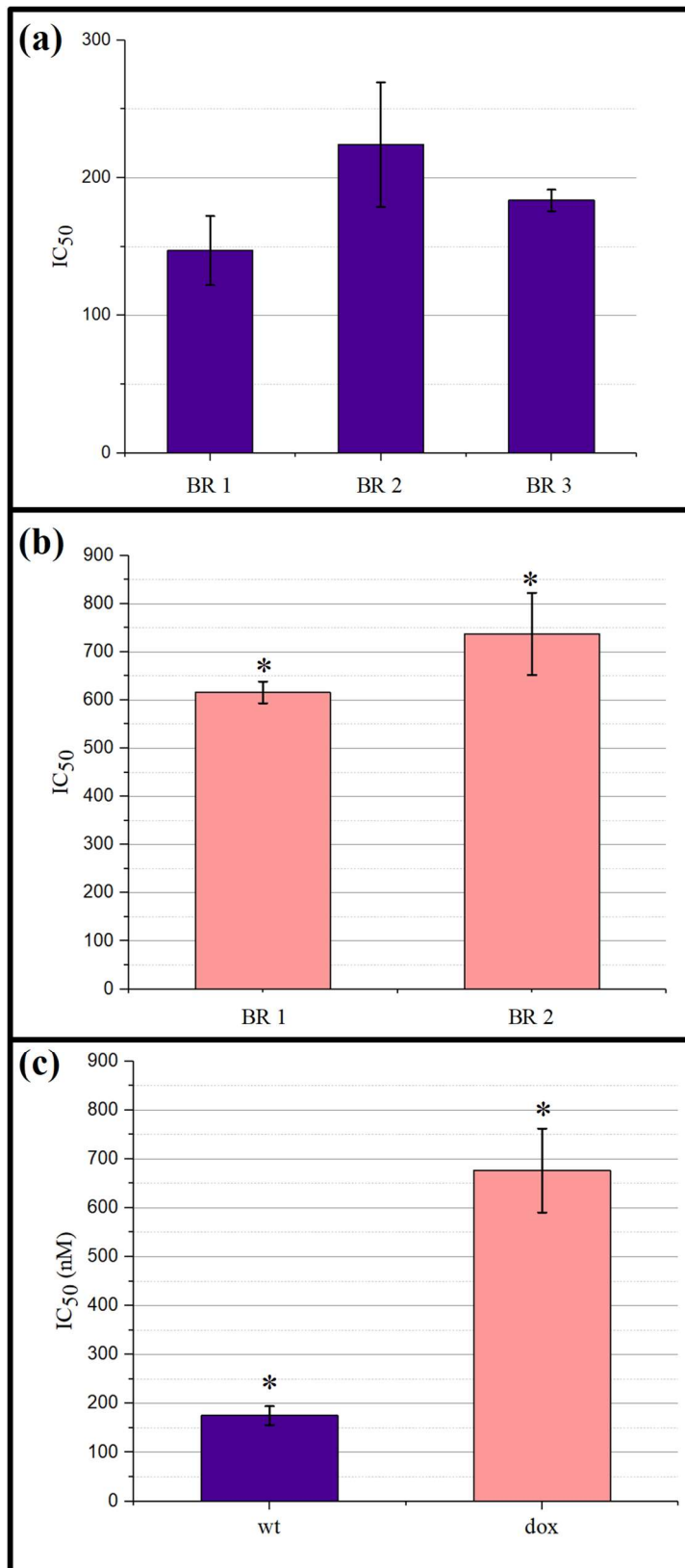


Figure 2.22: IC_{50} values of CCRF-CEM/wt (n=3) (a) and CCRF-CEM/doxR cells (n=2) (b). (c) Comparison of IC_{50} values of CCRF-CEM/wt and CCRF-CEM/doxR cells. Data is presented as mean \pm stdev. * $p < 0.05$ significantly different results. BR: Biological replicate

HL60/wt and HL60/ATRAR cells under ATRA exposure: In order to decide assay time, XTT assay for the exposure of ATRA through 8, 18, and 24h was carried out. Cell proliferation was almost 100% for the drug exposure (5 μ M) along all durations. Although pharmacological concentration value of ATRA is 1 μ M, cell proliferation is 75% at 40 μ M for 48h (n=1) (Fig. 2.23). This is interpreted as assay time was not enough and according to literature, it can take 3-10 days [83]. Therefore, XTT analyses of HL60 cells under the effect of *ATRA* were stopped at that point.

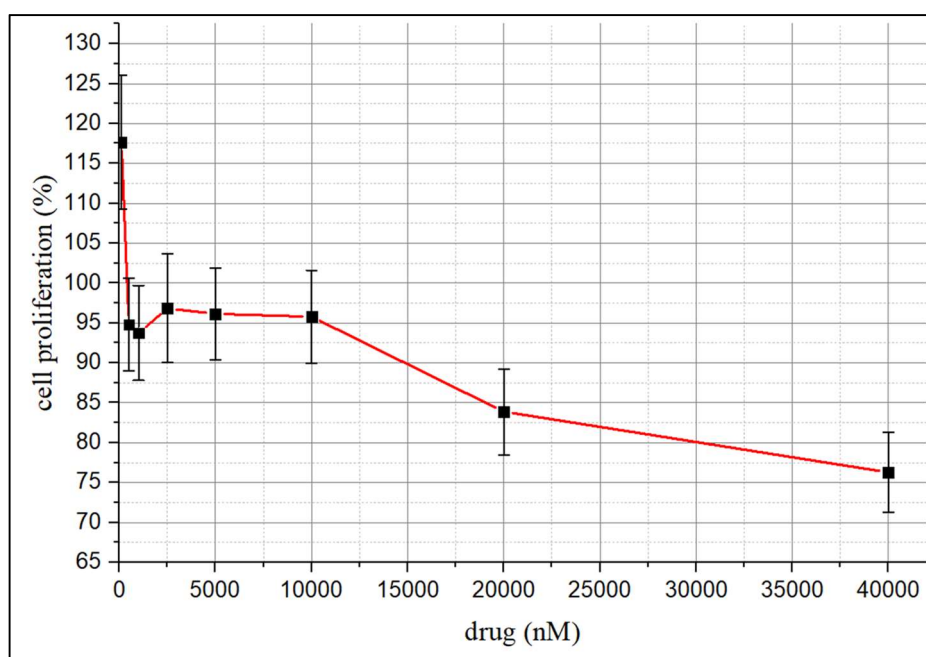


Figure 2.23: 48h *ATRA* response of HL60 cells. Measurements were taken from 3 different wells (n=1). Data presented as mean \pm stdev.

2.3.3.3 Discussion

The drug response of cancer cells changes according to exposure duration and dose. Therefore, these variations should be analyzed to reach accurate values of dose and time. IC_{50} determination is one of the hallmarks of these analyses. XTT cell proliferation assays were utilized to determine IC_{50} values in this study. It was shown that correct time and doses changed from drug to drug and cell line to cell line. 48h was determined to detect resistance level in K562 cells under *imatinib* exposure. IC_{50}

value of K562/wt cells was measured as 253 nM which is between the values (100-500 nM) presented in the literature [78]. K562/imaR cell line with 60-fold resistance to *imatinib* was utilized as high-level laboratory model to detect electrical differences between wild type and resistant cells (Explained in Chapter 3). IC₅₀ value of CCRF-CEM/wt cells was measured as 179 nM while that of CCRF-CEM/doxR cell line was 738 nM, indicating 4-fold resistance. This clinically-relevant drug resistant cell line was exploited to understand whether electrical differences between MDR and wild type cell lines exist or not by establishing minimum resistance level limit. IC₅₀ value of HL60 cell lines was not detectable for 48h exposure of *ATRA*. This cell line and its drug exposed progeny, HL60/ATRAR, were utilized to understand whether *ATRA* response of HL60 cells is detectable by electrical analysis instead of biological assays.

XTT assays are approved biological analyses for cytotoxicity of drugs. However, they may not be the best choice for each drug and cell type. Moreover, they are rougher analyses than apoptosis assays since they can overestimate IC₅₀ values, labeling cells as alive in the stage of early apoptosis [89].

Chemotherapy drugs are designed to induce apoptotic cell death in cancer cells. However, some of them can cause cell cycle arrest and senescence-like phenotype, providing that cancer cells are still alive. Lüpertz *et al.* presented that *doxorubicin* mediated DNA damage in Hct-116 colon carcinoma cell lines can lead to cell cycle arrest in dose- and time-dependent manner. They concluded that at a particular dose and treatment conditions, *doxorubicin* can induce apoptosis while under a threshold with continuous exposure, cells can show senescence-like phenotype [67]. Therefore, in order to make exact cytotoxicity analysis for a drug, cell cycle and apoptosis assays should be carried out as complementary of XTT. In the next section, apoptosis assays are explained in detail.

2.3.4 Drug effects on apoptotic cell death: Time and dose dependency

Apoptosis is controlled cell death. Chemotherapy drugs aim to induce apoptosis in cancer cells. On the other hand, their effects are dependent highly on dose and the exposure time. Moreover, XTT assays overestimate IC₅₀ value if time is not chosen accurately as presented in the previous section. At early apoptosis, cells are still alive.

However, after cell- and drug-specific duration passes, they will become death. According to literature, during these stages, their electrical properties vary [89]. The purpose of these analyses in this study is to determine accurate time and dosages for the monitoring of apoptosis progression in wild type and drug resistant cells by electrical techniques. In the following subsections, details of these analyses are presented.

2.3.4.1 Annexin-V/PI assay

Phosphatidylserine (PS) is a kind of phospholipid in the inner leaflet of cell membrane where it is located under normal conditions in a living cell. When cell decides to die, i.e. apoptosis begins, PSs start to translocate to the outer leaflet of cell membrane as one of the earliest signs of apoptosis. Annexins, a protein family discovered as vascular protein having strong anticoagulant properties in 1985, can bind phospholipids, including PSs. Moreover, annexins can be labeled with fluorescence tags. This makes comprehensive analysis possible, providing sorting with flow cytometry (Fig. 2.24) [92].

Propidium iodide (PI) is a red fluorescent nuclear stain, passing through the membrane of dead cells. This stain is not permeant to early apoptotic cells. Therefore, when it is used together with Annexin-V, a population can be classified as live, early/late apoptotic, and dead. For example, Mulhall *et al.* reported the apoptotic response of Jurkat cells under the effect of 0.5 μM staurosporine, an apoptosis inducing agent, for 0.5, 1, 2, 4, 6 and 24 hours (Fig. 2.25) [93]. Quadrant 1 (Q1) shows dead cells since they did not show PS expression and highly stained with PI. In Q2, cells stained with both Annexin-V and PI. This indicates late apoptosis. Q3 was for living cells. In Q4, early apoptotic cells were stained with Annexin-V while they were not labeled by PI since their membrane was not permeable for it yet.

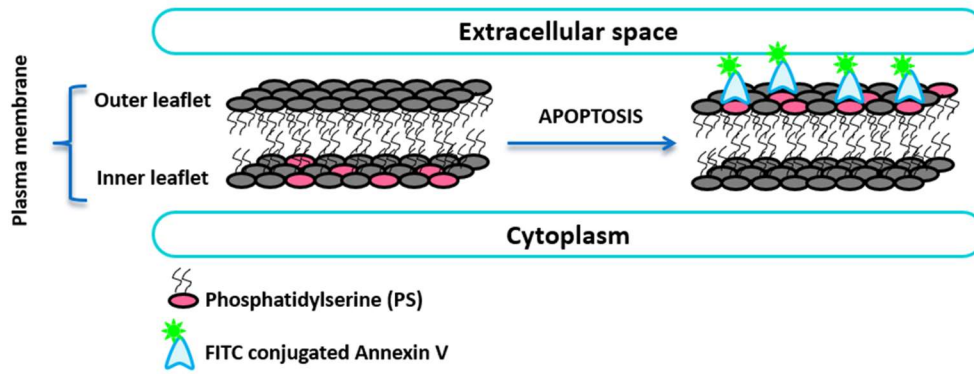


Figure 2.24: As an early sign of apoptosis, PSs translocate into outer leaflet. Fluorescently tagged Annexin-V can bind to PSs. Utilizing flow cytometry PSs can be detected.

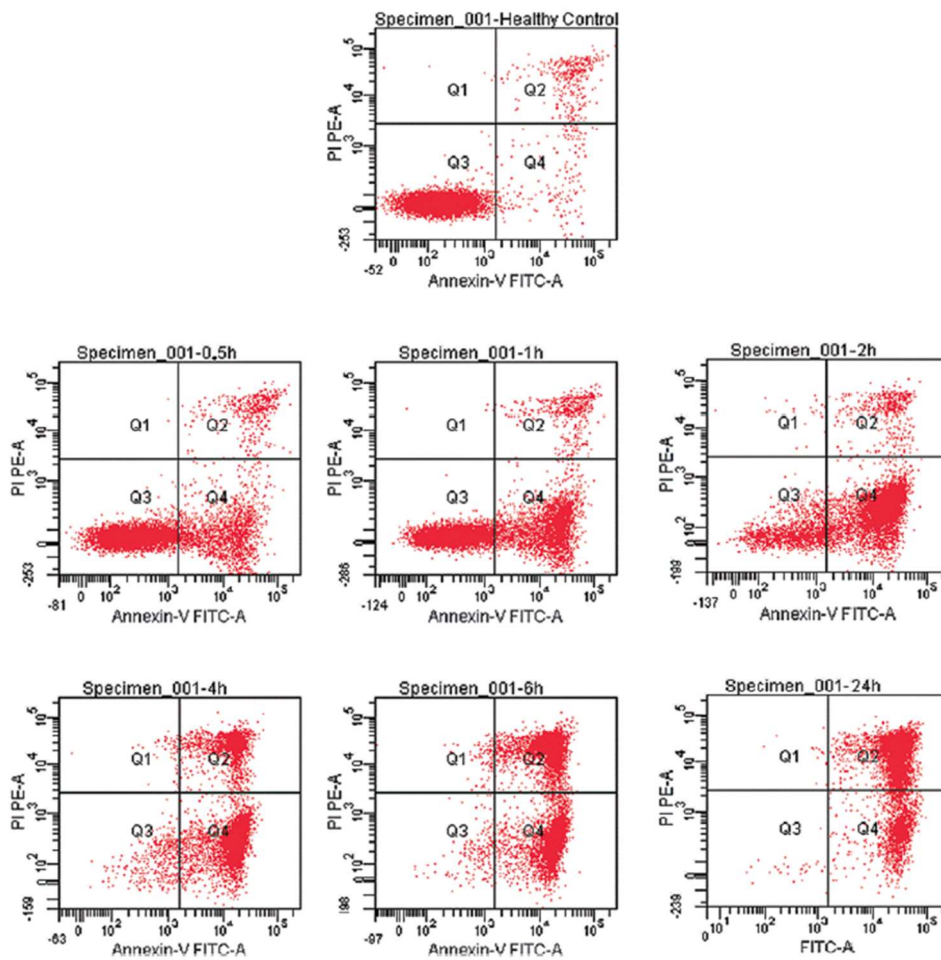


Figure 2.25: Time dependent effect of 0.5 μM staurosporine on Jurkat cells, examined with Annexin-V/PI assay by using flow cytometry [93].

2.3.4.2 Materials and methods

Cell culture and drug preparations for K562 and CCRF-CEM cells were same with the XTT assays.

Apoptosis analysis: “*The Muse Count & Viability Assay Kit*” was used with *MUSE Cell Analyzer* (Fig. 2.26). This kit consists of Annexin-V and PI stains. Cell viability was checked with Trypan blue (1:1, Sigma Aldrich) staining in Automatic Cell Counter (TC20, Bio-Rad Laboratories Inc.) before Annexin-V/PI staining for comparison purposes.



Figure 2.26: MUSE cell analyzer.

2.3.4.3 Results

Apoptosis analyses were carried out for K562 and CCRF-CEM cell lined under the effect of *imatinib* and *doxorubicin*, respectively. Results were presented as follows:

Imatinib effects on the apoptotic death of K562 cells: According to XTT assay results, it was decided to expose 100, 300, 500, and 1000 nM *imatinib* to K562/wt cells during 24 and 48h in order to detect early apoptosis. Experiments were carried out with 2 biological replicates. Cells, utilized in the apoptosis analysis, were analyzed with trypan blue in Automatic Cell Counter, also. Table 2.3 presents cell viability ratio obtained by this analysis.

Table 2.3: K562/wt cell viability under the effect of *imatinib* during 24 and 48h.

Cell type	Viability (%) 24h	Viability (%) 48h
K562/wt DMSO control	96.5±2.1	97.0±2.8
K562/wt under exposure of 100 nM ima	92.5±3.5	-
K562/wt under exposure of 300 nM ima	98.5±0.7	89.5±6.4
K562/wt under exposure of 500 nM ima	95.5±2.1	-
K562/wt under exposure of 1000 nM ima	90.5±2.1	45.0±2.8

Figure 2.27 and 2.28 present the results of apoptosis measurements for 24h and 48h, respectively, indicating that 24h was not enough to obtain accurate IC₅₀ values like in XTT assays. 48h exposure results show that cell death in the half of population was observed in higher dosages of drug than that of XTT analysis. Although flow cytometry is the most sensitive analysis to detect early apoptosis, cell viability (57.5%) was greater than that of obtained in trypan blue viability test (45.0%). This can be interpreted that a part of the cells did not chose apoptosis as the mechanism of death under the effect of *imatinib*.

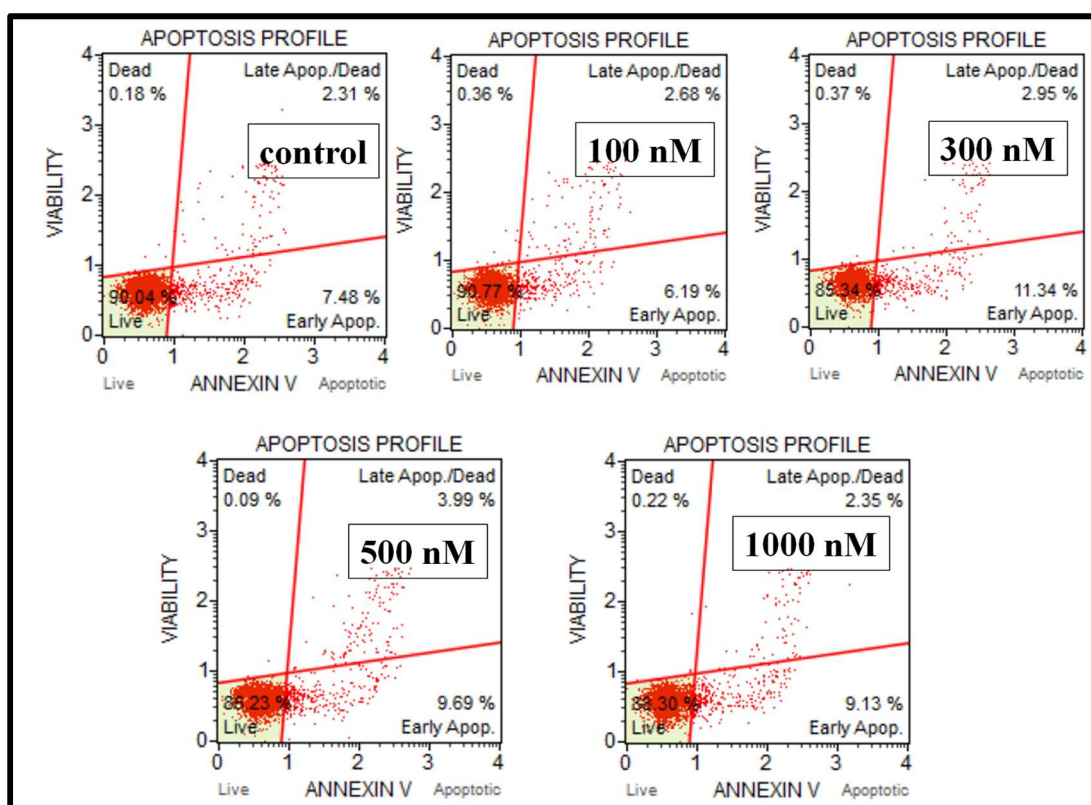


Figure 2.27: Apoptosis profile of K562/wt cells under the effect of *imatinib* for 24h.

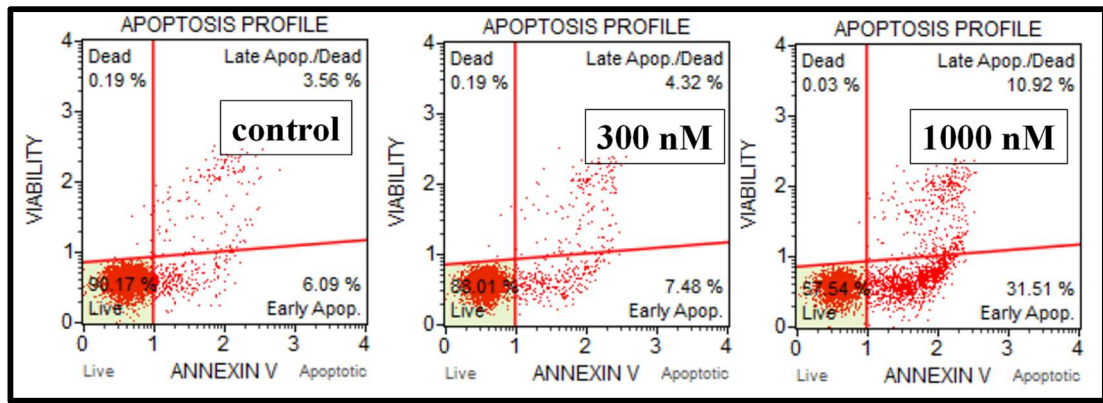


Figure 2.28: Apoptosis profile of K562/wt cells under the effect of *imatinib* for 48h.

Doxorubicin effects on the apoptotic death of CCRF-CEM cells: Doxorubicin is a fluorescent drug. MUSE fluorescence measurement system can detect *doxorubicin* with its light cubes. In order to prevent misinterpretation of results, unstained and drug exposed cells were utilized as the reference group of stained and drug exposed cells in this analysis.

According to XTT assays, IC_{50} of CCRF-CEM/wt cells was determined as 220 nM (maximum). It was decided to expose 250 nM *doxorubicin* to CCRF-CEM/wt cells during 18-24h in order to detect early apoptosis. Table 2.4 presents cell viability ratio obtained by trypan blue viability analysis and Figure 2.29 presents the 18h (a) and 24h (b) flow cytometry results, indicating similarity between apoptosis and XTT assays.

Table 2.4: CCRF-CEM/wt cell viability under the effect of *doxorubicin* during 18 and 24h. One measurement was taken.

Cell type	Viability (%) 18h	Viability (%) 24h
CCRF-CEM/wt DMSO control	89.0	90.0
CCRF-CEM/wt under exposure of 250 nM dox	81.0	72.0

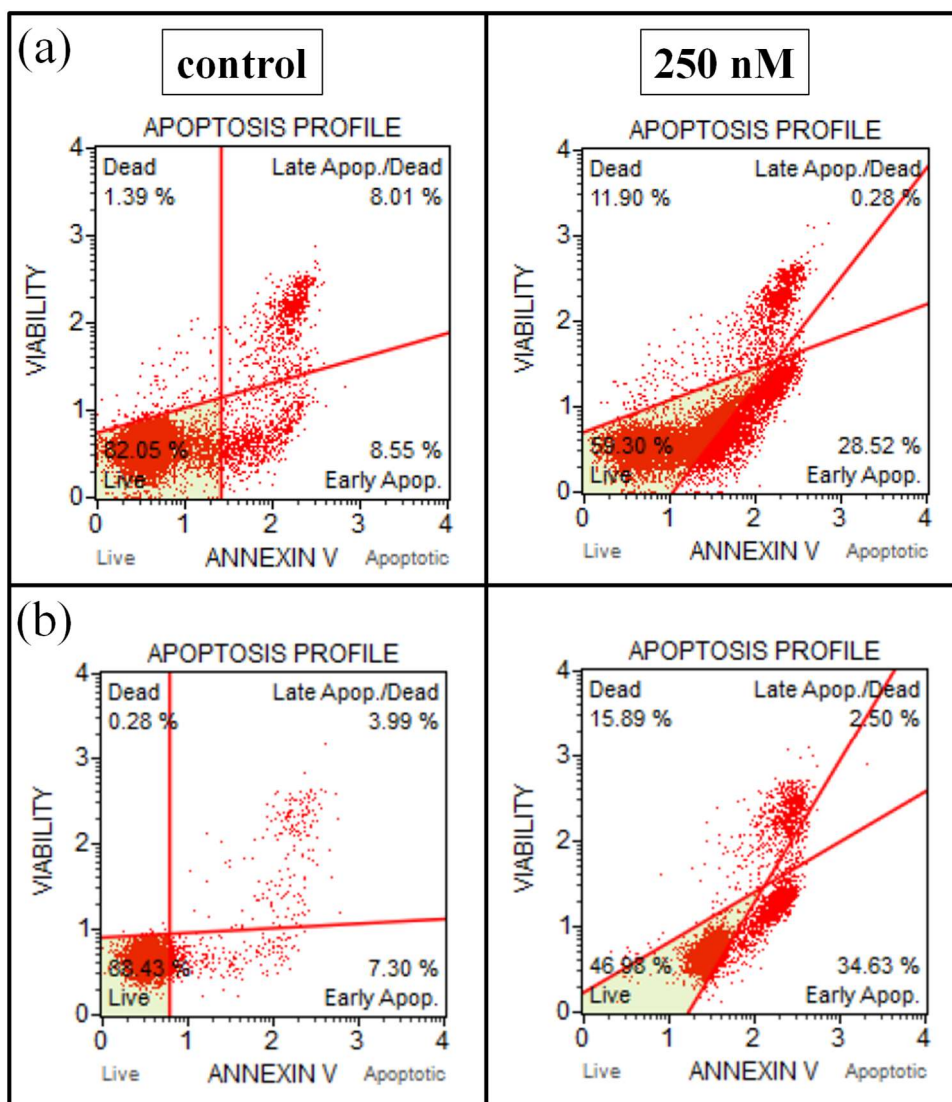


Figure 2.29: Apoptosis profile of CCRF-CEM/wt cells under the effect of 250 nM *doxorubicin* during 18h (a) and 24h (b).

2.3.4.4 Discussion

Doxorubicin effect on CCRF-CEM cells were observed like in XTT assays. For K562 cells, XTT assay results were interpreted that early apoptosis should be detected with Annexin-V/PI analysis in a duration shorter than 48h. However, results showed that under the effect of *imatinib*, K562 cells can choose another way for death. Therefore, screening of *imatinib* effect with flow cytometry for K562 cells was not more accurate than XTT assay. To make more interpretation about death in K562 cells under the effect of *imatinib*, cell cycle analysis was carried out as explained below.

2.3.5 Cell cycle effects of drugs

Cell cycle arrest and death of cells under the effect of drugs should be distinguished to examine whether they are effective. Dose response relationships obtained through cell proliferation assays give the cytotoxicity of a drug if accurate time is determined, exactly. However, they do not examine the phase-specific arrest of cells [94]. Therefore, cell cycle analysis was included to scope to obtain complementary results with XTT and apoptosis assays.

2.3.5.1 Muse™ Cell cycle assay

This assay consists of a patented mixture of some reagents, including PI and RNase A. RNase develops the precision of DNA staining by intercalating of PI. Fluorescence intensity of cells at G₂/M stage is twice the intensity of cells at G₀/G₁. As a result, this assay can classify the cells according to their cell cycle phase, G₀/G₁, S or G₂/M.

2.3.5.2 Materials and methods

Cell culture and drug preparations for K562 were same with the XTT assays.

Cell cycle analysis: “Muse™ Cell cycle assay” was used with MUSE Cell Analyzer (Fig. 2.26). After cells had been fixated with ethanol, the procedure explained detailed in [95] was followed.

2.3.5.3 Results

Under effect of *imatinib* (300 and 1000 nM), K562 cell cycle is presented in the following figure at the end of 48h. According to these results, almost 70% of cells in control group were in S-phase of cell cycle while 56% of cells stayed in S-phase under the effect of 1000 nM *imatinib* for 48h. Instead of death, 15% of them chose to stay at G₀/G₁ state.

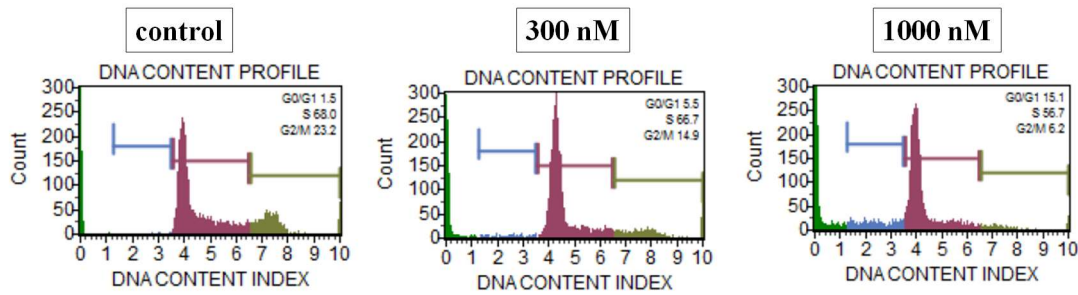


Figure 2.30: *Imatinib* response of K562 cell with cell cycle assay.

2.3.5.4 Discussion

Cell cycle analysis was carried out to provide inspection about the high cell proliferation in apoptosis assays than that of XTT analysis. However, there is not significant increase in the number of hyperploid cell population to prove that major cell death mode was not apoptosis. Therefore, the analysis of expression of senescence markers, such as *SA-β-gal*, can be inserted into cell cycle analysis.

2.4 Conclusion

In order to determine resistance level of leukemia cells, XTT assays were carried out. The cell lines in our laboratory were classified as high-level laboratory and clinically relevant model of resistance. Next, the aim in the apoptosis assays was to determine correct time and doses for the screening of *imatinib* and *doxorubicin* effects on K562 and CCRF-CEM cells by electrical analysis. For CCRF-CEM/wt cells, time and dose were determined as 18 h and 250 nM doxorubicin while the major death mode in K562/wt cells was not observed as apoptosis. Therefore, 24 h and 300 nM *imatinib* were chosen for K562/wt cells' electrical examinations. The major cell death mode in K562 cells under the effect of *imatinib* can be detected through more comprehensive analysis. However, results did not change the parameter of dielectrophoretic detection unit. Therefore, this analysis can be carried out as future work.

CHAPTER 3

ELECTRICAL CHARACTERIZATION OF WILD TYPE AND DRUG RESISTANT LEUKEMIA CELLS USING IMPEDANCE SPECTROSCOPY

Plasma membrane, selective barrier between cell interior and its milieu, provides the homeostasis of cell. It transports essential molecules, including glucose, amino acids, and ions. The transportation of molecules is ensured by the transport proteins. The amount and functionality of these proteins in the membrane vary according to the environmental and physiological conditions of cells [96]. Variations in transport molecules create differences in the dielectrical properties of both cell membrane and cytoplasm. These cell-specific dielectrical characteristics enable the cell manipulation through dielectrophoresis (DEP). In order to choose the proper operational parameters for DEP, cells should be characterized dielectrically under different biological conditions.

In this chapter, firstly, a review of ion transport and ion content of mammalian cells are presented. Next, the characterization of K562 (CML), CCRF-CEM (ALL), HL60 (APL) cell lines, and their drug resistant progenies through ion release-based impedance spectroscopy (IRbIS) technique is reported, for the first time in the literature.

3.1 Overview of membrane transport proteins

4% of genes in human genome encode membrane transporters. 406 of them encode ion channels and 350 of them are sorted as intracellular transporters [97]. Lots of the molecules and ions are transported through cell membrane by the assistance of these proteins. In fact, the transportation of molecules which can diffuse from membrane is enhanced by them. There are 3 types of membrane transport proteins: (1) Ion channels,

(2) ATP-powered pumps, and (3) Transporters, having high grade of specificity for their substances [98] (Fig. 3.1)

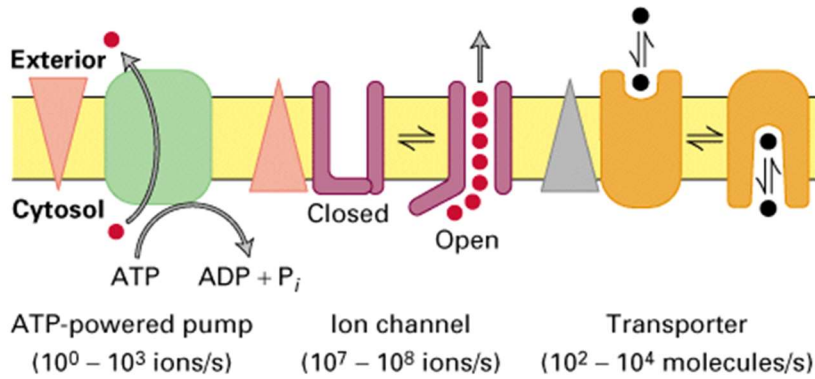


Figure 3.1: Membrane transport proteins: Ion channels, ATP-powered pumps, and transporters [98].

3.1.1 Ion channels

Ion channels provide the movement of specific ions down their electrochemical gradient. They produce electric potential across membrane. These electric potential is negative inside of the cell membrane, being ~70 mV in all cells [98].

Main ions in the cytoplasm are potassium (K⁺), sodium (Na⁺), chloride (Cl⁻), and calcium (Ca²⁺). Table 3.1 presents typical ion concentrations inside a mammalian cell and blood.

Table 3.1: Typical ion concentrations inside a mammalian cell and blood [98].

Ion	Cell cytoplasm (mM)	Blood (mM)
K ⁺	139	4
Na ⁺	12	145
Cl ⁻	4	116
Ca ²⁺	<0.0002	1.8

Lots of open K⁺ channels exist on the membrane as others have few of them. Therefore, they create the major ionic transfer across the plasma membrane. Patch clamping technique provides the examination of these ion channels in terms of their functions and regulations by measuring the electric current [98].

3.1.2 ATP-powered Pumps

ATP-powered pumps enable the transportation of ions and numerous small molecules against their concentration gradients. Figure 3.2 presents four main types of ATP-powered pumps: P, F, V, and ABC superfamily classes [98].

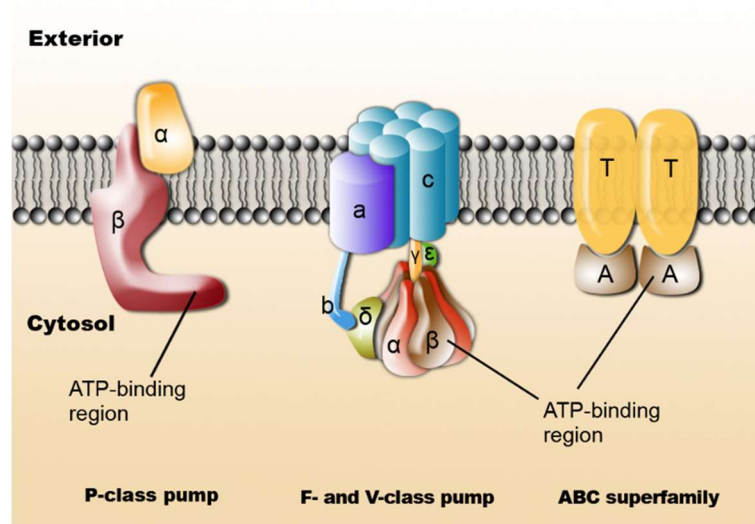


Figure 3.2: Four main sub-classes of ATP-powered pumps.

P-class ion pumps are phosphorylated and carry ions, including Na^+/K^+ typically in mammalian cells, Ca^{+2} in muscle cells, and H^+ in plant, fungi, and bacterial cells [98].

F- and V-class ion pumps have similar structure which is different than P-class. V-class ones work to provide low pH in vacuoles of plant cells, lysosomes, and acidic vesicles of animal cells. F-class pumps (proton pumps) are located in the mitochondria and chloroplasts, having function in the ATP synthesis [98].

ABC superfamily has more than 100 proteins in 7 subfamilies. They are specific for unique substrates, including ions, sugars, peptides, and polysaccharides. They are composed of a pair of ATP-binding domains and two sets of transmembrane (TM) domains. ABC genes are vital for many processes in the cell. Mutations occurred in these genes have some roles in various human disorders, including cystic fibrosis,

neurological disease, retinal degeneration, cholesterol and bile transport defects, anemia, and drug response.

Up to now, it was shown that 3 subfamilies are related with MDR. They are the ABCB subfamily, including P-gp (MDR1 or ABCB1), the ABCC subfamily, including multidrug-resistance protein (MRP1 or ABCC1), and the ABCG subfamily, including breast cancer resistance protein (ABCG2 or MXR). Although P-gp, MRP1, and ABCG2 are the most common in MDR, their contribution is still not well characterized. In addition to these three proteins, there exist at least 11 ABC transporters, linked to MDR. They are ABCA2, ABCA3, ABCB4, ABCB5, ABCB11, ABCC2, ABCC3, ABCC4, ABCC5, ABCC10, and ABCC11 [99].

3.1.3 Transporters: Symporters and Antiporters

Transporters use energy, obtained from the membrane potential or stored in the concentration gradient of ions to provide the uphill movement of molecules. For example, energetically favored transfer of Na^+ ions can be coupled with the glucose or lysine movement against their concentration gradient. When transported molecule and its cotransporter ion are in the same direction, this is named as symporter. If they are in opposite direction, antiporters work. Figure 3.3 presents a symporter mechanism for Na^+ and glucose.

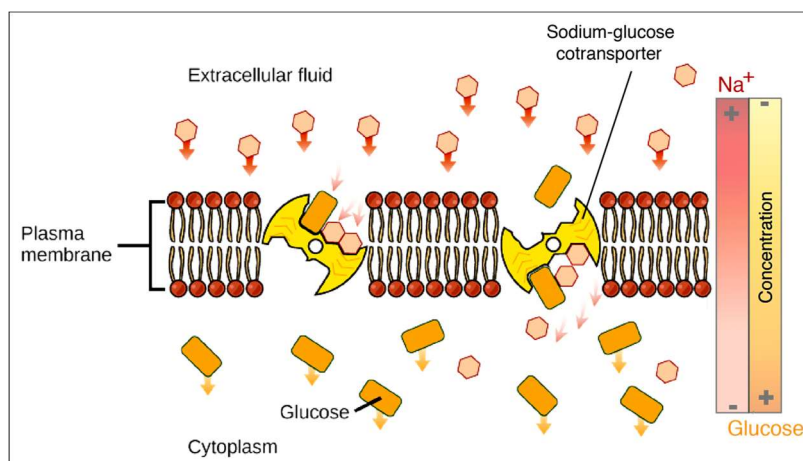


Figure 3.3: Transportation of glucose by the aid of sodium symporter [100].

3.2 Ions, apoptosis, and multidrug resistance

Major intracellular ions are sodium (Na^+), potassium (K^+), chloride (Cl^-), and calcium (Ca^{2+}). Through metabolic activities of cells, their values can change. For example, the main reason of apoptotic volume decrease (AVD) is the variations in intracellular ion concentrations [101].

The potassium channels have essential role in the apoptosis, regulating the cell volume [102]. Studies reported that the inhibition of some potassium channels prevents cell death although the exact mechanism has not been determined, yet. For example, when potassium channels of SGC7901 gastric cancer cells were inhibited, they developed resistance against some apoptosis-inducing drugs, including *doxorubicin*, *vincristine*, and *cisplatin* [102]. According to Bortner *et al.*, the effective type and role of potassium channels can be different in apoptosis according to cell type and death stimulus [101]. For instance, in some cancers, higher mitochondrial membrane potential and lower expression of the redox-sensitive K^+ channel have been observed that caused the development of resistance to apoptosis.

Na^+ and Cl^- are also critical in apoptosis. Increase in intracellular sodium has been stated in cell death. A volume sensitive outwardly rectifying (VSOR) chloride channel has also been suggested as a main anionic conductance during apoptosis [101]. Although Ca^{2+} is in nM range concentration, it has some functions as central cell death regulator. [103] reviewed these regulations.

Figure 3.4 summarizes ions and ion channels, having role in apoptosis. Reviews can be examined for more detailed information, like [105, 106, 107]. More specifically, other studies exist according to cancer types, such as breast [5], gastric [107], and leukemia [108].

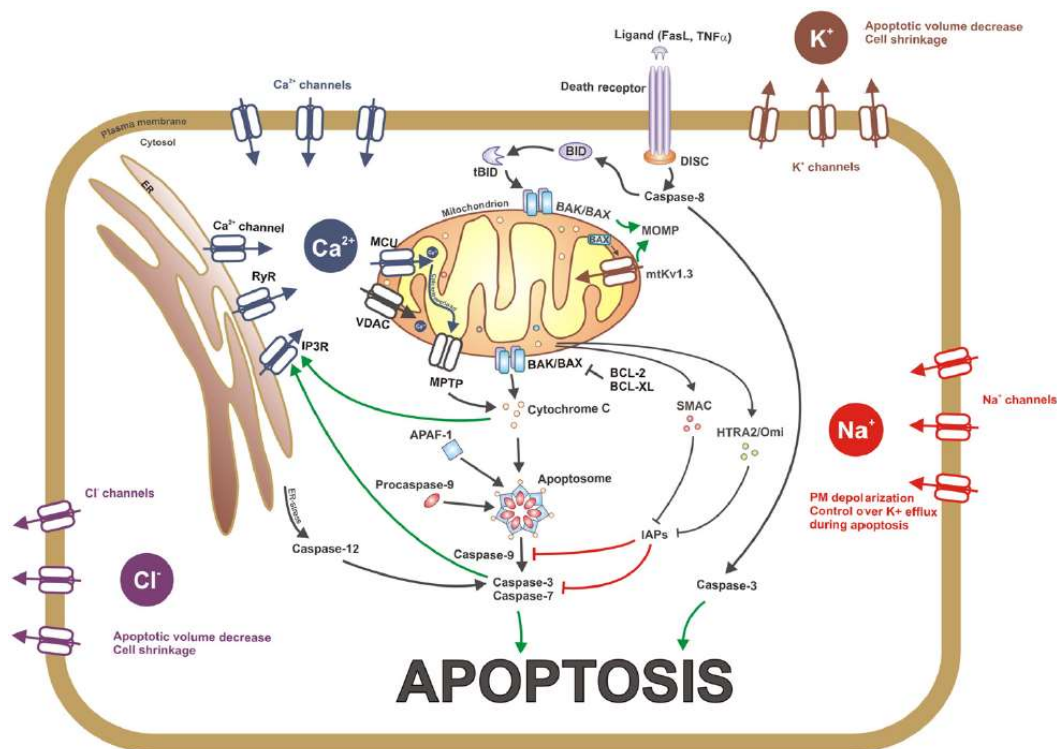


Figure 3.4: Ions and ion channels, having role in apoptosis [104].

Drug resistance detection is the main subject of this thesis. Therefore, from this point, ion channel studies related with the development of drug resistance in cancer cells will be presented. According to Huang *et al.*, various kinds of membrane transporters are responsible for the chemo-sensitivity and -resistance of tumor cells. Plasma membrane is not permeable for water-soluble drugs, such as *cisplatin*. Therefore, they are transported through hydrophilic channels. Resistance against these drugs can be caused by either downregulation of uptake transporters or enhanced drug efflux. Hydrophobic drugs, such as *doxorubicin* and *paclitaxel*, can diffuse across the plasma membrane. Diffusion is enhanced by transport proteins. However, due to increased drug efflux, cells can develop resistance against these drugs. These are direct mechanisms between transport proteins and drugs. Besides, there exist indirect mechanisms, including maintaining nutrients to cells, modulation of electrochemical gradient on the cell membrane, and alterations in apoptotic pathways [97].

Hoffman *et al.* says that in the drug resistance, caused by the damage in apoptotic pathways, the modulation of ion channels and transporters is one of the major

mechanisms [109]. In their review [109], they deliberated how the modulation of ion channels affects the development of drug resistance and tried to explain mechanisms behind them. Figure 3.5 presents the anti- and pro-apoptotic ion channels in cell membrane, involved in MDR. Downregulation of pro-apoptotic channels, including K^+ , Cl^- , and Ca^{2+} , is observed in MDR. In addition, the upregulation of anti-apoptotic ones can provoke the development of MDR [109].

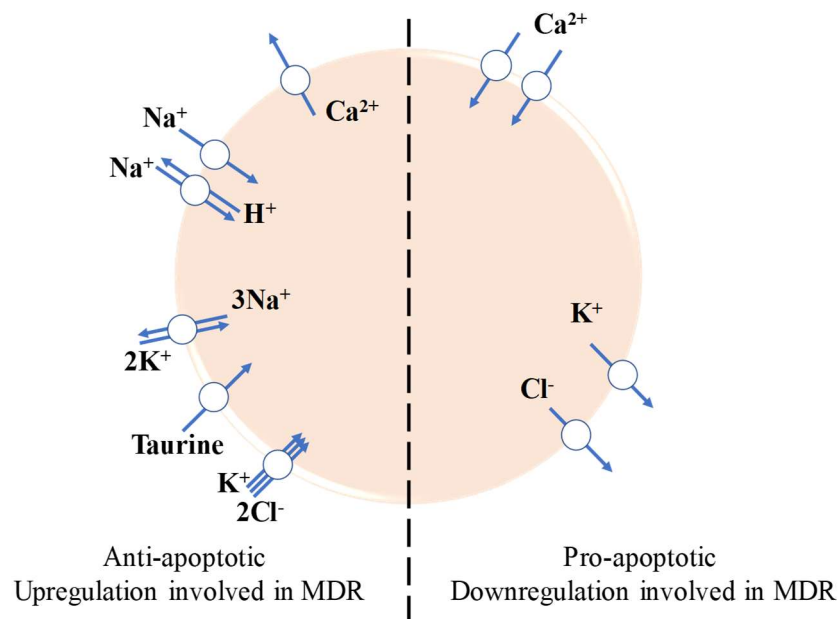


Figure 3.5: Anti- and pro-apoptotic ion channels in cell membrane, involved in MDR (Adapted from [109]).

According to studies with wild type Ehrlich ascites tumor cells (EATC), under the effect of *cisplatin*, AVD substantiates in three stages. Firstly, volume decreases (AVD₁). Next, an increase in volume occurs as a translational stage (AVD_T). Finally, volume decreases under the level at which the end of first stage (AVD₂). Figure 3.6 presents ion levels during these stages. These results indicate that for the AVD₁, net loss of KCl is observed. Next, in AVD_T, NaCl uptake starts for volume compensation. At the end, KCl is lost for net volume decrease.

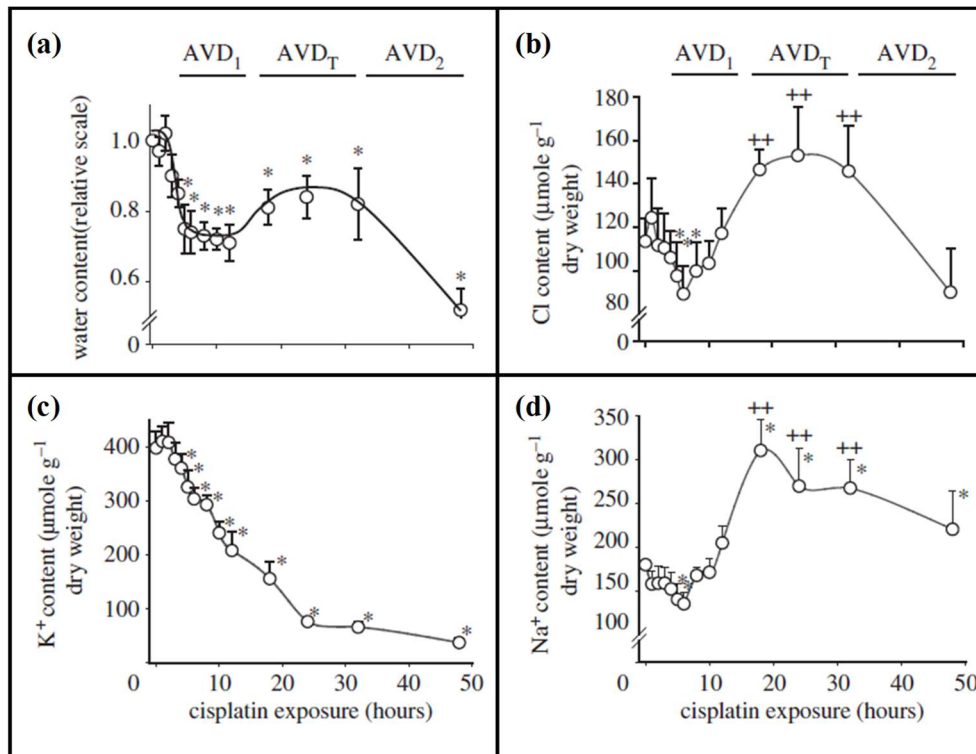


Figure 3.6: Water (a) and ion content (Cl⁻ (b), K⁺ (c), and Na⁺ (d)) of wild type EATC cells under the effect of 5 μM *cisplatin* during apoptosis.

Figure 3.7 was obtained as the AVD response of MDR EATC cells. Results show that under the effect of *cisplatin*, MDR EATC cells showed neither AVD₁ stage nor a significant increase in caspase 3 activity. On the other hand, wild type ones started apoptosis, increasing the level of caspase 3 activity in the 14h after drug addition. After 18h, both cell lines showed increase in caspase 3 activity. Moreover, although the variation trend of ions was the same in both MDR and wild type cells (Fig. 3.8), some differences occurred in the Cl⁻ and Na⁺ content after 20 hours [110].

In order to obtain information about ionic content of wild type and resistant cancer cells, both ion content analysis with fluorescence stains in flow cytometry and ion-release based impedance spectroscopy have been exploited as explained below in detail.

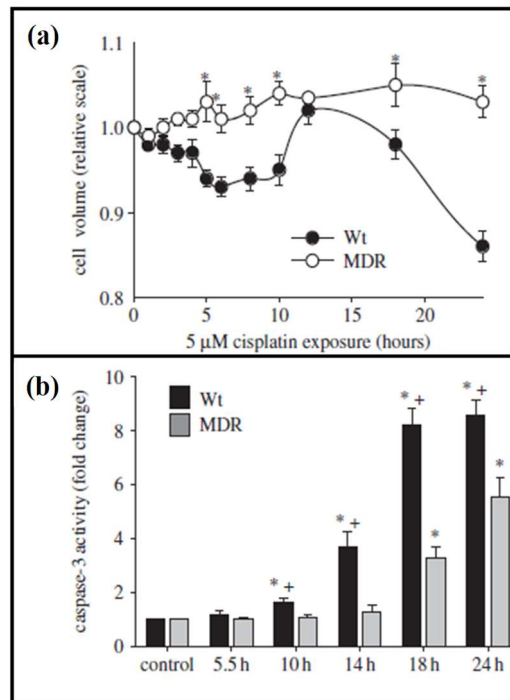


Figure 3.7: Cell volume change (a) and caspase 3 activity (b) in MDR and wild type (Wt) EATC cells under the effect of 5 μM *cisplatin* according to time.

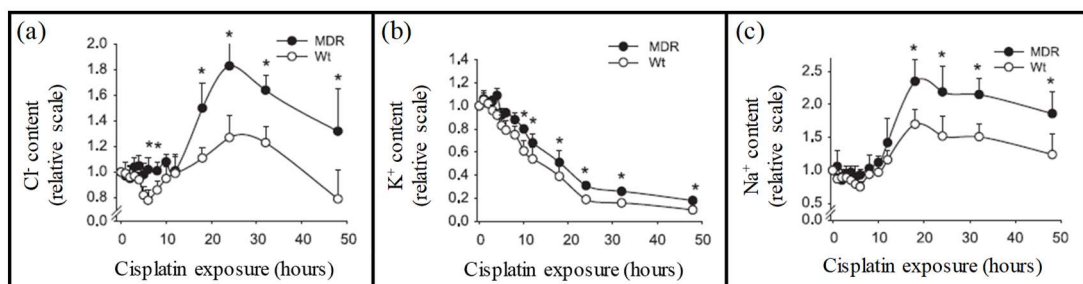


Figure 3.8: Cl⁻ (a), K⁺ (b), and Na⁺ (c) content during apoptosis in wild type and MDR EATC cells under the exposure of *cisplatin* (5 μM) [110].

3.3 Cell ion release-based impedance spectroscopy (IRbIS) using microfluidic systems

Biological cells can be identified by means of many techniques in microfluidics, including electrical, magnetic, acoustic, etc. Electrical techniques provide the characterization of cells according to their sizes and dielectrical properties. They are generally achieved in two ways: AC electrokinetics and impedance spectroscopy (IS). Particle behavior in a fluid under the effect of AC electric field is studied in AC

electrokinetics techniques, such as dielectrophoresis (DEP) and electrorotation (ER) [111].

Impedance is the preventing ability of a material the alternating current [112]. It can be defined as the complex ratio of voltage to current in another way. In IS techniques, dielectrical properties of biological cells are determined, measuring their electrical response under electric field. According to [113], the first bio-impedance measurement was achieved by Höber who measured the low and high frequency conductivity of red blood cells (RBCs) [114].

Fricke aimed to derive a formula to investigate the specific conductivity of a cellular substance from specific conductivity of a cell suspension in 1924 [115]. He identified conductivity and capacity of disperse systems exploiting Maxwell principles (1873). The capacitance and cell membrane thicknesses, defined by Fricke, are considerably close to the ones used today [113]. Cole characterized the behavior of cell membrane and invented Cole-Cole plot by studying on oocytes. By the contribution of all these researchers, first single-cell measurements were achieved by Curtis and Cole by using marine and frog eggs in 1937 [116]. Schwan is another famous name in this area who characterized three major dispersions for biological cell suspensions. α -dispersion appears at low frequencies (kHz range) and responsible for the formation of double layer around particle. β -dispersion forms at MHz range frequencies due to charging of cell membrane. γ -dispersion is originated from the dipolar relaxation of water in GHz regimes [113].

In 1956, Coulter counter were invented by Wallace Henry Coulter. DC is applied in this technique so it is resistance based. Single cell impedance measurement in a flow system was achieved by Hoffman and Britt in 1979 [116]. In 1980s, adherent cell impedance spectroscopy was discovered and named as electrical cell-substrate impedance sensing (ECIS). In this study, Giaever and Keese cultured mammalian fibroblast on gold electrodes and monitored them under 4 kHz frequency [117].

By means of these early studies and the development of microfabrication and microfluidic technologies, impedance measurement technology have been evolved

and exploited in many different fields, such as cell sorting, cancer research, drug screening, environmental pollution, and food safety detection [116].

Cell based applications of impedance sensing can be separated into three parts: Electric cell-substrate impedance sensing (ECIS), electric impedance spectrum (EIS), and impedance flow cytometry (IFC) [116]. In ECIS, adherent cells are grown on electrodes. Therefore, the impedance of electrodes alters. By monitoring of these variations, information about cell proliferation and viability, cell cycle, metastasis, cell migration, and invasion can be obtained which enables cytotoxicity tests (including drug screening), detection of the killing capacity of natural killer cells in immunotherapy, cancer and metastasis diagnosis, etc. By means of EIS, suspended cells at steady state can be monitored for proliferation or metabolism [116].

The first example of IFC is Coulter counter. Although this technique does not give any information about the interior properties of cells, simplifying them as homogenous dielectric spherical particles, it can discriminate them if they have different sizes, like RBCs and WBCs. AC based IFC can be applied for the electrical characterization of cells at single cell level. For example, Zheng *et al.* determined the cytoplasmic conductivity and specific membrane capacitance of AML2 and HL60 cell lines. In their study, a channel, having smaller dimensions than cells, provides the cells being constricted (Fig. 3.10). This enables the calculation of resistance change in the measurement area. After cell is constricted, impedance spectrum is taken. Utilizing electrical equivalent circuit and applying curve fitting, cell properties can be calculated. Although scanned frequency interval is considerably large providing highly sensitive information about cell and system, testing is challenging and time-consuming to obtain information about large number of cells.

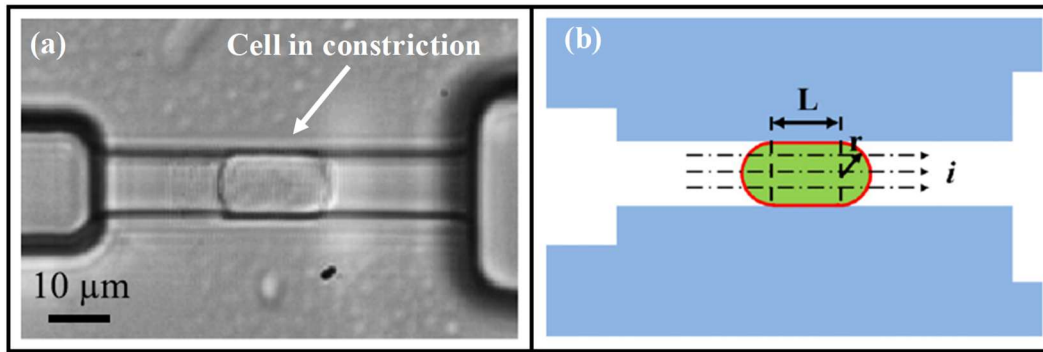


Figure 3.9: (a) A constricted cell and (b) Schematic view of geometrical model of its.

Cell ion release-based impedance spectroscopy (IRbIS) is another technique, utilized to determine cell number. However, cells are lysed in this method. Therefore, it cannot be categorized as cell-based. Cheng *et al.* described this technique as the measurement of conductivity variation, caused by ion released from surface immobilized cells inside microchannel. Cells specifically immobilized on electrodes by antibody interaction. Next, they are lysed by using hypotonic media. According to impedance change, the determination of immobilized cell number can be achieved. They reported that the number of cells is directly related with the increase in solution conductance. Their method is sufficiently sensitive to count 20 cells in a microliter [118]. Damhorst *et al.* operated the same method to detect HIV qualitatively. In this method, surface inside microchannel is coated for HIV immobilization. To detect this immobilization, the antibody coated and ion (concentrated PBS) encapsulating liposomes are used to enhance signal [119].

In this thesis, IRbIS technique was chosen to determine total ion concentration of single cell as average by reversing analysis method, for the first time in the literature. In the following subsections, device design, fabrication, experimental design, and results will be presented.

3.3.1 Interdigitated electrode (IDE) design

In order to measure impedance inside a microchannel, different electrode types can be preferred, such as interdigitated coplanar (IDEs) and top-bottom electrodes. Cheng *et al.* compared the cell counting performance of top-bottom, interdigitated coplanar,

and two-rail coplanar electrodes in IRbIS. They reported that top-bottom electrodes have the highest detection efficiency while the two-rail ones have the lowest [118]. In this thesis, platinum IDEs have been preferred due to simpler fabrication than top-bottom electrodes and higher detection efficiency than two-rail ones. Figure 3.11 (a) presents the structure of an IDE with geometrical design parameters. Electrical equivalent circuit of IDE has 3 elements (Fig. 3.11 (b)). C_{di} is the parasitic capacitances due to substrate and solution. Z_{dl} is the double layer element [118, 120]. It depends to frequency and properties of electrode and solution (Eq. 3.1). R_{sol} stands for the solution resistance, depending on the solution conductivity [118].

$$Z_{dl} = \frac{1}{(j\omega)^n B} \quad (3.1)$$

Here, n and B symbolize constant phase element parameters, j is $\sqrt{-1}$, and ω is the angular frequency.

Figure 3.11 (c) and (d) shows the impedance magnitude and phase variation of an IDE according to frequency. From these characteristics, it can be interpreted that at low frequencies, double layer impedance is effective while at high frequencies, parasitic capacitances affect the impedance spectrum. At mid-frequencies, impedance is constant. This constant magnitude region is named as plateau. Solution conductivity can be calculated from solution resistance at plateau (Eq. 3.2).

$$R = \kappa \sigma^{-1} \quad (3.2)$$

where κ is the cell constant (Eq. 3.3a, [120]) and R is the resistance. σ stands for conductivity.

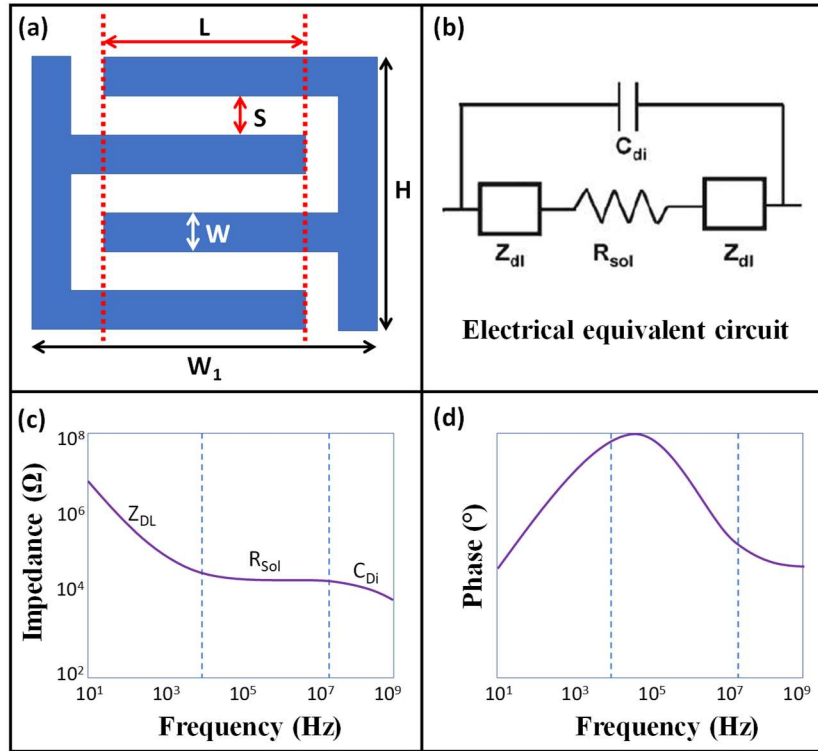


Figure 3.10: Structure (a), electrical equivalent circuit (b), magnitude (c) and phase (d) characteristics of an IDE.

Each conductivity measurement cell has a cell constant (κ). Cell constant is related with geometrical properties (Eq. 3.3). For an IDE conductivity measurement cell, these are W : Electrode width, S : Spacing between fingers, N : Finger number, and L : Overlap length.

$$\kappa = \frac{2}{(N-1)L} \frac{K(k)}{K(\sqrt{1-k^2})} \quad (3.3a)$$

$$K(k) = \int_0^1 \frac{1}{\sqrt{(1-t^2)(1-k^2t^2)}} dt \quad (3.3b)$$

$$k = \cos\left(\frac{\pi}{2} \cdot \frac{W}{S+W}\right) \quad (3.3c)$$

The function $K(k)$ is the incomplete elliptic integral of the first kind [120].

The equivalent impedance of IDEs is presented in Equation 3.4.

$$Z_{eq} = \frac{2 + R_{sol}Bj^n\omega^n}{2j\omega C_{di} + R_{sol}BC_{di}j^{n+1}\omega^{n+1} + j^nB\omega^n} \quad (3.4)$$

In this study, an IDE cell was designed having the design parameters as follows:

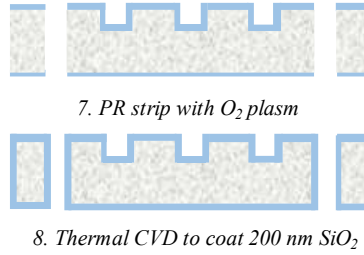
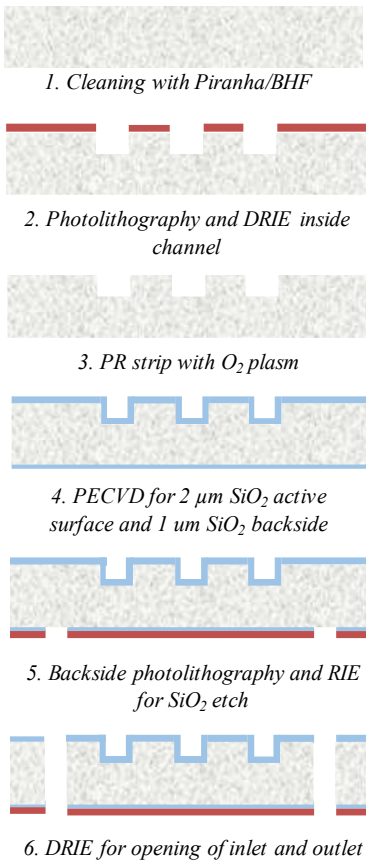
Table 3.2: Geometrical properties of IDEs.

	N	W (μm)	S (μm)	L (μm)
IDE cell (ideal)	17	15.0	7.5	100.0
IDE cell (fabricated)	17	15.8	6.7	100.8

3.3.2 Fabrication

The material of electrodes in IDE devices was platinum. Fabrication flow, made by Taylan Töral, is given in Figure 3.11. Fabricated devices are presented in Figure 3.12. To decrease parasitic impedances and noise while taking impedance spectrum, a special chip holder was designed by Dr. Sertan Sukas (Fig. 3.13). Additionally, this holder facilitated the microfluidic tests by means of sealed microfluidic connections.

Si-wafer



Glass-wafer

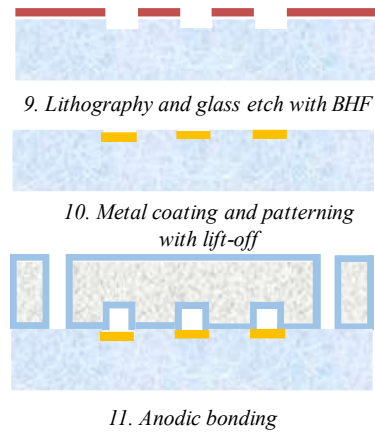


Figure 3.11: Si-glass fabrication flow of IDE devices.

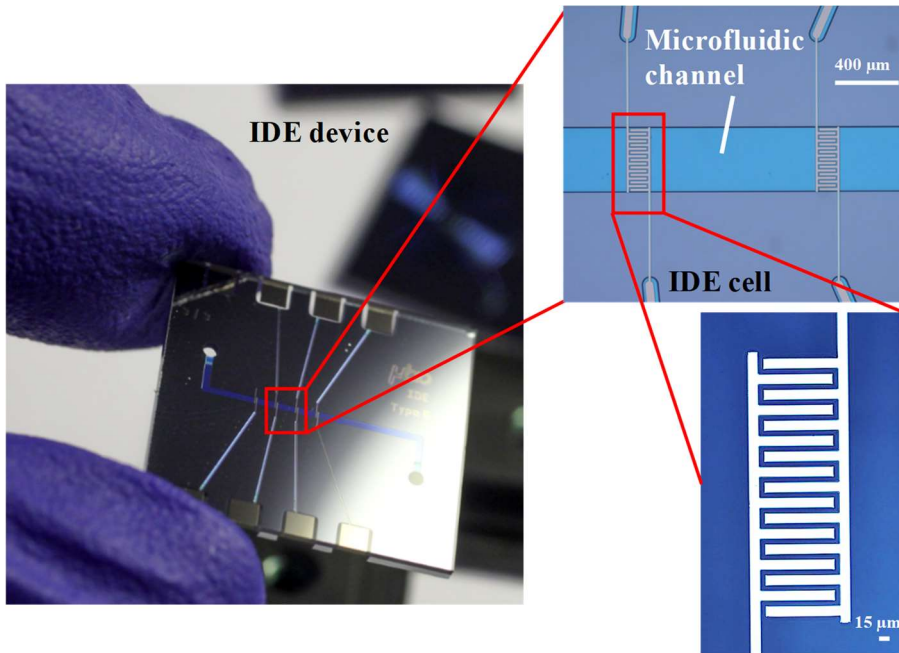


Figure 3.12: Fabricated devices and IDE structure.

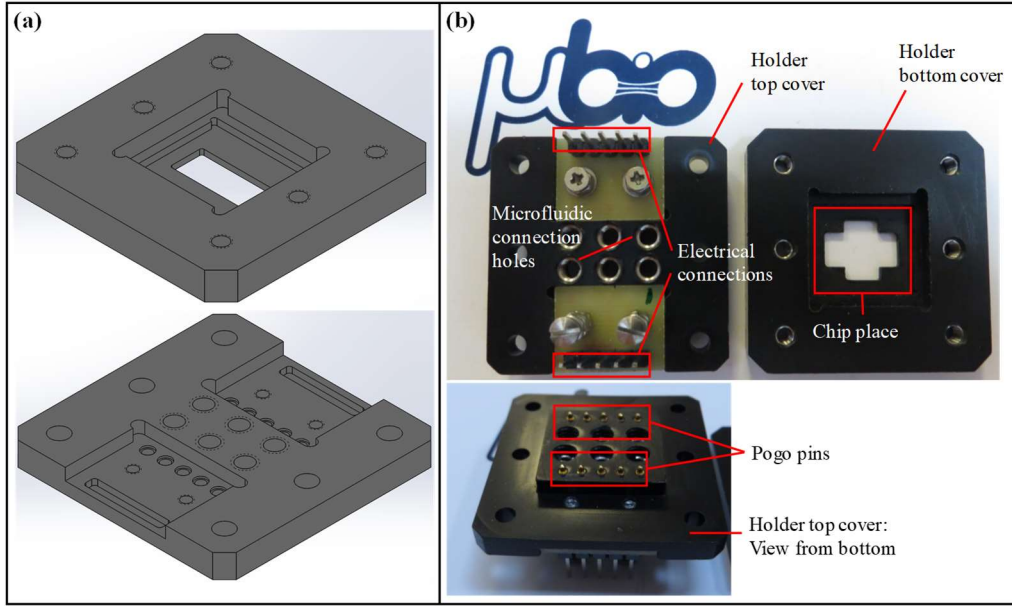


Figure 3.13: Chip holder designed by Dr. Sertan Sukas.

3.3.3 Method of operation

IDEs provide electrical information about solution. As it is presented in Equation 3.4, there exist 4 unknowns while 2 different equations are obtained from equivalent impedance as magnitude and phase. Therefore, after taking impedance spectrum, nonlinear fitting with estimated initial parameters should be carried out using the following expressions for magnitude and phase of equivalent impedance in *OriginPro* language.

Expressions:

Magnitude:

$$m = \text{imabs} \left(\frac{2 + (x_2 \cdot x_3 \cdot (1i^{x_1}) \cdot ((2 \cdot \pi \cdot X)^{x_1}))}{(2 \cdot 1i \cdot (2 \cdot \pi \cdot X)^{x_4}) + (x_2 \cdot x_3 \cdot x_4 \cdot (1i^{(x_1+1)}) \cdot ((2 \cdot \pi \cdot X)^{(x_1+1)})) + ((1i^{x_1}) \cdot ((2 \cdot \pi \cdot X)^{x_1}) \cdot x_3)} \right);$$

Phase:

$$p = (\text{imargument} \left(\frac{2 + (x_2 \cdot x_3 \cdot (1i^{x_1}) \cdot ((2 \cdot \pi \cdot X)^{x_1}))}{(2 \cdot 1i \cdot (2 \cdot \pi \cdot X)^{x_4}) + (x_2 \cdot x_3 \cdot x_4 \cdot (1i^{(x_1+1)}) \cdot ((2 \cdot \pi \cdot X)^{(x_1+1)})) + ((1i^{x_1}) \cdot ((2 \cdot \pi \cdot X)^{x_1}) \cdot x_3)} \right)) \cdot (180/\pi);$$

Initial values of parameters of n , B , R_{sol} , and C_{di} can be guessed on the order of magnitude for starting point of iterations. Chi-square minimization was used as fitting

criteria. 400 was chosen for the maximum iteration number. To understand that fitting is successful, the message: “*Fit converged. Chi-square tolerance value of 1E-9 was reached.*” was taken into account. Figure 3.14 presents representative fits of magnitude and phase of an IDE cell.

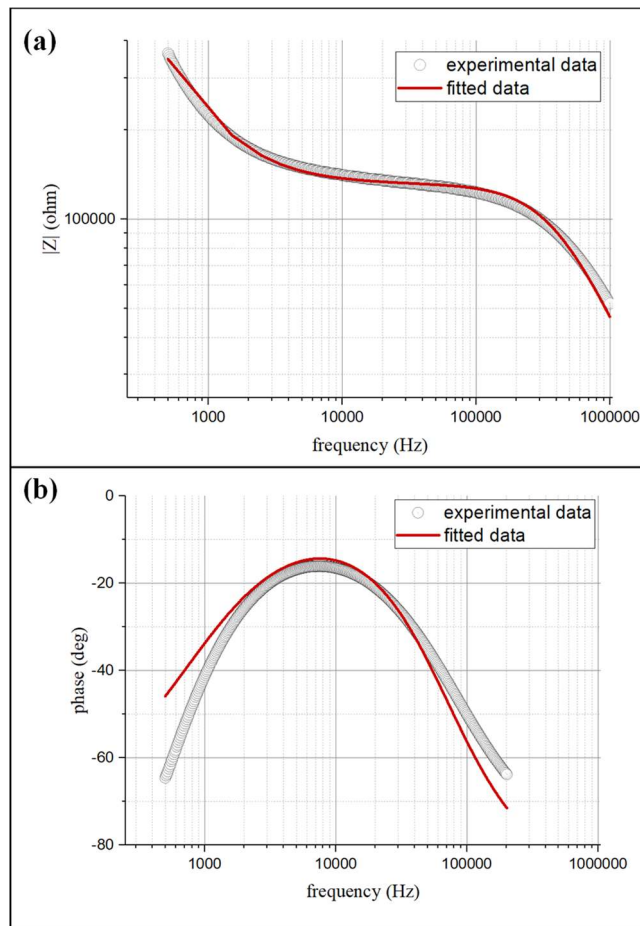


Figure 3.14: Representative fitting curves and experimental data.

All conductivity cells should be calibrated before measurement. In order to make calibration of an IDE conductivity measurement cell, cell constant should be experimentally determined.

3.3.3.1 Determination of cell constant and calibration curve

With the purpose of cell constant (κ) determination, an experiment was designed and explained in detail as follows:

Procedure:

- 1) Make calibration of conductivity meter (*Hanna Instruments*). Our conductivity/pH meter has a conductivity probe whose cell constant is 1.15 cm^{-1} .
- 2) Prepare 6 different solution measuring their conductivities with the conductivity meter. Conductivity of these solutions should be between 0.5-150 mS/m.
- 3) Take impedance spectrum of these solutions by IDE device.
- 4) Make nonlinear curve fitting (*OriginPro 2017*).
- 5) Obtain R_{sol} value of each solution from fitting.
- 6) Plot the graph of “*resistance vs resistivity*”. Set X-axis as measured resistivities by conductivity meter and Y-axis as measured resistances with IDE device.
- 7) Make linear fitting with “ $y=ax$ ” equation. Slope “ a ” is the cell constant of IDE cell under interest. Take care a criterion that R^2 value is at least 0.99.

Figure 3.15 shows the linear fitting plot of 3 different IDE devices exploited in this study as examples.

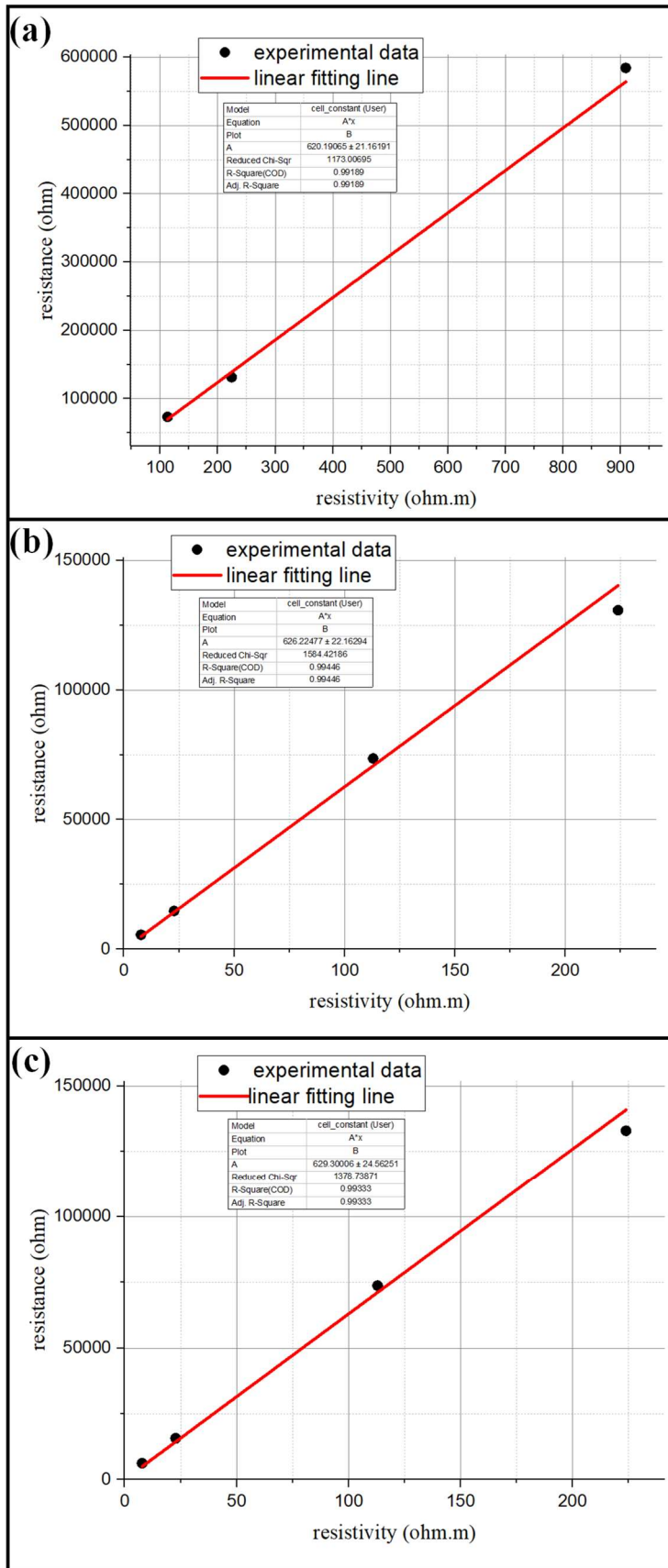


Figure 3.15: Linear fitting curves of IDE cell₁ (a), cell₂ (b), and cell₃ (c) for cell constant calculation.

There exist 3 different cell constants for an IDE cell. The first one (κ_1) is the ideal one calculated utilizing design parameters in Table 3.3, directly. The second cell constant (κ_2) is obtained using geometrical parameters measured after fabrication (Table 3.3). Final one (κ_3) is calculated experimentally.

Table 3.3: Calculated cell constants for 3 different IDE devices.

	$\kappa_1 (cm^{-1})$	$\kappa_2 (cm^{-1})$	$\kappa_3 (cm^{-1})$
IDE 1	8.6	8.2	6.2±0.21
IDE 2	8.6	8.2	6.3±0.22
IDE 3	8.6	8.2	6.3±0.25

Calibration curve can be obtained by following the procedure below after determination of cell constant.

Procedure:

- 1) Make calibration of conductivity meter (*Hanna Instruments*).
- 2) Prepare 0.01X PBS solution (*Sigma Aldrich*) and measure its conductivity with conductivity meter. Its conductivity is 12-15 mS/m.
- 3) Prepare 9 different solution with serial dilution of 0.01X PBS solution using fresh DI water. It is assumed that their conductivities become 8, 4, 2, 1, 0.5, 0.4, 0.3, 0.2, 0.1 mS/m.
- 4) Take impedance spectrum of all solutions by each IDE device.
- 5) Make nonlinear curve fitting (*OriginPro 2017*).
- 6) Obtain R_{sol} value of each solution from fitting.
- 7) Calculate conductivity from resistance by using cell constant (Eq. 3.3).
- 8) Plot the graph of “conductivity vs conductivity”. Set X-axis as measured conductivities with IDE device and Y-axis as estimated conductivities (8, 4, 2, 1, 0.5, 0.4, 0.3, 0.2, 0.1 mS/m).
- 9) Make linear fitting and obtain calibration curve of each IDE device. Take care a criterion that R^2 value is at least 0.99.

Figure 3.16 shows the calibration curves of 3 different IDE devices utilized in this study.

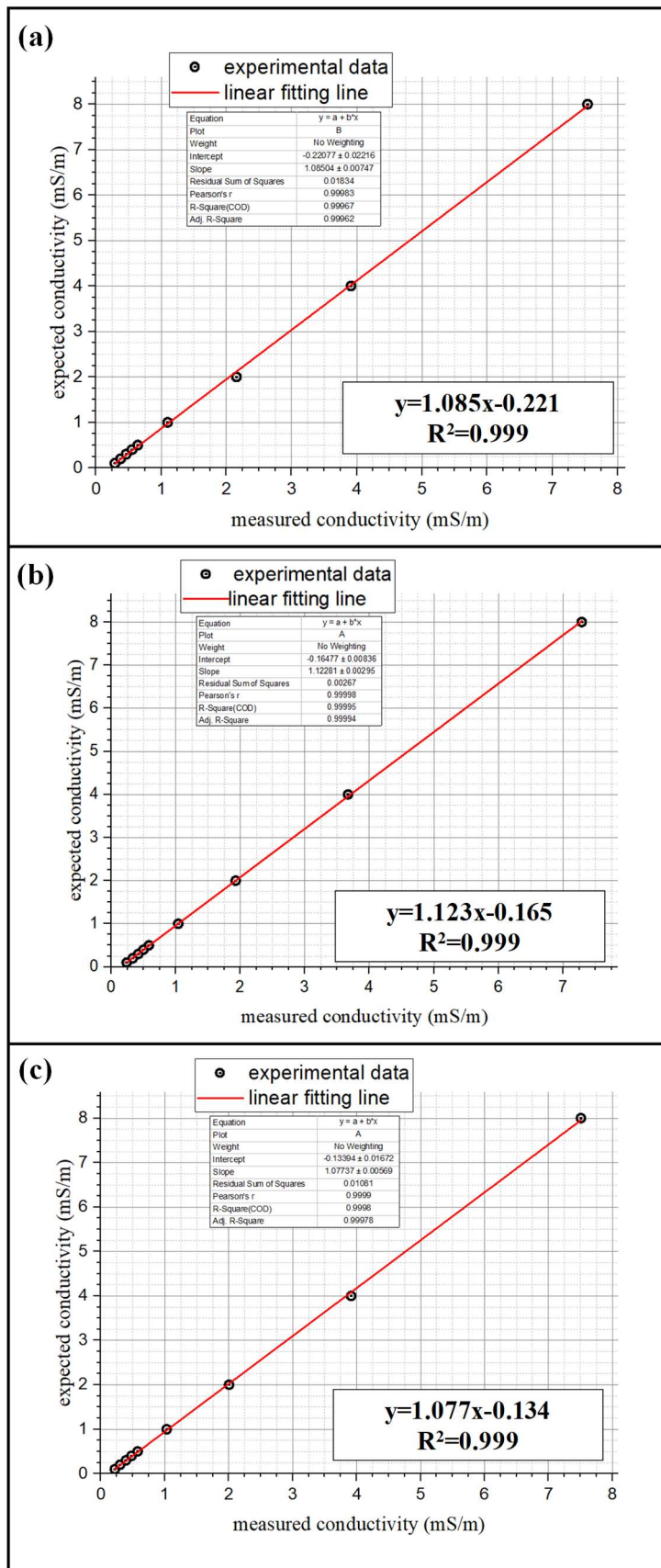


Figure 3.16: Calibration curves of IDE devices.

3.3.3.2 Cell lysis: Method development

Main purpose of this study is to determine total ion concentration inside the cytoplasm of one cell by measuring bulk conductivity having lysed cells. In order to make accurate determination of total ion content inside cell cytoplasm, the following specifications should be achieved.

- The cell number and size should be known without significant error.
- All cells should be lysed properly.
- Lysis solution should be proper for impedance measurement.

In order to provide these conditions, 14 different procedure was tried and the following procedure was developed (Fig. 3.17).

Lysis procedure:

- 1) Wash cells with a low conductivity buffer (8.5% (w/v) sucrose and 0.3% (w/v) dextrose) 3 times at 300 g for 5 min.
- 2) Suspend cells into the same medium.
- 3) Determine final cell concentration with double counting by automated cell counter (TC20, Bio-Rad Laboratories Inc.). Save cell size and number information.
- 4) With serial dilution, prepare 3 different cell solutions immersing them into fresh DI water having 8 ml total volume. Adjust initial concentration providing that immersed cell volume is limited with 300 μ l.
- 5) Put sample tube into boiling water for 45 sec.
- 6) Wait 1 h before analysis.
- 7) Check the cell solution under microscope and count again in automated cell counter to be sure lysis completed.

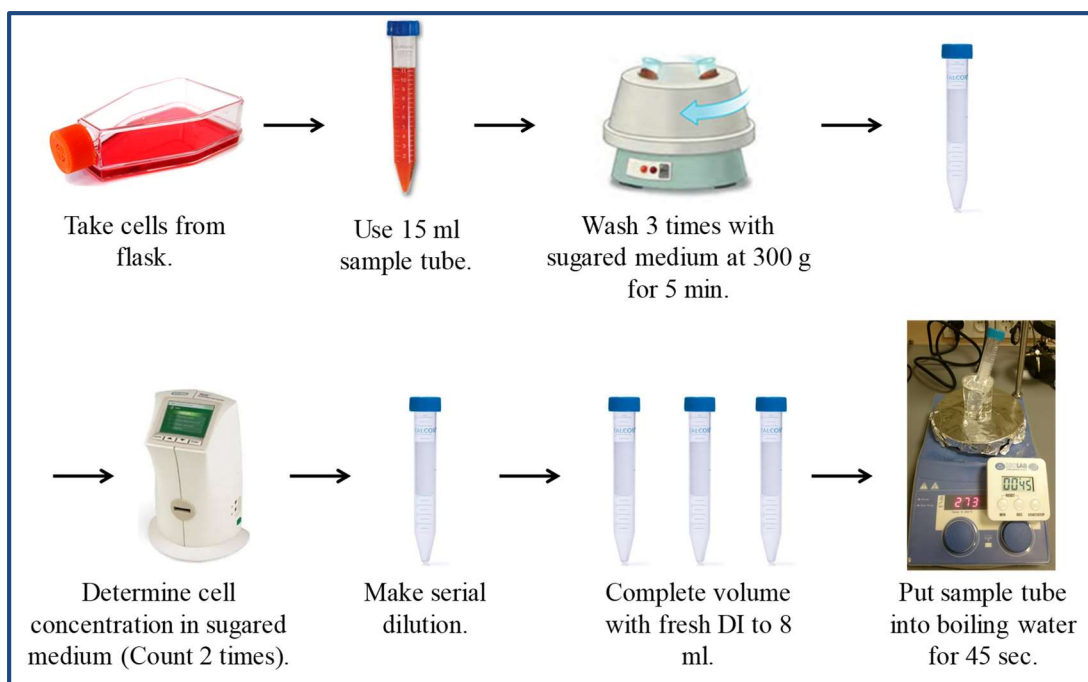


Figure 3.17: Cell lysis procedure.

Each cell type has different ionic content. This determines minimum cell number to be able to obtain measurable impedance difference. Additionally, cells have different resistance to water. This resistance limits the cell number which can be lysed in water. Minimum and maximum cell numbers were determined before total ion concentration analyses for each cell type (Table 3.4).

Table 3.4: Minimum and maximum cell numbers were used in the analyses of total ion concentration inside cytoplasm.

	Minimum ($\times 10^5$ cells)	Maximum ($\times 10^5$ cells)
K562/wt	4	6
K562/imaR	4	6
CCRF-CEM/wt	6	10
CCRF-CEM/doxR	4.5	6
HL60	3	5
HL60/ATRAR	2	3

3.3.3.3 Total ion concentration estimation

After lysis was completed, 3 different cell solutions at different cell concentrations were prepared for each cell type, having 8 ml total volume. The following procedure was developed to determine total ion concentration inside a single cell.

Procedure:

- 1) Take 1 ml of cell solution.
- 2) Take impedance spectrum.
- 3) Take another 1 ml of the same solution.
- 4) Take the impedance spectrum.
- 5) Repeat step 1-4 for each solution.
- 6) Make nonlinear fitting for each measurement (*OriginPro 2017*).
- 7) Obtain R_{sol} value of each solution from fitting.
- 8) Calculate conductivity from resistance by using cell constant (Eq. 3.3).
- 9) Convert conductivity values by using calibration curve (Fig. 3.16).
- 10) Plot “conductivity vs total cell number” graph.
- 11) Make linear fitting with y error (*OriginPro 2017*).
- 12) Obtain the equation for concentration- conductivity relation of each cell type. This relation should be linear according to the criteria $R^2 > 0.99$.
- 13) For each concentration value, calculate the total amount of mole-ion inside the solution by using the relation: “*The solution conductivity can be calculated to increase by $0.03 \text{ M}\Omega^{-1} \cdot \text{cm}^{-1}$ from an increase of 0.3 mM in ionic concentration.*” [118]. Variation in capacitance was neglected since it is several orders of magnitude lower than the change in bulk conductance according to Cheng *et al.*
- 14) Divide the total amount of mole-ion by cell number to find the total amount of mole-ion for one cell.
- 15) Calculate total ion concentration of a cell by dividing ion amount by cell volume.

Cell culture: All cells were cultivated into RPMI1640 medium (1X, Gibco) with 10% fetal bovine serum (Gibco), 1% nonessential aminoacids (Gibco), and 1% penicillin/streptomycin (Sigma Aldrich) in T25 flasks. K562 and HL60 cells were subcultured every 48h. Medium change was made for CCRF-CEM cells every 48h. They were subcultured by Trypsin-EDTA solution (0.2%, Sigma Aldrich) treatment (1 ml, 3 min for T25 flask) when 100% confluency were reached. At each subculture, 7×10^5 cells were seeded into T25 flask for all cell types. Wild type (K562/wt) and *imatinib* resistant K562 cells (K562/imaR) were taken from the research laboratory of

Prof. Dr. Ufuk Gündüz. K562/imaR cells were cultivated under the 500 nM *imatinib* (Selleckchem) exposure. CCRF-CEM cell line was bought from DSMZ. To develop resistance, *doxorubicin* (*Adrimisin*, Saba) were added to different culture medium with gradual increment in the concentration until 100 nM. HL60 cells were kindly gifted by Dr. Güneş Esendağlı from Hacettepe University. To develop resistance, *ATRA* (Selleckchem) were added to different culture medium with gradual increment in their concentration up to 5 μ M.

Drug preparations: *Imatinib* and *ATRA* were bought from Selleckchem as powder, 100 mg and 50 mg, respectively. 20 mM stock solution with DMSO (Sigma Aldrich) was prepared and stored at -80°C as suggested in their datasheets. 1 mM stock was prepared, stored at $+4^{\circ}\text{C}$, and used in cell culture for 2 weeks. DMSO greater than 0.2% is toxic to cells. Therefore, while adding drugs to cells, this ratio was protected. Commercial form of *doxorubicin* (*Adrimisin*, Saba, 10 mg as powder) was utilized in this study. It was dissolved in its 5 ml injection water, having 3.4 mM concentration, and stored at -20°C for 1 month. Dilution was carried out with PBS if necessary (1X, Sigma Aldrich).

Experimental setup: Experimental setup is presented in Figure 3.18. Impedance spectrometer of Zurich Instruments (HF2IS) and its preamplifier were used to take impedance spectrum of solutions. Spectrums were taken between 100 Hz- 1 MHz with 500 data points under 1 V_{peak} sinusoidal voltage. To drive fluidic into microchannel, mass flow controller (Elveflow, OB1) was operated at a flow rate of 50 $\mu\text{l}/\text{min}$ for solution change and 2 $\mu\text{l}/\text{min}$ while taking spectrums. Inverted microscope (Leica, DMI8) and inserted monochromatic camera (Hamamatsu ORCAFlash 4.0) were utilized to monitor channel to be sure about that there is not any cell flow or air bubble formation while taking impedance spectrum.

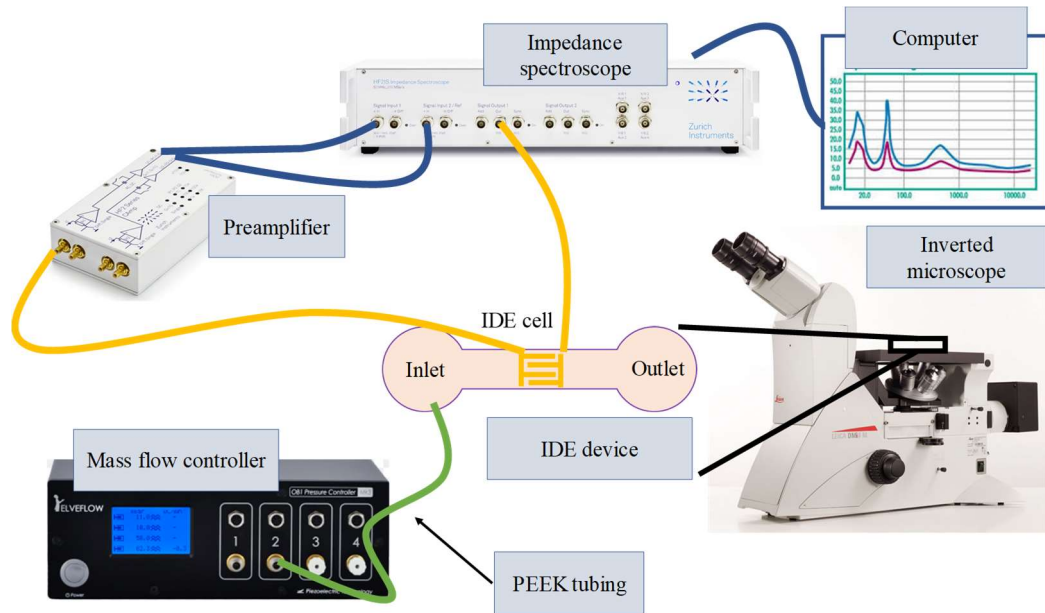


Figure 3.18: Experimental setup.

Statistical analysis: Analyses were repeated with 3 biological replicates. In order to determine correlation between repeated measurements, one-way ANOVA test with Fisher LSD for means comparison and Levene test for equal variance were utilized in all tests. $p < 0.05$ was evaluated as statistically different.

3.3.4 Results: Total ion concentration of leukemia cells under typical growth conditions

Cells were analyzed in logarithmic phase of their growth to examine dielectrical properties of cells under typical growth conditions. According to literature, while membrane dielectrical properties of drug resistant and wild type cells are similar, cytoplasmic conductivities of them differentiate [4]. To examine this anchorage in K562, CCRF-CEM, and HL60 cells, total ion concentration was determined since it is directly related with the conductivity of an electrolyte through the following formula [121, 122].

$$\sigma = z\mu FC \quad (3.5)$$

where σ , μ , and C are solution conductivity, ion mobility, and ion concentration, respectively. F stands for Faraday constant and equals to $96485.33 \text{ (sec. A.mol}^{-1}\text{)}$.

K562/wt and K562/imaR cells: Measurable electrical differences between K562/wt and K562/imaR cells as high-level laboratory model are expected. Therefore, analyses were started with these cells. In all experiments, cell sizes were determined with Automated Cell Counter (TC20, BioRad). Double counting and measurement were carried out with a mixture having 10 μ l cell solution and 10 μ l Trypan blue (Sigma Aldrich) at each analysis. Viability was determined as >97% for each experiment. As it is seen in Figure 3.19, cell radius can change. For example, according to $p < 0.05$ criteria, the 2nd and 3rd biological replicates of K562/wt cells had significantly different sizes while the sizes of K562/imaR cells did not differentiate. Moreover, the average radii of K562/wt and K562/imaR cells are not significantly different (Fig. 3.19 (c)). Therefore, volume, calculated by using the radius measured in the experiment day, was utilized while calculating total ion concentration (Table 3.5).

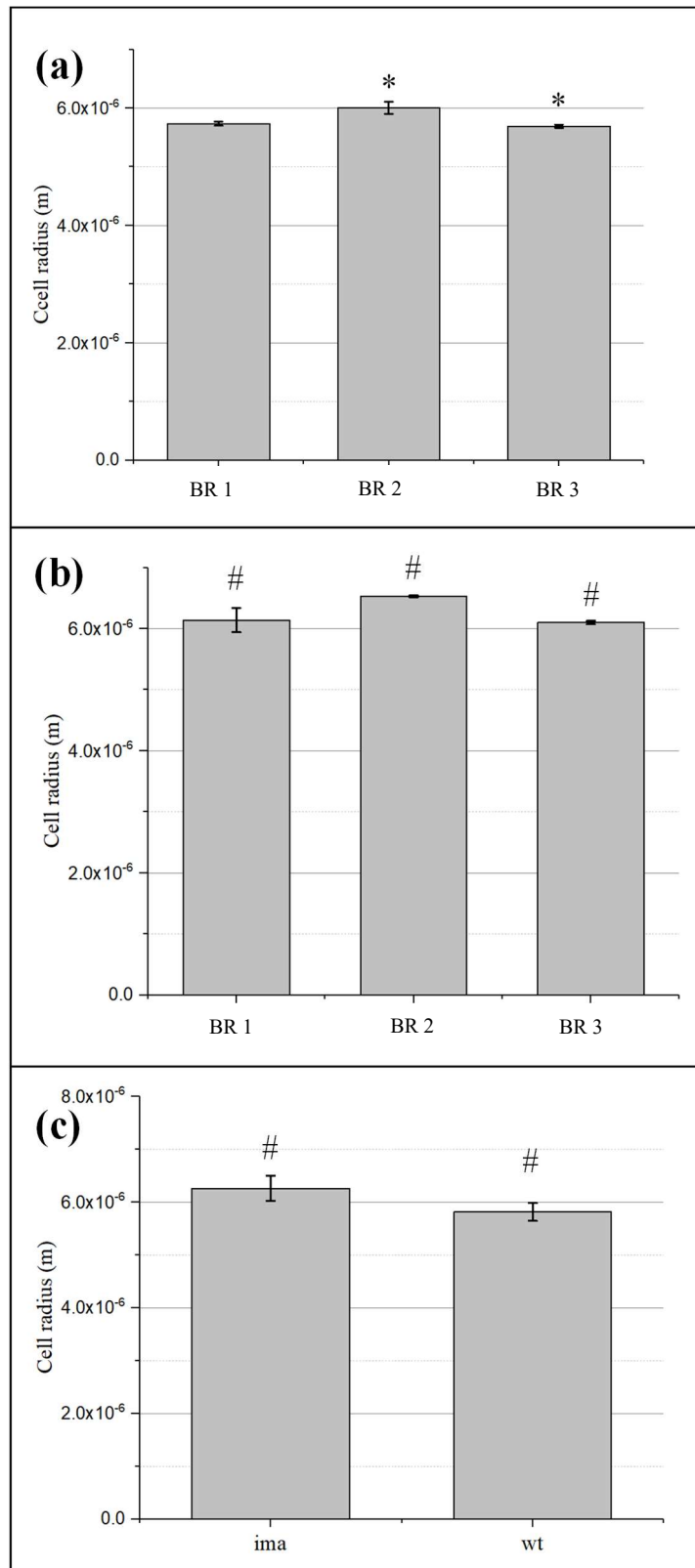


Figure 3.19: Comparison of (a) K562/wt cells' radius and (b) K562/imaR cells' radius for 3 biological replicates (BR) (n=3) with duplicate measurements for each replicate. (c) The radius comparison between K562/wt and K562/imaR cells (n=3). Data is presented as mean±stdev. * p<0.05 significantly different measurements. # shows that means are not significantly different at 0.05 level.

Table 3.5: Cell radius (r). Measurements are presented as mean±stdev (n=3). AVG: average and pl: picolitre.

	BR 1 r (μm)	BR 2 r (μm)	BR 3 r (μm)	AVG r (μm)	Volume (pl)
K562/wt	5.74±0.04	6.00±0.11	5.69±0.03	5.81±0.17	0.80±0.07
K562/imaR	6.14±0.20	6.63±0.01	6.10±0.03	6.26±0.24	1.03±0.12

Figure 3.20 presents the “conductivity vs total cell number” graph of 1st analysis of K562/wt (a) and K562/imaR (b) cells as representative data. Relations are linear ($R^2>0.99$). This shows that analyses were accurate enough to calculate total ion concentration inside a cell. Table 3.6 presents the total ion concentrations of K562/wt and K562/imaR cells. There were no significant differences between the biological replicates of the same cell type (n=3) (Fig. 3.21 (a) and (b)). A typical mammalian cell has 150 mM ion concentration inside cytoplasm [118]. Wild type cancer cells have higher cytoplasmic ion concentration than that of a typical mammalian cell according to these analyses. Moreover, the total ion concentration of K562/imaR cells were 1.78 times higher than that of K562/wt ones (Fig. 3.21 (c)).

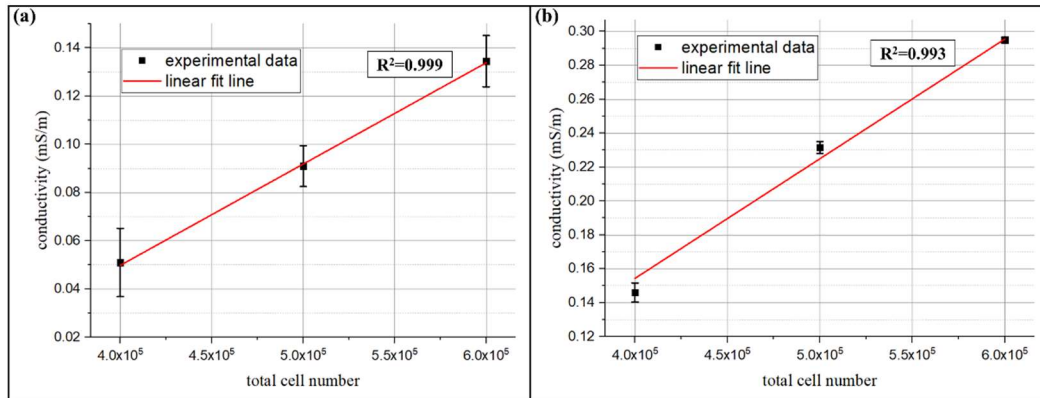


Figure 3.20: Conductivity vs total cell number plots of the of K562/wt (a) and K562/imaR (b) cells. 2 measurements were taken for each cell number. Linear fitting was applied and $R^2>0.99$ criteria were taken into account.

Table 3.6: Total ion concentrations [I] of K562/wt and K562/imaR cells. Calculations are presented as mean±stdev (n=3). AVG: average and mM: millimolar.

	BR 1 [I] (mM)	BR 2 [I] (mM)	BR 3 [I] (mM)	AVG [I] (mM)
K562/wt	180.3±49.2	187.7±45.3	180.3±31.0	182.7±4.2
K562/imaR	362.7±54.6	292.0±44.2	320.7±41.5	325.1±35.5

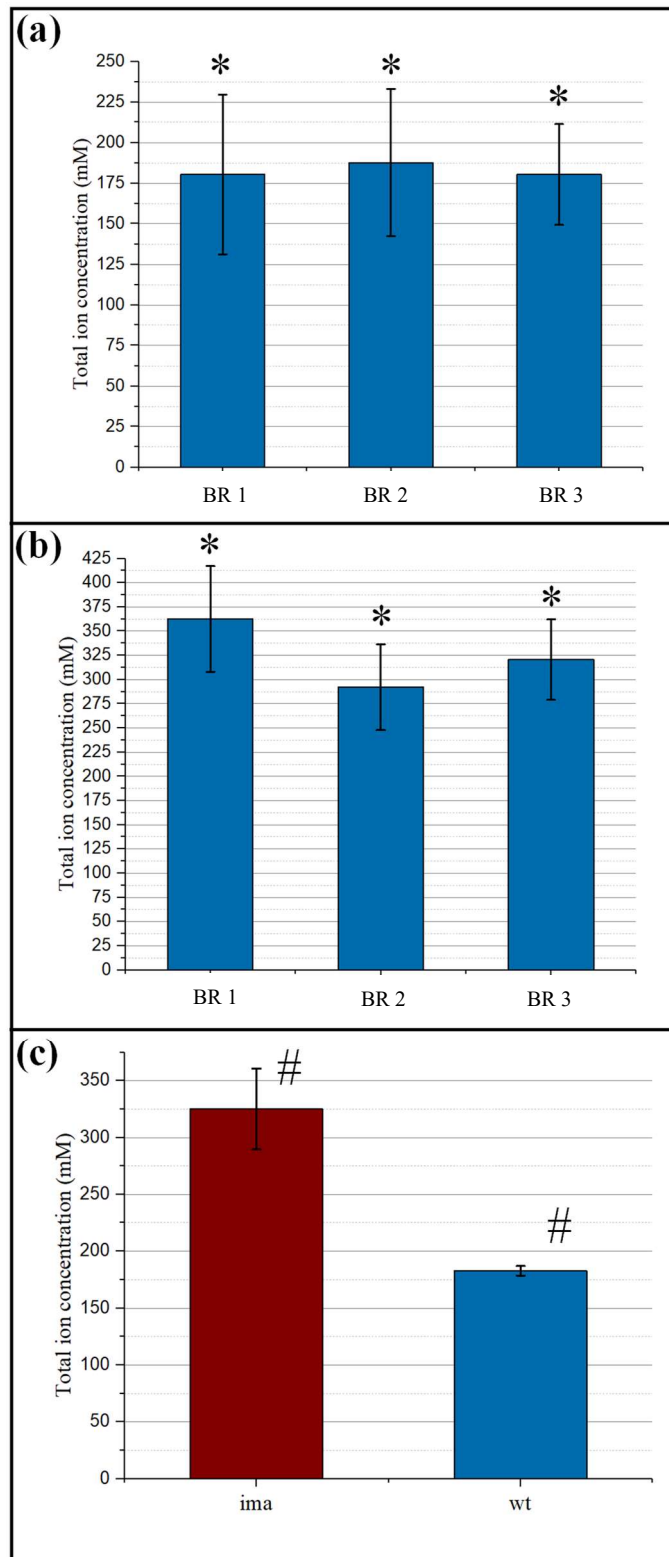


Figure 3.21: Total ion concentrations (mM) of a single cell inside 3 biological replicates of K562/wt (a) and K562/imaR (b) cells. (c) The comparison of total ion concentration inside cytoplasm of a single cell of wt and imaR. Data is presented as mean \pm stdev. * $p > 0.05$ not significantly different measurements. # shows that means are significantly different at 0.05 level (n=3).

CCRF-CEM/wt and CCRF-CEM/doxR cells: In order to detect electrical differences between CCRF-CEM/wt and CCRF-CEM/doxR cells as clinically-relevant model, IRbIS measurements were carried out. In all experiments, cell sizes were determined with Automated Cell Counter (TC20, BioRad). Double counting and measurement were carried out with a mixture, consisting of 10 μ l cell solution and 10 μ l Trypan blue (Sigma Aldrich), at each analysis. Viability was determined as >97% for each experiment.

As it is seen in Figure 3.22, cell radius can change. For example, according to $p < 0.05$ criteria, all biological replicates of CCRF-CEM/wt and CCRF-CEM/doxR cells had significantly different sizes. Therefore, while calculating total ion concentration, volume, calculated by using the radius measured in the experiment day, was used (Table 3.7).

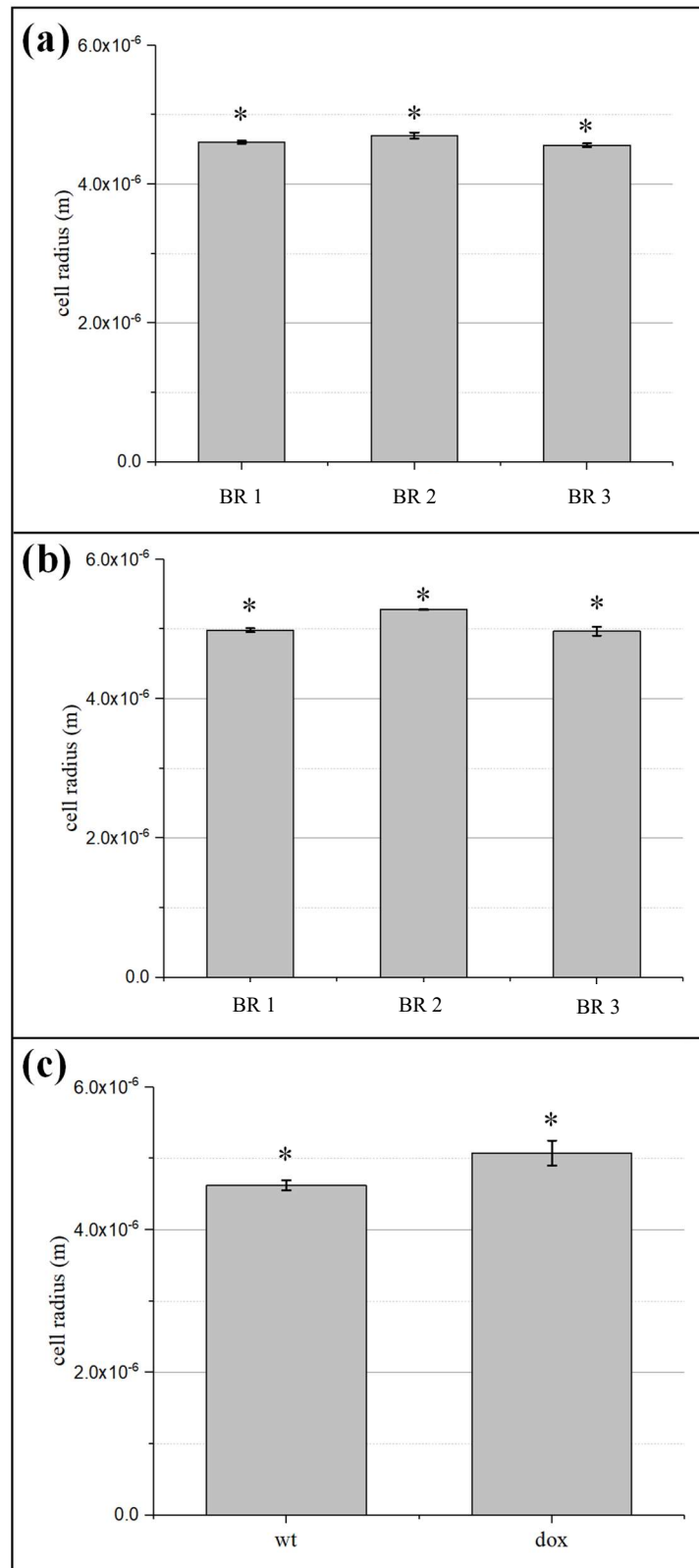


Figure 3.22: Comparison of (a) CCRF-CEM/wt cells' radius (n=3) and (b) CCRF-CEM/doxR cells' radius (n=3). (c) The radius comparison between CCRF-CEM/wt and CCRF-CEM/doxR cells (n=3). Data is presented as mean \pm stdev. * shows that means are significantly different at 0.05 level.

Table 3.7: Cell radius (r). Measurements are presented as mean±stdev (n=3). AVG: average, pl: picolitre, and BR: biological replicate.

	BR 1 r (µm)	BR 2 r (µm)	BR 3 r (µm)	AVG r (µm)	Volume (pl)
CCRF-CEM/wt	4.61±0.02	4.70±0.04	4.56±0.03	4.62±0.07	0.41±0.02
CCRF-CEM/doxR	4.98±0.03	5.28±0.01	4.97±0.06	5.07±0.18	0.55±0.06

Table 3.8 presents the total ion concentrations of CCRF-CEM/wt and CCRF-CEM/doxR cells. There were no significant differences between the biological replicates of the same cell type (n=3) (Fig. 3.23 (a) and (b)). Moreover, CCRF-CEM/doxR cells have 1.2 times higher ion concentration than wild type ones. On the other hand, this difference is not significant at 0.05 level (Fig. 3.23 (c)).

Table 3.8: Total ion concentrations [I] of CCRF-CEM/wt and CCRF-CEM/doxR cells. Calculations are presented as mean±stdev for 3 different measurements (n=3). AVG: average, mM: millimolar, and BR: biological replicate.

	BR 1 [I] (mM)	BR 2 [I] (mM)	BR 3 [I] (mM)	AVG [I] (mM)
CCRF-CEM/wt	126±52.5	174±7.2	183±5.3	161±30.6
CCRF-CEM/doxR	176±48.1	197±26.8	225±25.0	199±24.6

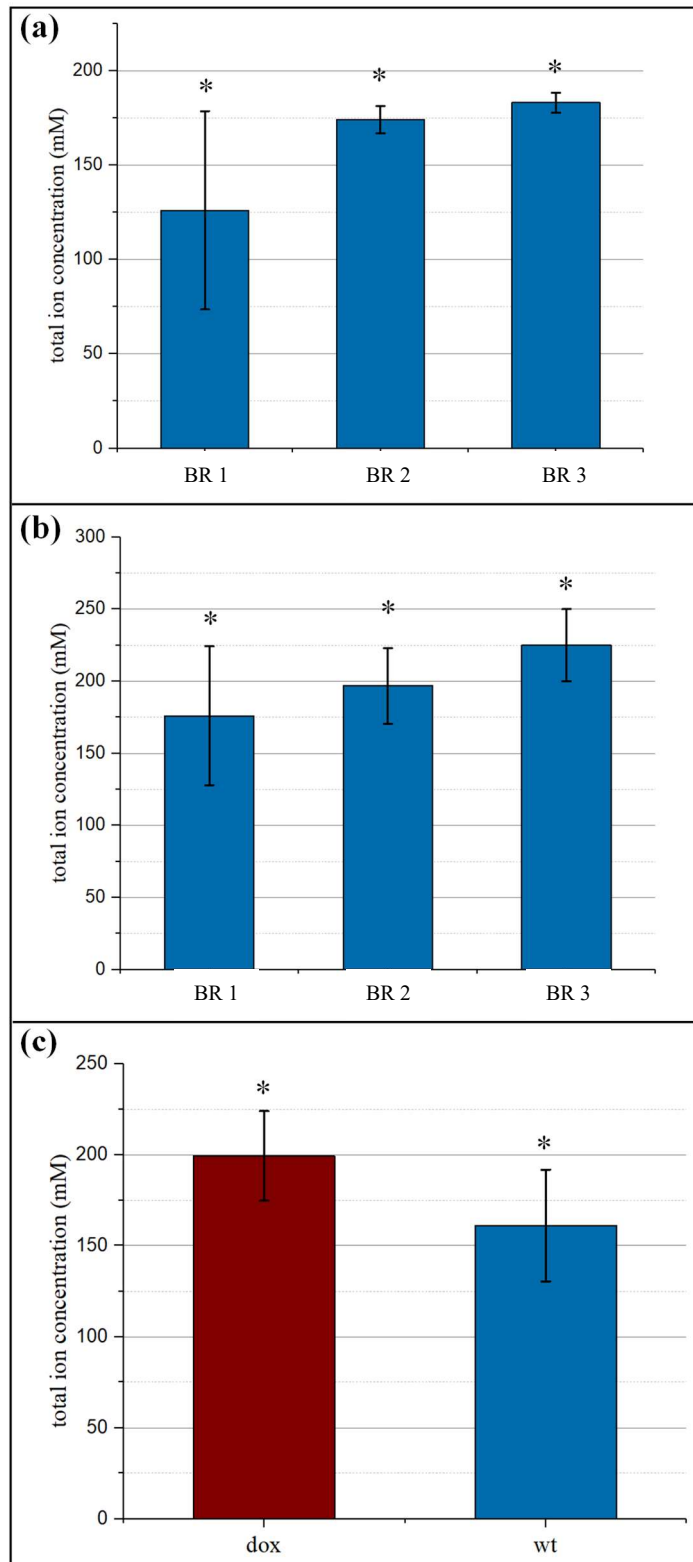


Figure 3.23: Total ion concentrations (mM) of a single cell for 3 biological replicates of CCRF-CEM/wt (a) and CCRF-CEM/doxR (b) cells (n=3). (c) The comparison of total ion concentration inside cytoplasm of a single cell of wt and doxR (n=3). Data is presented as mean±stdev for triplicate measurements for each replicate. * $p > 0.05$ not significantly different measurements.

HL60/wt and HL60/ATRAR cells: In XTT analyses, although the application of 5 times higher drug concentration than the pharmacological dose (1 μ M, [86]) and 48h long assay time, IC₅₀ value of HL60 cells has not been obtained. According to literature, this can take 3-10 days [83]. Therefore, it was decided to examine whether electrical difference exist between these cells. In order to detect electrical differences between HL60/wt and HL60/ATRAR cells, IRbIS measurements were carried out. In all experiments, cell sizes were determined with Automated Cell Counter (TC20, BioRad). Double counting and measurement were carried out with a mixture, consisting of 10 μ l cell solution and 10 μ l trypan blue (Sigma Aldrich), at each analysis. Viability was determined as >97% for each experiment.

Results are presented in Figure 3.24. There was no significant difference between total ion concentration of HL60/wt and HL60/ATRAR cells. Therefore, these cell lines were not utilized in DEP experiments.

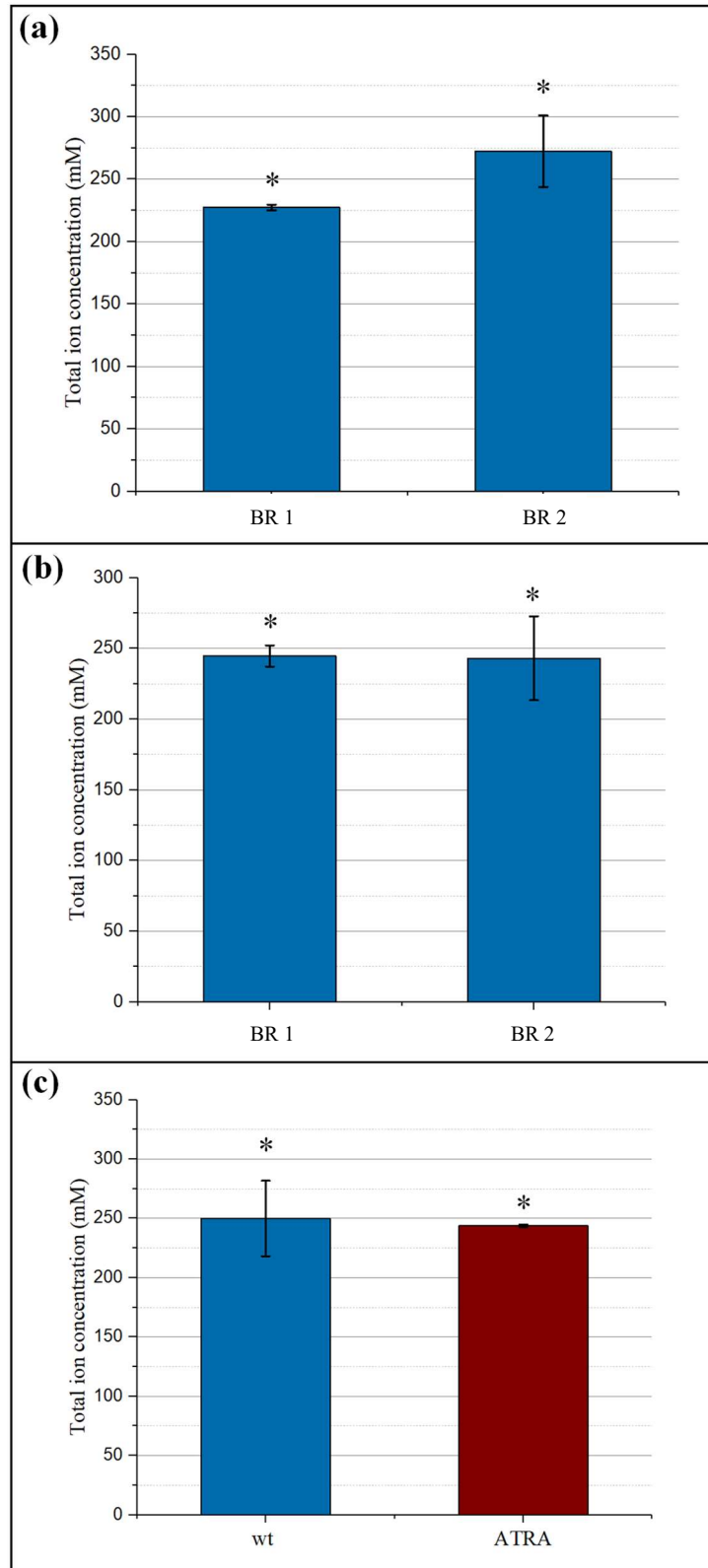


Figure 3.24: Total ion concentrations (mM) of a single cell for 2 biological replicates of HL60/wt (a) and HL60/ATRAR (b) cells (n=2). (c) The comparison of total ion concentration inside cytoplasm of a single cell of wt and ATRAR (n=6). Data is presented as mean±stdev for triplicate measurements. * p>0.05 not significantly different measurements.

3.3.5 Estimation of DEP operation conditions

Due to macromolecular crowding, ions inside biological cells do not have the same mobility measured in bulk. According to literature, in mammalian cells, the velocity of ions decreases 2-7 times [123]. K^+ ions are abundant in the cells. Therefore, assuming all the ions are potassium and its mobility is decreased by 2-7 times, the following cytoplasmic conductivities of K562/wt, K562/imaR, CCRF-CEM/wt, and CCRF-CEM/doxR cells were calculated.

Table 3.9: Estimated cytoplasmic conductivity (mS/m) of K562 and CCRF-CEM cells.

	2x	3x	4x	5x	6x	7x
K562/wt	661	441	331	265	221	189
K562/imaR	1190	794	596	477	398	340
CCRF-CEM/wt	585	390	292	234	195	167
CCRF-CEM/doxR	723	484	362	290	236	207

Dielectrophoresis (DEP) is a technique, providing the manipulation of dielectrical particles under the nonuniform electric field. In order to produce enough polarization, biological cells are suspended in low conductivity buffers, whose conductivity is 100 times smaller than that of cells. In LOC system, presented in Chapter 4, a solution conductivity which is equal to the average cytoplasmic conductivity of wild type cells was utilized. By means of this technique, a threshold for resistance level in wild type cancer cells was tried to be set. By assuming medium conductivity as 221, 265, and 331 mS/m, a frequency at which K562/imaR cells are affected by DEP force maximally was simulated in MATLAB (The code is presented in Appendix A for this simulation) (Fig. 3.25). Single shell cell modeling was carried out in this simulations [22]. For CCRF-CEM cells, medium conductivity was set to 160 mS/m and frequency was determined as 6.15 MHz.

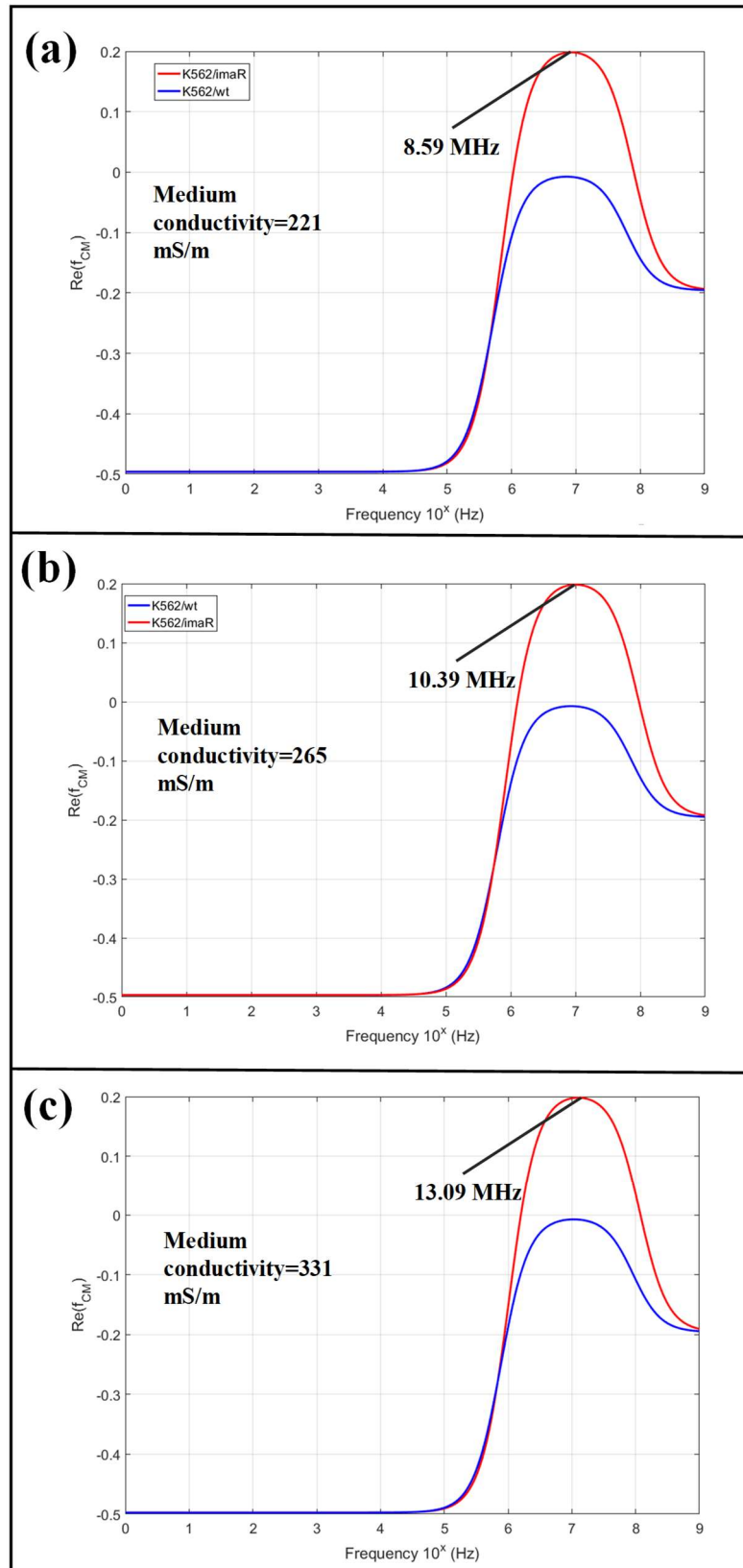


Figure 3.25: Simulations of $Re(f_{CM})$ to determine frequencies at which the maximum $Re(f_{CM})$ value obtained for K562/imaR cells in DEP medium, having conductivity of (a) 221, (b) 265, and (c) 331 mS/m.

3.4 Conclusion

Cell physiological conditions determine the cytoplasmic ion concentration, directly affecting their DEP response. Therefore, total ion concentration of wild type and drug resistant cells were determined through ion release-based impedance spectroscopy. This technique is utilized for the determination of ion concentration inside a cell for the first time in the literature. Results show that wild type and drug resistant cancer cells have different electrical properties in high level laboratory model. A high conductivity DEP buffer can be determined, setting a threshold value for the resistance level.

The difference between total ion concentrations of wild type and resistant types in clinically-relevant cell line were not significant at $p < 0.05$ level.

By exploiting total ion concentration values, DEP medium conductivity and operation frequency were determined as 200 mS/m and 8.59 MHz for K562 cells while 160 mS/m and 6.15 MHz frequency was chosen for CCRF-CEM cells. These values were used in the analysis of LOC system presented in Chapter 4.

HL60 cells were discarded after that point since their electrical properties were not proper for the detection of MDR like biological results.

CHAPTER 4

DIELECTROPHORETIC DETECTION AND IMPEDOMETRIC QUANTIFICATION OF LEUKEMIA CELL HETEROGENEITY IN TERMS OF DRUG RESPONSE

Chemotherapy is a cancer treatment, preferred to improve the life quality and extend disease-free survival time of patients. Lots of the clinical trials have reported that cancer patients whose chemotherapy is personalized progressed better than those treated with standard chemotherapy [124]. This is expectable result since chemotherapy response of each tumor is unique. To make treatment personal, chemosensitivity of patients should be examined. In the scope of this thesis, chemosensitivity analyses are separated into two parts: Monitoring of chemotherapy efficiency and detection of multidrug resistance (MDR).

According to type of cancer, the method of chemotherapy efficiency monitoring can be selected. For example, in patients with osteogenic sarcoma and Ewing's sarcoma, histopathological examination of the resected specimen is accepted as the gold standard for the evaluation of chemotherapy efficiency [125]. Moreover, in solid tumors, highly sensitive imaging methods to observe the tumor structure have been developed in non-invasive manner, including MRI, FDG-PET, and STIR [124, 125, 126, 127]. For the assessment of therapy response in leukemia, flow cytometry has been utilized [130]. Currently, Response Evaluation Criteria in Solid Tumors (RECIST) guideline is based on the measurement of tumor dimensions by imaging and the assay of tumor markers. On the other hand, Wang *et al.* claimed that it does not have enough resolution to observe chemotherapy response of patient since techniques require long duration (longer than a month) after chemotherapy to deliver the necessary information. To obtain synchronous information about whether chemotherapy is effective, studies proposed to carry out real-time apoptosis monitoring through total circulating DNA (tcDNA). Lymphocytes and other nucleated cells derive tcDNA at low levels, normally. On the other hand, this level

increases while both healthy and cancerous cells are killed by chemotherapy drugs. When the methylation level of genes in these tcDNAs is examined, it can be determined that they belong to which cell type (healthy or cancer) [124].

Chemotherapeutic drugs are produced to induce death in cancer cells, mostly by apoptosis. On the other hand, cancer cells can produce new mechanisms to escape from apoptosis since they have a mutation, causing infinite cell proliferation. This can be defined as chemotherapy resistance. It can develop for a single drug or multiple of them having different structure, named as multidrug resistance (MDR). If MDR develops after drug administration, it can be detected by the methods which monitor apoptosis explained in the previous paragraph. On the other hand, if it progresses inherently, i.e. without drug exposure, techniques for detection change. To detect MDR in cancer patients, the levels of membrane-associated proteins, which provide drug efflux, are analyzed through three different detection methods: (1) *in vivo* imaging, (2) protein assays, and (3) flow cytometry [2]. To obtain information about dynamic functions of P-gp and MRPs, *in vivo* imaging techniques, such as single-photon emission tomography and positron emission tomography, are exploited. In these techniques, substrates of P-gp and MRPs, tagged with different isotopes, are injected to patient's body. Labeling is made with undamaging dosages but repeated administration of such isotopes is not allowed due to the side effects. Protein assays diagnose MDR by detecting drug efflux pumps. Since they require isolation of cancer cells from the body and protein extraction from those cells, they are time-consuming. In flow cytometry, isolated cancer cells are tagged with fluorescently labeled antibodies raised against membrane proteins. Although these conventional methods are promising for MDR detection, their sensitivity is not adequate. Studies reported that patients did not overexpress P-gp while they were resistant to chemotherapy or vice versa [38]. For example, Figure 4.1 presents a study carried out with 91 lung tumors. 43 of them are P-gp positive while 48 of them are negative. In this study, *in vitro* short-term test shows that 64 of them are resistant to *doxorubicin*. This indicates that 39% of resistant tumors are P-gp negative [38].

All of these methods require expensive laboratory equipment and trained personnel. In addition, they are time-consuming due to labeling procedures and cannot be applied

for frequent use during prognosis, because of the side effects. Electrochemical DNA biosensors can be suggested as an alternative method to increase sensitivity [131]. However, the signal level is limited in this sensor even some methods have been tried to increase this level. For example, some nanomaterials have been used. On the other hand, this makes fabrication complex and adds molecule labeling steps [132]. In addition, the existence of a gene does not have a meaning that it synthesizes a protein although mutation detection is a promising way to diagnose [38]. As a result, a cost-effective, label-free, and user-friendly method is needed to provide effective diagnosis of MDR in cancer cells, without compromising the sensitivity and specificity [22].

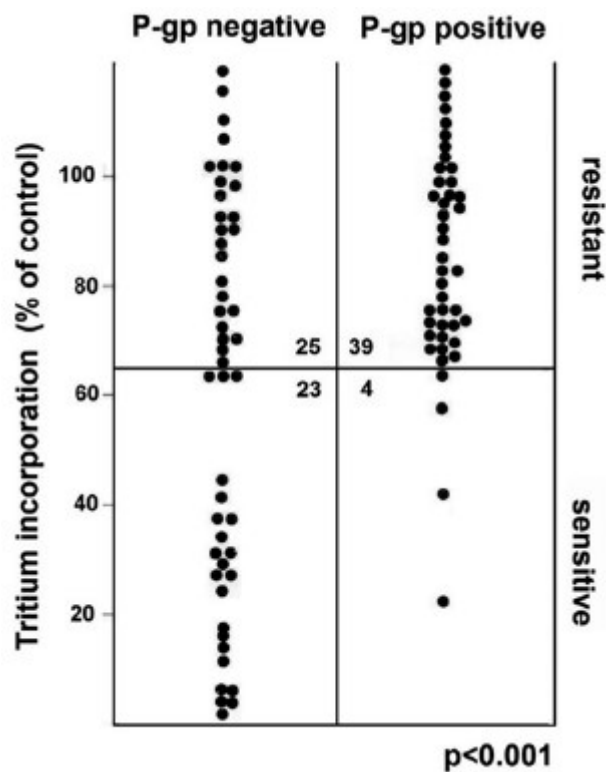


Figure 4.1: P-gp expression in the cancer cells of patients. Although the overexpression of P-gp was observed, patients may not be resistant or vice versa.

Dielectrophoresis (DEP) is a MEMS-enabled technique used to manipulate particles based on different sizes and/or dielectric properties under non-uniform electric field. Studies showed that dielectrical differences can occur between cancer cells due to the development of MDR [44]. Labeed *et al.* reported that the cytoplasmic conductivity

of multidrug resistant K562 leukemia cells are 2.2 times higher than that of drug sensitive ones. They claimed that this variation is most probably associated with the overexpression of P-gp, modulating the volume-activated Cl^- channels. On the other hand, membrane associated protein overexpression is not the only mechanism behind MDR as explained in Chapter 1 although this overexpression is the most abundant one. There exist seven potential mechanisms and four of them can create dielectrical differences through ionic changes in cytoplasm, including overexpression of membrane associated proteins. This indicates that DEP has potential to detect most of the MDR cases while it cannot give information about the mechanism behind. Moreover, DEP can be operated for the monitoring of apoptosis progression since ion level variations take place during the early and late apoptosis. In [93], they correlated the results of Annexin-V assay and electrophysiological properties of cells obtained by DEP during apoptosis. It was shown that cytoplasmic conductivity and the externalization of phosphatidylserine are inversely related. Mulhall *et al.* reported that increase in the intracellular Ca^{2+} level may be a mechanism behind this relationship since phosphatidylserine expression occurs by means of Ca^{2+} activated-scramblase enzymes. On the other hand, Ca^{2+} stimulates K^+ efflux. As a result, cytoplasmic conductivity decreases since increase in Ca^{2+} level (nM range) could not compensate K^+ level decrease (mM). In [89], they compared speed and accuracy of MTT, trypan blue, flow cytometry with Annexin V/PI, and DEP in the monitoring of drug response of Jurkat and HeLa cells by analyzing apoptosis. It was concluded that DEP is as precise as flow cytometry, the most accurate technique; as it is cost- and time-effective, and label-free method, providing simpler operation.

Throughout this thesis, both the real-time monitoring of apoptosis and MDR detection through LOC systems based on DEP has been carried out to analyze chemosensitivity in leukemia cells. In the following parts, these systems will be presented in detail.

4.1 Examination of P-gp, MRP1, and BCRP in K562 and CCRF-CEM cell lines by flow cytometry

The most common drug efflux pumps are in the family of ATP-binding cassette transporters. As explained in Chapter 3, this type of membrane proteins can be

responsible for ion transport, also. Therefore, their overexpression may cause some variations in the electrical properties of cell cytoplasm. Labeed *et al.* reported that the cytoplasmic conductivity of multidrug resistant K562 leukemia cells are 2.2 times higher than that of drug sensitive ones. They claimed that this variation is most probably associated with the overexpression of P-gp, modulating the volume-activated Cl⁻ channels. Moreover, Demircan *et al.* reported that *imatinib* resistant K562 cells could be trapped by DEP force, while the sensitive ones were not affected under the same experimental conditions at crossover frequency of sensitive K562 cells, obtained through single shell cell modeling using the electrical properties presented in the study of Labeed *et al.* [44].

In this thesis, *imatinib* and *doxorubicin* were used as chemotherapy drugs. Both of them are the substrate of P-gp, MRP1, and BCRP. Therefore, flow cytometric analysis of P-gp, MRP1, and BCRP expression was carried out in K562/wt, K562/imaR, CCRF-CEM/wt, and CCRF-CEM/doxR cells.

4.1.1 Materials and methods

Cell culture: All cells were cultivated into RPMI1640 medium (1X, Gibco) enriched with 10% fetal bovine serum (Gibco), 1% nonessential aminoacids (Gibco), and 1% penicillin/streptomycin (Sigma Aldrich) in T25 flasks. K562 cells were subcultured every 48h. Medium change was made for CCRF-CEM cells every 48h. They were subcultured by Trypsin-EDTA solution (0.2%, Sigma Aldrich) treatment (1 ml, 3 min for T25 flask) when 100% confluency were reached. At each subculture, 7×10^5 cells were seeded into T25 flask for all cell types. K562/wt and K562/imaR cells were taken from the research laboratory of Prof. Dr. Ufuk Gündüz. K562/imaR cells were cultivated under the 500 nM *imatinib* (Selleckchem) exposure. CCRF-CEM cell line was bought from DSMZ. To develop resistance, *doxorubicin* (*Adrimisin*, *Saba*) were added to different culture medium with gradual increment up to 100 nM *doxorubicin*.

Flow cytometry: Cells were centrifuged at 300 g for 5 min. Concentration was adjusted as 10^6 cells/ml with Automated Cell Counter (TC20, BioRad). Fluorescently tagged antibodies (Biolegend, Inc.): Anti CD243-PE, anti MRP1-Alex647, and anti CD338-FITC, were added into cell solutions to label P-gp, MRP1, and BCRP on the

membrane, respectively. 45 min. incubation was applied at 4°C. One washing was made to reduce background fluorescence. Finally, cells were analyzed with flow cytometry (BD FACSAria™ III, BD Biosciences) for the comparative expression level of proteins. Analyses were carried out with Utku Horzum in Hacettepe University.

4.1.2 Results

In the flow cytometry analyses, unstained K562/wt and CCRF-CEM/wt cells were utilized as reference. Fluorescence intensities greater than the one of unstained K562/wt cells were evaluated as protein expression. Figure 4.2 presents the shift in fluorescence intensities due to protein expression. Both K562/wt and K562/imaR cells expressed P-gp while BCRP and MRP1 were not expressed in both of them (Fig. 4.2 (a), (b), and (c)). The same result was obtained for the CCRF-CEM cells (Fig. 4.2 (d), (e), and (f)). The medians of fluorescence intensities and comparative values of P-gp expressions between tagged and untagged cells are presented in Table 4.1. These quantifications can be evaluated that MDR in those cells can develop due to the drug efflux by P-gp.

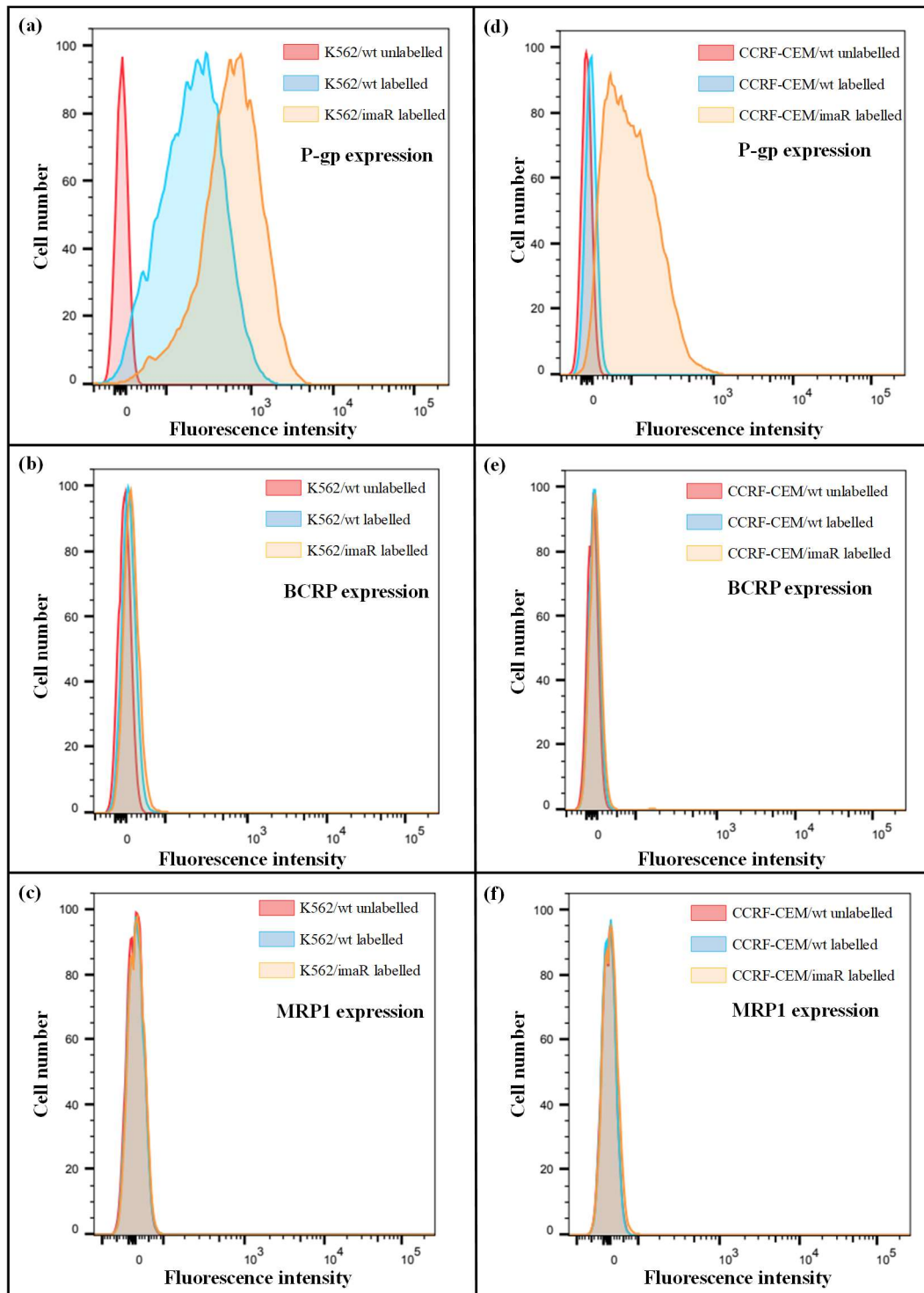


Figure 4.2: P-gp (a, d), BCRP (b, e), and MRP1 (c, f) expressions in K562 (left column) and CCRF-CEM (right column) cells.

Table 4.1: P-gp expression in K562 and CCRF-CEM cell lines.

	Median	Fold expression
K562/wt	213	47X
K562/imaR	607	107X
CCRF-CEM/wt	9	7X
CCRF-CEM/doxR	93	42X

4.1.3 Discussion

P-gp overexpression was obtained in both high-level laboratory and clinically-relevant model of MDR cells. P-gp expression in K562/imaR cells was 2.5 times higher than that of K562/wt cells. This was an expected result since K562 cells are 60-fold resistant to *imatinib* than their wild types (Data is presented in Chapter 2, obtained through XTT assays). It is confusing that although CCRF-CEM/doxR cells are resistant to *doxorubicin*, P-gp expression level is lower than that of K562/wt cells. The reason is because flow cytometry does not give functional information.

4.2 LOC system based on a microfilter integrated DEP system for MDR cell separation from RBCs

MDR is a condition enabling a cancer cell to resist distinct drugs of a wide variety of structure and function targeted at eradicating the cell. In case of MDR, patients do not respond chemotherapy so MDR detection in early stages of cancer is critical to envisage the most appropriate treatment and to speed up the recovery period [22]. In my MSc thesis, I showed that imatinib resistant K562 cells could be trapped utilizing DEP while the sensitive ones were not affected under the same experimental conditions. In my PhD thesis, the effects of drug resistance level on DEP response were examined as a first step. Details are explained below.

4.2.1 The effect of drug resistance level on DEP response of cancer cells

In order to examine the relationship between drug resistance level and DEP response in K562 cells, the same devices, designed and fabricated in my MSc thesis, were utilized. In this study, K562/doxR cells, resistant to 100, 300, 500 and 1000 nM doxorubicin, are trapped through 3D-electrode DEP devices at a flow rate of 5 $\mu\text{l}/\text{min}$ and under 9 V_{pp} voltage ($f=48.64$ MHz). Trapped cell number is determined by measuring the fluorescence intensity. Results present that the degree of MDR in K562

cells affects DEP response of them, indicating a nonlinear relationship between the drug resistance level and DEP response of cells, for the first time in literature (Fig. 4.3) [47]. The developed relationship can be used for label-free drug resistance degree determination in cancer cells.

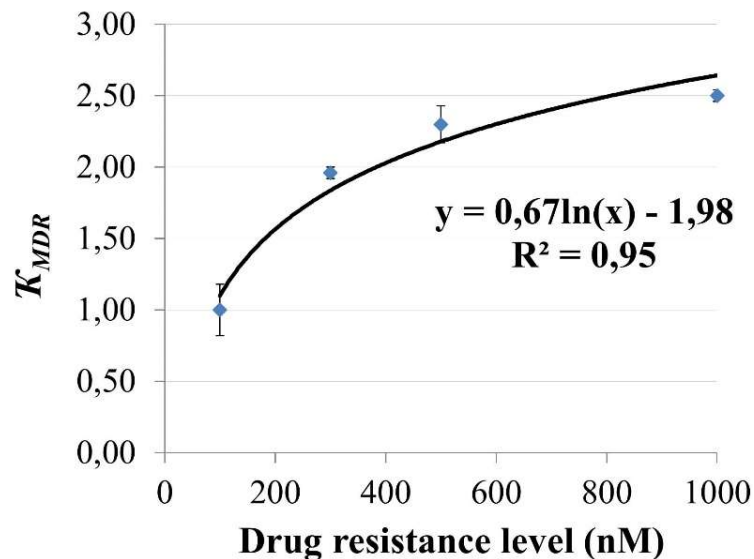


Figure 4.3: The relationship between the drug resistance level and DEP responses of K562 MDR cells.

Results explained up to here endorsed the claim that the separation of MDR cells from a mixture having wild type and resistant cells can be achieved by DEP. Therefore, utilizing the same devices, separation analysis was started as explained below.

4.2.2 The separation of MDR and wild type cells

The detection of MDR in K562 cells was achieved and published at a flow rate of 10 $\mu\text{l}/\text{min}$ by applying 9 V_{pp} , with 100% selectivity in a mixture containing less than 1% resistant cells [22]. Figure 4.4 (a) and (b) present time-lapse images of *imatinib* and *doxorubicin* resistance detection in K562 cells through the separation tests of MDR K562 and sensitive cells at 6.67 $\mu\text{l}/\text{min}$ flow rate along a 45 s test period, respectively. Green and red colored snapshots were presented together in this figure to prove that sensitive cells (green images) were not trapped while the trapping of MDR cells (red)

was achieved at the same time in the test, carried out with MDR and sensitive cell mixtures. The MDR detection test was repeated at a higher flow rate (10 $\mu\text{L}/\text{min}$) to test the dependence of cell capturing on flow rate for only the mixture of K562/imaR and sensitive K562 cells. Figure 4.4 (c) shows the screenshots through a 30 s test period that corresponds to the same sample amount passing through the channel. It was observed that the device is capable of detecting MDR. Although some sensitive cells were trapped at the beginning of the test, they were all released at the end even they were in 100 times higher concentration, indicating high selectivity of DEP device. The working frequency (48.64 MHz) was the f_{cross} of the sensitive K562 cells according to modeling. Therefore, the trapping of them was not expected. However, the dielectric characteristics of cells may change due to their dynamic nature, and trapping may occur. To further confirm that no trapping occurs for sensitive cells, the test using only the sensitive cell suspensions (2.5×10^5 cells/mL) was repeated at a flow rate of 6.67 $\mu\text{L}/\text{min}$ and 9Vpp voltage. Figure 4.4 (d) shows the screenshot images at different time instants. After 25 s, trapping was observed for a few cells. However, at the end of 45 s (steady state) no cell remained on the electrodes, which indicates that the sensitive cells were carried away with the flow.

These results inspired a LOC system based on a microfilter integrated DEP system for MDR cell separation from RBCs to be able to detect MDR in leukemia patients. Next sub-sections give details of system design, fabrication, and test results.

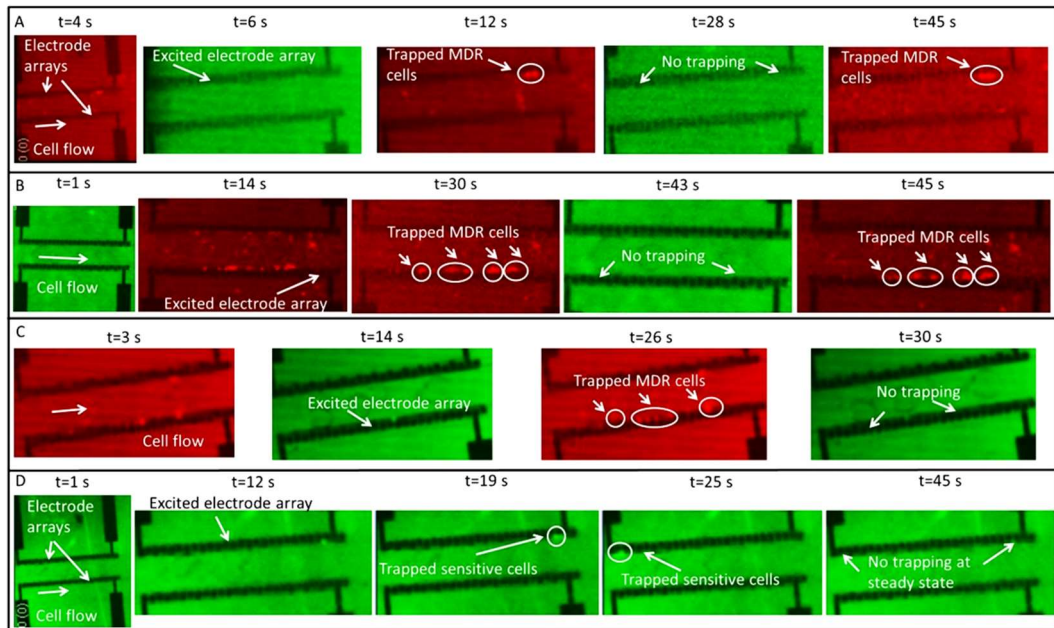


Figure 4.4: Pseudo-colored images taken during the detection of imatinib (A) and doxorubicin (B) resistance in K562 cells at a flow rate of $6.67 \mu\text{l}/\text{min}$, utilizing the MDR and drug sensitive cell mixtures. Flow rate performance analysis of DEP devices through the separation of K562/imaR cells and sensitive K562 cells at a flow rate of $10 \mu\text{l}/\text{min}$ (C). Working solution was the mixture of K562/imaR and sensitive K562 cells with $2.5 \times 10^3 \text{ cells}/\text{ml}$ and $2.5 \times 10^5 \text{ cells}/\text{ml}$, respectively ($f = 48.64 \text{ MHz}$, $V = 9 V_{pp}$). Pseudo-colored images taken during tests with only sensitive K562 cells (D). No trapping occurs until $t=12 \text{ s}$. A few cells, trapped during the flow, were carried away at the end of 45 s , necessary duration to reach steady state conditions. Through all tests, only one side-wall electrode array was energized to provide better visualization [22].

4.2.3 System design

The device schematic was presented in Figure 4.5. RBC depletion unit is composed of main channel ($1000 \mu\text{m W} \times 20 \mu\text{m H}$) and side channels ($500 \mu\text{m W} \times 20 \mu\text{m H}$) connected to each other via $8 \mu\text{m}$ filtering gaps on the sidewalls to realize size-based filtration. Planar electrodes with 15° angles were implemented throughout the channel to direct the cells through sidewall filtering gaps via DEP force. This part was implemented by Gürhan Özkayar in his MSc thesis. MDR detection unit has 2×29 3D-electrodearrays, with $40 \mu\text{m}$ width and $15 \mu\text{m}$ gaps in between, placed on the sidewalls of $300 \mu\text{m} \times 20 \mu\text{m}$ parylene microchannel. The channel also contains parylene drop-shaped posts for hydrodynamic focusing of cells to DEP traps, solving vortex formation problem, faced with in V-shaped obstacle devices in my MSC thesis. Isolation of both planar and 3D-electrodes from the solution is provided by means of thin parylene coating, reducing the *Joule* heating and cell damaging. In RBC depletion

unit, all cells are directed towards the sidewalls by sliding on the electrodes through pDEP force and hydrodynamic forces, at a frequency of 1 MHz. Small RBCs pass through the filters while cancer cells continue through the main channel. Based on the dielectric simulations, f_{cross} of sensitive K562 cells (48.64 MHz, Fig 4.6) was chosen as working frequency of MDR detection unit. This unit works based on electrohydrodynamic principles. Utilizing Newton's second law in the microchannel and assuming electroosmotic force and acceleration term as zero [46], the following inequality is obtained (Eq. 4.1), indicating that size and $Re(f_{CM})$ of particles determine their trapping conditions under the same hydrodynamic settings.

$$2\pi\epsilon_m r^3 Re(f_{CM}) \nabla E_{rms}^2 > 6\pi\mu r v_m \quad (4.1)$$

where, v_m is the velocity of medium and μ denotes the medium viscosity.

In this study, the average radius of drug sensitive and MDR K562 cells were $5.5 \mu\text{m}$ While RBCs were $3 \mu\text{m}$ in radius, determined by pixel measurement software measuring and averaging 100 cells' radius (*Pixel Ruler*). Moreover, as it is shown in Figure 4.6, $Re(f_{CM})$ of MDR K562 cells were 1.5 times higher than that of RBCs. This implies that the DEP trapping force on MDR K562 cells is 9.4 times higher than that of RBCs. If flow rate is optimized, the detection of MDR K562 cells can be achieved in MDR detection unit with high selectivity [49].

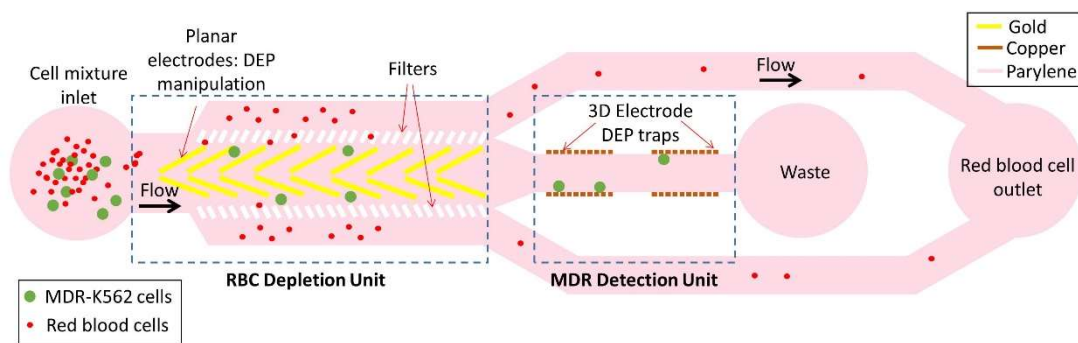
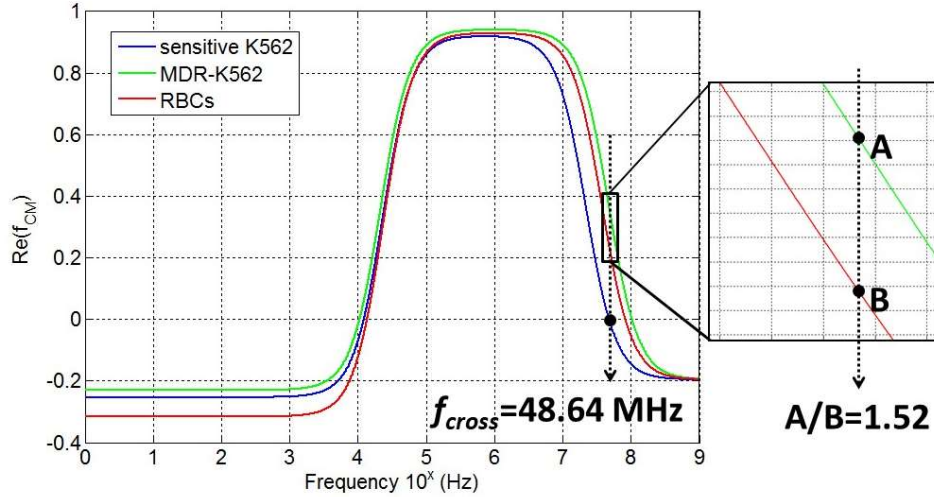


Figure 4.5: Device schematic. The system consists of 2 consecutive DEP units for the depletion of RBCs and capturing of MDR K562 cells [49].



Point A: $Re(f_{CM})$ of MDR-K562

Point B: $Re(f_{CM})$ of RBCs at f_{cross} of sensitive K562

Figure 4.6: $Re(f_{CM})$ vs. frequency graphs of RBCs, drug sensitive and MDR K562 cells in a medium with 2.5 mS/m conductivity and 78 permittivity coefficient.

4.2.4 Fabrication

Fabrication was started with dehydration of the 6" glass wafers which were cleaned with piranha and etched with BHF. Ti/Au was sputtered (*BESTEC dual chamber sputter system*) to form planar electrodes and a seed layer for Cu-electroplating. Utilizing wet etching, planar electrodes and the seed layer were patterned. To prevent parasitic capacitances between Au layer (used to short nonconsecutive electrodes) and 3D-electrodes, a parylene layer ($\sim 0.5 \mu\text{m}$) was coated (*Parylene deposition system, SCS 2010 LabcoterTM 2*). 3D-electrode places were patterned with parylene RIE (*STS Multiplex RIE system*). Cu-electroplating was carried out to obtain 20 μm thick 3D-electrodes. Another parylene layer ($\sim 0.5 \mu\text{m}$) was coated for insulation purposes. Next, the channel and parylene obstacles were formed with lithography and parylene coating ($\sim 20 \mu\text{m}$). Finally, sacrificial photoresist was released with acetone (Fig. 4.7). Figure 4.8 shows the fabricated device with details.

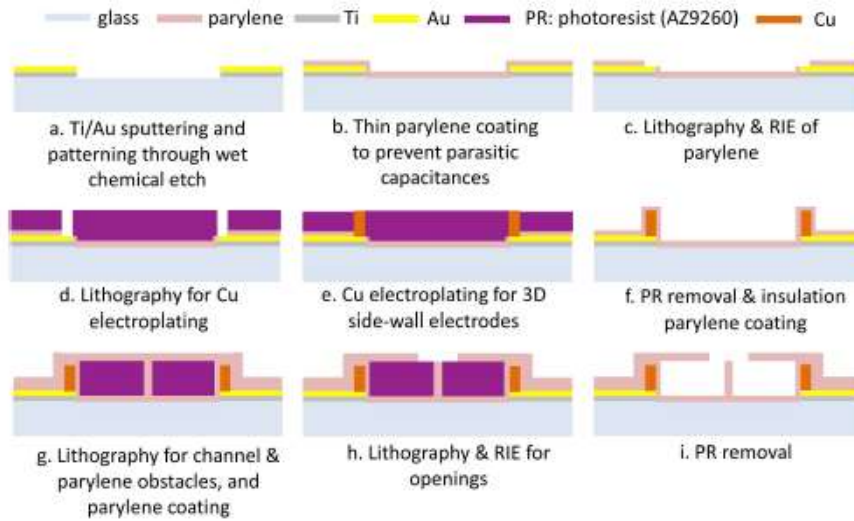


Figure 4.7: Fabrication flow.

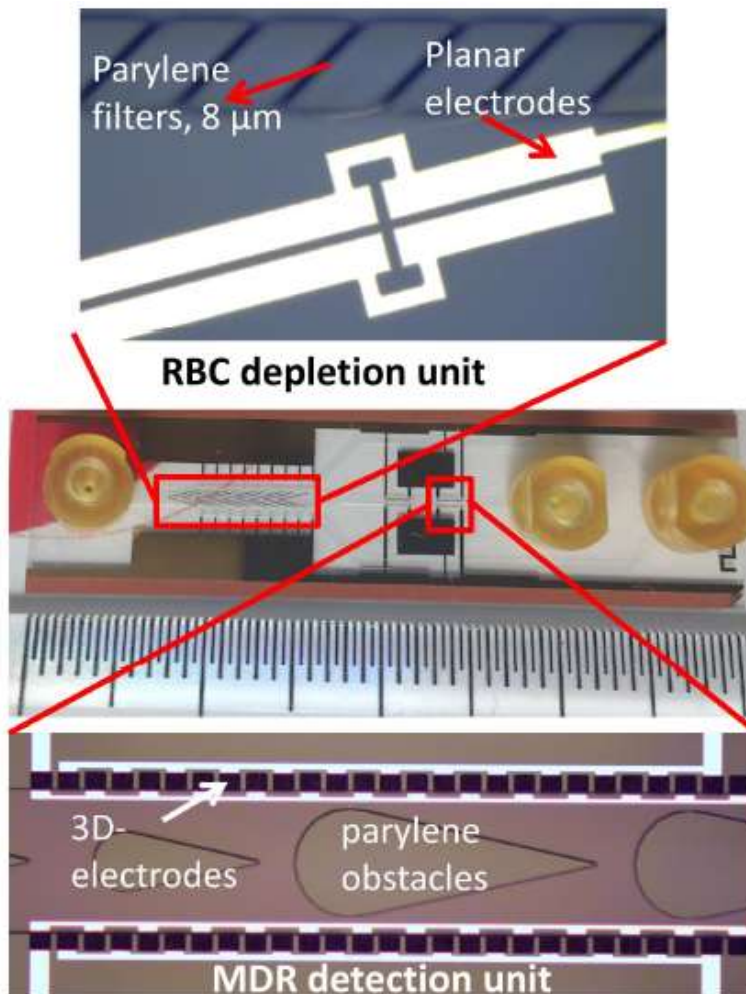


Figure 4.8: Fabricated device [49].

4.2.5 Materials and methods

4.2.5.1 Cell preparation

K562/wt and K562/doxR cells were taken from the research laboratory of Prof. Dr. Ufuk Gündüz. To develop resistance, they added *doxorubicin (Saba)* to different culture medium with gradual increment in their concentration until they become resistant to 1000 nM doxorubicin [10]. Whole blood (3 mL) was sampled from a healthy adult volunteer (woman) through venipuncture, utilizing EDTA treated tube to prevent coagulation. This sample was centrifuged at 900 rpm for 15 min. RBCs were harvested from the pellet.

4.2.5.2 Test setup and procedure

Tests were conducted under a fluorescent microscope (*Olympus, SZX12*). Observations were carried out under 20X magnification. A high-speed camera (*Evolve 128*) was utilized to observe the cell movement inside microchannel, under continuous flow and low fluorescence intensity. Flow rate was adjusted with a computer controlled microsyringe pump (*Lab Smith*). Real-time processing of screenshots was carried out with the computer software, *Winfluor*. DEP force was generated by energizing the electrode arrays with a signal generator (*Agilent, 81150A*). Two of its four outputs were utilized with 180° phase difference.

Cell preparation and test procedure are as follows. MDR K562 cells and RBCs were centrifuged at 1000 rpm for 5 min and 900 rpm for 15 min, respectively. The pellets were washed twice and suspended in an isotonic medium (8.5 % (w/v) sucrose and 0.3 % (w/v) dextrose) with a conductivity of 2.5 mS/m. These medium properties were adapted from the study of Labeed *et al.* For monitoring purposes, RBCs were stained with cell tracker red (*Invitrogen*), a fluorescent dye with red color, and observed under red filter (*31002 TRITC, Chroma*). MDR K562 cells were stained with fluorescein diacetate (*Invitrogen*), a fluorescent dye with green color, and observed under GFP filter. After 25 minutes incubation at 37°C, cells were washed with the suspension medium. Finally, they were mixed and working cell mixture was obtained. The ratio

of MDR K562 cells and RBCs were adjusted as 2, 0.3, 0.1, 0.05, keeping MDR K562 cell number constant.

4.2.6 Results

Detection tests were performed with $20 V_{pp}$ at a flow rate of $10 \mu\text{l}/\text{min}$. Figure 4.9 shows the screenshots of trapping tests of MDR K562 cells for different cell ratios. Table 4.1 presents the ratio of trapped MDR K562 cells to RBCs. This ratio is infinite for the condition that MDR K562 cells constitute less than 25% of overall population. This implies that MDR detection in K562 cells is achieved with 100% selectivity. On the other hand, increase in the number of RBCs was ensued with the trapping of them in MDR detection unit since RBC depletion unit was saturated and the harmony between electrical and hydrodynamic conditions was corrupted. This challenge can be overcome by increasing the length of RBC depletion unit.

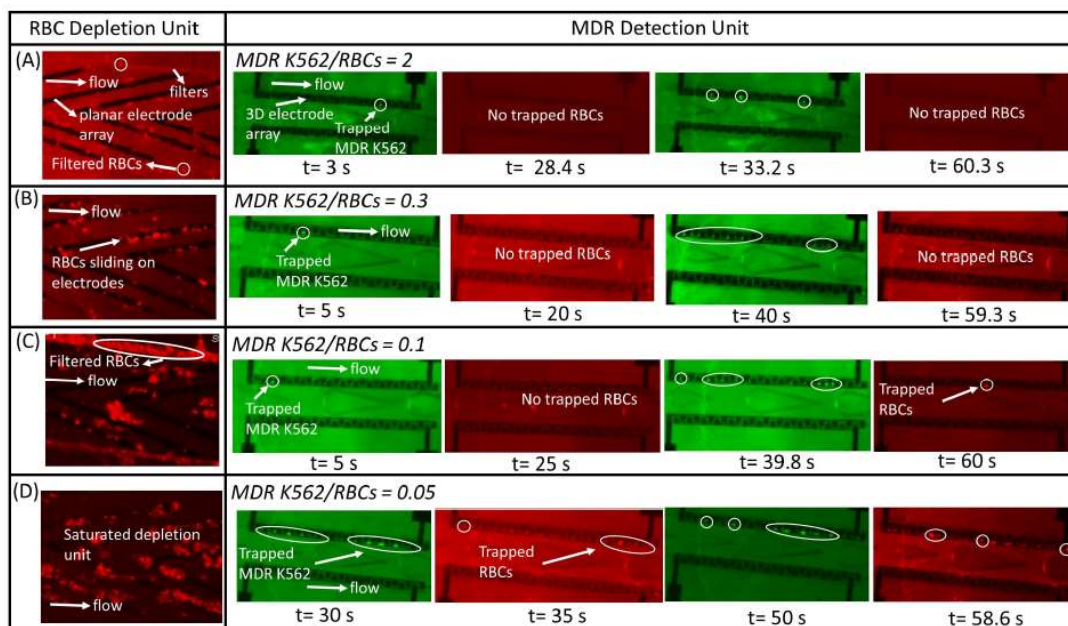


Figure 4.9: Pseudo-colored images taken during detection of MDR-K562 cells, green screens. Red screens show RBCs. Working solution was the mixture of MDR-K562 cells and RBCs with different concentrations ($f=1 \text{ MHz}$ and $f=48.64 \text{ MHz}$ for depletion and detection units, respectively. *Flow rate* = $10 \mu\text{l}/\text{min}$, *voltage* = $20 V_{pp}$) [49].

Table 4.2: The ratio of trapped MDR K562 cells to trapped RBCs for 4 cell mixtures, injected into channel with different ratios of MDR K562 cells to RBCs.

The ratio of MDR K562 to RBCs in inlet	2.00	0.30	0.10	0.05
The ratio of trapping MDR K562 to RBCs in inlet	∞	∞	4.00	1.75

4.2.7 Discussion

Cylindrical filters provided the depletion of RBCs, efficiently, when RBC number is low enough. On the other hand, increase in the number of RBCs caused clogging in the filters. Due to their elasticity, some of the cancer cells also passed through the filters although they had diameter greater than that of cylindrical filters.

As another filter type, conical filters, having built-up pressure greater than zero, was suggested by Tang *et al.*. They claimed that conical filters can eliminate blood cells more efficiently than cylindrical ones when they are placed on bottom of the channel, occupying large area. By inspiring this study, conical filters were placed in the side-wall of the channel (Fig. 4.10). However, smaller cells inside the population of K562, CCRF-CEM, and HL60 cell lines passed through these filters like in cylindrical ones (Fig. 4.11 (a)). Moreover, deformed cells clogged the filters (Fig. 4.11 (b)). HL60 cells are less elastic but clogging ratio of them has become higher in that case. This structure is not proper for the side-wall placement. As a result, RBC depletion part needed a complex microfluidic design. MDR detection is a versatile and complicated issue, also. Therefore, blood cell elimination studies were ceased at that point.

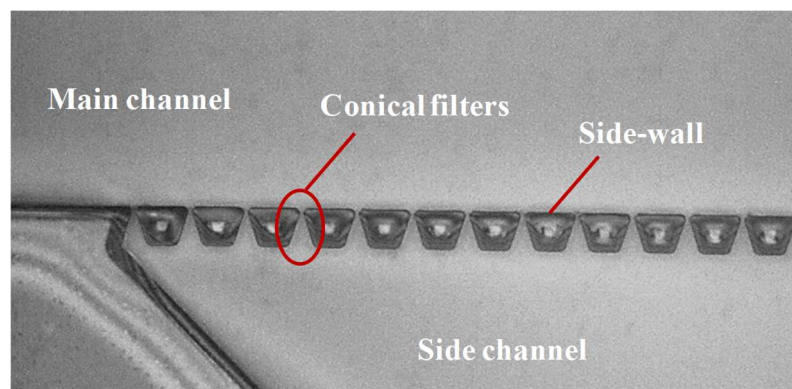


Figure 4.10: Conical filters placed on the side-walls of microchannel.

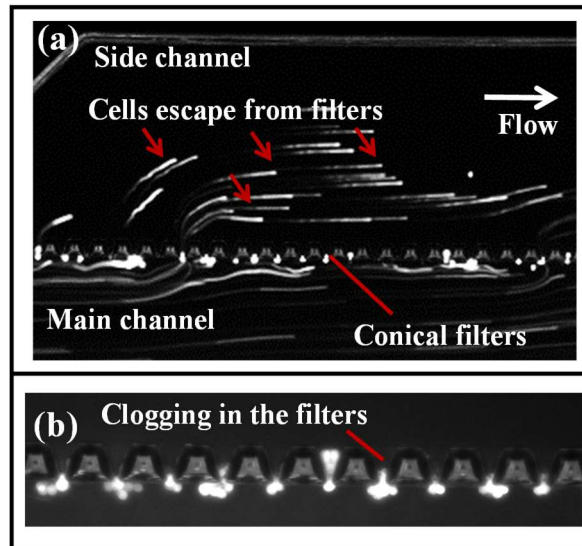


Figure 4.11: Cell escape (a) and clogging (b) in the conical filters.

4.3 LOC system integrating DEP detection and IS counting units for chemosensitivity analyses

Drug resistance is quantified comparatively. This means that for each drug and cancer cell, a threshold value in the drug concentration and expose duration should be determined. For example, in XTT analysis, cell proliferation of MDR cancer cells are divided into that of wild type ones under the same concentration of drug exposure. Result gives the resistance level. For the detection of MDR through DEP, a systematic way like XTT assays should be defined. However, DEP is not a tool which is able to make quantification. Therefore, impedance units were integrated with a DEP detection unit as explained below.

4.3.1 System design

System has one DEP unit for the detection of drug resistant cells by trapping them in pDEP regions. 2 different electrode structures were designed for this unit: Planar (*LOC-1*) and 3D-electrodes (*LOC-2*). One of the impedance based counting units was placed in the inlet of channel and the second one was placed in the outlet (Fig. 4.12). Due to cell adhesion on microfluidic connections and tubing, cells coming into the channel cannot be calculated directly from sample concentration and analyzed volume. IS unit in the inlet solves this problem. Outlet IS unit quantifies the leaving

cells. In the following sub-parts design details of planar and 3D-electrodes in DEP unit, IS units, and microfluidic connection part between DEP and IS units are explained.

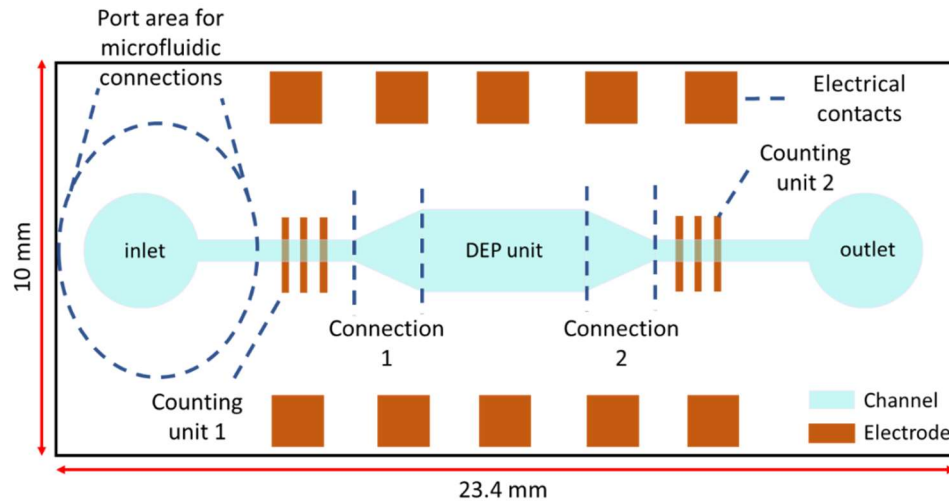


Figure 4.12: Schematic of the LOC system.

4.3.1.1 Planar electrode design

As explained in Chapter 2, wild type cells have resistant ones inside. Biological analysis gives inspection for this ratio. Moreover, electrical characterizations presented in Chapter 3 presents that some of the resistant cells and wild type ones can have cytoplasmic conductivity close to each other. In this study, high conductivity DEP buffer was exploited to set a threshold value to resistance level for the first time in the literature. However, high conductivity decreases DEP force, acting on resistant cell. DEP electrodes should have high variation in electric field to decrease the loss in trapping force, acting on resistant cells. Utilizing cell size and $Re(f_{CM})$ values, measured and simulated in Chapter 3, respectively, in equation 4.1, it was calculated that ∇E_{rms}^2 should be greater than $10^{16} \text{ V}^2/\text{m}^3$ for $1 \mu\text{l}/\text{min}$ flow rate (0.83 mm/sec as average velocity in the LOC system).

Castellated electrodes have been utilized in DEP devices to provide high forces. In this study, they were designed with gap between fingers as small as possible, taking

into account our fabrication limitations. Electrode width and space between fingers were chosen as $5\ \mu\text{m}$ (Fig. 4.13 (a)). Figure 4.13 (b) presents ∇E_{rms}^2 simulation results, providing expected magnitude. Simulations were carried out in *COMSOL Multiphysics* with AC/DC module. “*Electrostatics, generalized*” sub-module was utilized by solving Laplace equation inside the channel with insulating boundary conditions, since the walls of the microchannel is parylene. The electrode boundary conditions were determined as $\pm|V|\sin(\omega t)$ to apply sinusoidal voltage with 180° phase difference in between. Number of mesh element and degrees of freedom were 53184 and 106609, respectively.

Due to small sizes, castellated electrodes have large area to trap cells. However, this property can be disadvantageous when trapped cell number increases on a DEP cage since planar electrodes are spread whole channel in DEP detection unit. Therefore, as an alternative, diamond structured electrodes were designed to prevent cell fouling on electrodes (Fig. 4.13 (c) and (d)).

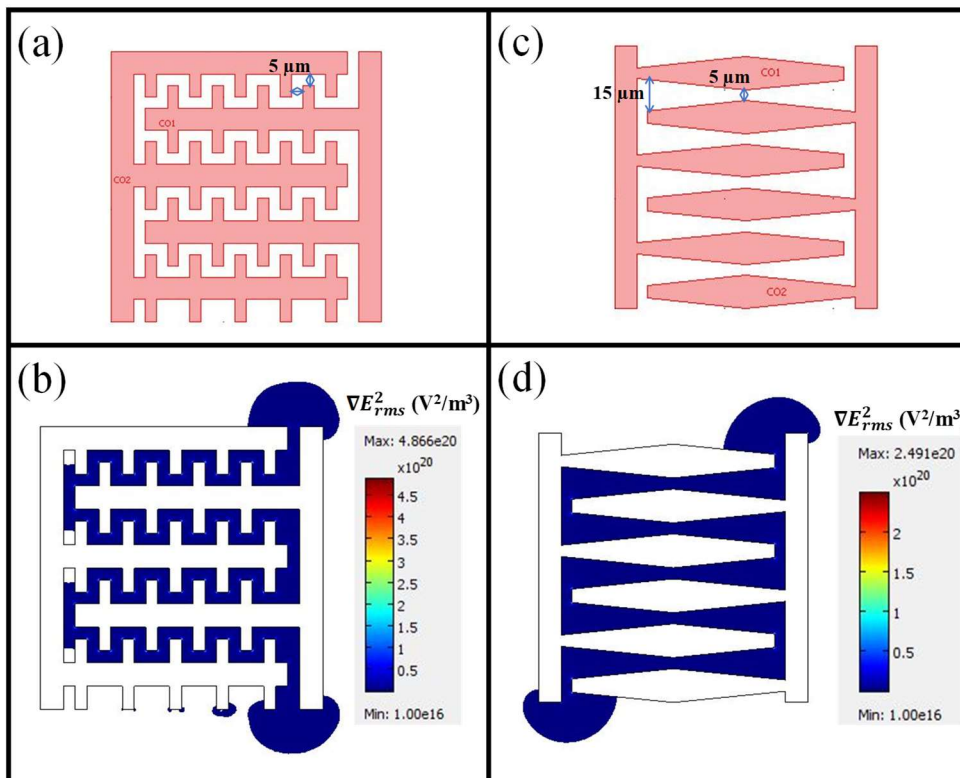


Figure 4.13: Schematic and electric field gradient simulations of castellated (a, b) and diamond (c, d) electrodes.

4.3.1.2 3D-electrode design

Providing the same DEP force through the channel height increases device efficiency although microchannel of LOC system has a height, comparable with the cell diameter. In the previous design, presented in section 4.2, 3D-electrodes were placed on side-walls of the channel. In this system, they were transferred into channel. Circular electrode structure was chosen. When a cell traps on electrode, the space between electrodes should permit the flow of cell. Providing cell flow, these electrodes should have minimum 40 μm space between each other. If this distance increases, DEP force decreases. Therefore, circular electrodes in the form of round arrangement were designed with 9.5 μm space in between.

The comparison of cell trapping efficiency of these two designs is shown in Figure 4.14. Firstly, electric field simulations were carried out with the same method explained in the previous part. Determined electric field gradient values were utilized in particle tracing simulations as the term of ∇E_{rms}^2 . No slip boundary conditions were utilized with *Incompressible Navier-Stokes* equation in the tracing of particles. Inlet velocity was calculated and chosen in simulations as 0.018 m/s to be able to apply 10 $\mu\text{l}/\text{min}$ flow rate. Outlet boundary condition was chosen as zero pressure because it is open to atmosphere throughout the tests. 3D-electrodes are fabricated with Cu-electroplating. Taking care of fabrication limitations, electrode diameter was determined as 10 μm and spacing between them was chosen as 9.5 μm .

4.3.1.3 IS unit design

Dr. Sertan Sukas studied on impedance spectroscopy. By the help of his experiences, an IS unit was designed with using 1.5 ratio between gap between electrodes and electrode width. Electrode width was determined as 20 μm since leukemia cell dimensions, exploited in this thesis, change between 10-20 μm . To determine cell number with high resolution, cells should pass on IS unit one by one. Therefore, channel height and width should be as small as cell without preventing cell passage. However, the width of DEP unit was designed as 1000 μm to trap the maximum number of cells staying in the microfluidic channel dimension limits. Therefore, IS

unit channel had 100 μm width as minimum. Its height was the same as DEP unit, 20 μm .

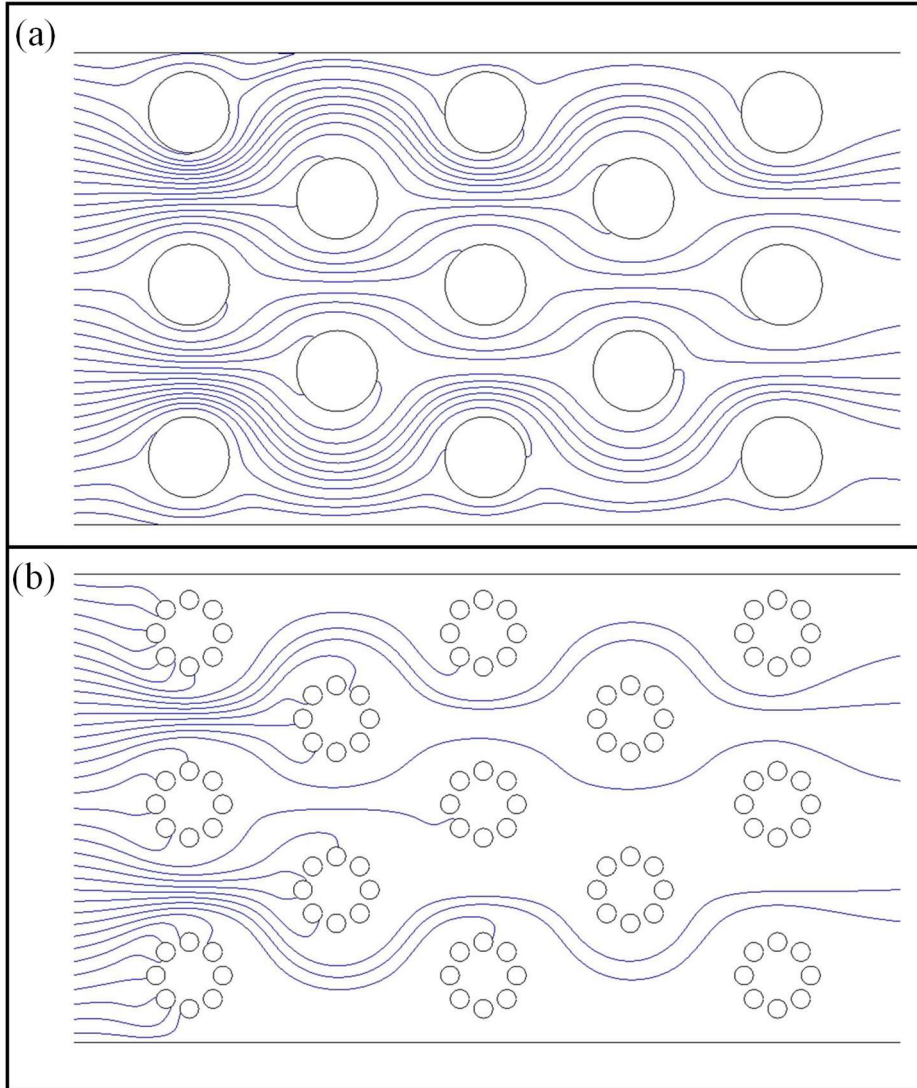


Figure 4.14: Comparison of cell trapping efficiency of circular electrodes (a) and circularly placed circular electrodes.

4.3.1.4 Design of microfluidic connection between IS and DEP units

The channel width in the IS units should be as small as possible and it was chosen as 100 μm . On the other hand, the one in DEP unit was determined as 1000 μm . Therefore, a hydrodynamic distribution channel should be inserted into design to

provide homogenous cell flow from IS unit to DEP unit. Design of this unit varied according to electrode type: Planar (a) and 3D-electrodes (b) (Fig. 4.15). In simulations, stationary laminar flow and time dependent particle tracing modules of COMSOL Multiphysics were utilized.

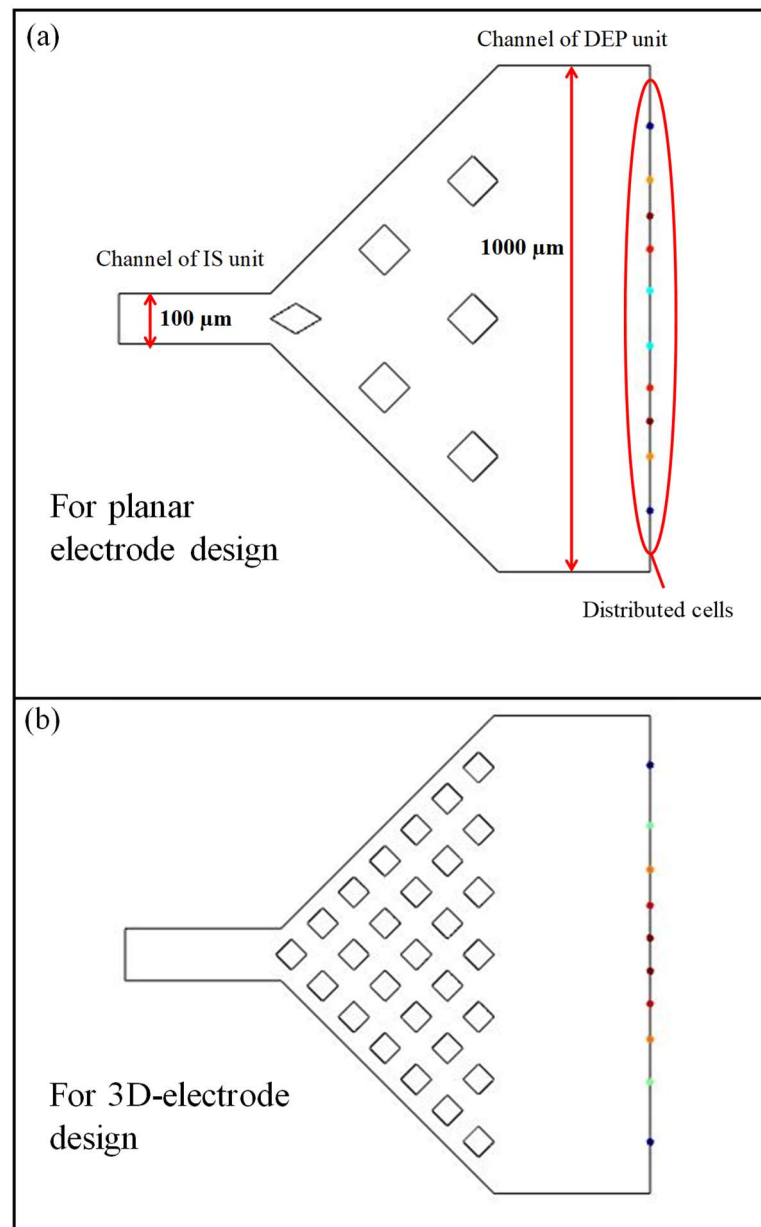


Figure 4.15: Particle tracing results of distribution unit for planar (a) and 3D-electrodes (b).

4.3.2 Fabrication

Fabrication flow for LOC-1 system: Fabrication was started with dehydration of the 6" glass wafers which were cleaned with piranha and etched with BHF. Ti/Au was sputtered (*BESTEC dual chamber sputter system*) to form planar electrodes. Utilizing wet etching, planar electrodes were patterned. A parylene layer ($\sim 0.5 \mu\text{m}$) was coated for insulation purposes. Next, the channel was formed with lithography and parylene coating ($\sim 20 \mu\text{m}$). Finally, sacrificial photoresist was released with acetone. Figure 4.16 and 4.17 present the fabrication flow and fabricated device with details, respectively.

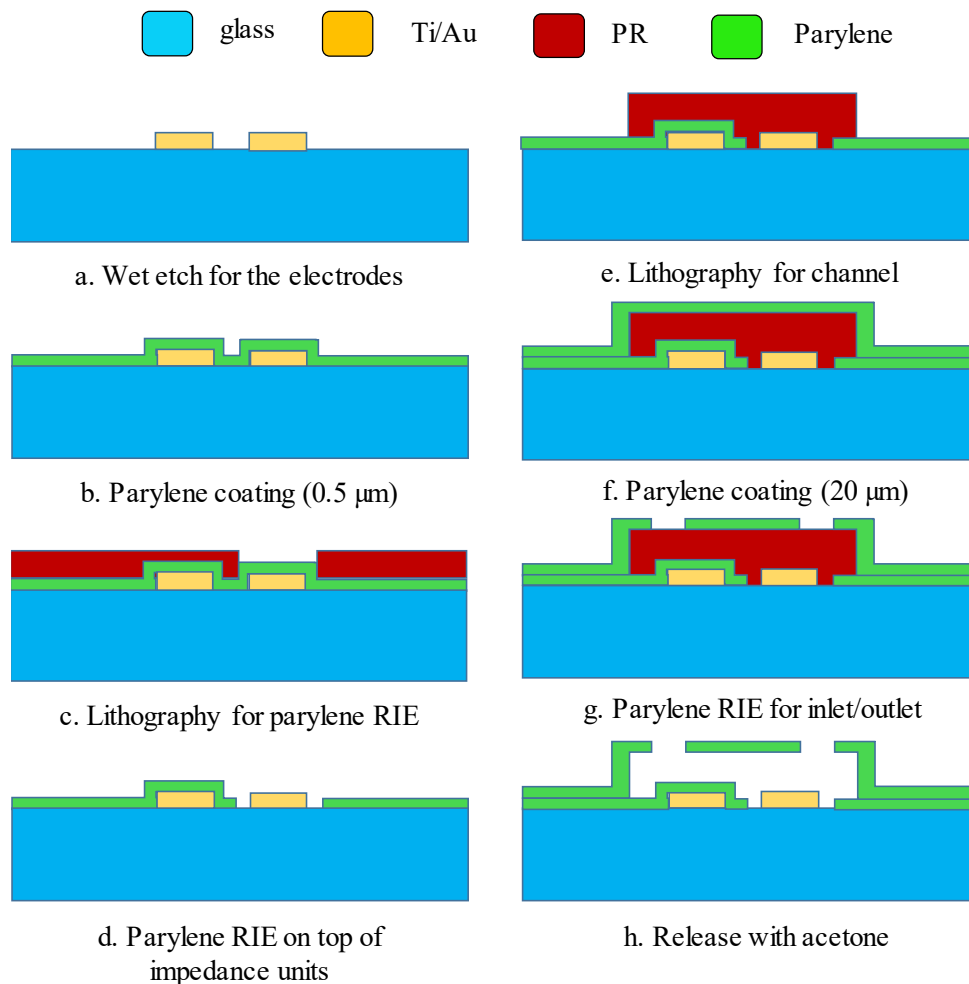


Figure 4.16: Fabrication flow of LOC-1.

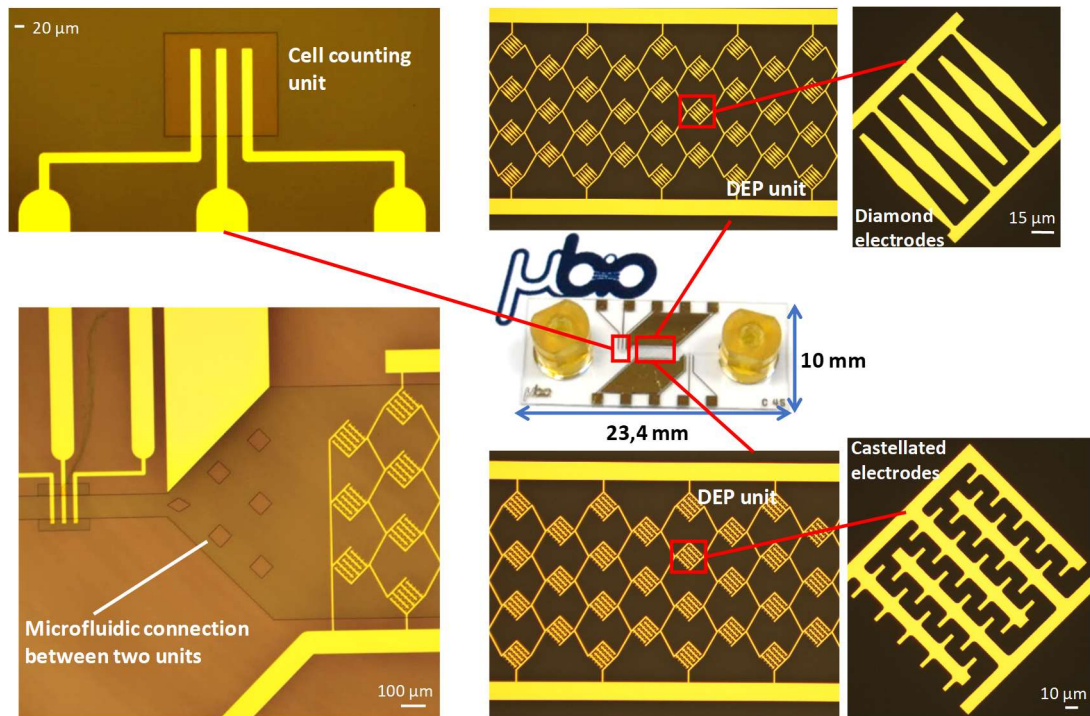


Figure 4.17: Fabricated LOC-1 focusing on the planar electrodes, IS unit, and microfluidic connection between units.

Fabrication flow for LOC-2 system: Fabrication was started with dehydration of the 6" glass wafers which were cleaned with piranha and etched with BHF. Ti/Au was sputtered (*BESTEC dual chamber sputter system*) to form electrodes. Utilizing wet etching, electrodes were patterned. A parylene layer ($\sim 5 \mu\text{m}$) was coated for insulation purposes. Next, lithography and parylene RIE were carried out to open the electrodes of IS units. With thick resist coating ($\sim 40 \mu\text{m}$), parylene RIE to open DEP electrodes and Cu-electroplating were achieved on them. A parylene layer ($\sim 0.5 \mu\text{m}$) was coated again for insulation purposes since Cu-electrodes in DEP unit should not touch to cell solution. After that, lithography and parylene RIE were carried out to open the electrodes of IS units. Then, the channel was formed with lithography and parylene coating ($\sim 20 \mu\text{m}$). Finally, sacrificial photoresist was released with acetone. Figure 4.18 and 4.19 show the fabrication flow and fabricated device with details, respectively.

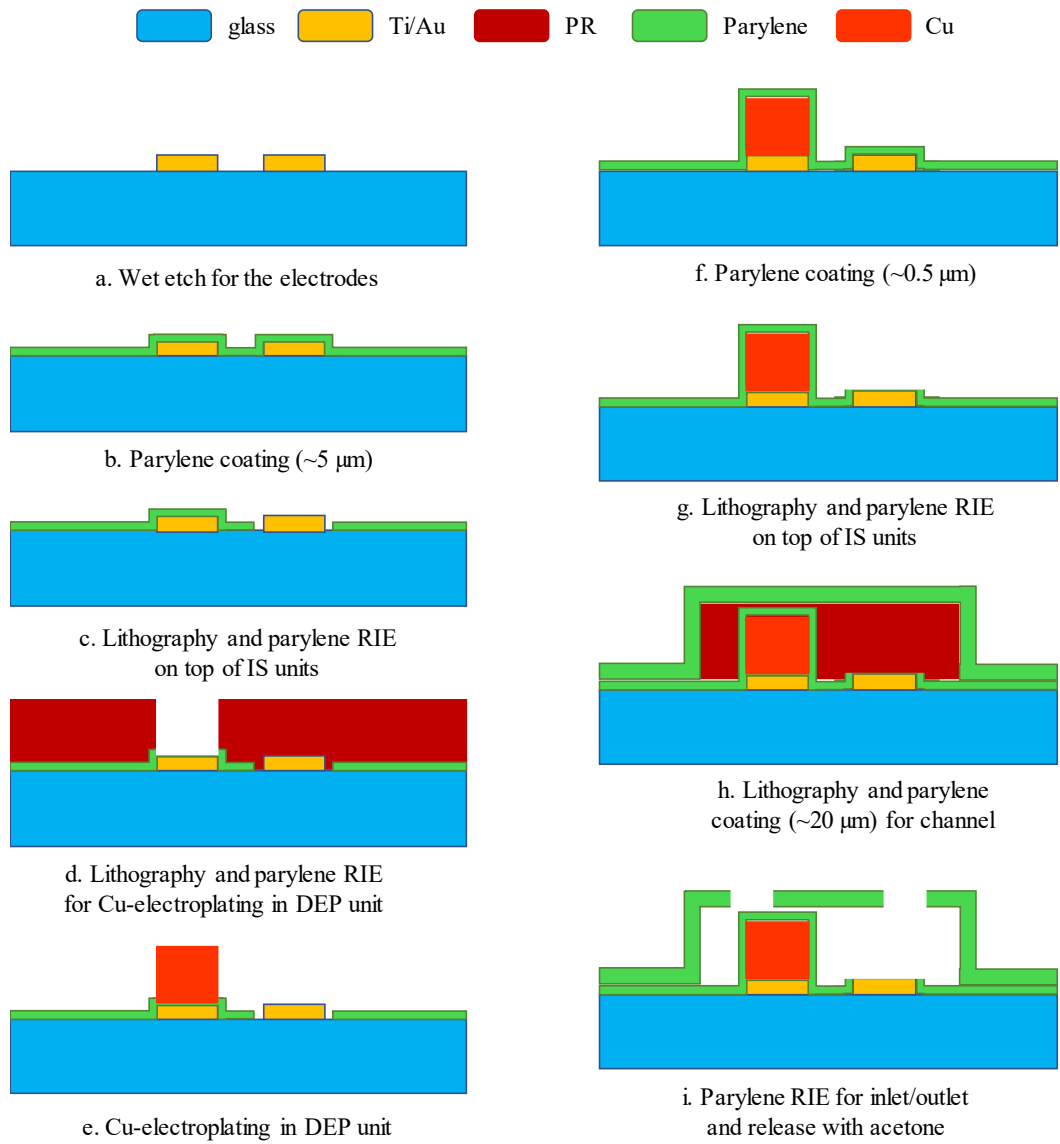


Figure 4.18: Fabrication flow of LOC-2.

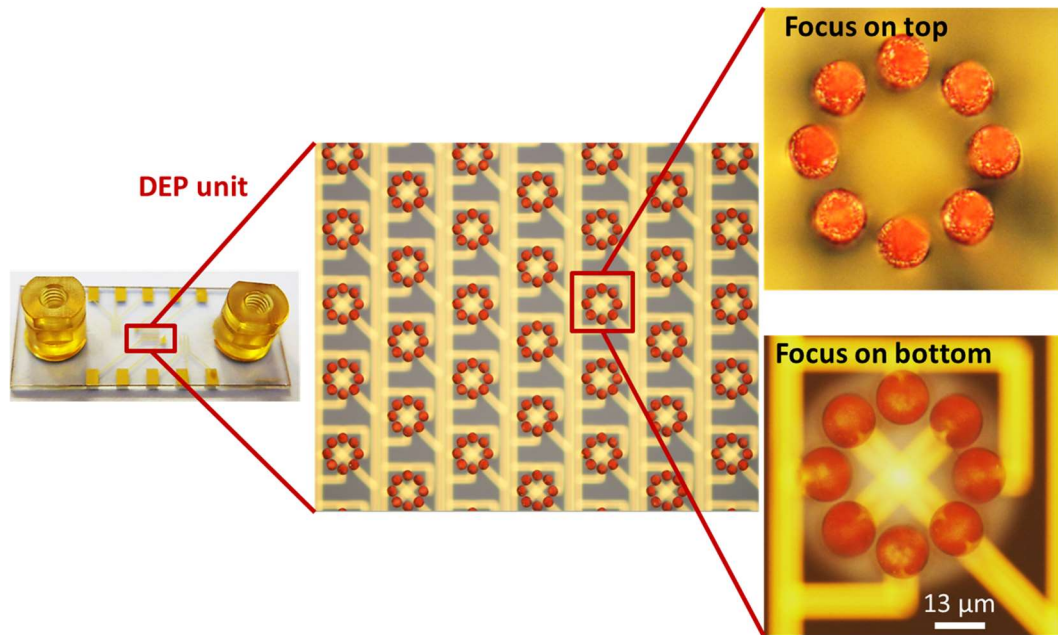


Figure 4.19: Fabricated device with 3D-electrodes.

4.3.3 Materials and methods

4.3.3.1 Test setup

DEP unit should operate at MHz range and 20 V_{pp} voltage while IS units work with 1-2 V_{pp} voltage at 100-200 kHz frequency. Cross-talk between DEP and IS units occurs. This cross-talk should be eliminated since it damages proper operation of both units. A flexible PCB was designed with Taylan Töral (Fig. 4.20). It provides proper operation of these units by means of ground lines between lines carrying different frequency voltages. This flexible PCB connected to a rigid PCB which distributes signals, coming from signal generator and impedance spectroscopy devices, with ground lines. Connection between these two PCBs was provided by ZIF connector (Fig. 4.20). LOC system was placed on flexible PCB by epoxy adhesive (Loctite, EA 1C, Henkel) and connections were made by wire-bonding. Wire-bonding was carried out by Murat Yağcı in METU MEMS Center. On wire-bonding lines, a globe top epoxy (Master bond, Supreme3HTND-2GT) was applied to protect them from liquids and physical damage.

DEP force was generated by energizing the electrode arrays with a signal generator (*Agilent, 81150A*). Two of its four outputs were utilized with 180° phase difference. Impedance spectrometer of Zurich Instruments (*HF2IS*) and its preamplifier were used to measure impedance in IS units. 1 V_{peak} sinusoidal voltage at 100 kHz was used to count cell number. Fluids were driven into LOC system by means of mass flow controller (*Elveflow, OB1*). Inverted microscope (*Leica, DMI8*) and inserted monochromatic camera (*Hamamatsu ORCAFlash 4.0*) were utilized to monitor channel to be sure about that there is not any air bubble formation while making the analysis.

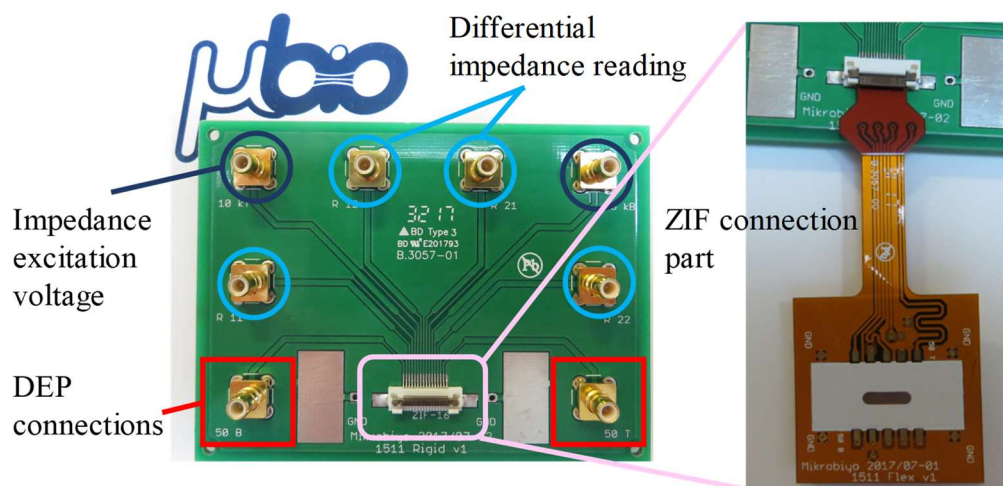


Figure 4.20: Rigid PCB connecting LOC system to signal generator and impedance spectrometer (left) and flexible PCB carrying LOC system (right).

4.3.3.2 Device preparation procedure

Parylene is a hydrophobic material. Therefore, surface should be treated by ethanol as a first step of an analysis to prevent air bubble formation. DI is used to get rid of ethanol. Next, PLL (20)- g [3.5]- PEG (2) coating was carried out to prevent non-specific cell trapping. According to literature, PEG application is 15 min for silicon channels. However, for proper operation in parylene microchannel, this duration was determined as 1h in this study. After that, DI cleaning was made. Finally, channel was filled with DEP solution.

4.3.3.3 Cell preparation

A physiological solution should have 290 mOsm/m. When high conductivity DEP solution is prepared, high volume of PBS (1X) is used. Therefore, sucrose and dextrose amount should be calculated to adjust osmotic pressure. After preparation of DEP solution according to this procedure, cells taken from culture conditions are washed 3 times at 300 g for 5 min with this solution. The cell concentration is adjusted as 5×10^5 cells/ml, utilizing Automatic Cell Counter (BioRad, TC20). Finally, they are driven into LOC system.

4.3.4 Theory of operation

Low conductivity buffers (LCBs) have been used in DEP since they provide enough polarization to manipulate cells. However, according to literature, cellular metabolism is affected and cells change their electrical properties in short durations (<10 min) in LCBs.

Switching between nDEP to pDEP or vice versa is achievable by means of LCBs. This creates crossover frequency (f_{cross}) term at which $Re(f_{CM})$ of cells is equal to zero (*i.e.* $F_{DEP}=0$). Cell separation should be achieved at f_{cross} with LCBs; although, single f_{cross} determination is not possible for a heterogeneous cell line. In contrast, in high conductivity buffers (HCBs), defined as a DEP buffer (osmolarity=290 mOsm/L) at a conductivity higher than that of cytoplasmic conductivity of cells, these cells always experience nDEP. If there exists another group of cells, having higher cytoplasmic conductivity than that of medium, they can be affected by pDEP force. By means of this, these 2 groups of cells can be separated. For example, particles presented in Figure 4.21 have different cytoplasmic conductivities, varying between 180-400 mS/m. Medium conductivity was chosen as 200 mS/m in this simulation. When $Re(f_{CM})$ values are examined, it can be interpreted that cells inside these heterogeneous population, having cytoplasmic conductivity greater than 200 mS/m, can be manipulated by pDEP.

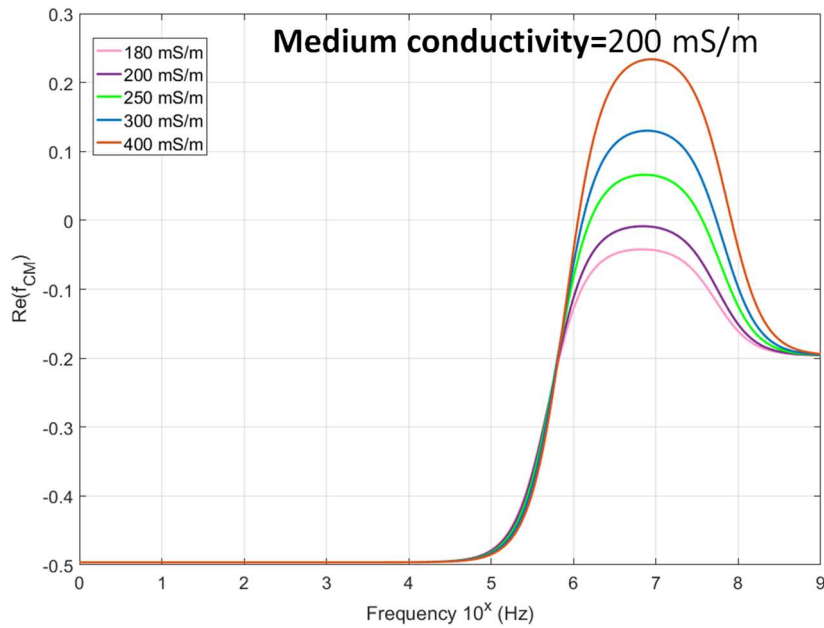


Figure 4.21: $\text{Re}(f_{CM})$ vs frequency simulation of cells with cytoplasmic conductivity changing between 180-400 mS/m in a DEP solution at a conductivity of 200 mS/m.

Although the usage of HCBs increases the possibility of sample heating and electrochemical damage, these effects can be minimized by decreasing voltage and increasing frequency.

In this study, high conductivity DEP buffer provided a threshold value for MDR detection. Cytoplasmic conductivity values, estimated in Chapter 3, were used to choose HCB's conductivity as 200 mS/m and 160 mS/m for K562 and CCRF-CEM cells, respectively.

The cell numbers entering into and leaving from channel were determined by IS units. Difference between them stands for trapped cells. The ratio of trapped cells into the number of cells entering into channel was the result under interest. However, a delay exist the data coming from IS units due to the traveling time of a cell from inlet to outlet (Fig. 4.22). Firstly, this delay should be determined for each device and eliminated. A *MATLAB* script was utilized for this purpose, using “*XCORR*” function in signal processing tool (Appendix B). Using this delay, samples at the end of inlet IS units and at the beginning of outlet IS units were deleted. Finally, peak detection was carried out to determine cell number.

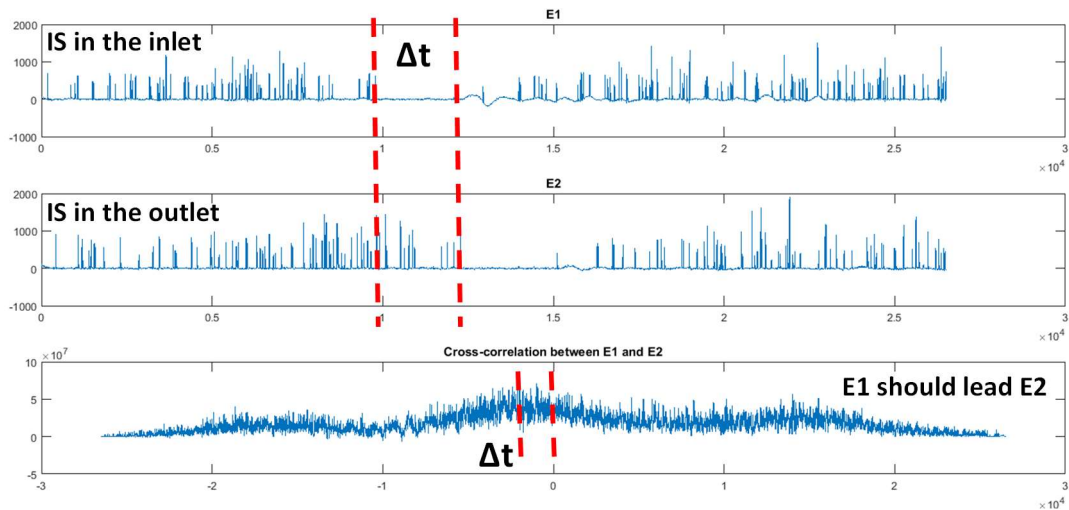


Figure 4.22: Impedance vs time data taken by both IS units (E_1 : at the inlet and E_2 : at the outlet). Cross-correlation was carried out in MATLAB to eliminate delay between data.

4.3.5 Results

Utilizing the parameters determined in Chapter 3, first analysis was carried out in LOC-2 with 3D-obstacle electrodes. However, these electrodes acted like hydrodynamic traps. K562 cells were trapped inside electrode cages due to their elasticity; although, electric field in DEP region was off (Fig. 2.23). Next, tests were continued with LOC-1, having planar electrodes.

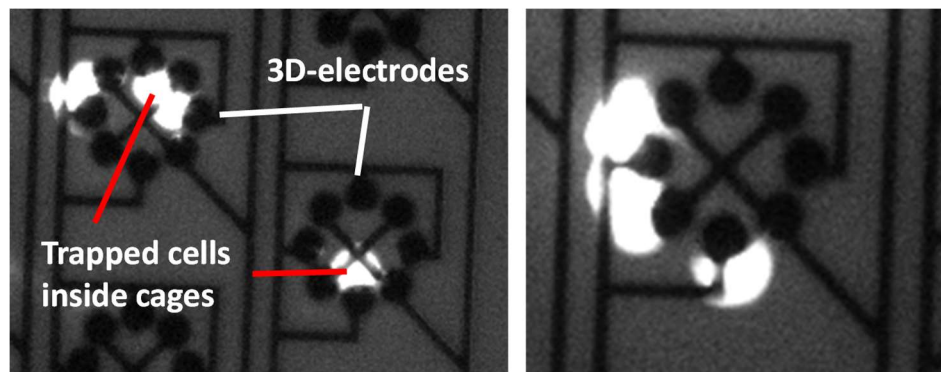


Figure 4.23: Trapped cells inside 3D-electrode cages due to cell elasticity.

This system is a totally label-free since quantification and detection were achieved electrically. Cell staining was not made since it can change cell electrical properties. Therefore, wild type and resistant cells were not mixed. They should be given to system consecutively after cleaning step. While this operation, flow rate and form of channel should not change. At 1 $\mu\text{l}/\text{min}$ flow rate, delay between the time at which a cell enters the channel and the time at which a cell leaves from the channel was determined as 5-6 sec. This duration was exploited as a checkpoint to ensure that flow rate did not change from test to test in the same device.

Under normal growth conditions, 3 biological replicates of K562/wt and K562/imaR cells were analyzed with LOC-2 at 8.59 MHz and 20 V_{pp} voltage immersing them into a DEP solution, having 200 mS/m conductivity. Table 4.3 presents the number of cells entering into and leaving from the channel when DEP voltage was off and on. These results show that although DEP was not in action, cell adhesion occurred due to parylene-cell interaction. PLL (20)- g [3.5]- PEG (2) was applied for 1h in these tests. Cell adhesion was decreased to $\sim 6\%$ from $\sim 45\%$. In some of the analysis at which DEP voltage was OFF, outgoing cell number was higher than that of incoming ones. This indicates that some inaccuracies occurred in counting unit but it was under the critical value for the trapping experiments.

Figure 4.24 presents that the trapping trend of K562/imaR cells ($57.3\% \pm 6.7$) was significantly different than K562/wt ones ($20.3\% \pm 4.2$) at $p < 0.05$ level. K562 cells were high-level laboratory model for MDR and this difference was expected according to results obtained in electrical characterization (Chapter 3). Non-zero trapping of wild type cells is interpreted that 20% of them was different than others in terms of their electrical properties. At that point, it cannot be claimed that this 20% was drug resistant. To approve this claim, trapped cells should be given from channel as viable. They should be proliferated and exposed by drug. To decide the time and dose of drug exposure, XTT, apoptosis, and cell cycle analysis can be utilized, presented in Chapter 2.

Table 4.3: Adhesion and trapping ratio of K562/imaR and K562/wt cells when DEP voltage is OFF and ON.

imaR		DEP OFF			DEP ON		
Number of cells	Incoming	Outgoing	Adhesion ratio	Incoming	Outgoing	Trapping ratio	
BR 1	419	395	6%	171	85	50%	
BR 2	314	319	~0%	295	109	63%	
BR 3	230	238	~0%	303	124	59%	
wt		DEP OFF			DEP ON		
Number of cells	Incoming	Outgoing	Adhesion ratio	Incoming	Outgoing	Trapping ratio	
BR 1	281	264	6%	145	109	25%	
BR 2	104	98	6%	63	52	17%	
BR 3	-	-	-	163	132	19%	

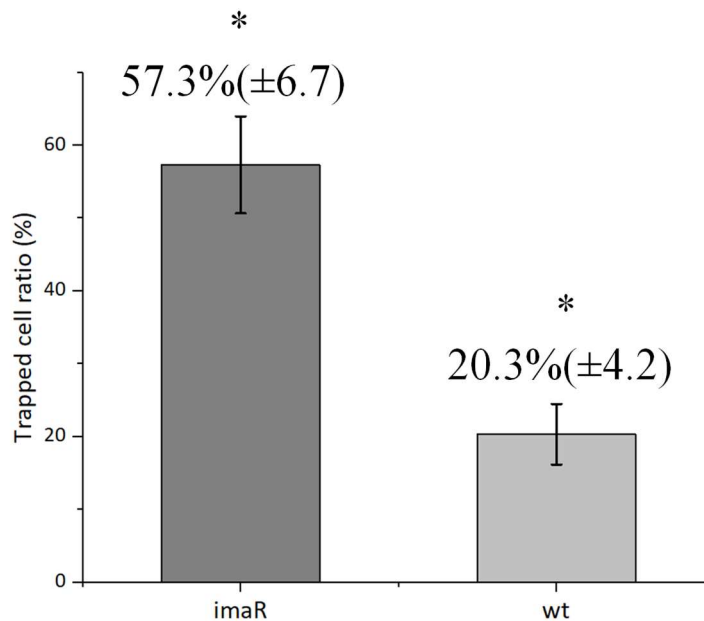


Figure 4.24: Trapped cell ratio of K562/imaR (left column) and K562/wt (right column) cells under the same experimental conditions (frequency=8.59 MHz, voltage=20 V_{pp}, solution conductivity=200 mS/m, cell concentration=5x10⁵ cells/ml). Results are presented as mean±stdev. * p<0.05 significantly different trapping trends (n=3).

As explained in Chapter 2, CCRF-CEM cells were clinically-relevant model for MDR. Their electrical properties were not significantly different, presented in Chapter 3. According to analysis of them carried out with LOC-2, CCRF-CEM/wt cells were trapped with a ratio of 56% while the trapping ratio of doxorubicin resistant ones was 58%. As expected by the leading of electrical characterizations, their trapping trends were similar.

As a proof of concept study, it was claimed that trapping ration of wild type cells under drug exposure decreases. Drug dose and time was chosen as 300 nM and 24h for K562/wt cells and 250 nM and 18h for CCRF-CEM/wt cells, respectively. Results show that the trapping ratio of K562/wt cells exposed to drug was decreased to half of K562/wt cells under normal growth conditions. Like K562/wt cells, CCRF-CEM/wt cell trapping trend was changed under drug exposure. The ratio of trapping was decreased by 1.6.

4.4 Conclusion

Two different LOC systems were designed and implemented, integrating DEP detection and impedimetric counting units. First one has planar electrodes having easier fabrication. Second one has 3D-obstacle electrodes providing higher and uniform DEP force through channel height. Although higher DEP force is necessary in HCB based DEP, 3D-obstacle electrodes acted like hydrodynamic traps due to the elasticity of leukemia cells and misinterpretation in trapping analysis occurred. Therefore, analyses were continued with planar electrode devices. An algorithm was produced using cross-correlation tool in *MATLAB*. By means of this algorithm, the examination of cell trapping was achieved in accurate way.

Providing totally label-free analysis for the first time in the literature with a DEP based detection device, it was shown that MDR detection can be achieved electrically. Moreover, drug screening can also be carried out with this system. Despite of all these promising results, system has some challenges. First of all, cell adhesion occurred due to parylene-cell interaction. As 1st solution, the duration of PEG was prolonged. However, this problem continued. Therefore, optimum conditions for PEG coating should be determined. As another way, channel material can be changed.

Test duration was 2 min and flow rate was 1 $\mu\text{l}/\text{min}$. 2 μl solution was enough to obtain trapping trend. However, a mass flow controller and microfluidic connections with large volumes were utilized in these tests. Therefore, 1 ml sample at inlet was exploited. This large volume caused cell precipitation in the inlet reservoir as second problem. There exists zero-dead volume sample loading interface studies, like [133]. Hatipoğlu *et al.* presented a system, shown in Figure 4.25. This tool can be a solution to this problem.

Finally, system cleaning was a challenge since microfluidic tubing should be demounted from the system for cleaning with DI. When it was remounted to system after DI cleaning, air bubbling can occur. Therefore, a valve and tubing system should be constructed for cleaning of channel without demounting of any parts between each run by preventing misinterpretation of results.

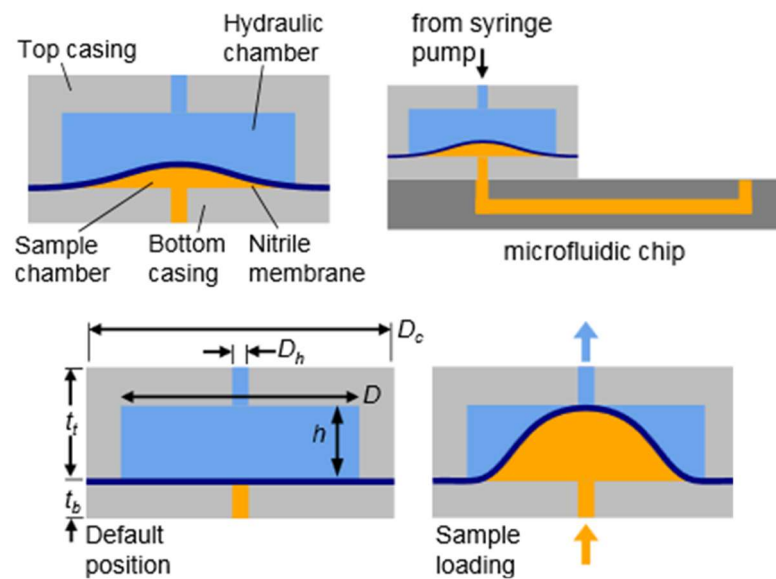


Figure 4.25: Flexible Hydraulic Reservoir (FHR) proposed by [133] as zero-dead volume sample loading interface.

CHAPTER 5

CONCLUSION AND OUTLOOK

In order to increase the disease-free survival of the patient, the key parameter of the treatment method in cancer is the accurate diagnosis. Tumor heterogeneity is the major challenge to determine the right treatment method since it is caused by the presence of genetically, epigenetically, and phenotypically different sub-clones inside cancer cell population of an individual patient, preventing to target a single genetic abnormality to control the cancer optimally [50].

Chemotherapy is a cancer treatment, preferred to improve the life quality and extend disease-free survival time of patients. However, chemotherapy response of each tumor is unique. Lots of the clinical trials have reported that cancer patients whose chemotherapy is personalized progressed better than those treated with standard chemotherapy [124]. To make treatment personal, chemosensitivity of patients should be examined. In the scope of this thesis, chemosensitivity analyses can be separated into two parts: Detection of multidrug resistance (MDR) and monitoring of chemotherapy efficiency.

A cost-effective, label-free, and user-friendly method is needed to provide effective diagnosis of MDR in cancer cells, without compromising the sensitivity and specificity [22]. Dielectrophoresis (DEP) is a MEMS-enabled technique used to manipulate particles based on different sizes and/or dielectric properties under non-uniform electric field. Studies showed that dielectrical differences can occur between cancer cells due to the development of MDR [44]. Labeed *et al.* reported that the cytoplasmic conductivity of multidrug resistant K562 leukemia cells are 2.2 times higher than that of drug sensitive ones. They claimed that this variation is most probably associated with the overexpression of P-gp, modulating the volume-activated Cl⁻ channels. On the other hand, membrane associated protein

overexpression is not the only mechanism behind MDR as explained in Chapter 1 although this overexpression is the most abundant one. There exist seven potential mechanisms and four of them can create dielectrical differences through ionic changes in cytoplasm, including overexpression of membrane associated proteins. This indicates that DEP has potential to detect most of the MDR cases while it cannot give information about the mechanism behind.

Throughout this thesis, to quantify tumor heterogeneity in leukemia cells in terms of their drug response and drug screening through LOC systems based on DEP has been carried out to. The achievements are as follows:

- i. Differences in drug response alter electrical properties of cells. They are dynamic organizations; hence, drug responses changes according to exposure time and dose. In order to determine resistance level of leukemia cells, XTT assays were carried out. The cell lines in our laboratory were classified as high-level laboratory and clinically relevant model of resistance. Next, the aim in the apoptosis assays was to determine correct time and doses for the screening of *imatinib* and *doxorubicin* effects on K562 and CCRF-CEM cells by electrical analysis. For CCRF-CEM/wt cells, time and dose were determined as 18h and 250 nM doxorubicin while the major death mode in K562/wt cells was not observed as apoptosis. Therefore, 24h and 300 nM imatinib were chosen for K562/wt cells' electrical examinations.
- ii. Cell cytoplasmic conductivity is one of the key parameters, changing according to physiological properties of cells. Ion release-based impedance spectroscopy was utilized for the first time in the literature to determine average total ion concentration of a cell. Results show that the total ion concentration of K562/imaR cells was 1.78 times higher than that of K562/wt ones while CCRF-CEM/doxR cells have 1.2 times higher ion concentration than wild type ones. Using the ratio between K562 cells, DEP medium conductivity and operation frequency were determined as 200 mS/m and 8.59 MHz. The parameters were identified as 160 mS/m and 6.15 MHz for CCRF-CEM cells.

- iii. A totally label-free LOC system was implemented. Analysis method was developed.
- iv. Under normal growth conditions, 3 biological replicates of K562/wt and K562/imaR cells were analyzed with this LOC system at 8.59 MHz and 20 V_{pp} voltage immersing them into a DEP solution, having 200 mS/m conductivity. 57.3% ($\pm 6.7\%$) of resistant cells were trapped on electrodes while wild type ones were trapped with a ratio of 20.3% ($\pm 4.2\%$). This can be interpreted as the tumor heterogeneity can be determined in terms of MDR level.
- v. Drug exposed K562 cells during 24h were analyzed by the LOC system. Results show that the trapping ratio of wild type cells exposed to drug was decreased to half of control group, endorsing that DEP can achieve drug screening.
- vi. Under normal growth conditions, trapping trend of wild type and resistant CCRF-CEM cells was similar. When 250 nM doxorubicin was applied during 18h, trapping ratio was decreased by 1.6.

As a future work, it was planned that solutions for the challenges of this system should be applied. First of all, cell adhesion occurred due to parylene-cell interaction. As 1st solution, the duration of PEG was prolonged. However, this problem continued. Therefore, optimum conditions for PEG coating should be determined. As another way, channel material can be changed. Secondly, due to usage of large volume in the inlet reservoir, cell precipitation occurred. Therefore, zero-dead volume sample loading interface can be exploited in the inlet of this LOC system. Finally, system cleaning was a challenge since microfluidic tubing should be demounted from the system for cleaning with DI. When it was remounted to system after DI cleaning, air bubbling can occur. Therefore, a valve and tubing system should be constructed for cleaning of channel without demounting of any parts between each run by preventing misinterpretation of results.

After these problems are solved, this system can be utilized for the drug-screening analysis by increasing the number of cell lines under examination.

There are eight different MDR mechanisms, defined up to now. The most abundant one is the overexpression of membrane proteins providing drug efflux. The relation between one of them, P-gp, and variations in electrical properties was defined. On the other hand, if mechanism behind MDR does not change the dielectrical properties of cells, MDR detection is not possible by electrical methods. Moreover, the level of MDR directly affects DEP response. MDR detection in the clinically-relevant model, developed in this study, was not achieved by the LOC system. Although this is a considerably big obstacle for clinical usage of dielectrophoretic detection of MDR, the utilization of this system in the chemotherapy guidance can work for highly resistant cancers if a threshold value is determined for the level of resistance, detectable by DEP.

Finally, to study with this system, first of all cancer cells should be separated from blood cells. Fortunately, there are lots of studies in this area for both the detection and classification of leukemia cells and CTCs. Therefore, when all these systems complete their maturation, they can be combined.

REFERENCES

- [1] S. Ogino, C. S. Fuchs, and E. Giovannucci, “How many molecular subtypes? Implications of the unique tumor principle in personalized medicine,” *Expert Rev Mol Diagn.*, vol. 12, no. 6, pp. 621–628, 2012.
- [2] J. Zhou, *Multi-Drug Resistance in Cancer*. Hertfordshire: Humana Press, 2010.
- [3] Y. Demircan, E. Özgür, and H. Külah, “Dielectrophoresis: Applications and future outlook in point of care,” *Electrophoresis*. pp. 1008–1027, 2013.
- [4] F. H. Labeed, H. M. Coley, H. Thomas, and M. P. Hughes, “Assessment of Multidrug Resistance Reversal Using Dielectrophoresis and Flow Cytometry,” vol. 85, no. September, pp. 2028–2034, 2003.
- [5] L. Jameson and D. Longo, “Precision Medicine — Personalized, Problematic, and Promising,” *N. Engl. J. Med.*, vol. 362, no. 5, pp. 567–571, 2011.
- [6] O. E. Streeter, P. J. Beron, and P. N. Iyer, “Precision Medicine,” *Otolaryngol. Clin. North Am.*, 2017.
- [7] P. FDA, “Where science meets technology,” 2016.
- [8] N. R. C. of the N. Academies, *Toward Precision Medicine: Building a Knowledge Network for Biomedical*. Washington, 2011.
- [9] V. T. DeVita and E. Chu, “Principles of Cancer Chemotherapy,” in *Physicians’ Cancer Chemotherapy Drug Manual 2015*, E. Chu and V. T. DeVita, Eds. Jones and Bartlett Learning, 2015.

- [10] J. J. Mondal, AK Panigrahi, and AR. Khuda-Bukhsh, “Conventional Chemotherapy: Problems and Scope for Combined Therapies with Certain Herbal Products and Dietary Supplements,” *Austin J Mol Cell Biol.*, vol. 1, no. 1, p. :10, 2014.
- [11] “What is chemotherapy?,” 2016. [Online]. Available: http://www.chemotherapy.com/new_to_chemo/what_is_chemo/. [Accessed: 30-Oct-2017].
- [12] S. Knapton, “Chemotherapy warning as hundreds die from cancer-fighting drugs,” *The Telegraph*, 2016. [Online]. Available: <https://www.telegraph.co.uk/science/2016/08/30/chemotherapy-warning-as-hundreds-die-from-cancer-fighting-drugs/>. [Accessed: 15-Oct-2017].
- [13] D. B. Longley and P. G. Johnston, “Molecular mechanisms of drug resistance,” *J. Pathol.*, vol. 205, no. 2, pp. 275–292, 2005.
- [14] S. Ogino, C. S. Fuchs, and E. Giovannucci, “How many molecular subtypes? Implications of the unique tumor principle in personalized medicine,” *Expert Rev Mol Diagn.*, vol. 12, no. 6, pp. 621–628, 2012.
- [15] N. Servant *et al.*, “Bioinformatics for precision medicine in oncology: Principles and application to the SHIVA clinical trial,” *Front. Genet.*, vol. 5, , pp. 1–16, 2014.
- [16] A. Benson, “Precision medicine in oncology: a complicated idea needs a simple solution,” Boston University, 2016.
- [17] “Gene ID:1950.” [Online]. Available: <https://www.ncbi.nlm.nih.gov/gene/1950>. [Accessed: 01-Aug-2017].
- [18] F. Ciardiello *et al.*, “Delivering precision medicine in oncology today and in

- future-the promise and challenges of personalised cancer medicine: A position paper by the European Society for Medical Oncology (ESMO),” *Ann. Oncol.*, vol. 25, no. 9, pp. 1673–1678, 2014.
- [19] C. Fedele, R. W. Tothill, and G. A. McArthur, “Navigating the challenge of tumor heterogeneity in cancer therapy,” *Cancer Discov.*, 2014.
- [20] B. Zhao, J. R. Pritchard, D. A. Lauffenburger, and M. T. Hemann, “Addressing genetic tumor heterogeneity through computationally predictive combination therapy,” *Cancer Discov.*, 2014.
- [21] J. Barretina, G. Caponigro, and N. Stransky, “The Cancer Cell Line Encyclopedia enables predictive modeling of anticancer drug sensitivity,” *Nature*, vol. 483, no. 7391, pp. 603–607, 2012.
- [22] Y. Demircan, A. Koyuncuoğlu, M. Erdem, E. Özgür, U. Gündüz, and H. Kūlah, “Label-free detection of multidrug resistance in K562 cells through isolated 3D-electrode dielectrophoresis,” *Electrophoresis*, vol. 36, no. 9–10, pp. 1149–1157, 2015.
- [23] M. Kartal-Yandim, A. Adan-Gokbulut, and Y. Baran, “Molecular mechanisms of drug resistance and its reversal in cancer,” *Crit. Rev. Biotechnol.*, vol. 36, no. 4, pp. 716–726, 2016.
- [24] K. Kapoor, H. M. Sim, and S. V. Ambudkar, “Multidrug Resistance in Cancer: A Tale of ABC Drug Transporters,” in *Molecular Mechanisms of Tumor Cell Resistance to Chemotherapy Resistance to Targeted Anti-Cancer Therapeutics*, B. Bonavida, Ed. Los Angeles, USA: Springer, 2013, pp. 1–34.
- [25] Z. Chen *et al.*, “Mammalian drug efflux transporters of the ATP binding cassette (ABC) family in multidrug resistance: A review of the past decade,” *Cancer Lett.*, vol. 370, no. 1, pp. 153–164, 2016.

- [26] R. L. Juliano and V. Lingbc, "A surface glycoprotein modulating drug permeability in Chinese hamster ovary cell mutants," *Biochim. Biophys. Acta-Biomembr.*, vol. 455, no. 1, pp. 152–162, 1976.
- [27] A. J. Gifford *et al.*, "Role of the E45K-reduced folate carrier gene mutation in methotrexate resistance in human leukemia cells," *Leukemia*, vol. 16, no. 12, pp. 2379–2387, 2002.
- [28] H. S. Friedman, S. H. Kaufmann, and S. M. Ludeman, "Cyclophosphamide Resistance in Medulloblastoma," *Cancer Res.*, vol. 52, no. 19, pp. 5373–5378, 1992.
- [29] C. O'Loughlin, M. Heenan, S. Coyle, and M. Clynes, "Altered cell cycle response of drug-resistant lung carcinoma cells to doxorubicin," *Eur. J. Cancer*, vol. 36, no. 9, pp. 1149–1160, 2000.
- [30] M. Motwani, T. M. Delohery, and G. K. Schwartz, "Sequential Dependent Enhancement of Caspase Activation and Apoptosis by Flavopiridol on Paclitaxel-treated Human Gastric and Breast Cancer Cells Sequential Dependent Enhancement of Caspase Activation and Apoptosis by Flavopiridol on Paclitaxel-treated Hum," *Clin. Cancer Res.*, vol. 5, no. July, pp. 1876–1883, 1999.
- [31] T. E. Merchant, P. Meneses, L. W. Gierke, W. Den Otter, and T. Glonek, "31P Magnetic Resonance Phospholipid Profiles of Neoplastic Human Breast Tissues," *Br. J. Cancer*, vol. 63, no. 5, pp. 693–698, 1991.
- [32] T. E. Merchant, P. W. de Graaf, B. D. Minsky, H. Obertop, and T. Glonek, "Esophageal cancer phospholipid characterization by 31P NMR," *NMR Biomed.*, vol. 6, no. 3, pp. 187–193, 1993.
- [33] Y. A. Luqmani, "Mechanisms of Drug Resistance in Cancer Chemotherapy,"

Med. Princ. Pract., vol. 14, no. 1, pp. 35–48, 2008.

- [34] R. B. Mokhtari *et al.*, “Combination therapy in combating cancer,” *Oncotarget*, vol. 8, no. 23, pp. 38022–38043, 2015.
- [35] H. Bu, Y. Gao, and Y. Li, “Overcoming multidrug resistance (MDR) in cancer by nanotechnology,” *Sci. China Chem.*, vol. 53, no. 11, pp. 2226–2232, 2010.
- [36] Q. Wu, Z. Yang, Y. Nie, Y. Shi, and D. Fan, “Multi-drug resistance in cancer chemotherapeutics: Mechanisms and lab approaches,” *Cancer Lett.*, vol. 347, no. 2, pp. 159–166, 2014.
- [37] P.-C. Mahmood, Tahrin, Yang, “Western Blot: Technique, Theory, and Trouble Shooting,” *N Am J Med Sci.*, vol. 4, no. 9, pp. 429–434, 2012.
- [38] T. A. Therapeutics, *Resistance to Targeted ABC Transporters in Cancer*, vol. 4. 2015.
- [39] E. A. Henslee *et al.*, “Rhythmic potassium transport regulates the circadian clock in human red blood cells,” *Nat. Commun.*, 2017.
- [40] J. Lee, Y. Kim, and M. Kim, “Negative-dielectrophoresis separation modules based high throughput and high efficient cell sorting platform for leukemia cell,” *Sensors*, 2011.
- [41] P. R. C. Gascoyne, J. Noshari, T. J. Anderson, and F. F. Becker, “Isolation of rare cells from cell mixtures by dielectrophoresis,” *Electrophoresis*, vol. 30, no. 8, pp. 1388–1398, 2009.
- [42] A. C. Sabuncu, A. J. Asmar, M. W. Stacey, and A. Beskok, “Differential dielectric responses of chondrocyte and Jurkat cells in electromanipulation buffers,” *Electrophoresis*, 2015.

- [43] S. Park, Y. Zhang, T.-H. Wang, and S. Yang, “Continuous dielectrophoretic bacterial separation and concentration from physiological media of high conductivity,” *Lab Chip*, 2011.
- [44] L. Duncan, H. Shelmerdine, H. Coley, and F. Labeed, “Assessment of the dielectric properties of drug sensitive and resistant leukaemic cells before and after ion channel blockers using dielectrophoresis,” *NSTI-Nanotech*, vol. 2, pp. 45–48, 2006.
- [45] H. M. Coley, F. H. Labeed, H. Thomas, and M. P. Hughes, “Biophysical characterization of MDR breast cancer cell lines reveals the cytoplasm is critical in determining drug sensitivity,” *Biochim. Biophys. Acta - Gen. Subj.*, vol. 1770, no. 4, pp. 601–608, 2007.
- [46] Y. Demircan, A. Koyuncuoğlu, M. Erdem, E. Özgür, U. Gündüz, and H. Külah, “Detection of imatinib resistance in K562 leukemia cells by 3D-electrodes contactless dielectrophoresis,” vol. 1, June, pp. 2086–2089, 2013.
- [47] Y. Demircan, M. Erdem, E. Ozgur, U. Gunduz, and H. Kulah, “Determination of multidrug resistance level in K562 Leukemia cells by 3D-electrode contactless dielectrophoresis,” *Proc. IEEE Int. Conf. Micro Electro Mech. Syst.*, pp. 837–840, 2014.
- [48] Y. Demircan, M. Erdem, E. Özgür, U. Gündüz, and H. Külah, “Label-free Multidrug Resistance Detection in MCF7 Cells by Isolated 3D-electrode Dielectrophoresis,” in *Dielectrophoresis 2014*, 2014.
- [49] Y. Demircan Yalçın, G. Özkayar, E. Özgür, U. Gündüz, and H. Külah, “A DEP-Based Lab-On-A-Chip System for Detection of Multidrug Resistance in K562 Leukemia Cells,” in *Hilton Head 2016*, 2016, pp. 316–319.
- [50] L. Gay, A.-M. Baker, and T. A. Graham, “Tumour Cell Heterogeneity,”

F1000Research, vol. 5, p. 238, 2016.

- [51] S. Maddika *et al.*, “Cell survival, cell death and cell cycle pathways are interconnected: Implications for cancer therapy,” *Drug Resist. Updat.*, vol. 10, no. 1–2, pp. 13–29, 2007.
- [52] J. J. Tyson, A. Csikasz-Nagy, and B. Novak, “The dynamics of cell cycle regulation,” *BioEssays*, vol. 24, no. 12, pp. 1095–1109, 2002.
- [53] H. Lodish *et al.*, Eds., “Regulating the eukaryotic cell cycle,” in *Molecular Cell Biology*, 6th ed., USA: W.H. Freeman and Company, 2008.
- [54] M. Graw-Hill, “The cell cycle.” [Online]. Available: <https://www.tes.com/lessons/V39SnUYVKZKyBg/cell-cycle-m-phase%0A>. [Accessed: 15-Oct-2017].
- [55] “No Title.” [Online]. Available: <http://ib.bioninja.com.au/standard-level/topic-1-cell-biology/16-cell-division/mitosis.html%0A>. [Accessed: 15-Oct-2017].
- [56] M. B. Kastan and J. Bartek, “Cell-cycle checkpoints and cancer,” *Nature*, vol. 432, no. 7015, pp. 316–323, 2004.
- [57] H. Lodish *et al.*, Eds., “Regulation of the Eukaryotic Cell Cycle,” in *Molecular Cell Biology*, 4th ed., New York: W. H. Freeman.
- [58] Z. Darzynkiewicz and H. Zhao, “Cell Cycle Analysis by Flow Cytometry,” *eLS*, 2014.
- [59] B. Alberts, A. Johnson, J. Lewis, M. Raff, K. Roberts, and P. Walter, Eds., “The Cell Cycle and Programmed Cell Death,” in *Molecular Biology of the Cell*, 4th ed., 2002.

- [60] G. Kroemer *et al.*, “Classification of Cell Death 2009,” *Cell Death Differ.*, vol. 16, no. 1, pp. 3–11, 2009.
- [61] J. F. R. Kerr, A. H. Wyllie, and A.R: Currie, “Apoptosis: a Basic Biological Phenomenon With Wide- Ranging Implications in Tissue Kinetics,” *J. Intern. Med.*, vol. 258, no. 6, pp. 479–517, 1972.
- [62] N. Kumar, “Apoptosis: Influence of the Xenobiotics and Diseases conditions,” 2015. [Online]. Available: <https://www.slideshare.net/naveenkumarsingh165/apoptosis-56205153>. [Accessed: 15-Oct-2017].
- [63] A. Ghali and S. J., “Regulation of Ceramide Channel Formation and Disassembly: Insights on the Initiation of Apoptosis,” *Saudi J Biol Sci.*, vol. 22, no. 6, pp. 760–772, 2015.
- [64] G. Murti, “apoptosis akyuvar,” 2013. [Online]. Available: Col Sem Of White Blood Cell Undergoing Apoptosis is a photograph by Dr Gopal Murti which was uploaded on May 5th, 2013.%0A. [Accessed: 13-Nov-2017].
- [65] K. Kumaraswamy, M. Archana, Bastian, and T. Yogesh, “Various methods available for detection of apoptotic cells- A review,” *Indian J. Cancer*, vol. 50, no. 3, p. 274, 2013.
- [66] H. Lodish *et al.*, Eds., “Cancer,” in *Molecular Cell Biology*, 4th ed., New York: W. H. Freeman.
- [67] R. Lüpertz, W. Wätjen, R. Kahl, and Y. Chovolou, “Dose- and time-dependent effects of doxorubicin on cytotoxicity, cell cycle and apoptotic cell death in human colon cancer cells,” *Toxicology*, vol. 271, no. 3, pp. 115–121, 2010.
- [68] “American Cancer Society.” [Online]. Available: <https://www.cancer.org/>.

[Accessed: 13-Nov-2017].

- [69] C. L. Sawyers, “Chronic myeloid leukemia,” *N. Engl. J. Med.*, vol. 340, no. 17, pp. 1330–40, 1999.
- [70] C.-H. Pui, L. L. Robison, and A. T. Look, “Acute lymphoblastic leukaemia,” *Lancet*, vol. 371, no. 9617, pp. 1030–1043, 2008.
- [71] “National Cancer Institute.” [Online]. Available: <https://www.cancer.gov/>. [Accessed: 05-Jan-2018].
- [72] WebMD, “Drugs & Medications Search.” [Online]. Available: <https://www.webmd.com/drugs/condition-486-Acute+Promyelocytic+Leukemia>. [Accessed: 10-Jan-2017].
- [73] C. Sullivan, C. Peng, Y. Chen, D. Li, and S. Li, “Targeted therapy of chronic myeloid leukemia,” *Biochem. Pharmacol.*, vol. 80, no. 5, pp. 584–591, 2010.
- [74] E. J. Jabbour and H. Kanterjian, “CME Information: Chronic myeloid leukemia: 2014 update on diagnosis, monitoring, and management Instructions on Receiving Credit,” *Am. J. Hematol.*, vol. 91, no. 5, pp. 252–65, 2016.
- [75] S. P. Hunger and C. G. Mullighan, “Re-defining ALL classification: toward detecting high-risk ALL and implementing precision medicine,” *Blood*, vol. 125, no. 26, pp. 3977–3988, 2015.
- [76] R. P. Warrell *et al.*, “Differentiation therapy of acute promyelocytic leukemia with tretinoin (all-trans-retinoic acid),” *The New England Journal of Medicine*, vol. 324, no. 20, pp. 1385–1393, 1991.
- [77] J. J. L. Lertora and K. M. Vanevski, “Introduction to pharmacokinetics and pharmacodynamics,” *Small Mol. Ther. Genet. Dis.*, pp. 35–54, 2010.

- [78] M. Deininger, E. Buchdunger, and B. J. Druker, "Review in translational hematology The development of imatinib as a therapeutic agent for chronic myeloid leukemia," *Blood*, vol. 105, no. 7, pp. 2640–2653, 2005.
- [79] T. Mughal and A. Schrieber, "Principal long-term adverse effects of imatinib in patients with chronic myeloid leukemia in chronic phase," *Biol. Targets Ther.*, p. 315, 2010.
- [80] J. Cunha, "Gleevec Side Effects," 2017. [Online]. Available: <https://www.rxlist.com/gleevec-side-effects-drug-center.htm>. [Accessed: 10-Jan-2018].
- [81] N. P. Shah, C. Tran, F. Y. Lee, P. Chen, D. Norris, and C. L. Sawyers, "Overriding Imatinib Resistance with a Novel ABL Kinase Inhibitor," vol. 305, no. July, pp. 399–402, 2004.
- [82] M. A. Sliwinska *et al.*, "Induction of senescence with doxorubicin leads to increased genomic instability of HCT116 cells," *Mech. Ageing Dev.*, vol. 130, no. 1–2, pp. 24–32, 2009.
- [83] L. Delva *et al.*, "Resistance to all-trans retinoic acid (ATRA) therapy in relapsing acute promyelocytic leukemia: study of in vitro ATRA sensitivity and cellular retinoic acid binding protein levels in leukemic cells," *Blood*, vol. 82, no. 7, pp. 2175–81, 1993.
- [84] C. Haung Meng-Er, Shu-rong, L. Jia-xiang, and G. Long-jun, "Acid in the Leukemia Treatment," *Blood*, vol. 72, no. 2, pp. 567–572, 1988.
- [85] M. S. Tallman and J. Andersen, "Journal Medicine ©," *Library (Lond)*., vol. 337, pp. 949–955, 1997.
- [86] A. Tomita, H. Kiyoi, and T. Naoe, "Mechanisms of action and resistance to all-

trans retinoic acid (ATRA) and arsenic trioxide (As₂O₃) in acute promyelocytic leukemia,” *Int. J. Hematol.*, vol. 97, no. 6, pp. 717–725, 2013.

- [87] J. L. Wilding and W. F. Bodmer, “Cancer cell lines for drug discovery and development,” *Cancer Res.*, vol. 74, no. 9, pp. 2377–2384, 2014.
- [88] M. McDermott *et al.*, “In vitro Development of Chemotherapy and Targeted Therapy Drug-Resistant Cancer Cell Lines: A Practical Guide with Case Studies,” *Front. Oncol.*, vol. 4, no. March, 2014.
- [89] E. A. Henslee *et al.*, “Accurate quantification of apoptosis progression and toxicity using a dielectrophoretic approach,” *Analyst*, vol. 141, no. 23, pp. 6408–6415, 2016.
- [90] M.V. Berridge, P.M. Herst, and A.S. Tan, Tetrazolium dyes as tools in cell biology: New insights into their cellular reduction. *Biotechnology Annual Review* 11, pp. 127-152, 2005.
- [91] ATCC, “XTT Cell Proliferation Assay Kit Instruction Manual”, 2011.
- [92] V. Istvan *et al.*, “A novel assay for apoptosis Flow cytometric detection of phosphatidylserine early apoptotic cells using fluorescein labelled expression on Annexin V,” *ournal Immunol. Methods*, vol. 184, no. 95, pp. 39–51, 1995.
- [93] H. J. Mulhall, A. Cardnell, K. F. Hoettges, F. H. Labeed, and M. P. Hughes, “Apoptosis progression studied using parallel dielectrophoresis electrophysiological analysis and flow cytometry,” *Integr. Biol.*, vol. 7, no. 11, pp. 1396–1401, 2015.
- [94] G. Sena, C. Onado, P. Cappella, F. Montalenti, and P. Ubezio, “Measuring the complexity of cell cycle arrest and killing of drugs: Kinetics of phase-specific effects induced by taxol,” *Cytometry*, vol. 37, no. 2, pp. 113–124, 1999.

- [95] I. EMD Millipore Corporation, “Muse™ Cell Cycle Kit User ’ s Guide,” vol. 100106, 2013.
- [96] B. Alberts, A. Johnson, J. Lewis, M. Raff, K. Roberts, and P. Walter, Eds., “Membrane Transport of Small Molecules and the Electrical Properties of Membranes,” in *Molecular Biology of the Cell*, 4th ed., New York, 2002.
- [97] Y. Huang and W. Sadée, “Membrane transporters and channels in chemoresistance and -sensitivity of tumor cells,” *Cancer Lett.*, vol. 239, no. 2, pp. 168–182, 2006.
- [98] H. Lodish *et al.*, Eds., “Transmembrane transport of ions and small molecules,” in *Molecular Cell Biology*, 6th ed., England: W.H. Freeman and Company, 2008.
- [99] B. Bonavida, *Molecular Mechanisms of Tumor Cell Resistance to Chemotherapy*, vol. 1. 2013.
- [100] K. Academy, “Active transport.” [Online]. Available: <https://www.khanacademy.org/science/biology/membranes-and-transport/active-transport/a/active-transport%0A>. [Accessed: 15-Oct-2017].
- [101] C. D. Bortner and J. A. Cidlowski, “Ion channels and apoptosis in cancer,” *Philos. Trans. R. Soc. B Biol. Sci.*, vol. 369, no. 1638, pp. 20130104–20130104, 2014.
- [102] V. Lehen’kyi, G. Shapovalov, R. Skryma, and N. Prevarskaya, “Ion channels and transporters in cancer. 5. Ion channels in control of cancer and cell apoptosis,” *AJP Cell Physiol.*, vol. 301, no. 6, pp. C1281–C1289, 2011.
- [103] S. Orrenius, B. Zhivotovsky, and P. Nicotera, “Regulation of cell death: The calcium-apoptosis link,” *Nat. Rev. Mol. Cell Biol.*, vol. 4, no. 7, pp. 552–565,

2003.

- [104] A. Kondratskyi, K. Kondratska, R. Skryma, and N. Prevarskaya, “Ion channels in the regulation of apoptosis,” *Biochim. Biophys. Acta - Biomembr.*, vol. 1848, no. 10, pp. 2532–2546, 2015.
- [105] T. J. Jentsch, “VRACs and other ion channels and transporters in the regulation of cell volume and beyond,” *Nat. Rev. Mol. Cell Biol.*, vol. 17, no. 5, pp. 293–307, 2016.
- [106] W. J. Brackenbury, *Ion Channels in Cancer*. 2016.
- [107] J. Xia *et al.*, “Ion channels or aquaporins as novel molecular targets in gastric cancer,” *Mol. Cancer*, vol. 16, no. 1, pp. 1–10, 2017.
- [108] S. Pillozzi *et al.*, “HERG potassium channels are constitutively expressed in primary human acute myeloid leukemias and regulate cell proliferation of normal and leukemic hemopoietic progenitors,” *Leukemia*, vol. 16, no. 9, pp. 1791–1798, 2002.
- [109] E. K. Hoffmann and I. H. Lambert, “Ion channels and transporters in the development of drug resistance in cancer cells,” *Philos. Trans. R. Soc. B Biol. Sci.*, vol. 369, no. 1638, pp. 20130109–20130109, 2014.
- [110] K. A. Poulsen *et al.*, “Deregulation of apoptotic volume decrease and ionic movements in multidrug-resistant tumor cells: role of chloride channels,” *Am. J. Physiol. Physiol.*, vol. 298, no. 1, pp. C14–C25, 2010.
- [111] M. A. Mansor and M. R. Ahmad, “Single cell electrical characterization techniques,” *Int. J. Mol. Sci.*, vol. 16, no. 6, pp. 12686–12712, 2015.
- [112] Agilent, “Agilent Impedance Measurement Handbook A guide to measurement

- technology and techniques,” *Measurement*, p. 140, 2009.
- [113] T. Sun and H. Morgan, “Single-cell microfluidic Impedance cytometry: A review,” *Microfluid. Nanofluidics*, vol. 8, no. 4, pp. 423–443, 2010.
- [114] U. Kiel, V. Rudols, and W. Erkli, “Eine Methode, die elektrische Leits,” vol. 237, pp. 237–238.
- [115] H. Fricke, “A mathematical treatment of electrical conductivity of colloids and cell suspensions.,” pp. 375–384, 1924.
- [116] Y. Xu, X. Xie, Y. Duan, L. Wang, Z. Cheng, and J. Cheng, “A review of impedance measurements of whole cells,” *Biosens. Bioelectron.*, vol. 77, pp. 824–836, 2016.
- [117] I. Giaever and C. R. Keese, “Monitoring fibroblast behavior in tissue culture with an applied electric field,” *Proc. Natl. Acad. Sci. U. S. A.*, vol. 81, no. 12, pp. 3761–3764, 1984.
- [118] X. Cheng *et al.*, “Cell detection and counting through cell lysate impedance spectroscopy in microfluidic devices,” *Lab Chip*, vol. 7, no. 6, pp. 746–755, 2007.
- [119] G. L. Damhorst, “Detection,” vol. 15, no. 5, pp. 895–905, 2014.
- [120] M. Ibrahim, J. Claudel, D. Kourtiche, B. Assouar, and M. Nadi, “Physical and electrical modeling of interdigitated electrode arrays for bioimpedance spectroscopy,” *Lect. Notes Electr. Eng.*, vol. 83 LNEE, pp. 169–189, 2011.
- [121] E. R. Cohen *et al.*, *Quantities, Units and symbols in Physical Chemistry*, 3rd ed. Cambridge, UK: RSC Publishing, 2007.

- [122] S. C. Grant and D. J. W. Wallwork, *Physical chemistry for students of pharmacy and biology*, 2nd ed. New York: Longmans Green & Co., 1977.
- [123] G. Guigas, C. Kalla, and M. Weiss, “The degree of macromolecular crowding in the cytoplasm and nucleoplasm of mammalian cells is conserved,” *FEBS Lett.*, vol. 581, no. 26, pp. 5094–5098, 2007.
- [124] H. Wang *et al.*, “Real-time monitoring efficiency and toxicity of chemotherapy in patients with advanced lung cancer,” *Clin. Epigenetics*, vol. 7, no. 1, pp. 1–11, 2015.
- [125] Van der Woude, “Preoperative evaluation and monitoring chemotherapy in patients with high-grade osteogenic and Ewing’s sarcoma: review of current modalities,” *Skeletal Radiol.*, vol. 27, no. 1, pp. 18–21, 1998.
- [126] L.-F. de Geus-Oei, D. Vriens, H. W. M. van Laarhoven, W. T. A. van der Graaf, and W. J. G. Oyen, “Monitoring and Predicting Response to Therapy with 18F-FDG PET in Colorectal Cancer: A Systematic Review,” *J. Nucl. Med.*, vol. 50, no. Suppl_1, p. 43S–54S, 2009.
- [127] B. J. Tromberg *et al.*, “Diffuse optics in breast cancer: Detecting tumors in premenopausal women and monitoring neoadjuvant chemotherapy,” *Breast Cancer Res.*, vol. 7, no. 6, pp. 279–285, 2005.
- [128] M. Lobbes, R. Prevos, and M. Smidt, “Response monitoring of breast cancer patients receiving neoadjuvant chemotherapy using breast MRI – a review of current knowledge,” *J. Cancer Ther. Res.*, vol. 1, no. 1, p. 34, 2012.
- [129] W. A. Weber and H. Wieder, “Monitoring chemotherapy and radiotherapy of solid tumors,” *Eur. J. Nucl. Med. Mol. Imaging*, vol. 33, no. SUPPL. 13, 2006.
- [130] C. D. Jennings and K. A. Foon, “Flow cytometry: recent advances in diagnosis

- and monitoring leukemia,” *Cancer Investig.*, vol. 15, no. 4, pp. 384–399, 1997.
- [131] M. Chen, C. Hou, D. Huo, J. Bao, H. Fa, and C. Shen, “An electrochemical DNA biosensor based on nitrogen-doped graphene/Au nanoparticles for human multidrug resistance gene detection,” *Biosens. Bioelectron.*, vol. 85, pp. 684–691, 2016.
- [132] P. A. Rasheed and N. Sandhyarani, “Electrochemical DNA sensors based on the use of gold nanoparticles: a review on recent developments,” *Microchim. Acta*, vol. 184, no. 4, pp. 981–1000, 2017.
- [133] U. Hatipoglu, B. Çetin, and E. Yıldırım, “A novel zero-dead-volume sample loading interface for microfluidic devices : flexible hydraulic reservoir (FHR),” *J. Micromech. Microeng.*, vol. 28, 2018.

Appendix A: MATLAB code for $Re(f_{CM})$ vs frequency simulations

```
function
out=CM_with_effective_final(a_long,a_short,eps_i,eps_o,s
_i,s_o,eps_m,s_m)
r=(a_long/a_short)^3;
f=logspace(0,9,100000);
w=2*pi*f;
for k=1:100000
eps_1_comp=(eps_i-(1i*(s_i/w(1,k))));
eps_2_comp=(eps_o-(1i*(s_o/w(1,k))));
eps_med_comp=(eps_m-(1i*(s_m/w(1,k))));
num=(eps_1_comp-eps_2_comp);
den=(eps_1_comp+(2*eps_2_comp));
par=(num/den);
eps_eff_p=(eps_2_comp)*((r+(2*par))/(r-par));
CM=real((eps_eff_p-
eps_med_comp)/(eps_eff_p+(2*eps_med_comp)));
out(1,k)=CM;
end
p=plot(log10(f(1,:)),out(1,:));
xlabel('Frequency 10^x (Hz)');
ylabel('Re(f_C_M)');
title('Frequency vs Re(f_C_M)');
set(p,'Color','blue');
end
```


Appendix B: MATLAB code for the analysis of LOC system

Run_inspection.m file is compiled for the analysis.

Run_inspection.m

```
cytometry_data_view_doubleChannel_EF_Off  
cytometry_data_view_doubleChannel_EF_On
```

cytometry_data_view_doubleChannel_EF_Off.m

```
clear all; close all;  
%%% Data import %%%  
currentPath = pwd;  
inputPath = uigetdir('currentPath')  
file1Path = [inputPath, '\Freq1.csv'];  
importfilezurich(file1Path);  
%%% Impedance calculation %%%  
E1_complexCurrent = Freq1(:,2)+i*Freq1(:,3);  
E1_current = abs(E1_complexCurrent);  
voltage = 1; % real reading from 4 point measurements  
(0.5V was set)  
E1_impedance = voltage./E1_current; % correct for  
differential measurements  
E1_complexImp = voltage./E1_complexCurrent;  
E1_realImp = real(E1_complexImp);  
E1_imagImp = imag(E1_complexImp);  
E1_time = Freq1(:,1);  
E1_frequency = Freq1(:,4);  
time1 = E1_time;  
time10 = time1(1);  
time1 = time1 - time10; %seconds  
time1 = 1000*time1; %milliseconds  
disp('Impedance calculated!');  
%%% Baseline removal %%%  
E1_impedance_blineRemoved = msbackadj(time1,  
E1_impedance, ...  
'WindowSize', 5000, ...  
'StepSize', 300, ...  
'PreserveHeights', 'false', ...  
'SmoothMethod', 'none', ...  
'QuantileValue', 0.5, ...
```

```

'ShowPlot', 1);
disp('Baseline removed!');
%% Peak determination %%
[E1_imp_peaks, E1_imp_PFWHH, E1_imp_PExt] =
mspeaks(time1,
E1_impedance_blineRemoved,...
'Denoising', 'false',...
'FWHHFilter', 1,...
'OverSegmentationFilter', 5,...
'HeightFilter',100,...
'ShowPlot', 1);
disp('Peaks detected!');
%% Peak width calculation %%
E1_imp_numPeaks = length(E1_imp_peaks);
for i = 1:E1_imp_numPeaks
E1_imp_PExt_diff_temp(i) = E1_imp_PExt(i,2) -
E1_imp_PExt(i,1);
E1_imp_PFWHH_diff_temp(i) = E1_imp_PFWHH(i,2) -
E1_imp_PFWHH(i,1);
end
E1_imp_PExt_diff = transpose(E1_imp_PExt_diff_temp);
E1_imp_PFWHH_diff = transpose(E1_imp_PFWHH_diff_temp);
clear E1_imp_PExt_diff_temp E1_imp_PFWHH_diff_temp
%% Time conversion %%
time1_export = time1 / 1000; % milliseconds to seconds
%% Electrode impedance data export %%
E1_impedance_dataexport = [time1_export, E1_impedance,
E1_impedance_blineRemoved];
%% Peak data export %%
E1_imp_peak_time_export = E1_imp_peaks(:,1) / 1000; %
milliseconds to seconds
E1_imp_peak_dataexport = [E1_imp_peak_time_export,
E1_imp_peaks(:,2),
E1_imp_PExt_diff, E1_imp_PFWHH_diff];
%% Data plotting %%
figure
plot(time1_export, E1_impedance);
title('Absolute Impedance')
figure
plot(time1_export, E1_realImp);
title('Real Impedance')
figure
plot(time1_export, E1_imagImp);
title('Imaginary Impedance')
figure
plot(time1_export,E1_impedance_blineRemoved);
title('Baseline Removed Impedance')
%%
%%Channel2

```

```

%%% Data import %%%
file2Path = [inputPath, '\Freq2.csv'];
importfilezurich(file2Path);
%%% Impedance calculation %%%
E2_complexCurrent = Freq2(:,2)+j*Freq2(:,3);
E2_current = abs(E2_complexCurrent);
voltage = 1; % real reading from 4 point measurements
(0.5V was set)
E2_impedance = voltage./E2_current; % correct for
differential measurements
E2_complexImp = voltage./E2_complexCurrent;
E2_realImp = real(E2_complexImp);
E2_imagImp = imag(E2_complexImp);
E2_time = Freq2(:,1);
E2_frequency = Freq2(:,4);
time2 = E2_time;
time2_10 = time2(1);
time2 = time2 - time2_10; %seconds
time2 = 1000*time2; %milliseconds
disp('Ch2 Impedance calculated!');
%%% Baseline removal %%%
E2_impedance_blineRemoved = msbackadj(time2,
E2_impedance, ...
'WindowSize', 5000, ...
'StepSize', 300, ...
'PreserveHeights', 'false', ...
'SmoothMethod', 'none', ...
'QuantileValue', 0.5, ...
>ShowPlot', 1);
disp('Ch2 Baseline removed!');
%%% Peak determination %%%
[E2_imp_peaks, E2_imp_PFWHH, E2_imp_PExt] =
mspeaks(time2,
E2_impedance_blineRemoved, ...
'Denoising', 'false', ...
'FWHHFilter', 1, ...
'OverSegmentationFilter', 5, ...
'HeightFilter', 100, ...
>ShowPlot', 1);
disp('CH2 Peaks detected!');
%%% Peak width calculation %%%
E2_imp_numPeaks = length(E2_imp_peaks);
disp(E2_imp_numPeaks);
for j = 1:E2_imp_numPeaks
E2_imp_PExt_diff_temp(j) = E2_imp_PExt(j,2) -
E2_imp_PExt(j,1);
E2_imp_PFWHH_diff_temp(j) = E2_imp_PFWHH(j,2) -
E2_imp_PFWHH(j,1);
end

```

```

E2_imp_PExt_diff = transpose(E2_imp_PExt_diff_temp);
E2_imp_PFWHH_diff = transpose(E2_imp_PFWHH_diff_temp);
clear E2_imp_PExt_diff_temp E2_imp_PFWHH_diff_temp
%% Time conversion %%
time2_export = time2 / 1000; % milliseconds to seconds
%% Electrode impedance data export %%
E2_impedance_dataexport = [time2_export, E2_impedance,
E2_impedance_blineRemoved];
%% Peak data export %%
E2_imp_peak_time_export = E2_imp_peaks(:,1) / 1000; %
milliseconds to seconds
E2_imp_peak_dataexport = [E2_imp_peak_time_export,
E2_imp_peaks(:,2),
E2_imp_PExt_diff, E2_imp_PFWHH_diff];
%% Data plotting %%
figure
plot(time2_export, E2_impedance);
title('Ch2 Absolute Impedance')
figure
plot(time2_export, E2_realImp);
title('Ch2 Real Impedance')
figure
plot(time2_export, E2_imagImp);
title('Ch2 Imaginary Impedance')
figure
plot(time2_export, E2_impedance_blineRemoved);
title('Ch2 Baseline Removed Impedance')
%%
close all
%XCORR
Sample_Diff=xcorr_channels_func(
E1_impedance_blineRemoved,
E2_impedance_blineRemoved);
%Overwrite automatic value by inspection value
% Sample_Diff=1465;
disp('Sample Diff');
disp(Sample_Diff);
%%
%Calculate all with updated indexes
clearvars -except Sample_Diff inputPath
% close all
%%
%Repeat all
file1Path = [inputPath, '\Freq1.csv'];
importfilezurich(file1Path);
end_of_data=length(Freq1)-Sample_Diff;
%% Impedance calculation %%
E1_complexCurrent =
Freq1(1:end_of_data,2)+i*Freq1(1:end_of_data,3);

```

```

E1_current = abs(E1_complexCurrent);
voltage = 1; % real reading from 4 point measurements
(0.5V was set)
E1_impedance = voltage./E1_current; % correct for
differential measurements
E1_complexImp = voltage./E1_complexCurrent;
E1_realImp = real(E1_complexImp);
E1_imagImp = imag(E1_complexImp);
E1_time = Freq1(1:end_of_data,1);
E1_frequency = Freq1(1:end_of_data,4);
time1 = E1_time;
time10 = time1(1);
time1 = time1 - time10; %seconds
time1 = 1000*time1; %milliseconds
disp('Impedance calculated!');
%% Baseline removal %%
E1_impedance_blineRemoved = msbackadj(time1,
E1_impedance, ...
'WindowSize', 5000,...
'StepSize', 300,...
'PreserveHeights', 'false',...
'SmoothMethod', 'none',...
'QuantileValue', 0.5,...
'ShowPlot', 1);
disp('Baseline removed!');
%% Peak determination %%%
[E1_imp_peaks, E1_imp_PFWHH, E1_imp_PExt] =
mspeaks(time1,
E1_impedance_blineRemoved,...
'Denoising', 'false',...
'FHHFilter', 1,...
'OverSegmentationFilter', 5,...
'HeightFilter',100,...
'ShowPlot', 1);
disp('Peaks detected!');
%% Peak width calculation %%%
E1_imp_numPeaks = length(E1_imp_peaks);
for i = 1:E1_imp_numPeaks
E1_imp_PExt_diff_temp(i) = E1_imp_PExt(i,2) -
E1_imp_PExt(i,1);
E1_imp_PFWHH_diff_temp(i) = E1_imp_PFWHH(i,2) -
E1_imp_PFWHH(i,1);
end
E1_imp_PExt_diff = transpose(E1_imp_PExt_diff_temp);
E1_imp_PFWHH_diff = transpose(E1_imp_PFWHH_diff_temp);
clear E1_imp_PExt_diff_temp E1_imp_PFWHH_diff_temp
%% Time conversion %%%
time1_export = time1 / 1000; % milliseconds to seconds
%% Electrode impedance data export %%%

```

```

E1_impedance_dataexport = [time1_export, E1_impedance,
E1_impedance_blineRemoved];
%% Peak data export %%
E1_imp_peak_time_export = E1_imp_peaks(:,1) / 1000; %
milliseconds to seconds
E1_imp_peak_dataexport = [E1_imp_peak_time_export,
E1_imp_peaks(:,2),
E1_imp_PExt_diff, E1_imp_PFWHH_diff];
%% Data plotting %%
figure
plot(time1_export, E1_impedance);
title('Absolute Impedance')
figure
plot(time1_export, E1_realImp);
title('Real Impedance')
figure
plot(time1_export, E1_imagImp);
title('Imaginary Impedance')
figure
plot(time1_export, E1_impedance_blineRemoved);
title('Baseline Removed Impedance')
%%
%%Channel2
%% Data import %%
file2Path = [inputPath, '\Freq2.csv'];
importfilezurich(file2Path);
%% Impedance calculation %%
E2_complexCurrent =
Freq2(Sample_Diff:end,2)+j*Freq2(Sample_Diff:end,3);
E2_current = abs(E2_complexCurrent);
voltage = 1; % real reading from 4 point measurements
(0.5V was set)
E2_impedance = voltage./E2_current; % correct for
differential measurements
E2_complexImp = voltage./E2_complexCurrent;
E2_realImp = real(E2_complexImp);
E2_imagImp = imag(E2_complexImp);
E2_time = Freq2(Sample_Diff:end,1);
E2_frequency = Freq2(Sample_Diff:end,4);
time2 = E2_time;
time2_10 = time2(1);
time2 = time2 - time2_10; %seconds
time2 = 1000*time2; %milliseconds
disp('Ch2 Impedance calculated!');
%% Baseline removal %%
E2_impedance_blineRemoved = msbackadj(time2,
E2_impedance, ...
'WindowSize', 5000,...
'StepSize', 300,...

```



```

'PreserveHeights', 'false',...
'SmoothMethod', 'none',...
'QuantileValue', 0.5,...
>ShowPlot', 1);
disp('Ch2 Baseline removed!');
%% Peak determination %%%
[E2_imp_peaks, E2_imp_PFWHH, E2_imp_PExt] =
mspeaks(time2,
E2_impedance_blineRemoved,...
'Denoising', 'false',...
'FWHHFilter', 1,...
'OverSegmentationFilter', 5,...
'HeightFilter', 100 ,...
>ShowPlot', 1);
disp('CH2 Peaks detected!');
%% Peak width calculation %%%
E2_imp_numPeaks = length(E2_imp_peaks);
disp(E2_imp_numPeaks);
for j = 1:E2_imp_numPeaks
E2_imp_PExt_diff_temp(j) = E2_imp_PExt(j,2) -
E2_imp_PExt(j,1);
E2_imp_PFWHH_diff_temp(j) = E2_imp_PFWHH(j,2) -
E2_imp_PFWHH(j,1);
end
E2_imp_PExt_diff = transpose(E2_imp_PExt_diff_temp);
E2_imp_PFWHH_diff = transpose(E2_imp_PFWHH_diff_temp);
clear E2_imp_PExt_diff_temp E2_imp_PFWHH_diff_temp
%% Time conversion %%%
time2_export = time2 / 1000; % milliseconds to seconds
%% Electrode impedance data export %%%
E2_impedance_dataexport = [time2_export, E2_impedance,
E2_impedance_blineRemoved];
%% Peak data export %%%
E2_imp_peak_time_export = E2_imp_peaks(:,1) / 1000; %
milliseconds to seconds
E2_imp_peak_dataexport = [E2_imp_peak_time_export,
E2_imp_peaks(:,2),
E2_imp_PExt_diff, E2_imp_PFWHH_diff];
%% Data plotting %%%
figure
plot(time2_export, E2_impedance);
title('Ch2 Absolute Impedance')
figure
plot(time2_export, E2_realImp);
title('Ch2 Real Impedance')
figure
plot(time2_export, E2_imagImp);
title('Ch2 Imaginary Impedance')
figure

```

```

plot(time2_export,E2_impedance_blineRemoved);
title('Ch2 Baseline Removed Impedance')
%%
%clc
disp('Electric Field Off');
giren = 'Giren: ';
X_print = [giren,num2str(E1_imp_numPeaks)];
disp(X_print);
cikan = 'Cikan: ';
Y_print = [cikan,num2str(E2_imp_numPeaks)];
disp(Y_print);

```

cytometry_data_view_doubleChannel_EF_On.m

```

%%
%Clear all except the channel delay when EF is OFF
clearvars -except Sample_Diff
% close all
%%
%Repeat all
currentPath = pwd;
inputPath = uigetdir('curentPath')
file1Path = [inputPath, '\Freq1.csv'];
importfilezurich(file1Path);
end_of_data=length(Freq1)-Sample_Diff;
%% Impedance calculation %%
E1_complexCurrent =
Freq1(1:end_of_data,2)+i*Freq1(1:end_of_data,3);
E1_current = abs(E1_complexCurrent);
voltage = 1; % real reading from 4 point measurements
(0.5V was set)
E1_impedance = voltage./E1_current; % correct for
differential measurements
E1_complexImp = voltage./E1_complexCurrent;
E1_realImp = real(E1_complexImp);
E1_imagImp = imag(E1_complexImp);
E1_time = Freq1(1:end_of_data,1);
E1_frequency = Freq1(1:end_of_data,4);
time1 = E1_time;
time10 = time1(1);
time1 = time1 - time10; %seconds
time1 = 1000*time1; %milliseconds
disp('Impedance calculated!');
%% Baseline removal %%
E1_impedance_blineRemoved = msbackadj(time1,
E1_impedance, ...
'WindowSize', 5000,...
'StepSize', 300,...
'PreserveHeights', 'false',...)

```

```

'SmoothMethod', 'none',...
'QuantileValue', 0.5,...
>ShowPlot', 1);
disp('Baseline removed!');
%% Peak determination %%%
[E1_imp_peaks, E1_imp_PFWHH, E1_imp_PExt] =
mspeaks(time1,
E1_impedance_blineRemoved,...
'Denoising', 'false',...
'FWHHFilter', 1,...
'OverSegmentationFilter', 5,...
'HeightFilter', 100,...
>ShowPlot', 1);
disp('Peaks detected!');
%% Peak width calculation %%%
E1_imp_numPeaks = length(E1_imp_peaks);
for i = 1:E1_imp_numPeaks
E1_imp_PExt_diff_temp(i) = E1_imp_PExt(i,2) -
E1_imp_PExt(i,1);
E1_imp_PFWHH_diff_temp(i) = E1_imp_PFWHH(i,2) -
E1_imp_PFWHH(i,1);
end
E1_imp_PExt_diff = transpose(E1_imp_PExt_diff_temp);
E1_imp_PFWHH_diff = transpose(E1_imp_PFWHH_diff_temp);
clear E1_imp_PExt_diff_temp E1_imp_PFWHH_diff_temp
%% Time conversion %%%
time1_export = time1 / 1000; % milliseconds to seconds
%% Electrode impedance data export %%%
E1_impedance_dataexport = [time1_export, E1_impedance,
E1_impedance_blineRemoved];
%% Peak data export %%%
E1_imp_peak_time_export = E1_imp_peaks(:,1) / 1000; %
milliseconds to seconds
E1_imp_peak_dataexport = [E1_imp_peak_time_export,
E1_imp_peaks(:,2),
E1_imp_PExt_diff, E1_imp_PFWHH_diff];
%% Data plotting %%%
figure
plot(time1_export, E1_impedance);
title('Absolute Impedance')
figure
plot(time1_export, E1_realImp);
title('Real Impedance')
figure
plot(time1_export, E1_imagImp);
title('Imaginary Impedance')
figure
plot(time1_export, E1_impedance_blineRemoved);
title('Baseline Removed Impedance')

```

```

%%
%%Channel2
%% Data import %%
file2Path = [inputPath, '\Freq2.csv'];
importfilezurich(file2Path);
%% Impedance calculation %%
E2_complexCurrent =
Freq2(Sample_Diff:end,2)+j*Freq2(Sample_Diff:end,3);
E2_current = abs(E2_complexCurrent);
voltage = 1; % real reading from 4 point measurements
(0.5V was set)
E2_impedance = voltage./E2_current; % correct for
differential measurements
E2_complexImp = voltage./E2_complexCurrent;
E2_realImp = real(E2_complexImp);
E2_imagImp = imag(E2_complexImp);
E2_time = Freq2(Sample_Diff:end,1);
E2_frequency = Freq2(Sample_Diff:end,4);
time2 = E2_time;
time2_10 = time2(1);
time2 = time2 - time2_10; %seconds
time2 = 1000*time2; %miliseconds
disp('Ch2 Impedance calculated!');
%% Baseline removal %%
E2_impedance_blineRemoved = msbackadj(time2,
E2_impedance, ...
'WindowSize', 5000,...
'StepSize', 300,...
'PreserveHeights', 'false',...
'SmoothMethod', 'none',...
'QuantileValue', 0.5,...
>ShowPlot', 1);
disp('Ch2 Baseline removed!');
%% Peak determination %%
[E2_imp_peaks, E2_imp_PFWHH, E2_imp_PExt] =
mspeaks(time2,
E2_impedance_blineRemoved,...
'Denoising', 'false',...
'FWHHFilter', 1,...
'OverSegmentationFilter', 5,...
'HeightFilter',100 ,...
>ShowPlot', 1);
disp('CH2 Peaks detected!');
%% Peak width calculation %%
E2_imp_numPeaks = length(E2_imp_peaks);
disp(E2_imp_numPeaks);
for j = 1:E2_imp_numPeaks
E2_imp_PExt_diff_temp(j) = E2_imp_PExt(j,2) -
E2_imp_PExt(j,1);

```

```

E2_imp_PFWHH_diff_temp(j) = E2_imp_PFWHH(j,2) -
E2_imp_PFWHH(j,1);
end
E2_imp_PExt_diff = transpose(E2_imp_PExt_diff_temp);
E2_imp_PFWHH_diff = transpose(E2_imp_PFWHH_diff_temp);
clear E2_imp_PExt_diff_temp E2_imp_PFWHH_diff_temp
%% Time conversion %%%
time2_export = time2 / 1000; % milliseconds to seconds
%% Electrode impedance data export %%%
E2_impedance_dataexport = [time2_export, E2_impedance,
E2_impedance_blineRemoved];
%% Peak data export %%%
E2_imp_peak_time_export = E2_imp_peaks(:,1) / 1000; %
milliseconds to seconds
E2_imp_peak_dataexport = [E2_imp_peak_time_export,
E2_imp_peaks(:,2),
E2_imp_PExt_diff, E2_imp_PFWHH_diff];
%% Data plotting %%%
figure
plot(time2_export, E2_impedance);
title('Ch2 Absolute Impedance')
figure
plot(time2_export, E2_realImp);
title('Ch2 Real Impedance')
figure
plot(time2_export, E2_imagImp);
title('Ch2 Imaginary Impedance')
figure
plot(time2_export, E2_impedance_blineRemoved);
title('Ch2 Baseline Removed Impedance')
%%
%clc
disp('Electric Field ON');
giren = 'Giren: ';
X_print = [giren, num2str(E1_imp_numPeaks)];
disp(X_print);
cikan = 'Cikan: ';
Y_print = [cikan, num2str(E2_imp_numPeaks)];
disp(Y_print);

```


CURRICULUM VITAE

PERSONAL INFORMATION

Surname, Name: Demircan Yalçın, Yağmur
Nationality: Turkish (TC)
Date and Place of Birth: 1 September 1988, Zonguldak
Marital Status: Married
Phone: +905546166973
email: www.e149720@metu.edu.tr

EDUCATION

Degree Institution Year of Graduation

MS METU Electrical and Electronics Engineering 2013
BS METU Electrical and Electronics Engineering 2010
Zonguldak Science High School, Zonguldak 2005

WORK EXPERIENCE

Year Place Enrollment

5.1 2015-present Mikro Biyosistemler Inc. R&D Engineer
2010-2015 METU Research and Teaching Assistant
2008 July ERDEMİR Intern Engineering Student
2009 August TUBITAK Intern Engineering Student

FOREIGN LANGUAGES

Advanced English

PUBLICATIONS

Conferences:

Y. Demircan and H. Kùlah, "A Parylene Based Contactless 3D Dielectrophoresis Chip for Continuous Cell Separation, Trapping, and Manipulation Applications," *Microfluidics 2012*, p. 109, Heidelberg, Germany, 2012.

Y. Demircan, A. Koyuncuoglu, M. Erdem, E. Ozgur, U. Gunduz, and H. Kùlah, "Detection of Imatinib Resistance in K562 Leukemia Cells by 3D-Electrode Contactless Dielectrophoresis," *International Conference on Solid-State Sensors*,

Actuators, and Microsystems, Transducers '13, pp. 2086-2089, Barcelona, Spain, on June, 2013.

Y. Demircan, M. Erdem, E. Ozgur, U. Gunduz, and H. K ulah, "Determination of Multidrug Resistance Level in K562 Leukemia Cells by 3D-Electrode Contactless Dielectrophoresis," *International Conference on Microelectromechanical Systems (MEMS'14)*, pp. 837-840, San Francisco, Ca, USA, Jan. 2014.

Y. Demircan, M. Erdem, E. Ozgur, U. Gunduz, and H. K ulah, "Label-free Multidrug Resistance Detection in MCF7 Cells by Isolated 3D-electrode Dielectrophoresis," *Dielectrophoresis 2014*, London, England, July 2014. (Best presentation award).

Y. Demircan, E.  zg r, U. G nd z, and H. K ulah, "Dielectrophoretic Detection of Multidrug Resistance in Cancer," *2nd International Biosensor Congress*, Izmir, Turkey, June 2015.

G. Ozkayar, Y. Demircan, E.  zg r, U. G nd z, and H. K ulah, "Enrichment of K562 Human Leukemia Cells From Diluted Whole Blood by Using Dielectrophoresis," *2nd International Biosensor Congress*, Izmir, Turkey, June 2015.

Y. Demircan, S.  rg c, J. Musayev, E.  zg r, M. Erdem, U. G nd z, S. Eminoglu, H. K ulah, and T. Akin, "Label-free detection of leukemia cells with a lab-on-a-chip system integrating dielectrophoresis and cmos imaging," *International Conference on Solid-State Sensors, Actuators, and Microsystems, Transducers '15*, pp. 1589-1592, Alaska, USA, June 2015.

G. Ozkayar, Y. Demircan Yal ın, E.  zg r, U. G nd z, and H. K ulah, "A high-throughput microfluidic rare cell enrichment system based on dielectrophoresis and filtering," *26th Anniversary World Congress on Biosensors*, Gothenburg, Sweden, May 2016.

M.K. Aslan, Y. Demircan Yal ın, E. Ozgur, U. Gunduz, S. Eminoglu, H. K ulah, and T. Akin, "A High Throughput Lab-On-A-Chip System For Label Free Quantification Of Breast Cancer Cells Under Continuous Flow," *26th Anniversary World Congress on Biosensors*, Gothenburg, Sweden, May 2016.

Y. Demircan Yal ın, G. Ozkayar, E.  zg r, U. G nd z, and H. K ulah, "A DEP-Based Lab-On-A-Chip System for Detection of Multidrug Resistance in K562 Leukemia Cells," *Hilton Head Workshop 2016: A Solid-State Sensors, Actuators and Microsystems Workshop*, pp. 316-319, Hilton Head Island, USA, June 2016.

Z. Caglayan, Y. Demircan Yal ın, G. Ozkayar, E. Ozgur, U. G nd z, and H. K ulah, "Dielectrophoretic Spectra of CD133+/EPCAM+ HUH7 cancer stem cells

and HUH7 cancer cells,” *Dielectrophoresis 2016*, Massachusetts, USA, July 2016.

Journal papers:

Y. Demircan, A. Koyuncuoglu, M. Erdem, E. Ozgur, U. Gunduz, and H. Kùlah, “Label-free detection of multidrug resistance in K562 cells through isolated 3D-electrode dielectrophoresis,” *Electrophoresis*, 36, pp. 1149-1157, 2015.

Y. Demircan, E. Ozgur, and H. Kùlah, “Dielectrophoresis: Applications and future outlook in point of care,” *Electrophoresis*, 34, pp. 1008-1027, 2013.

Book chapters:

Y. Demircan, G. Yilmaz, and H. Kùlah, in: Demirci, U., Khademhosseini, A., Langer, R., Blander, J. (Eds.), *Electrophoresis and dielectrophoresis for Lab-on-a-chip (LOC) Analyses*, World Scientific Publishers, Singapore 2012, pp. 341-376.

HOBBIES

Modern and folkloric dances, swimming, movies, computer games, reading